

**NONLINEAR DYNAMICS OF A VIBRO-IMPACT SYSTEM
SUBJECTED TO ELECTROMAGNETIC INTERACTIONS**

JONG SI-CHUNG, BEng.

**THESIS SUBMITTED TO THE UNIVERSITY OF NOTTINGHAM
FOR THE DEGREE OF DOCTOR OF PHILOSOPHY**

FEBRUART 2015

Abstract

Impact moling is an effective method of pile driving and percussive drilling to bore underground tunnel for various civil applications such as pipe, cable and ducts installation.

An effective electro-vibroimpact system has been built on the basis of interactions between two sources of electromagnetic force. A vertical downward progression of mechanism into hard or brittle material required an increased magnitude of impact force within a compact geometry. Horizontal progression into clay is tested by combining periodic impact and static forces that produces an effective progression rate.

As a consequence of this experimental work, a prototype electro-vibroimpact system is tested. Electrical circuitry consists of a timer and batteries which is a compact arrangement, functioning as waveform generator, and power supply. A cylindrical hollow aluminium tube houses the main components such as electromagnetic solenoids and oscillating bar within. This protects the main components from clay while progressing into soil and also reduces soil resistance with a minimal surface area.

A mathematical model has also been numerically solved for both single and two degree-of-freedom system. Correlation has been achieved to a certain extent, and it is possible either deploy or further optimise this system.

Acknowledgements

I, Si-Chung Jong, research student of The University of Nottingham Malaysia Campus, take this opportunity to express my appreciation to my supervisor, Dr. Ko-Choong Woo for his continuous advice and guidance during the span of this research. My gratitude also goes to Dr. Vincent Lee of Curtin University who has greatly assisted me in the modelling and manufacturing of the first successful prototype alongside with Dr Woo.

Dr. Jee-Hou Ho also helped in starting up with writing the program script to solve the numerical model. Besides that, I sincerely thank my other supervisor, Professor Atanas Popov for helping me in developing my numerical coding techniques and provide ideas to improve the mathematical model.

It is my privilege to work in research laboratory NA16, where colleagues have been very supportive in technical and morale aspects. The environment of learning and running experiments together builds each other up while promotes perseverance in facing research hardships.

In addition, the team of Mr Winson Khoo, Mr Goh-Chun Lee, Mr Zhen-Yue Lim and Mr Zheng Yang Tai have contributed to manufacture the prototype experimental rig. The creativity and dedication that they possessed in carrying the project are truly remarkable.

Most importantly, I would like to thank The University of Nottingham for the Inter-Campus scholarship and the opportunity of research exchange program in the UK Campus. It was indeed an eye-opening experience

Table of Contents

Abstract	i
Acknowledgement	ii
Table of Contents	iv
Nomenclature	viii
Abbreviations	xi
List of Figures	xii
List of Tables	xxv

1. Introduction

1.1 Background	1
1.2 Aims and Objectives	4
1.3 An Overview of the Thesis	5

2. Literature Review	6
-----------------------------	----------

3. Experimental Rig

3.1 Introduction	15
3.2 Electromagnetic interactions between two sources	17
3.3 One degree-of-freedom electro-vibroimpact system in a vertical orientation	23
3.4 Two degree-of-freedom electro-vibroimpact system in vertical orientation	31
3.5 Two degree-of-freedom electro-vibroimpact system in horizontal orientation	47
3.6 Conclusions	59

4. Mathematical Model of Electro-Vibroimpact System

4.1 Introduction	61
4.2 Mathematical Model	63
4.3 Empirical or semi-empirical formulae	66
4.4 Obtaining an inductance equation of circuit	77

4.5 Equation of current variation	82
4.6 Mathematical model of one degree-of-freedom electro-vibroimpact system	92
4.7 Mathematical model of two degree-of-freedom electro-vibroimpact system	95
4.8 Experimental Correlation	101
4.9 Conclusions	102

5. Prototype Electro-Vibroimpact System

5.1 Introduction	104
5.2 Prototype experimental rig description	104
5.3 Schematic diagram	116
5.4 Results and discussions	117
5.5 Conclusions	135

6. Conclusions

6.1 Optimised electro-vibroimpact system	136
6.2 Mathematical model	139
6.3 Recommendations for future work	140
Appendix A. Datasheet of RS346-356 solenoid	141
Appendix B. Matlab script of plotting data from experimental results	143
Appendix C. Matlab and Dynamics script of numerical solution of the vibro- impact system	146
Appendix D. Time history of varying DC power supply to linear actuator	160
Appendix E. Time history of varying SSRL signal frequency	164
Appendix F. Engineering drawing of electro-vibroimpact system prototype	171
Reference	175

Nomenclature

- Ω Operating/signal frequency of the solid state relay turning on/off, Hz.
- ω Main frequency of the system supply, $2\pi f$ in rad/s.
- A Constant of inductance in Gaussian's form, H.
- B Constant of inductance in Gaussian's form.
- C Capacitance of the RLC circuit, F.
- C_1 Capacitance of the LM555 timer, F.
- c Damping coefficient of the stopper, Ns/m.
- e Distance of oscillating bar's initial position from the stopper surface, m.
- F_1 Electromagnetic force of the DC Solenoid, N.
- F_2 Electromagnetic force of the AC Solenoid, N.
- F_s Soil resistance acting on the electro vibro-impact machine, Ns/m.
- f Main frequency of the system supply, Hz.
- f_L Signal frequency of the AC voltage to the inductance test circuit, Hz.
- g Gravitational acceleration, ms^{-2} .

- i Current passing the coils of solenoid 2, A.
- k Stiffness of the stopper, N/m.
- L Inductance of the coil of the solenoid, H.
- l_c Length of the oscillating bar/conductor, m.
- l_s Length of RS 346-356 Solenoid, m.
- m_1 The mass of the oscillating bar, kg.
- m_2 Total mass of the electro vibro-impact rig and the oscillating bar, kg.
- P_{ctr} Switching control of operating frequency from on/off.
- Q The impedance of the inductance of the inductance test circuit, H/s.
- R Resistance of the RLC circuit, Ω .
- R_a Resistance of an added resistor to the inductance test circuit, Ω .
- R_s Resistance of a pure resistor modelled from Solenoid 2, Ω .
- R_1 Fixed resistor in the LM555 timer circuit, Ω .
- R_2 Resistance of a potentiometer that adjust the operating frequency in the LM555 timer circuit, Ω .

- T_{CD} Total cycle time of the LM555 timer, s.
- t Time, s.
- t_C Charging time of the LM555 timer, s.
- t_D Discharge time of the LM555 timer, s.
- V_0 The potential difference over the resistor R_a , V.
- V_s AC voltage supply from the variac to the RLC circuit, V.
- V_{ss} Supplied AC voltage in square wave to the inductance test circuit, V.
- X_1 Relative displacement of oscillating bar to the electro-vibroimpact machine, m.
- X_2 Displacement of the vibro-impact machine into soil, m.
- x_a Relative displacement of the centre of oscillating bar with respect to the centre of Solenoid 1 (DC Solenoid).
- x_b Relative displacement of the centre of oscillating bar with respect to the centre of Solenoid 2 (AC Solenoid).
- y Inter-solenoid distance, from centre of solenoid 1 to centre of solenoid 2, m.

Abbreviations

AC	Alternating Current
DC	Direct Current
D.O.F	Degree-of-freedom
DOS	Disk operating system
DPDT	Double pole double throw
FFT	Fast Fourier transform
LVDT	Linear variable displacement transducer
MEMS	Microelectromechanical system
MRR	Material removal rate
PC	Personal computer
PCB	Printed circuit board
RLC	Resistance, inductor and capacitor
ROP	Rate of progression
SSRL	Solid state relay logic

List of Figures

- 1.1 Figure 1.1: Switching signal of solid state relay at 5 Hz operating frequency.
- 3.1 Schematic diagram of electro- vibroimpact system.
- 3.2 Photograph of electro-vibroimpact system.
- 3.3 Previous vibroimpact machine operated by spring and solenoid mechanism.
- 3.4 Experimental setup with permanent magnet replacing the mechanical spring.
- 3.5 Schematic diagram of vibroimpact system with permanent magnet.
- 3.6 Magnetic force rating of solenoid RS 346-356 (according to RS catalogue).
- 3.7 Diagram of the one degree-of-freedom vibroimpact machine.
- 3.8 Schematic diagram of one degree-of-freedom electro-vibroimpact system in a vertical orientation.
- 3.9 (a) Experimental time histories of conductor bar vibro-impact oscillations at operating frequency of 2 Hz (b) validated against an oscilloscope reading.
- 3.10 (a) Experimental time histories of conductor bar vibro-impact oscillations at operating frequency of 3 Hz (b) validated against an oscilloscope

- reading.
- 3.11 (a) Experimental time histories of conductor bar vibro-impact oscillations at operating frequency of 4 Hz (b) validated against an oscilloscope reading.
 - 3.12 (a) Experimental time histories of conductor bar vibro-impact oscillations at operating frequency of 5 Hz (b) validated against an oscilloscope reading.
 - 3.13 (a) Experimental time histories of conductor bar vibro-impact oscillations at operating frequency of 6 Hz (b) validated against an oscilloscope reading.
 - 3.14 (a) Experimental time histories of conductor bar vibro-impact oscillations at operating frequency of 7 Hz (b) validated against an oscilloscope reading.
 - 3.15 (a) Experimental time histories of conductor bar vibro-impact oscillations at operating frequency of 8 Hz (b) validated against an oscilloscope reading.
 - 3.16 (a) Experimental time histories of conductor bar vibro-impact oscillations at operating frequency of 9 Hz (b) validated against an oscilloscope reading.
 - 3.17 (a) Experimental time histories of conductor bar vibro-impact oscillations at operating frequency of 10 Hz (b) validated against an oscilloscope reading.
 - 3.18 Transmission of impact force to a brick sample.

- 3.19 Slider bearing and sensor connection to the rig.
- 3.20 (a) Photograph and (b) Schematic of two degree-of-freedom electro-vibroimpact system.
- 3.21 Showing the (a) brick sample of 1 cm thickness, (b) combined time history of conductor oscillations (red line) and rig downward progression (blue line), (c) zoomed in time history of conductor oscillations (red line) and rig downward progression (blue line) at first 4 seconds and (d) time history of conductor oscillation in 1 second for solid state relay frequency of 2 Hz.
- 3.22 Showing the (a) brick sample of 1 cm thickness, (b) combined time history of conductor oscillations (red line) and rig downward progression (blue line), (c) zoomed in time history of conductor oscillations (red line) and rig downward progression (blue line) at first 4 seconds and (d) time history of conductor oscillation in 1 second for solid state relay frequency of 3 Hz.
- 3.23 Showing the (a) brick sample of 1 cm thickness, (b) combined time history of conductor oscillations (red line) and rig downward progression (blue line), (c) zoomed in time history of conductor oscillations (red line) and rig downward progression (blue line) at first 2 seconds and (d) time history of conductor oscillation in 1 second for solid state relay frequency of 4 Hz.
- 3.24 Showing the (a) brick sample of 1 cm thickness, (b) combined time history of conductor oscillations (red line) and rig downward progression (blue line), (c) zoomed in time history of conductor oscillations (red line) and rig downward progression (blue line) at first 1.6 seconds and (d) time history of conductor oscillation in 1 second for solid state relay frequency of 5 Hz.

- 3.25 Showing the (a) brick sample of 1 cm thickness, (b) combined time history of conductor oscillations (red line) and rig downward progression (blue line), (c) zoomed in time history of conductor oscillations (red line) and rig downward progression (blue line) at first 1.4 seconds and (d) time history of conductor oscillation in 1 second for solid state relay frequency of 6 Hz.
- 3.26 Showing the (a) brick sample of 1 cm thickness, (b) combined time history of conductor oscillations (red line) and rig downward progression (blue line), (c) zoomed in time history of conductor oscillations (red line) and rig downward progression (blue line) at first 1.2 seconds and (d) time history of conductor oscillation in 1 second for solid state relay frequency of 7 Hz.
- 3.27 Showing the (a) brick sample of 1 cm thickness, (b) combined time history of conductor oscillations (red line) and rig downward progression (blue line), (c) zoomed in time history of conductor oscillations (red line) and rig downward progression (blue line) at first 1 seconds and (d) time history of conductor oscillation in 1 second for solid state relay frequency of 8 Hz.
- 3.28 Showing the (a) brick sample of 1 cm thickness, (b) combined time history of conductor oscillations (red line) and rig downward progression (blue line), (c) zoomed in time history of conductor oscillations (red line) and rig downward progression (blue line) at first 1 seconds and (d) time history of conductor oscillation in 1 second for solid state relay frequency of 9 Hz.
- 3.29 Showing the (a) brick sample of 1 cm thickness, (b) combined time history of conductor oscillations (red line) and rig downward progression (blue line), (c) zoomed in time history of conductor oscillations (red line) and rig

- downward progression (blue line) at first 1 seconds and (d) time history of conductor oscillation in 1 second for solid state relay frequency of 10 Hz.
- 3.30 Schematic of mole head.
 - 3.31 Diagram of the experimental rig in horizontal orientation.
 - 3.32 Schematic diagram of the experimental rig in horizontal orientation.
 - 3.33 Diagram of the static load suspended by pullies.
 - 3.34 Schematic diagram of the vibro-impact machine with static load.
 - 3.35 Time histories of (a) conductor bar oscillation, (b) progression rate of the vibro-impact rig and (c) superimpose time history of conductor oscillation (dotted red line) and rig progression (blue line) at operating frequency of 5 Hz.
 - 3.36 Time histories of (a) conductor bar oscillation, (b) progression rate of the vibro-impact rig and (c) superimpose time history of conductor oscillation (dotted red line) and rig progression (blue line) at operating frequency of 6 Hz.
 - 3.37 Time histories of (a) conductor bar oscillation, (b) progression rate of the vibro-impact rig and (c) superimpose time history of conductor oscillation (dotted red line) and rig progression (blue line) at operating frequency of 7 Hz.
 - 3.38 Time histories of (a) conductor bar oscillation, (b) progression rate of the vibro-impact rig and (c) superimpose time history of conductor oscillation (dotted red line) and rig progression (blue line) at operating frequency of 8 Hz.

- 3.39 Time histories of (a) conductor bar oscillation, (b) progression rate of the vibro-impact rig and (c) superimpose time history of conductor oscillation (dotted red line) and rig progression (blue line) at operating frequency of 9 Hz.
- 3.40 Time histories of (a) conductor bar oscillation, (b) progression rate of the vibro-impact rig and (c) superimpose time history of conductor oscillation (dotted red line) and rig progression (blue line) at operating frequency of 10 Hz.
- 3.41 Rig progression comparison of various operating frequency.
- 4.1 Schematic drawing of conductor and solenoids.
- 4.2 Free body diagram of conductor bar in (a) the free region, and (b) the impact region.
- 4.3 Schematic of conductor bar's relative position with respect to the center of Solenoid 1.
- 4.4 Schematic diagram of experimental setup to quantify electromagnetic force of DC solenoid.
- 4.5 Graph of solenoid attractive force against conductor displacement at 20 V, crosses represents experimental data and solid line represents curve fitted line.
- 4.6 Plot of DC electromagnetic force against absolute conductor displacement.
- 4.7 Time history of model with DC solenoid and weight.
- 4.8 Schematic of conductor's relative position with respect to Solenoid 2.
- 4.9 Schematic diagram of Solenoid 2 with resistor in series circuit.

- 4.10 Inductance value of experiment data and Gaussian's form.
- 4.11 Gaussian's form first derivative of inductance against conductor displacement.
- 4.12 Gaussian's form second derivative of inductance against conductor displacement.
- 4.13 Waveform of main electric supply.
- 4.14 FFT of experimental data at operating frequency 2 Hz at range (a) 0-20 Hz and (b) 40-60 Hz.
- 4.15 Fourier Transform of experimental data at operating frequency 3 Hz at range (a) 0-20 Hz and (b) 40-60 Hz.
- 4.16 Fourier Transform of experimental data at operating frequency 4 Hz at range (a) 0-20 Hz and (b) 40-60 Hz.
- 4.17 Fourier Transform of experimental data at operating frequency 5 Hz at range (a) 0-20 Hz and (b) 40-60 Hz.
- 4.18 Fourier Transform of experimental data at operating frequency 6 Hz at range (a) 0-20 Hz and (b) 40-60 Hz.
- 4.19 Fourier Transform of experimental data at operating frequency 7 Hz at range (a) 0-20 Hz and (b) 40-60 Hz.
- 4.20 Fourier Transform of experimental data at operating frequency 8 Hz at range (a) 0-20 Hz and (b) 40-60 Hz.
- 4.21 Fourier Transform of experimental data at operating frequency 9 Hz at range (a) 0-20 Hz and (b) 40-60 Hz.
- 4.22 Fourier Transform of experimental data at operating frequency 10 Hz at

- range (a) 0-21 Hz and (b) 39-61 Hz.
- 4.23 Switching solid state relay signal against time.
- 4.24 The combined effect of main supply and SSRL switching at operating frequency of 5 Hz.
- 4.25 Time history of conductor bar oscillation with only AC solenoid.
- 4.26 Graph of AC electromagnetic force against time, t .
- 4.27 Numerical time history at operating frequency (a) 2 Hz, (b) 3 Hz, (c) 4 Hz, (d) 5 Hz, (e) 6 Hz, (f) 7 Hz, (g) 8 Hz, (h) 9 Hz and (i) 10 Hz obtained from Matlab simulation.
- 4.28 Comparison of experimental (dotted green line) and numerical (blue line) results of (a) Conductor oscillation and (b) Rig progression of 5 Hz operating frequency.
- 4.29 Comparison of experimental (dotted green line) and numerical (blue line) results of (a) Conductor oscillation and (b) Rig progression of 6 Hz operating frequency.
- 4.30 Comparison of experimental (dotted green line) and numerical (blue line) results of (a) Conductor oscillation and (b) Rig progression of 7 Hz operating frequency.
- 4.31 Comparison of experimental (dotted green line) and numerical (blue line) results of (a) Conductor oscillation and (b) Rig progression of 8 Hz operating frequency.
- 4.32 Comparison of experimental (dotted green line) and numerical (blue line) results of (a) Conductor oscillation and (b) Rig progression of 9 Hz

- operating frequency.
- 4.33 Comparison of experimental (dotted green line) and numerical (blue line) results of (a) Conductor oscillation and (b) Rig progression of 10 Hz operating frequency.
- 5.1 (a) Photograph of circuitry for alternating and direct current, and (b) corresponding schematic.
- 5.2 The circuit board LM555 the timer and potentiometer that manipulates the operating frequency of AC power supply.
- 5.3 Schematic diagram of the LM555 Timer.
- 5.4 Photograph of (a) moling head connected to the body cover and (b) that of the bolted plate cover of the moling head connector.
- 5.5 Engineering drawing of moling head and aluminium cylinder.
- 5.6 The launch frame in (a) upper side view and (b) upper front view.
- 5.7 (a) Cytron MO-HTA1800-200 linear actuator and (b) the bolted connection from the actuator to the vibro-impact rig body.
- 5.8 Schematic of circuitry operating a linear actuator.
- 5.9 (a) The soil box that contains soil with a circular opening for entry of motion and (b) the concrete slab which acts as surcharge on the soil for the first 0.55 m after entry.
- 5.10 Vibro-impact machine and the circuit diagram.
- 5.11 (a) LVDT and linear actuator installed at the rigid frame and (b) their connection to the rear end of prototype rig.
- 5.12 Time history of rig progression before smoothing.

- 5.13 Time history of rig progression after smoothing.
- 5.14 Time histories of rig progression into soil at (a) 40 V AC, (b) 50 V AC, (c) 60 V AC, (d) 70 V, (e) 80 V AC, (f) 90 V AC, (g) 100 V AC and (h) 110 V AC power supply, 6 Hz signal frequency and 8 V DC supplied to linear actuator.
- 5.15 Comparison of rig progression at 40 V, 50 V and 60 V of AC power supply.
- 5.16 Comparison of rig progression at 70 V, 80 V and 90 V of AC power supply.
- 5.17 Time histories of rig progression into soil at (a) 6 V, (b) 8 V, (c) 10 V, (d) 12 V, (e) 14 V, (f) 16 V, (g) 18 V and (h) 20 V DC supplied to linear actuator, 50 V AC power supply and 6 Hz signal frequency.
- 5.18 Combined time histories of rig progression into soil at various voltages supplied to linear actuator and at 50 V alternating supply to solenoid.
- 5.19 Combined time histories of rig progression into soil at various voltages supplied to linear actuator and at 50 V alternating supply to solenoid.
- 5.20 Combined time histories of rig progression into soil at various voltages supplied to linear actuator and at 50 V alternating supply to solenoid.
- 5.21 Time histories of rig progression into soil at (a) 4 Hz, (b) 5 Hz, (c) 6 Hz, (d) 7 Hz and (e) 8 Hz signal frequency, 90 V AC power to solenoid and 10 V DC supply to linear actuator.
- 5.22 Time history of rig progression of vibro-impact machine into the soil box with continuous measurement at 6 Hz signal frequency, 90 V AC supply to

the periodic impact and 10 V DC supply to the static force.

- D.1 Time history at 6 V DC power supply to linear actuator, 6 Hz of signal frequency and 70 V AC power to solenoid.
- D.2 Time history at 8 V DC power supply to linear actuator, 6 Hz of signal frequency and 70 V AC power to solenoid.
- D.3 Time history at 10 V DC power supply to linear actuator, 6 Hz of signal frequency and 70 V AC power to solenoid.
- D.4 Time history at 12 V DC power supply to linear actuator, 6 Hz of signal frequency and 70 V AC power to solenoid.
- D.5 Time history at 14 V DC power supply to linear actuator, 6 Hz of signal frequency and 70 V AC power to solenoid.
- D.6 Time history at 16 V DC power supply to linear actuator, 6 Hz of signal frequency and 70 V AC power to solenoid.
- D.7 Time history at 18 V DC power supply to linear actuator, 6 Hz of signal frequency and 70 V AC power to solenoid.
- D.8 Time history at 20 V DC power supply to linear actuator, 6 Hz of signal frequency and 70 V AC power to solenoid.
- D.9 Time history at 6 V DC power supply to linear actuator, 6 Hz of signal frequency and 90 V AC power to solenoid.
- D.10 Time history at 8 V DC power supply to linear actuator, 6 Hz of signal frequency and 90 V AC power to solenoid.
- D.11 Time history at 10 V DC power supply to linear actuator, 6 Hz of signal frequency and 90 V AC power to solenoid.

- D.12 Time history at 12 V DC power supply to linear actuator, 6 Hz of signal frequency and 90 V AC power to solenoid.
- D.13 Time history at 14 V DC power supply to linear actuator, 6 Hz of signal frequency and 90 V AC power to solenoid.
- D.14 Time history at 16 V DC power supply to linear actuator, 6 Hz of signal frequency and 90 V AC power to solenoid.
- D.15 Time history at 18 V DC power supply to linear actuator, 6 Hz of signal frequency and 90 V AC power to solenoid.
- D.16 Time history at 20 V DC power supply to linear actuator, 6 Hz of signal frequency and 90 V AC power to solenoid.
- E.1 Rig displacement for control signal frequency of 4.0 Hz.
- E.2 Rig displacement for control signal frequency of 4.2 Hz.
- E.3 Rig displacement for control signal frequency of 4.4 Hz.
- E.4 Rig displacement for control signal frequency of 4.6 Hz.
- E.5 Rig displacement for control signal frequency of 4.8 Hz.
- E.6 Rig displacement for control signal frequency of 5.0 Hz.
- E.7 Rig displacement for control signal frequency of 5.2 Hz.
- E.8 Rig displacement for control signal frequency of 5.4 Hz.
- E.9 Rig displacement for control signal frequency of 5.6 Hz.
- E.10 Rig displacement for control signal frequency of 5.8 Hz.
- E.11 Rig displacement for control signal frequency of 6.0 Hz.
- E.12 Rig displacement for control signal frequency of 6.2 Hz.
- E.13 Rig displacement for control signal frequency of 6.4 Hz.

- E.14 Rig displacement for control signal frequency of 6.6 Hz.
- E.15 Rig displacement for control signal frequency of 6.8 Hz.
- E.16 Rig displacement for control signal frequency of 7.0 Hz.
- E.17 Rig displacement for control signal frequency of 7.2 Hz.
- E.18 Rig displacement for control signal frequency of 7.4 Hz.
- E.19 Rig displacement for control signal frequency of 7.6 Hz.
- E.20 Rig displacement for control signal frequency of 7.8 Hz.
- E.21 Rig displacement for control signal frequency of 8.0 Hz.
- E.22 Rig displacement for control signal frequency of 8.2 Hz.
- E.23 Rig displacement for control signal frequency of 8.4 Hz.
- E.24 Rig displacement for control signal frequency of 8.6 Hz.
- E.25 Rig displacement for control signal frequency of 8.8 Hz.
- F.1 Housing cover detailed drawing.
- F.2 Mole head housing detailed drawing.
- F.3 Back head housing detailed drawing.
- F.4 Mole head detailed drawing.
- F.5 Schematic diagram of launch frame.
- F.6 Schematic diagram of electro-vibroimpact prototype.

List of Tables

- 3.1 Specifications of solenoid RS 346-356 (according to RS catalogue).
- 4.1 Conductor bar displacement from Solenoid 1 and electromagnetic force at 20 V.
- 4.2 Inductance at various position of conductor bar in Solenoid 2.
- 5.1 Calculations of operating frequency of timer.
- 5.2 Progression rate at different ratios of dynamic to static force at 50 V alternating supply to solenoid.
- 5.3 Progression rate at different ratios of dynamic to static force at 70 V alternating supply to solenoid.
- 5.4 Progression rate at different ratios of dynamic to static force at 90 V alternating supply to solenoid.
- 5.5 Progression rate of vibro-impact machine at varying signal frequencies.
- B.1 Matlab script that plot time history of 1 D.O.F experimental result for oscillating bar.
- B.2 Matlab script that plot time history of 1 D.O.F experimental result compared to numerical simulation from Dynamics.
- B.3 Matlab script that plot time history of 2 D.O.F experimental result for oscillating bar and rig progression.
- B.4 Matlab script of fast fourier transform analysis on experimental data to obtain the frequency domain plot.

- C.1 Matlab script describing the mathematical model of a vibro-impact system in 1 D.O.F experiment.
- C.2 Sub-program representing the free region of 1 D.O.F oscillation mathematical model.
- C.3 Sub-program representing the impact region of 1 D.O.F oscillation mathematical model.
- C.4 Matlab script describing the mathematical model of a vibro-impact system in 2 D.O.F horizontal orientation experiment.
- C.5 Sub-program representing the free region of 2 D.O.F oscillation mathematical model.
- C.6 Sub-program representing the Impact region of 2 D.O.F oscillation mathematical model.
- C.7 Sub-program that determines the function and input parameters of 4th order Runge-Kutta method.
- C.8 Sub-program of 4th order Runge-Kutta operating algorithms.
- C.9 Sub-program of DC solenoid electromagnetic force as a function of bar position.
- C.10 Sub-program script of AC solenoid electromagnetic force as a function of bar position and current within the solenoid.
- C.11 Sub-program to calculate the inductance, first derivative and second derivatives of inductance values.
- C.12 Sub-program of SSRL in the function of time.
- C.13 Sub-program of root finding algorithm to determine the point of time

where region switches from free to impact.

- C.14 Dynamics script that describes the mathematical model of 2 D.O.F vibro-impact machine.

CHAPTER 1

INTRODUCTION

1.1 Background

Vibro-impact systems consists of a vibrational part that produces systematic collisions between the elements of kinematic pairs and high stiffness structure, creating impacts [2, 55]. The potential applications of vibro-impact system include pile driving [5, 8, 26, 54], ground moling [32, 60] and percussive drilling [6, 59].

This work puts forth a solution to optimize vibro-impact dynamics such that it is feasible to progress in soil media, even in a horizontal orientation without assistance from gravitational forces. This has been made possible by interactions between electromagnetic forces and a ferrous conductor. Based on a basic electro-vibroimpact mechanism [32], a new system capable of overcoming soil resistive forces is developed. Two solenoids, one connected to alternating current and the other powered by direct current are two sources of electromagnetic flux. At the same time, these are nonlinear restoring forces to a vibro-impact oscillator. This new system has a more compact geometry than its immediate predecessor [20] and can penetrate into even horizontally without assistance from gravity in the vertical direction. While efficiency of the former system was maintained in a vertical orientation by implementing a phase feedback control strategy, the current electro-vibroimpact system operates without a control algorithm, influence mainly by the ratio of amplitudes, of dynamic and static force.

The switching on and off of a solenoid experiencing alternating current is still an integral part of electro-vibroimpact system. A mechanical spring connected to a reciprocating bar had been replaced with solenoid connected to a direct current (DC) supply. A new vibro-impact system is created from interactions between electromagnetic fluxes from both solenoids. This had been inspired by a permanent magnet substitute inter alia, which in turn, necessitated replacement due to declining magnetism with time and repeated impacts. Accentuation of impact forces is made possible by adjustment of voltage supplied to each solenoid. The ratio of voltages is crucial to elicit a local maxima in impact force. The DC solenoid at the same time, functions as a nonlinear restoring force which nonlinearity and magnitude is easily adjusted. Mechanical fatigue and wear, usually encountered in mechanical springs is avoided by replacing it with an electromagnet.

Compared to previous versions of electro-vibroimpact system, this experimental rig is faster and more compact in geometry. It is also capable of breaking hard or brittle material. The author is also in a position to extend this work to practical or engineering application readily. A compact solenoid of smaller diameter is used, and head of penetrating device is assumed by a machined steel bolt or stepped conical head, aligning only essential components such as solenoids, conductor bar, drill head and transducer sensors on an aluminium base plate. By adjustment of position of stop, solenoid positions and electrical parameter values, optimization is achieved to magnify impact. A

mathematical model has also been established for numerical parametric studies, and also to determine extent of experimental correlation.

In a previous rig, a series RLC circuit is connected to the solenoid, and the wave form is provided by a function generator that relied on an AC supply from a variac (staco variable transformer) [32]. This arrangement is replaced by programming a block diagram (Appendix I) in LabView software that provides output in the form of signal function and frequency through hardware data acquisition. Power from an AC is supplied with the same method and amplified by a power amplifier (TIRA Power Amplifier Type BAA 120) before connection to the solenoid. Periodic switching of alternating current solenoid has also been implemented with solid state relay and function generator. The square wave solid state relay signal is shown in Figure 1.1. This second method of activating alternating current solenoid allows for higher values of voltage to be applied across solenoid. The absence of voltage limitation on supply from a variac has been important to development of this system.

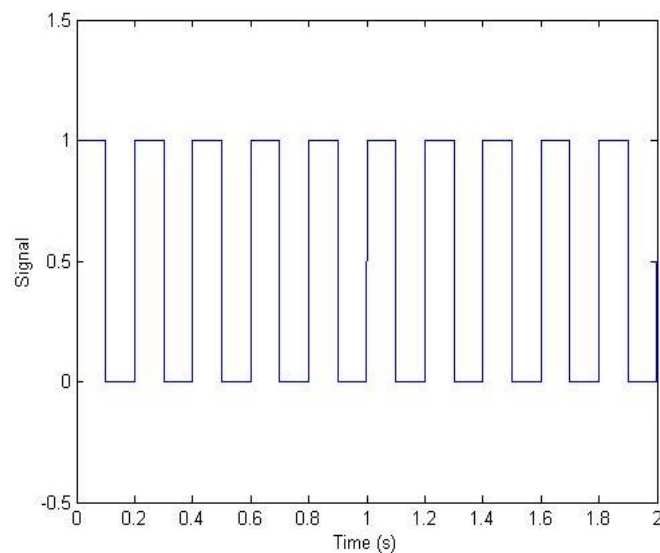


Figure 1.1: Switching signal of solid state relay at 5 Hz operating frequency.

The current capability of new system is forward or downward progression into soil and penetration into hard, brittle objects such as rocks and bricks which are commonly found in a soil medium. For such materials, a slow and gradual progression, if any, is a prelude to a sudden fracture of the material after a prolonged period of vibration and impact. Development of cracks within the material is instrumental to fracture of medium. Destruction of materials of larger volumes necessitates imposition of an increasing static mass of experimental rig as a necessary condition for brittle fracture. This is practically feasible should a linear actuator be used.

Numerical solution to mathematical model has been compared to experimental observations, in particular, time histories of vibro-impact conductor oscillations and forward progression of experimental rig. Direct numerical integration is conducted in Dynamics software [38] using a Runge-Kutta algorithm. Focus is placed on a 1 degree-of-freedom system, as well as 2 degrees-of-freedom system with forward progression. Comparison between numerical and experimental results shows similarity in qualitative response and frequency dependence.

1.2 Aims and Objectives

Achievement of electro-vibroimpact system capable of progression into soil without assistance from gravitational forces is a primary objective of this work. As such, it has been necessary to:

- Construct an experimental rig proving that it is practical and feasible to capitalize on electromagnetic interactions within a compact geometry.
- Acquire data and identify a set of parameters pertaining to an optimal and effective operating mode.
- Compare numerical results with experimental results, investigating the matching of both outcomes in terms of amplitude, waveform and frequency response of rig progression and impact oscillation time histories.
- Propose recommendations for deployment of electro-vibroimpact system in some practical situations.

1.3 An Overview of the Thesis

This thesis has the following structure. Chapter One introduces this work and justifies a motivation, detailing aims and objectives of this development and investigation. Chapter Two surveys past and current work to date, defining how this thesis makes a positive contribution to this technology. Chapter Three describes development of experimental rig, presenting results and discussing them, to justify effectiveness of system. Chapter Four establishes a mathematical model and its numerical solution, integrating experimental correlation. Chapter Five describes extended work on a working prototype prior to a conclusion to this case for defense of PhD. Chapter Six concludes this thesis and makes recommendations for future work.

CHAPTER 2

LITERATURE REVIEW

In addition to fundamental work on vibro-impact systems by Peterka [42], Babitsky [2] has described a vibro-impact system in the context of vibration of a mechanical system where systematic collisions occur between the elements of kinematic pairs and structures. There are many engineering applications of vibro-impact systems. In particular, the contribution of vibro-impact motion to pile driving was highlighted, especially with regards to increase downward progression rate. Previous work by Tsaplin [14, 54] and Barkan [5] had investigate impact forces. Of particular concern was size of machine. Reduction of noise and installation time had been achieved by Benamar [8], introducing a new concept of positioning an impact hammer inside a pile. As such, the traditional pile top driving method is optimized to a “down-the-hole” method. In this case, impacts have been generated without vibration.

Introduction of vibration to impact can be seen in an effort of synchronizing percussive striker and drill bit by a single rotating drive was undertaken by Batako, Babitsky and Halliwell [7, 6], in which the model incorporates friction force as the self-excitation of the coupled vibration. After analyzing and obtaining a solution to the system, an increase in penetration rate is observed with increased impact intensity and hardening of the medium. Wiercigroch, Wojewoda and Krivtsov [59] performed a study on

introducing high frequency axial vibration into downhole drilling. It significantly enhances drilling rates compared to the traditional rotary type method.

To address a need to maximize vibration and impact in a compact geometry, Nguyen and Woo [32] presented a new system for ground moling based on vibro-impact dynamics and actuated by electromechanical means. By introduction of solenoid in the mechanism, connection to a switched series RLC circuit together with a mechanical spring induced oscillation of an inertial object. Usage of solenoid as conductor switching device had been previously featured in the work of Ahn and Yokota [1] who implemented inexpensive on/off solenoid valves, rather than expensive servo valves, to develop a fast, accurate, inexpensive and intelligent pneumatic control system taking account of the changes of external loads. The challenges are the difficulties of fine motion control due to the discrete on/off nature of solenoid and long valve response time. Miller and Bredernyer [30] also mentioned using a solenoid as remote operated valve component of a switching device. Topcu, Yuksel and Karmis [53] have manufactured a fast pneumatic switching solenoid valve with switching time of about 4.5 ms and provides a 460 l/min of flow rate at standard air conditions. It can thus be seen that solenoids are a feasible mean of switching and direction reversal.

Usage of solenoid can be found in many modern electromechanical devices, an example can be found in the work of Gomis-Bellmunt *et al* [18] who optimized linear electromagnetic actuators focusing on the solenoid and moving coil actuators, with the application of model-based design rules. It was proposed that solenoid actuators can

perform higher force per cross-section and energy per volume than moving coil actuators. Kallenbach *et al* [22] reported that for new polarized electromagnet actuators, a bi-stable polarized solenoid actuator is integrated into a miniaturized pneumatic valve, which is a very small and compact device. Rashedin and Meydan [44] proposed to apply solenoid actuators into a loudspeaker, which leads to a statement that solenoids are useful in simple and low cost application but limited by its non-linearity and inefficiency operating at high frequency. Xu and Jonesa [61] are of an opinion that solenoid actuators are widely used in engineering applications, engaging the prediction of its dynamics performance. The method they used is based on a reciprocal of the square root of magnetic force being proportional to the stroke displaced within a certain range. Fang *et al* [16] fabricated a solenoid inductor by using microelectromechanical system (MEMS) technology with air-core structure with the area of 880 μm by 350 μm with a height of 45 μm . This solenoid inductor has low series resistance and stable inductance over a wide range of operating frequencies. Hasegawa *et al* [19] described the development of a multi-directional micro-switching method that includes a micro-solenoid drive switching valve chip to provide simple and quick operation. Park *et al* [39] invented a micro-machined electronic compass with two-axis micro-fluxgate sensors that measure the magnitude of X-axis and Y-axis magnetic field. The sensors are composed of magnetic core, solenoid excitation and pick up.

Several efforts have been made to investigate the behavior of a dynamic system with electromagnetic properties. Connection of a solenoid in series to an RLC circuit in which the capacitance is adjusted to induce electrical resonance, the conductor, which is

a metal bar, inside the tube of solenoid will oscillate. The oscillation is being regulated and enhanced by a mechanical spring that is attached to it. This phenomenon is reported as a linear reluctance self-oscillating motion [29, 28]. Blakley and Pudlowski [9] describes the function of electromechanical oscillations with differential equations with the aid of a digital computer to obtain a form of exact solution. The calculation of energy and force of solenoid is mentioned by El-Derini [15], where a solenoid is represented by many circular filaments where its self-inductance and mutual inductances are calculated. The radial and axial force on a solenoid is calculated by using the principle of virtual work, which utilizes the change in energy with respect to a small dimensional increment of that axis. Magnetic stiffness is also discussed by Sugiura, Ura and Kurado [49] for a superconducting levitation system. By conducting experiments and deriving the equations of motion of electromagnets, due to nonlinearity of a magnetic force, apparent stiffness and natural frequency increase with the amplitude of vibration. Besides a potential to create impact of a solenoid, the possibility of it giving a reverse effect, or damping to the system is also considered so that the electromagnet pair works in optimum condition. Pranoto *et al* [43] discussed about electromagnet dampers which slow or stop motions and vibrations, which state that vibration of low frequency and small oscillating mass is proven to damp easily through experimental and theoretical study done. Satoru [45] also designed magnetic passive dampers using electromagnets, and the formulation of equivalent spring stiffness and damping factor to define natural frequency and damping ratio is done.

Hence, there is a need for a new and effective electro-vibroimpact system. While Nguyen and Woo [32] had initiated an electro-vibroimpact system capable of overcoming frictional resistive forces, and Ho and Woo [21] had deployed an experimental rig in a vertical orientation, capable of penetrating into clay. In addition, hard and brittle material such as brick and stone is often found in soil. Rate of progression (ROP) is highly suitable for soil calculation as the impact head slowly moves into soil with small displacements per unit time. However, material removal rate (MRR) would be a more suitable parameter for hard material as the tool does not progress through the material constantly, but initiates and propagates cracks before final brittle fracture. The material removal rate had been a focus of Wiercigroch *et al* [58, 56] to drill into hard material at ultrasonic frequencies, where the MRR is highly associated with high amplitudes forces generated by impacts, developing micro-cracking in the cutting zone. It is also explained that MRR could be maximized by varying a static load but a overloading would decrease drilling efficiency significantly [59]. An approach to calculate MRR had been introduced by Krivtsov and Wiercigroch [23], which could explain the fall of MRR at an excessive static load [23, 27].

As it is known from experiment Wagg, Karpodinis and Bishop [55] recorded spike train type signal data of oscillations of a vibro-impacting cantilever beam. An observation by Nguyen, Woo and Pavlovskaja [33, 34] was that altering the input frequency is one of the main factors that changes the amplitude of a vibro-impact oscillating mass for optimum performance in rig progression.

Luo and Yao [26] performed a dynamics analysis on a pile driver with vibro-impact system which could predict much of its system qualitative response. The approach entails developing a mathematical model that analyzes a small vibro-impact pile driver by means of a three-dimensional map, with transition conditions between free flight and sticking solutions.

Numerical analysis on a mathematical model is done to validate the experimental results. Numerical integration verifying the approximate analytical solution had been undertaken by Ho and Woo [20] and corresponding results had been compared with experimental solution where correlating in frequency of oscillation is obtained and similarity in waveform are observed. Experiments and analytical work showed that altering the input frequency influenced the amplitude of the oscillating mass and the optimum performance occurs between 6 Hz to 7 Hz [33, 34]. Bifurcation analysis is useful, especially for impact oscillators. Peterka [41] states that periodic and chaotic motions exist even for simple systems excited by external forces. There is a region of system parameters in which a stable solution exists, where the boundary or transition to this region is being described by jump phenomena, period doubling and saddle-node bifurcations. Ding, Xie and Sun [13] studied the interaction dynamics of Hopf and period doubling bifurcation of the two degree-of-freedom vibro-impact system, by theoretical analysis and numerical simulations and discussed the difference of local dynamical behavior when control parameters change near the critical point.

Pavlovskaja, Wiercigroch and Grebogi [40] developed a two-dimensional analytical map described by several parameters that include time, relative displacement, velocity

of oscillator and relative displacement of the slider top. In addition to the use of parameters, Peterka [41] states that there is a region of system parameters in which a stable solution exists. Corresponding to this stable solution, Tamas, Stepan and Moon [51] mentioned the existence of a subcritical Hopf bifurcation in the differential equation model of a vibration machine tool. Shaw and Holmes [46, 47] analyzed on a one-dimensional dynamic mapping, showing stable periodic orbits exist at almost all forcing frequencies but chaotic motions can also occur. Harmonic, subharmonic and chaotic motions are found to exist and could be identify by bifurcation analysis [48]. Thus, bifurcation analysis is important for analysis within this stable solution or region. Nordmark [35] studied the singularities caused by grazing impact using analytical methods, and showed that bifurcation occurs as a stable periodic orbit comes to grazing impact under the control of a single parameter. Nordmark [36] also discussed the creation of periodic orbits associated with grazing bifurcation and a numerical example for an impacting system with one degree-of-freedom.

In order to obtain this range of stable solution, numerical solutions by simulating the mathematical model are essential to validate the experimental outcome. There are some work achieved with similar strategy, Moon and Shaw [31] performed digital simulation of a single mode mathematical model of a beam with one end clamped using a Runge-Kutta algorithm, which forms the basis of direct numerical integration. The theoretical model used by Chu and Moon [12] showed actual magnetic force measurements to predict the dynamic behaviour in functions of speed and geometry position of a oscillator with magnets employed. From another approach of analysis, Galvanetto and

Bishop [17] presented some numerical techniques investigating the non-linear dynamics that allow detection of separate slip-stick phase points. Nordmark, Dancowicz and Champneys [37] show how discontinuities in the impact law associates with the discontinuity-induced bifurcations of periodic trajectories. In addition, it has been pointed out by Wiercigroch [57] that detection of the precise time of discontinuity is crucial to determine an actual topology.

Similar to the 1 degree-of-freedom vibro-impact rig, Bapat [4] studied on a single degree-of-freedom oscillator in which the oscillating mass collides on one or both sides. An inclined angled oscillator [3] is also being tested which relates to how a horizontal vibro-impact machine is being operated in vertical orientation. Numerical simulations of motion on a digital computer are being compared with theoretical estimations and results indicate good correlation.

Krivtsov and Wiercigroch's [24] investigated the relationship of a percussive drilling dynamic model and its material removal rate. In his model, it focuses on a rotary ultrasonic drilling powered by harmonic force and static force. He concluded that the amplitude of static force should be lower than 39% the harmonic force to produce decent material removal rate. This is observed by the fall of material removal rate when the amplitude of static force and the bit weight of downhole drilling is further increased. Fathi and Popplewell investigated several numerical procedures to obtain the contact forces and their peak values of an elastic beam with a repetitive collision upon a resilient stop. This would be helpful to verify the relationship of static force and harmonic force

as mentioned by Krivtsov [25] regarding the efficiency of material removal rate. The variable of interest highly affects the strategy used to model the computational calculation, which in this case is switching frequency of the AC solenoid.

Yu, Popplewell and Shah [62] studied on a periodic plunge that loses stability and bifurcates into a quasi-periodic motion. He suggested that increment in the inertia to mass ratio counteracts the initiation and dynamic instability effects. The resonance response of an impact oscillator is found in a certain frequency range, as suggested by Thompson and Ghaffari [52]. After an infinite cascade of period-doubling bifurcations, chaotic motion of a strange attractor occurs.

As the mathematical model of electro-vibroimpact machine would be expressed in terms of a discontinuous system due to the switching of solid state relay , Cao *et al.* [10, 11] study the transition from smooth to discontinuous dynamics of an archetypal oscillator. In the smooth region, the oscillator behaves like a Duffing oscillator. The departure from smooth system occurs when the smoothness parameter decreases to zero, with damping and external excitation, an oscillation becomes chaotic with a high periodic value.

To date, there has been a developed understanding of vibro-impact systems, and intermediate prototype of electro-vibroimpact experimental rig. As such, there is a need to realize and optimize practical and effective implementation of system, aided by tools of nonlinear dynamics, as reviewed in this chapter.

CHAPTER 3

EXPERIMENTAL RIG

3.1 Introduction

This chapter describes the design, manufacture and operation of a new vibro-impact machine in which an alternating current (AC) as well as direct current (DC) solenoid are two sources of electromagnetic force. Its application is mainly for ground moling and rock breaking. A previous system developed by Nguyen and Woo [32] generated impact and vibration by switching on and off an alternating current (AC) solenoid periodically to excite a ferrous conductor attached to a mechanical spring. Forward progressive motion in a horizontal orientation overcame resistive frictional forces.

For practical deployment in soil media, it was necessary to amplify the impact forces, as well as reducing resistive forces by reducing cross-sectional area. As such, this work focusses on an experimental rig which is compact in geometry, especially when compared to the previous versions of machine. In addition, it needed to be effective in a horizontal orientation, in which there is no assistance from gravitational downward force. By variation of operating frequency experimental data pertaining to (a) progression rate into soil as well as (b) oscillations of impacting conductor is acquired. This is useful to scrutinise a mathematical model presented in Chapter 4. Comparison is made to the previous experimental rig in Section 3.3.

The experimental rig has been found to perform optimally when a cylindrical mild steel bar is used as conductor, and two are solenoids powered by direct current (DC) and alternating current (AC) power supplies, respectively. DC solenoid supplies a constant electromagnetic flux. This interacts with a periodically varying vector field from the AC solenoid. A conductor bar within these two solenoids oscillates to and fro. A stop in the path of oscillations impacts are generated when the conductor hits the surface, which acts as a restoring spring of very high stiffness.

A variety of periodic nonlinear dynamic responses has been observed by attaching a Linear Variable Displacement Transducer (LVDT) to the conductor bar. This records a displacement time history of conductor oscillations and impacts. The calibration of the LVDT is documented as well. Frequency response, vibro-impact waveform and amplitude are measured and plotted. It is logical to deduce that a magnitude of the impact force on the stopper depends on the magnitude of vibro-impact oscillations.

Experiments have also been conducted to break stone samples when the experimental rig is placed in a vertical orientation. A conductor bar of 0.155 kg in mass was able to generate impact to propagate cracks in brick material, prior to eventual brittle fracture. Results and discussion of experimental work act as a basis on which a mathematical model is derived, with a view to experimental correlation and system optimisation.

The maximum moling diameter of 60 mm is sufficient for underground cable and pipes installations. For other applications such as rail tunnel moling and underground piling, a

larger moling diameter is needed. However, the dynamics behaviour and moling performance of the machine do not behave linearly with respect to the scaling of rig dimension.

3.2 Electromagnetic interactions between two sources

The first electro-vibroimpact system developed by Nguyen and Woo [32] was based on one single solenoid, an individual source of electromagnetic force. This was capable of overcoming frictional resistive forces generated by clamps on guide rails. To be able to progress, an impact strong enough to effect in a forward progressive motion were necessary to generate periodic vibro-impact motion. This experimental rig consists of a base plate, impact stop, solenoid, metal bar, guide rails and two linear variable differential transformer (LVDT) sensors or displacement transducers. A schematic of this experimental setup is shown in Figure 3.1 and a corresponding photograph in Figure 3.2.

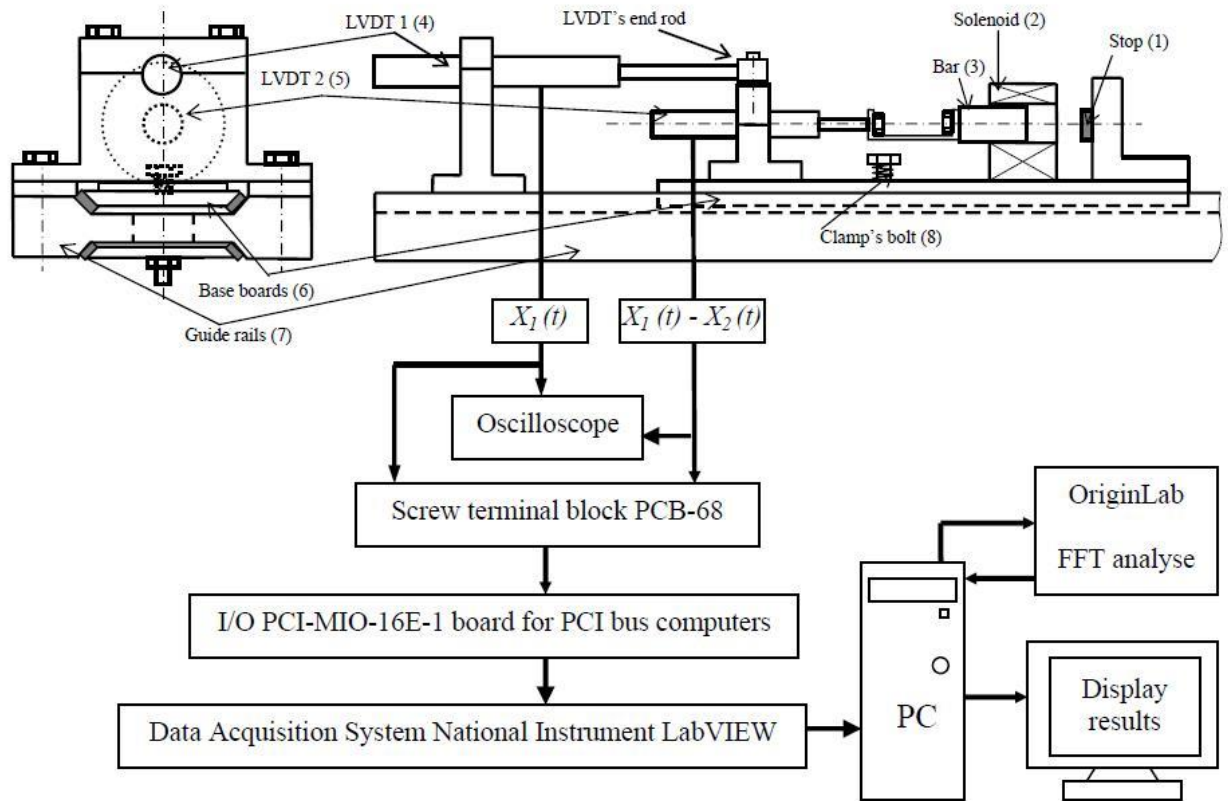


Figure 3.1: Schematic diagram of electro- vibroimpact system [32].

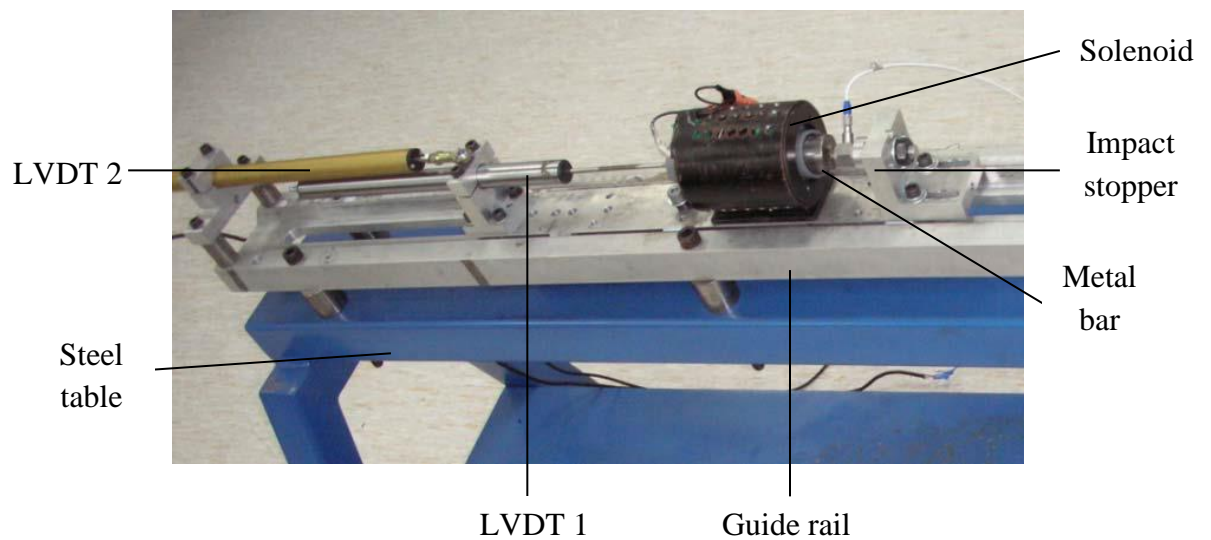


Figure 3.2: Photograph of electro-vibroimpact system [32].

The base plate is an aluminium plate on which solenoid and LVDT are mechanically fastened. The conductor within the solenoid hits a stop. This is an aluminium block clamped at one end of the solenoid. When the metal bar conductor collides with the stopper, the impact force is transmitted to the base plate. The whole system slides forward in the direction of impact on the set of guide rails. The solenoid is connected to an alternating current (AC) power supply, providing a potential difference varying at 50 Hz from a mains supply. In addition, a function generator is switched on and off in accordance to a set frequency. The oscillating conductor is a cylindrical mild steel bar placed within the solenoid. In order to guide the vibro-impact machine to move in a straight line, an aluminium rail had been designed and manufactured. It is mechanically fastened to the top of a steel table to function as a rigid support. One LVDT sensor is attached to the metal bar to record the displacement of conductor vibro-impact oscillations. Another LVDT sensor is fastened also by a screwthread to the base plate, so as to record the displacement of overall progression of the rig. This prototype involved the motion of a total system mass of 3 kg, progressing forward against a frictional force of 13.7 N. The solenoid had an outward diameter of the outer of 100 mm. The work in this thesis seeks to (a) increase the resistive force that can be overcome beyond 13.7 N and (b) reduce the outer diameter to less than 100 mm so as to achieve a compact geometry. A smaller cross-sectional area results in a reduced frontal resistance, which facilitates a faster forward progression rate.

While a mechanical spring had been instrumental in an initial prototype of electro-vibroimpact machine, a more dynamic restoring force had been necessary to achieve the

objectives (a) and (b) stated in the previous paragraph. In initial experiments, a strong permanent magnet in lieu of mechanical spring was found to increase impact force and vibratory frequency significantly. This exerted a constant upward force to the conductor bar. The interactions between flux permanent magnet and electromagnetic field from switched solenoid had been extremely beneficial to the engineering purpose.

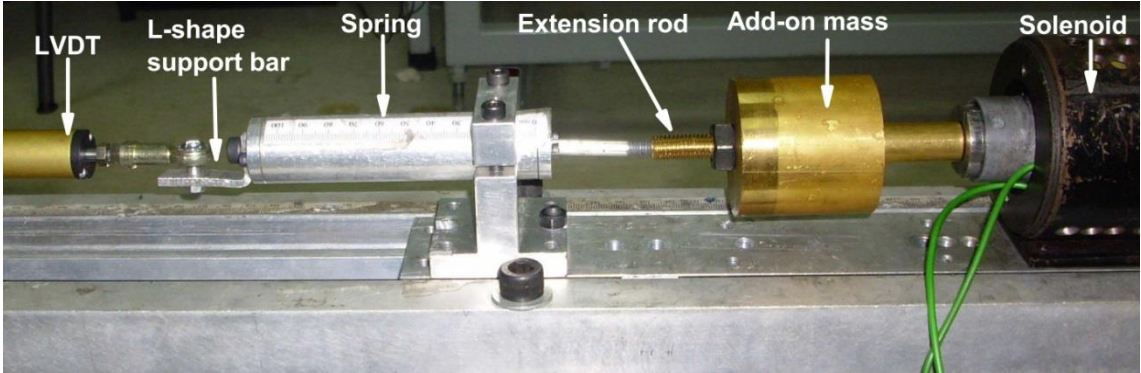


Figure 3.3: Previous vibroimpact machine operated by spring and solenoid mechanism.

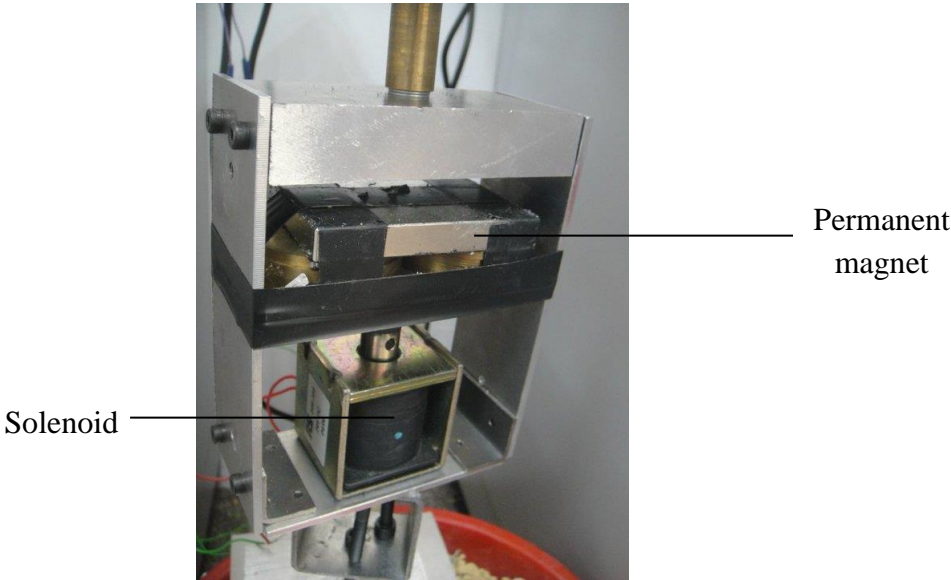


Figure 3.4: Experimental setup with permanent magnet replacing the mechanical spring.

The significant improvements in impact force have, at the same time, caused the permanent magnet to lose its magnetism over time. As such, the permanent magnet is replaced with an electromagnet. A solenoid is connected to a DC power supply. The switched AC solenoid is activated first, before switching on the DC solenoid, gradually increasing its voltage until periodic vibro-impact motion is achieved. In this way, the problem of decaying magnetic field as time passes is solved.

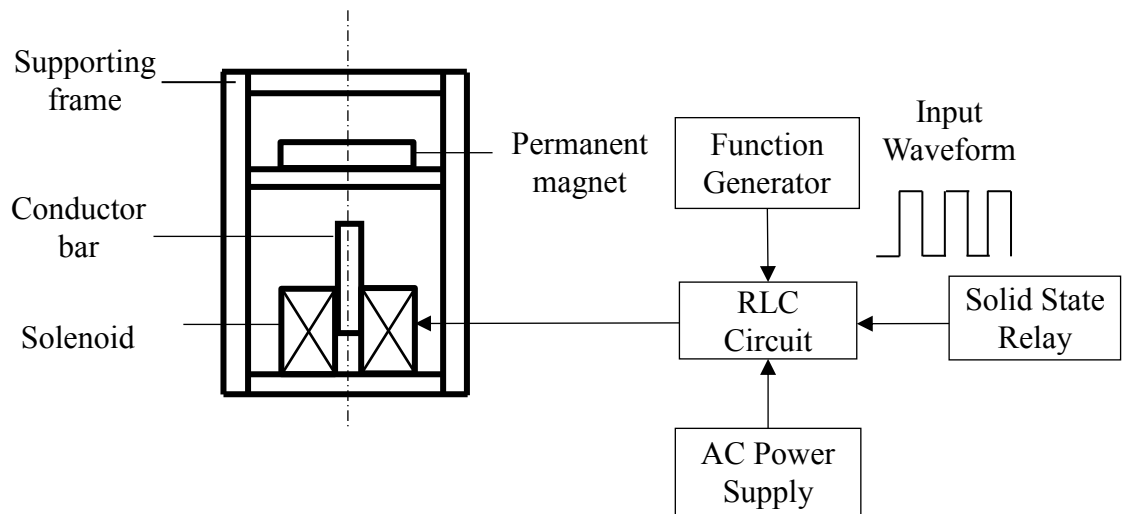


Figure 3.5: Schematic diagram of vibroimpact system with permanent magnet.

A solenoid is a coil wrapped into a tightly packed helix that produces a magnetic field when an electric current is passed through the coil. Connection to either DC or AC power supply would attract a conductor bar towards the centre of the solenoid from either extreme ends.

The solenoid is purchased from RS components of model number (RS 346-356) used in the experimental rig as both AC and DC solenoids. The technical data sheet of this model is in Appendix A. It is a light weight and compact solenoid that operates with a

minimal power supply that is able to produce sufficient electromagnetic force for the generation of vibro-impact motion. It also is economically accessible (RM 121.50, approximately £24 in 2011). The list of specifications of a solenoid RS 346-356 is shown in Table 3.1, and Figure 3.6 shows the magnetic force rating at different intermittent rates. Intermittent rate or duty cycle of a solenoid is the ratio of the “on-time” to the total time for one complete cycle (on/off) expressed as a percentage. For example, a solenoid application with an on-time of 1 second and an off-time of 3 seconds will have 25% duty cycle. This solenoid was manufactured with an intention to be powered by a direct current supply. Connection to an alternating current power supply has been found to be also effective in experiment.

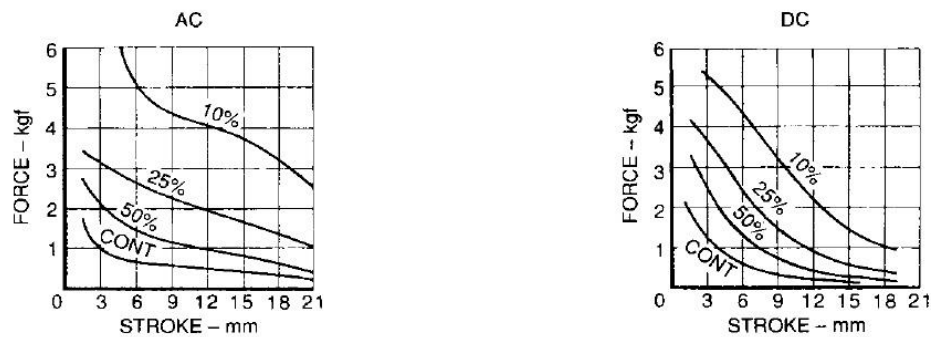


Figure 3.6: Magnetic force rating of solenoid RS 346-356 (according to RS catalogue).

Table 3.1: Specifications of solenoid RS 346-356 (according to RS catalogue).

Specification	Nominal Value
Maximum Stroke	21 mm
Action	Pull
Duty Cycle	100%
Magnetic Force	750 g
Closed Power Continuous	12 W
Supply Voltage	24 V DC
Length	47.5 mm
Width	41.5 mm
Depth	49.5 mm
Weight	425 g

3.3 One degree-of-freedom electro-vibroimpact system in a vertical orientation

Two solenoids (electromagnets) of differing nature actuate a cylindrical conductor bar made of mild steel into vibro-impact motion. The two solenoids are sources of electromagnetic fluxes, which interact with each other to generate oscillatory motion of the conductor bar. The solenoids and conductor bar with the impact stop are assembled onto an aluminium plate that acts as a base board, holding the components together.

In initial experimentation, the RS solenoids are clamped to a long aluminium plate by means of G-clamps. The rigid frame that supports the rig and the impact stopper are made of aluminium, as this material is non-magnetic and does not affect the electromagnetic field of the solenoids. The lower solenoid, connected to an AC power supply, is placed above the stop such that impact of conductor with stop is in turn

transmitted to the whole rig. The upper solenoid, connected to a DC power supply, is fastened at 63 mm above the former solenoid.

The stop prevents the conductor bar from moving out of and below the bottom of the AC solenoid. In the DC solenoid, a hole of diameter 15 mm, slightly larger than the conductor bar diameter (13.5 mm), tapped at the lower end of the solenoid to create a through hole for the conductor bar to move freely within both solenoids.

The conductor used is a cylindrically-shaped mild steel of diameter 13.5 mm, which is slightly less than the inner bore of solenoids, which is 15 mm. It has a length of 141 mm and mass of 155 g. In order to measure vertical vibrations of conductor, a screwthread 1 mm in diameter is tapped to a depth of 2.5 mm so that extension rod of a linear variable differential transformer (LVDT) displacement sensor may be attached to the conductor rigidly. The LVDT used is a Solartron M922938A433-03. This arrangement is shown in a photograph in Figure 3.7 and a schematic in Figure 3.8.

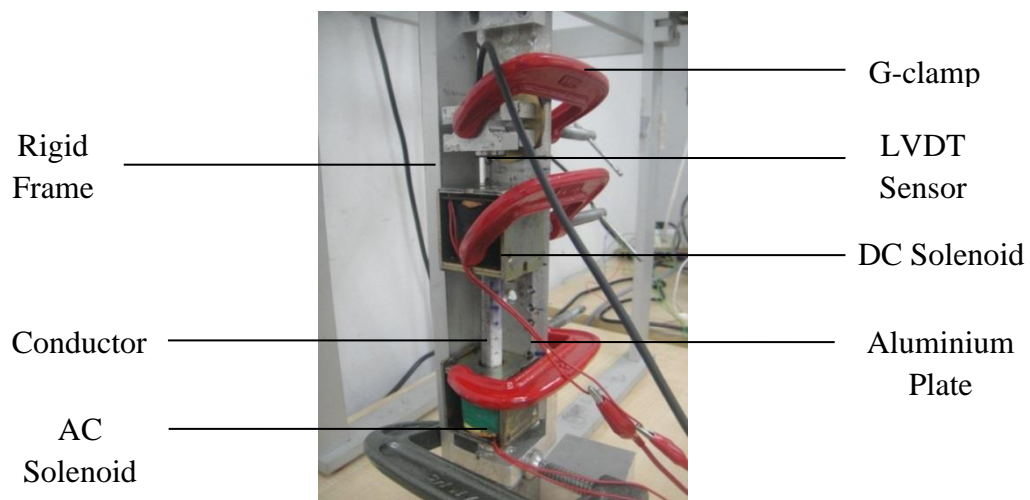


Figure 3.7: Diagram of the one degree-of-freedom vibroimpact machine.

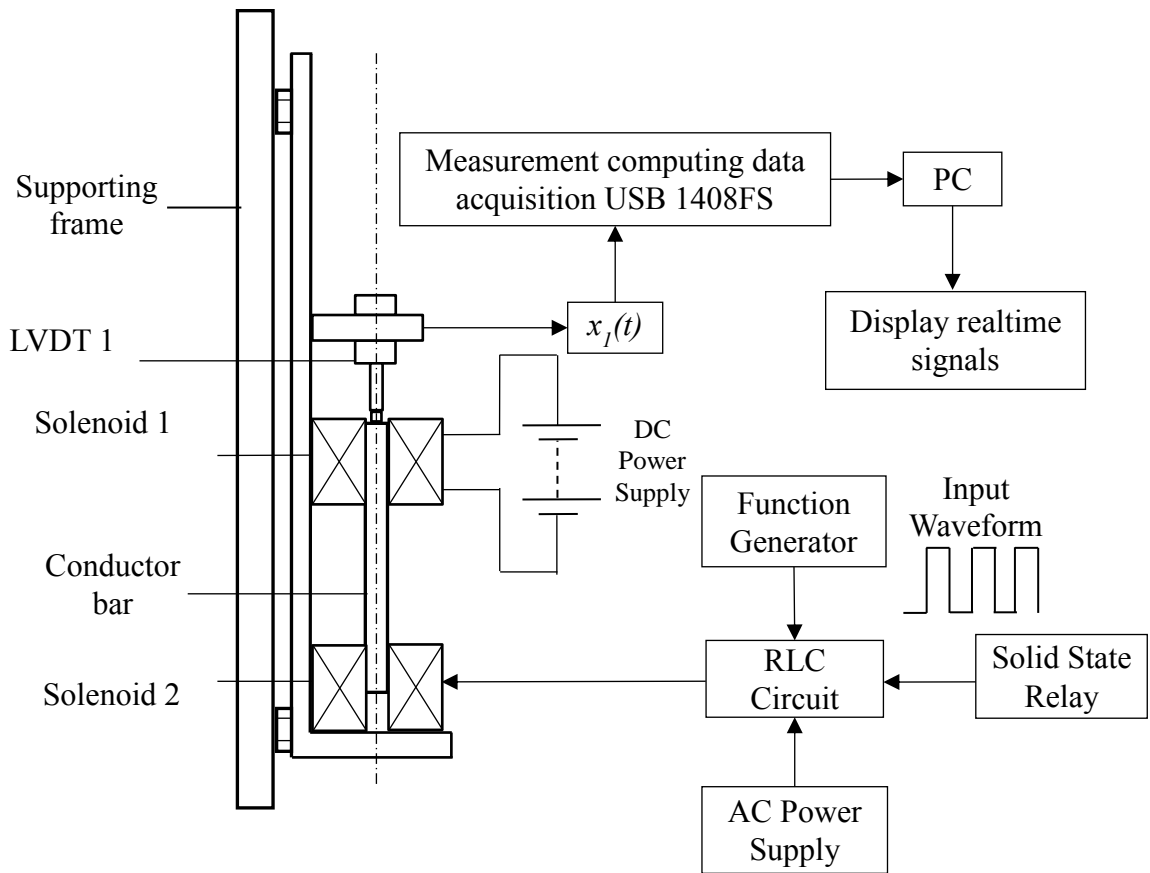


Figure 3.8: Schematic diagram of one degree-of-freedom electro-vibroimpact system in a vertical orientation.

The upper solenoid is connected to a GW laboratory DC power supply model GPS-3030. By supplying a voltage of 15 V to the solenoid, it acts primarily as a restoring force to recover the conductor bar's position, attracting the bar towards the upper solenoid after impact occurs.

Connection of upper solenoid to a direct current (DC) voltage power supply allows it to function as an electromagnet exerting a constant attractive force on the conductor. The

lower solenoid is connected to a switched series RLC circuit which turns on and off in accordance square waves from a function generator. Correspondingly, lower solenoid exerts a periodic train of attractive pulses on conductor, while at the same time the upper solenoid produces an attractive force, of which magnitude is displacement-dependant.

In order to understand the vibro-impact dynamics of the system, experiments were performed for a single degree-of-freedom system, by temporarily constraining the base plate. In this way, only the conductor is moving in the experiment. The aluminium plate that bears the solenoids, conductor and stop is clamped to a rigid frame using G-clamps, halting it from progressing downward, in the direction of by the impact. Friction of the inner wall of solenoid is reduced by application of grease and WD-40 lubricant. By constraining the conductor bar to oscillate only in vertical motion, the impact transmitted to rigid foundation is increased. The LVDT displacement sensor attached to the conductor bar records its displacement-time history for the whole duration of vibro-impact oscillation.

An end of the extension rod is threaded, which is mechanically attached to a tapped screwthread in the conductor. The origin of the conductor position is set to the impacting surface of the conductor bar at rest when in contact with the stop. Positive displacement is taken in the direction away from the stop, only for the purpose of analysis and sign convention. As operating frequency of solid state relay (SSRL) determines frequency of switching on AC power supply, the system dynamic response of conductor oscillations is measured. Time histories are recorded at various operating

frequencies, ranging from 2 Hz to 10 Hz. In addition to data acquisition in software, the analogue signals are also viewed on an oscilloscope to ensure integrity of the acquired data.

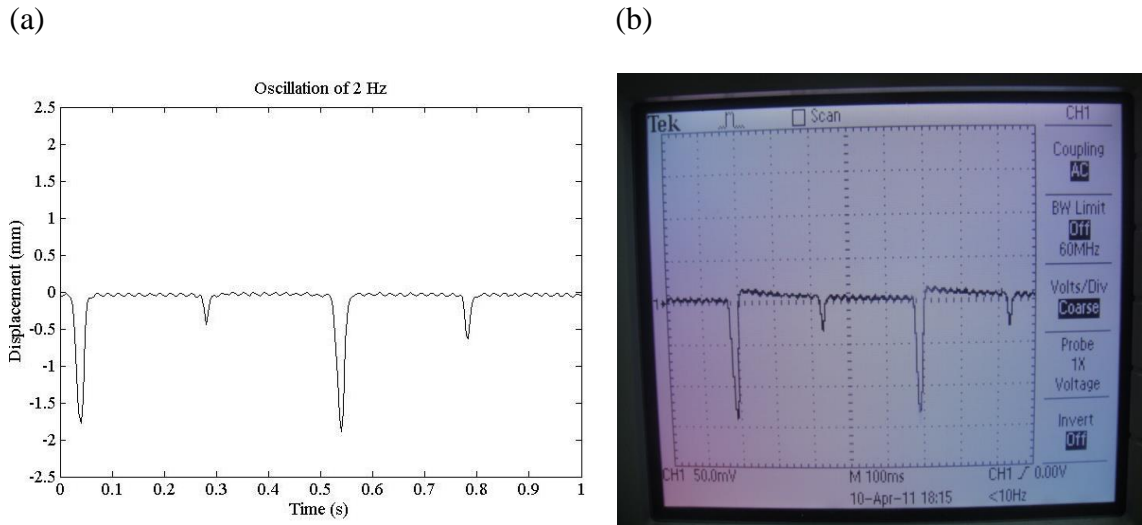


Figure 3.9: (a) Experimental time histories of conductor bar vibro-impact oscillations at operating frequency of 2 Hz (b) validated against an oscilloscope reading.

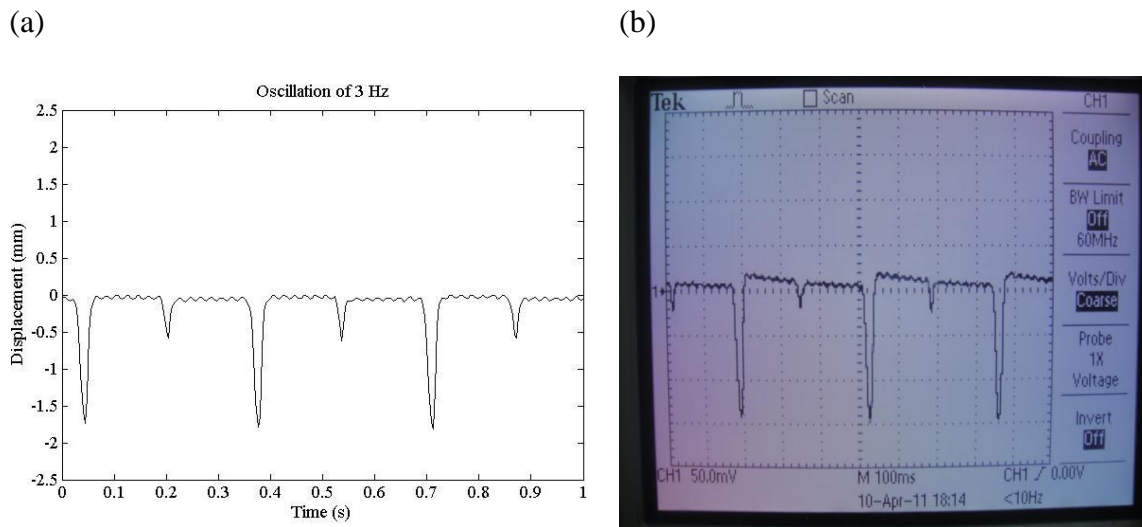


Figure 3.10: (a) Experimental time histories of conductor bar vibro-impact oscillations at operating frequency of 3 Hz (b) validated against an oscilloscope reading.

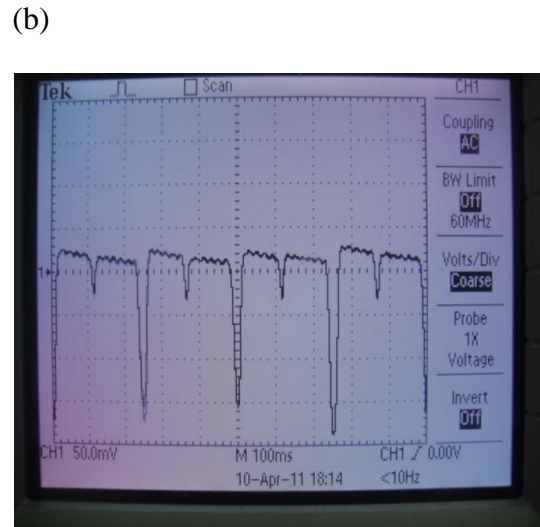
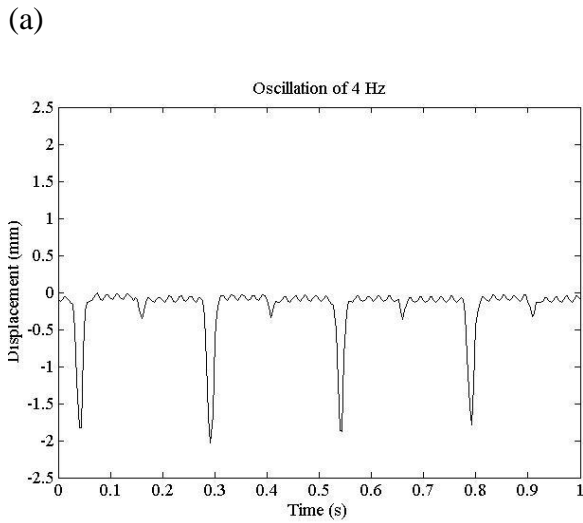


Figure 3.11: (a) Experimental time histories of conductor bar vibro-impact oscillations at operating frequency of 4 Hz (b) validated against an oscilloscope reading.

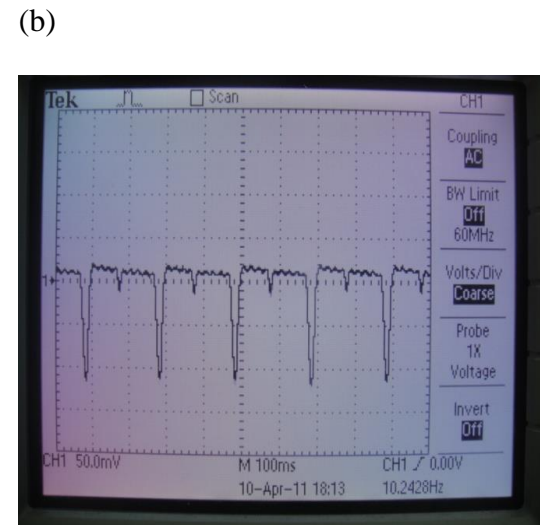
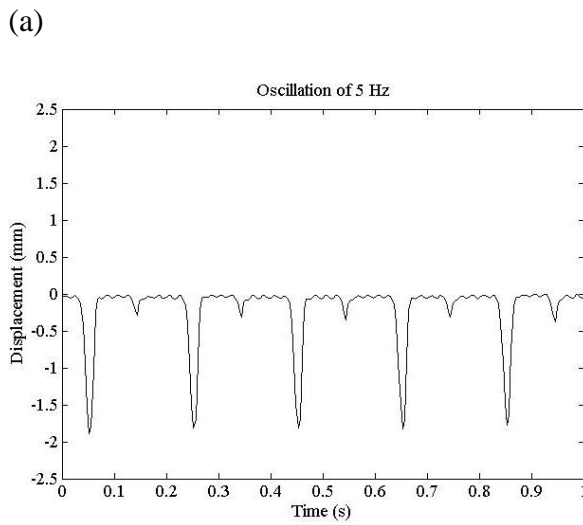


Figure 3.12: (a) Experimental time histories of conductor bar vibro-impact oscillations at operating frequency of 5 Hz (b) validated against an oscilloscope reading.

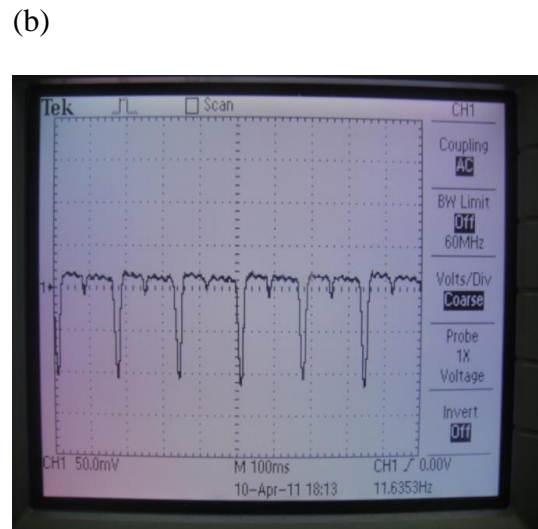
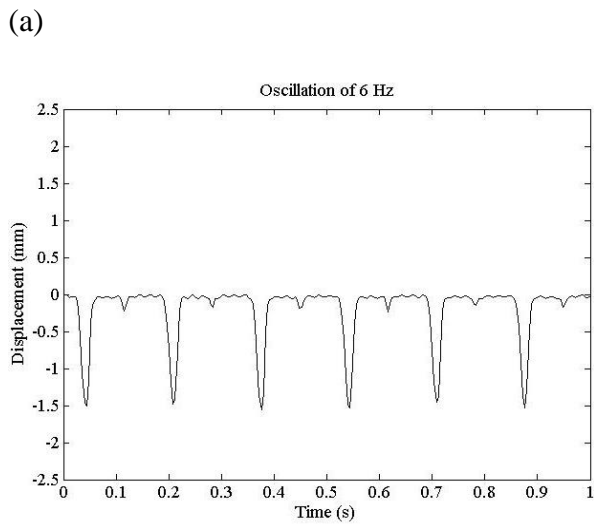


Figure 3.13: (a) Experimental time histories of conductor bar vibro-impact oscillations at operating frequency of 6 Hz (b) validated against an oscilloscope reading.

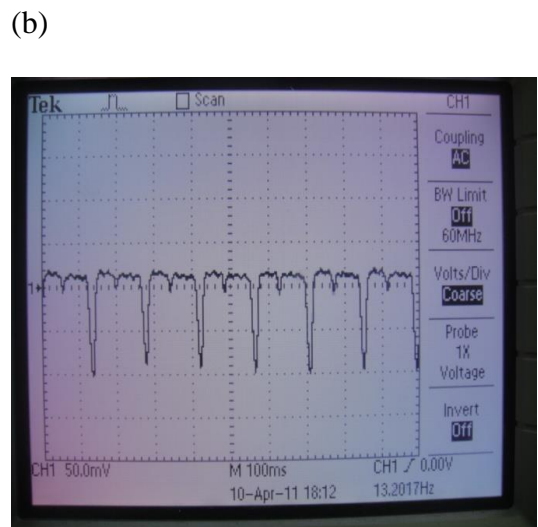
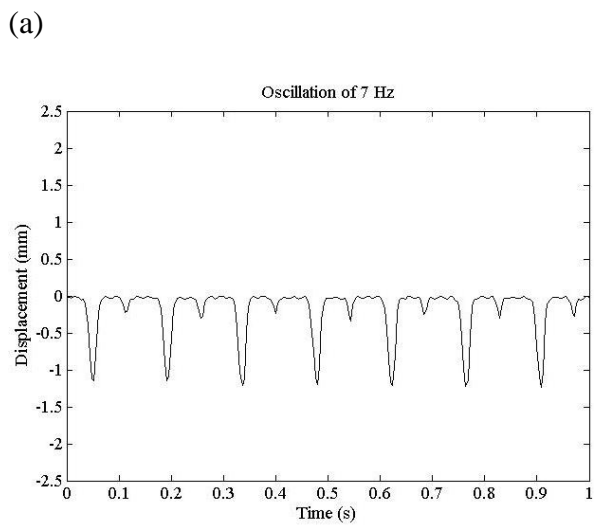


Figure 3.14: (a) Experimental time histories of conductor bar vibro-impact oscillations at operating frequency of 7 Hz (b) validated against an oscilloscope reading.

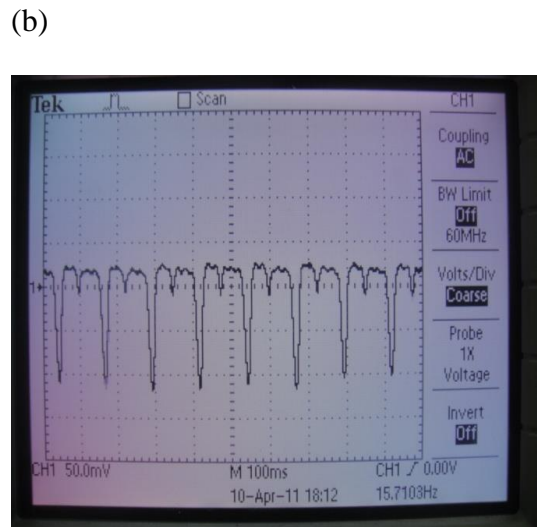
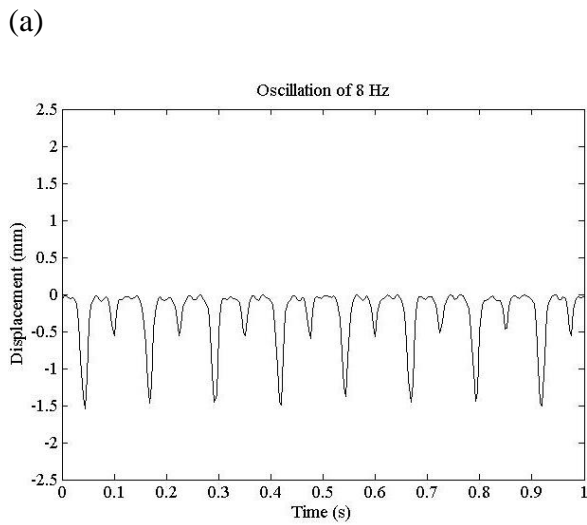


Figure 3.15: (a) Experimental time histories of conductor bar vibro-impact oscillations at operating frequency of 8 Hz (b) validated against an oscilloscope reading.

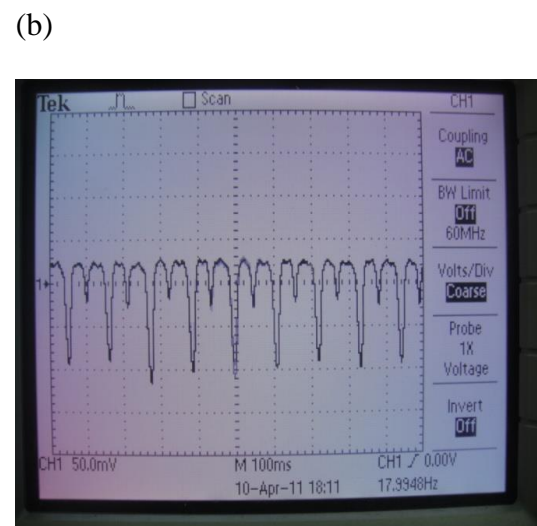
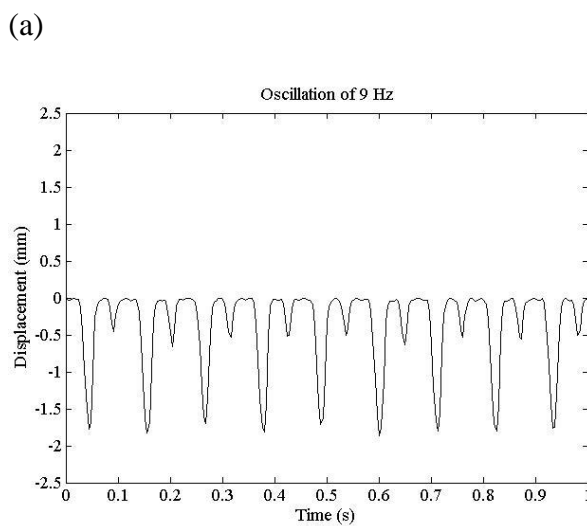


Figure 3.16: (a) Experimental time histories of conductor bar vibro-impact oscillations at operating frequency of 9 Hz (b) validated against an oscilloscope reading.

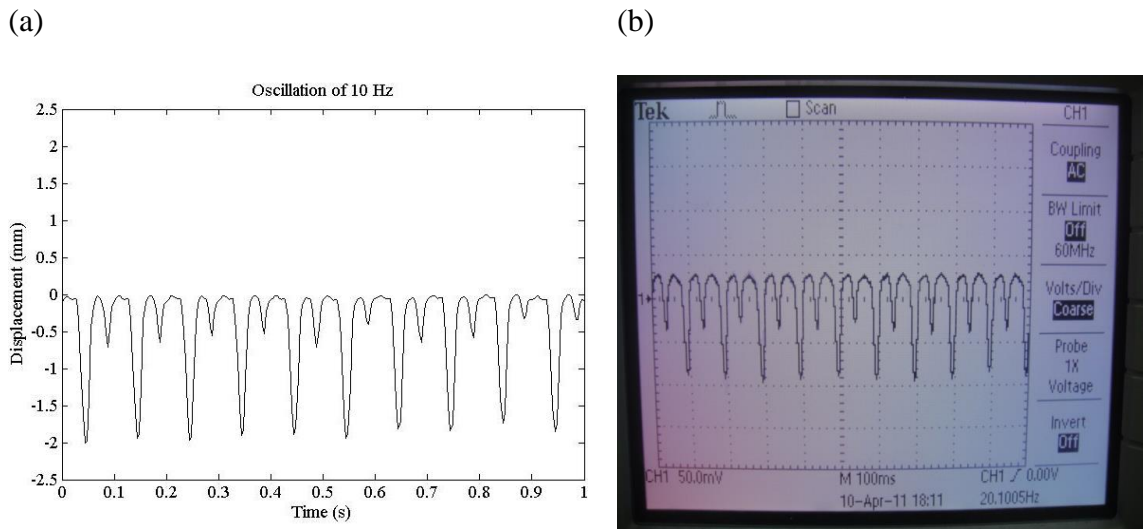


Figure 3.17: (a) Experimental time histories of conductor bar vibro-impact oscillations at operating frequency of 10 Hz (b) validated against an oscilloscope reading.

3.4 Two degree-of-freedom electro-vibroimpact system in a vertical orientation

To investigate the progression rate of experimental rig into brick sample, an additional LVDT transducer, measures the downward displacement of the experimental rig into the sample. Oscillation of the conductor bar and rig progression of the 2 degree-of-freedom vibroimpact system are being recorded. A bolt with a sharp end is attached to the bottom of the experiment machine to transmit impact created by the oscillating bar to the brick sample, as shown in Figure 3.18.

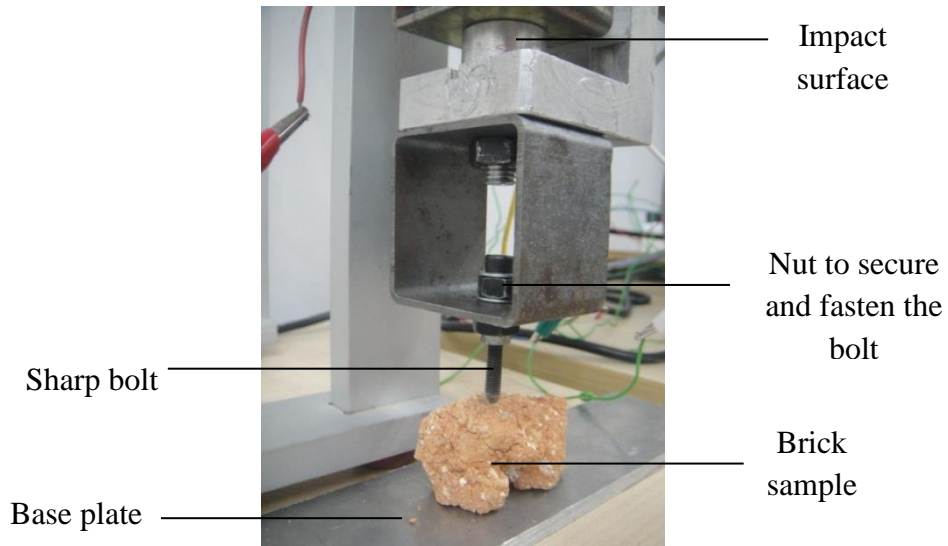


Figure 3.18: Transmission of impact force to a brick sample.

To maintain a vertical orientation, a cylindrical brass bar extends from the top of the rig and guided within an SKF linear ball bearing, ISO series 1. A threaded tap of diameter 4 mm is made in this piece of brass to a depth of 5 mm so that extension rod from a Sfernice WO3263 LVDT transducer can be connected rigidly, as shown in Figure 3.18.

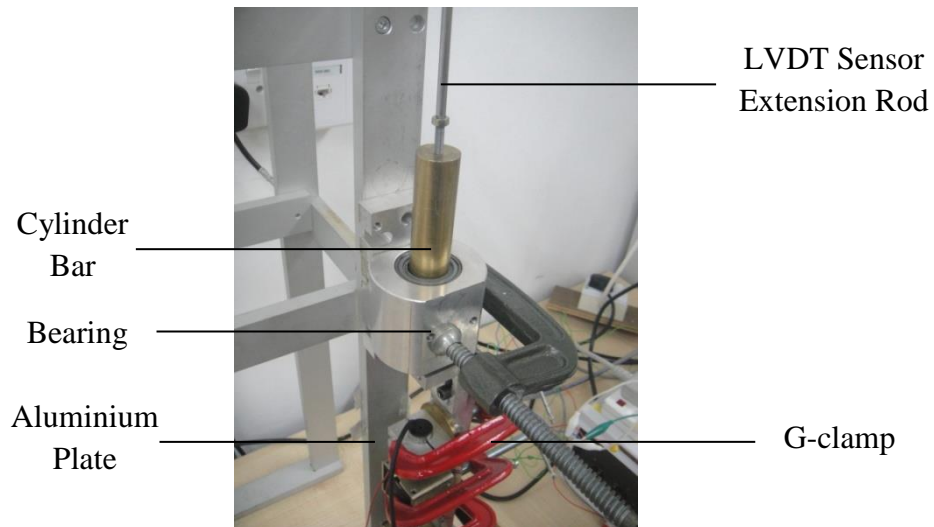


Figure 3.19: Slider bearing and sensor connection to the rig.

Before initiation of experiment, vertical orientation of rig is ensured by means of spirit level. This is to allow gravitational force to be a full vertical downward static component to assist downward progression. Data acquisition of electrical signals involved sampling at a rate of 250 Hz by means of National Instruments LabVIEW software, using National Instruments SCB-68 hardware and digitized from a vi file, generic to labview.

Figure 4.8 illustrates individual components of the electro-vibroimpact system. The first component at the top of the photograph is a SKF linear bearing. A Sfernice linear variable displacement transducer has an extension rod which is mechanically fastened to a brass cylindrical bar. This is in turn attached to an aluminium plate on which all components reside. Below this point of connection, a Solartron linear variable displacement transducer DF5 measures the oscillations of conductor bar. Two solenoids are positioned one on top of the other; the upper solenoid is connected to a DC power supply, and the lower solenoid is connected to an AC power supply. A cylindrical ferrous bar oscillates within the solenoids, and impacts on a stop surface. This impact force is transmitted, via a sharp bolt to the brick sample at the bottom of the photograph. Figure 3.20 (b) depicts a corresponding schematic diagram of the electro-vibroimpact system. Linear variable displacement transducer 1 and linear variable displacement transducer 2 record displacement of oscillating conductor bar, $x_1(t)$ and the downward progression, $x_2(t)$ respectively. Sampling of analogue electrical signals at 250 Hz acquires data in discrete in a text file storage in a personal computer (PC). The PC also

outputs a square wave signal and waveform, $V_{ctr}(t)$ the lower solenoid, Solenoid 2, on and off in accordance to an operating frequency.

(a)



Figure 3.20: (a) Photograph of two degree-of-freedom electro-vibroimpact system.

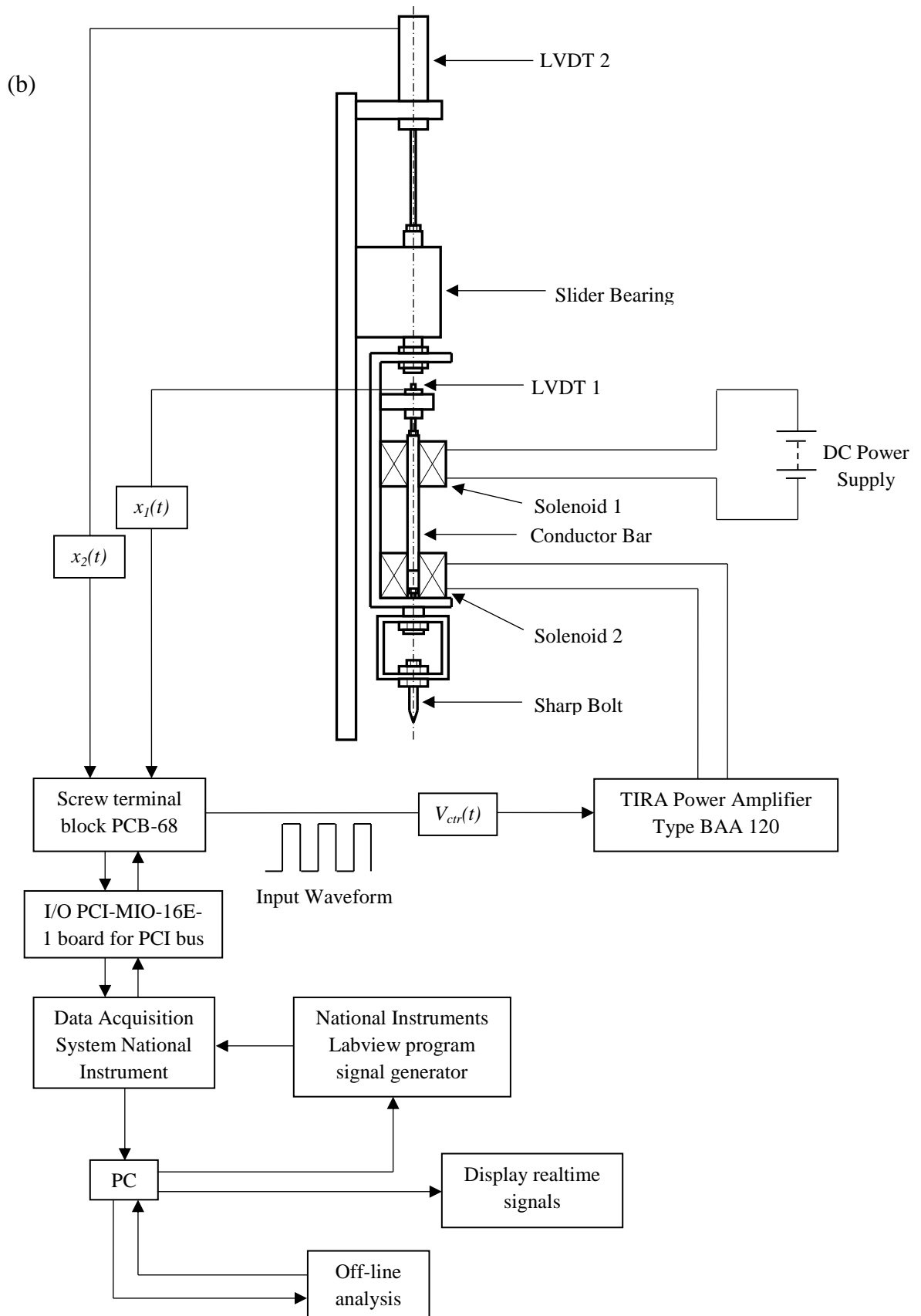


Figure 3.20: (b) Schematic of two degree-of-freedom electro-vibroimpact system.

The relative displacement of the conductor to the base plate is measured using a Solartron linear variable displacement transducer model DF5 (or M922938A433-03) from Solartron. The LVDT is clamped to the aluminium plate at a position above the oscillating bar. It is mechanically connected to the oscillating bar. A screw thread of 1mm is tapped into the bar to facilitate. The measurement range of this LVDT is 10 mm (or ± 5 mm). It accepts a DC input and provides a DC output relative to armature position. This is suitable for the measurement of conductor oscillations, especially due to its compact size; a total diameter of 19.0 mm and light nominal mass of 30.0 g. As such, it is easily installed into a compact machine. The material used in its casing is 400 Stainless Steel, that has a minimal interference to the electromagnetic field generated by solenoids. The required direct current power supply needed is 24 V. The maximum voltage output at its maximum stroke of +5 mm is 3.76 V, which gives the calibration factor of 1.33 from voltage output to the displacement in mm measured.

Consistent with work described in the preceding section, a frequency range of 2 Hz to 10 Hz is tested for this two degree-of-freedom system. Photographs of each brick before testing were taken to complement experimental data of vibro-impact oscillations, as well as that of downward progression of experimental rig.

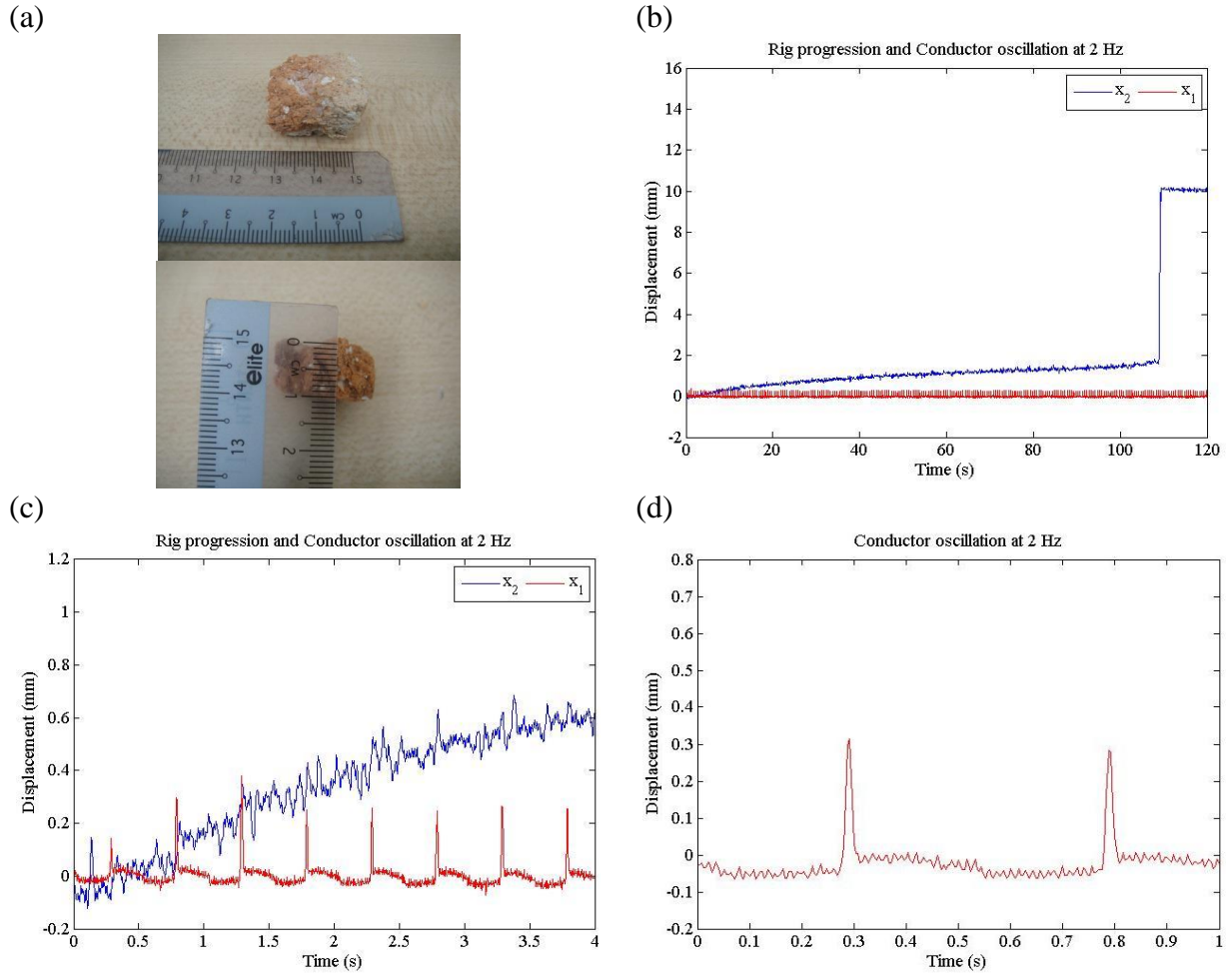
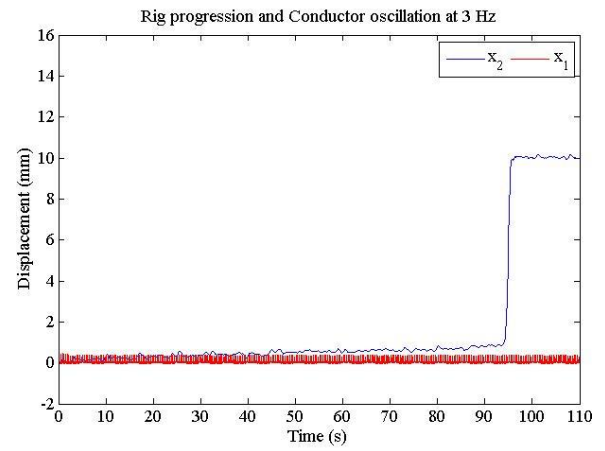


Figure 3.21: Showing the (a) brick sample of 1 cm thickness, (b) combined time history of conductor oscillations (red line) and rig downward progression (blue line), (c) zoomed in time history of conductor oscillations (red line) and rig downward progression (blue line) at first 4 seconds and (d) time history of conductor oscillation in 1 second for solid state relay frequency of 2 Hz.

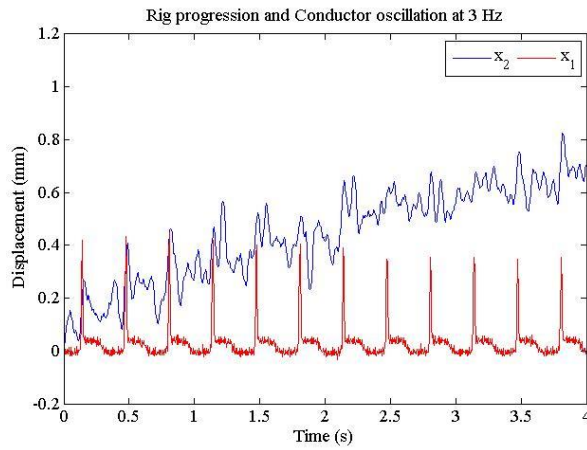
(a)



(b)



(c)



(d)

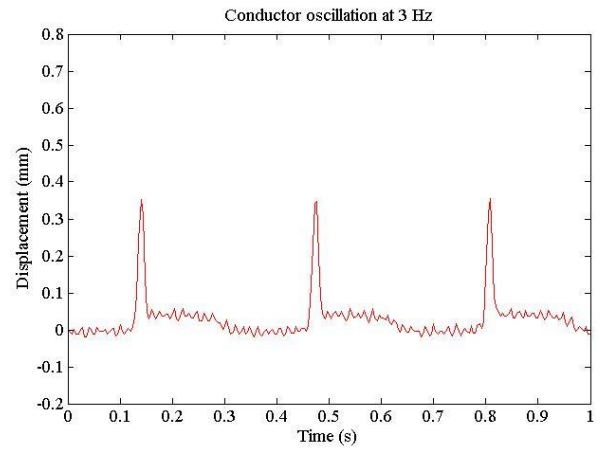
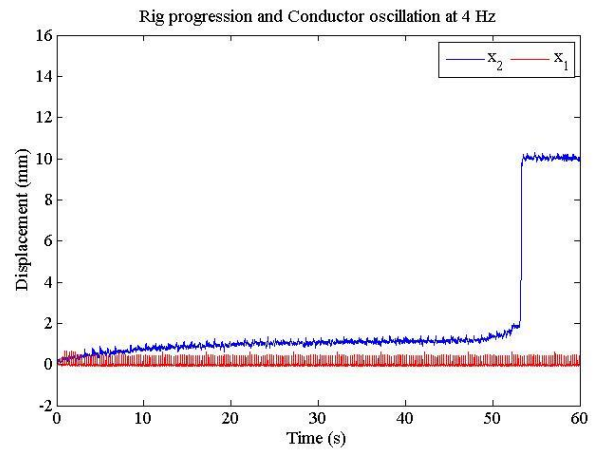


Figure 3.22: Showing the (a) brick sample of 1 cm thickness, (b) combined time history of conductor oscillations (red line) and rig downward progression (blue line), (c) zoomed in time history of conductor oscillations (red line) and rig downward progression (blue line) at first 4 seconds and (d) time history of conductor oscillation in 1 second for solid state relay frequency of 3 Hz.

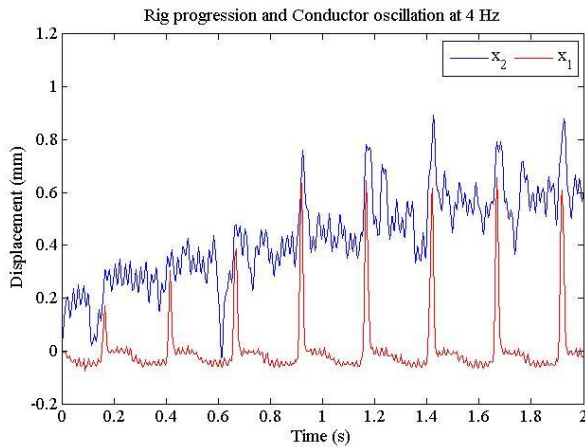
(a)



(b)



(c)



(d)

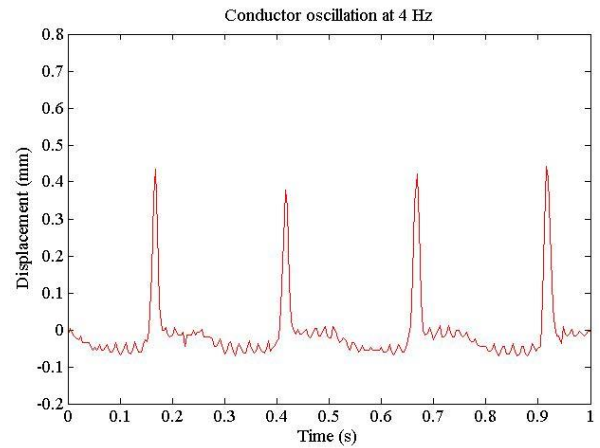
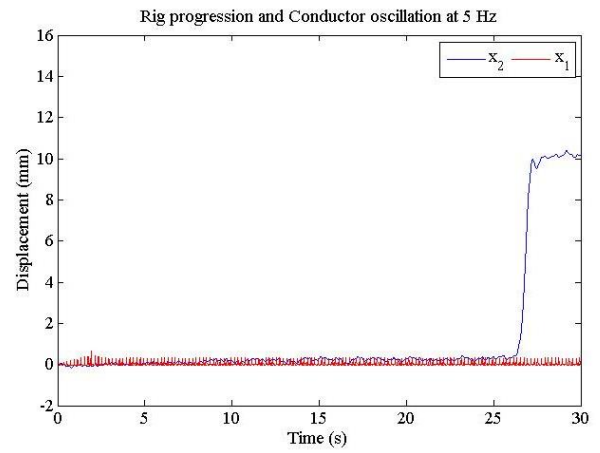


Figure 3.23: Showing the (a) brick sample of 1 cm thickness, (b) combined time history of conductor oscillations (red line) and rig downward progression (blue line), (c) zoomed in time history of conductor oscillations (red line) and rig downward progression (blue line) at first 2 seconds and (d) time history of conductor oscillation in 1 second for solid state relay frequency of 4 Hz.

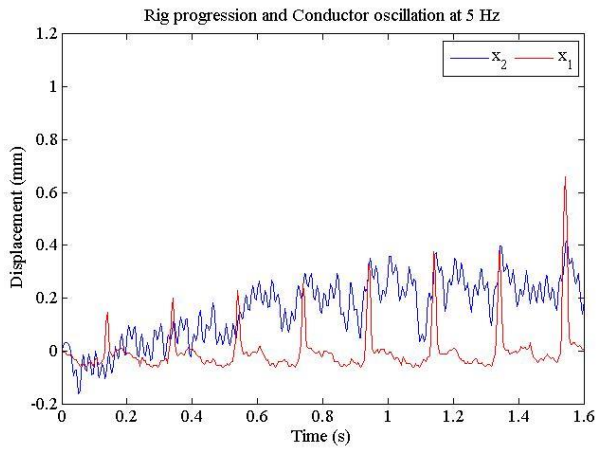
(a)



(b)



(c)



(d)

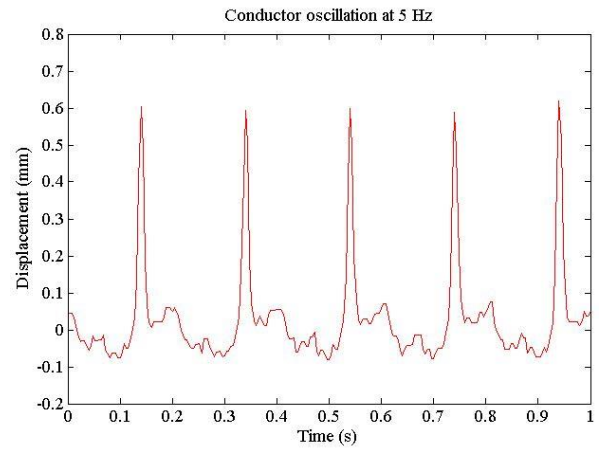
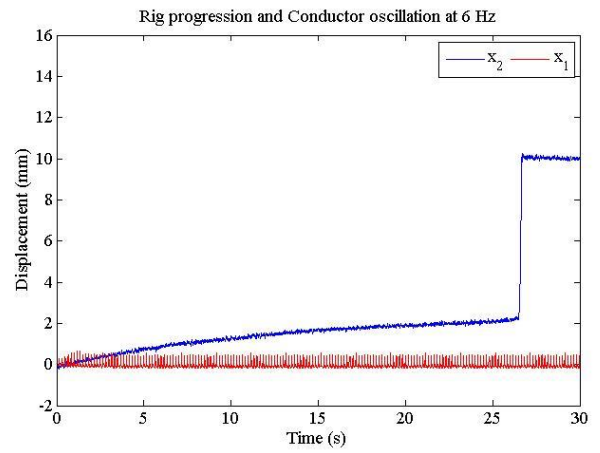


Figure 3.24: Showing the (a) brick sample of 1 cm thickness, (b) combined time history of conductor oscillations (red line) and rig downward progression (blue line), (c) zoomed in time history of conductor oscillations (red line) and rig downward progression (blue line) at first 1.6 seconds and (d) time history of conductor oscillation in 1 second for solid state relay frequency of 5 Hz.

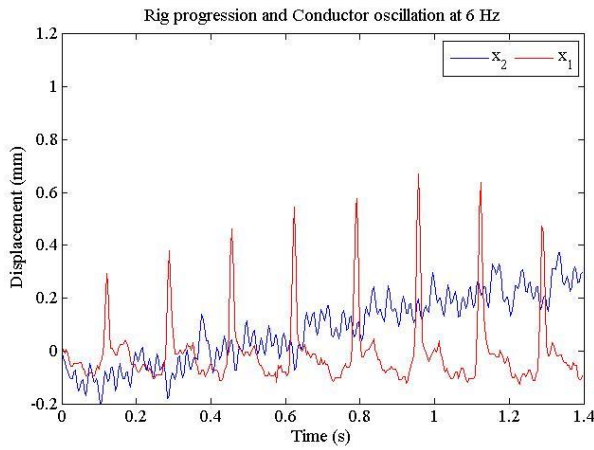
(a)



(b)



(c)



(d)

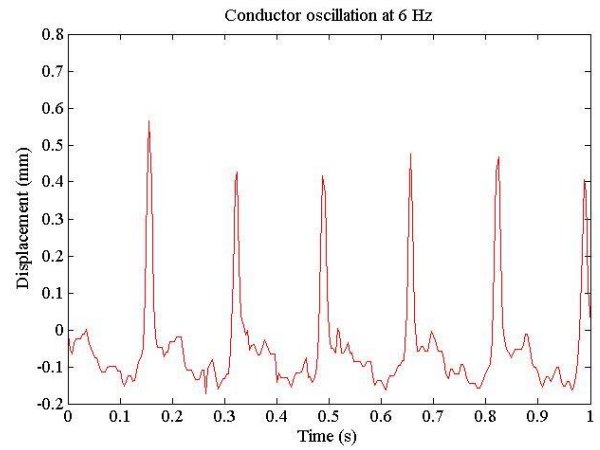
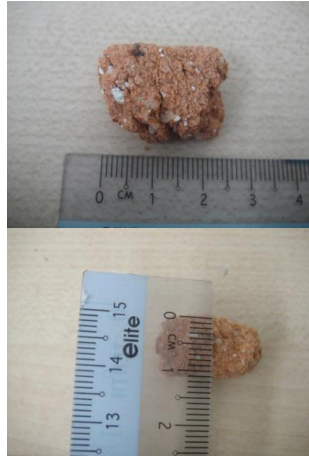
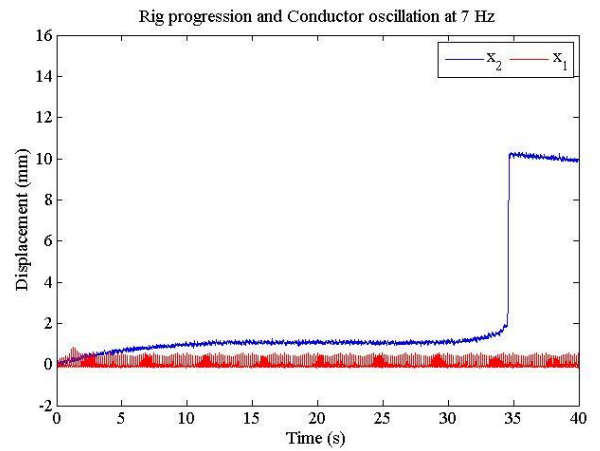


Figure 3.25: Showing the (a) brick sample of 1 cm thickness, (b) combined time history of conductor oscillations (red line) and rig downward progression (blue line), (c) zoomed in time history of conductor oscillations (red line) and rig downward progression (blue line) at first 1.4 seconds and (d) time history of conductor oscillation in 1 second for solid state relay frequency of 6 Hz.

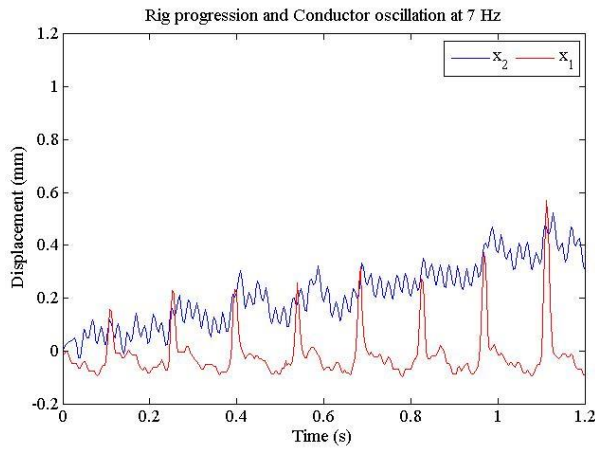
(a)



(b)



(c)



(d)

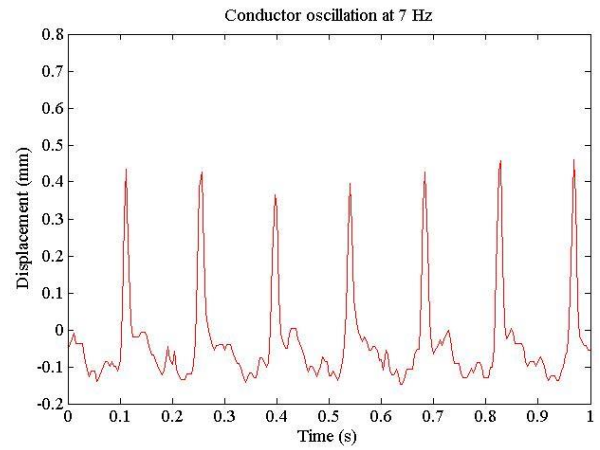
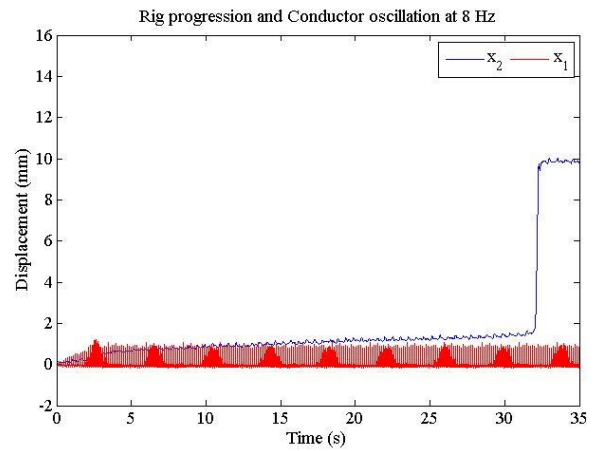


Figure 3.26: Showing the (a) brick sample of 1 cm thickness, (b) combined time history of conductor oscillations (red line) and rig downward progression (blue line), (c) zoomed in time history of conductor oscillations (red line) and rig downward progression (blue line) at first 1.2 seconds and (d) time history of conductor oscillation in 1 second for solid state relay frequency of 7 Hz.

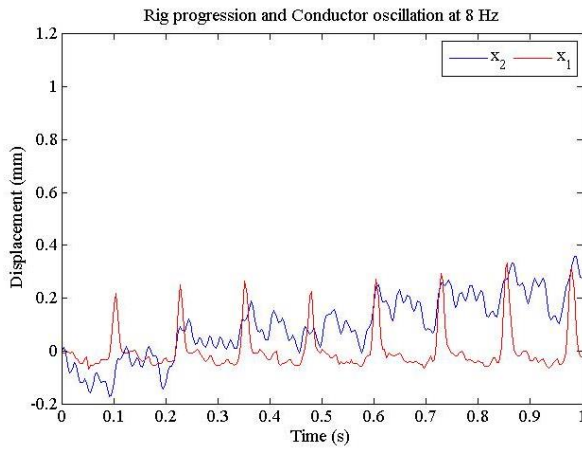
(a)



(b)



(c)



(d)

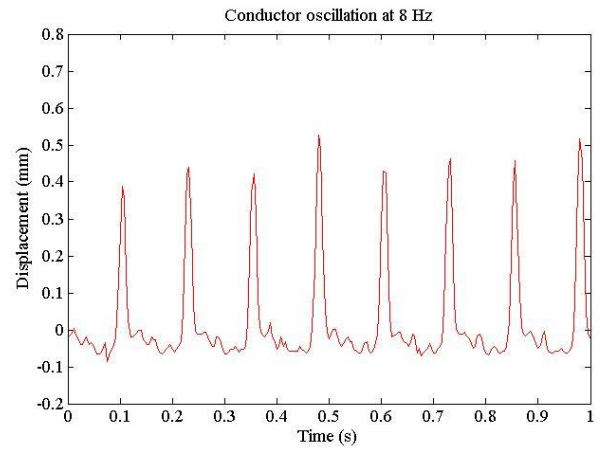


Figure 3.27: Showing the (a) brick sample of 1 cm thickness, (b) combined time history of conductor oscillations (red line) and rig downward progression (blue line), (c) zoomed in time history of conductor oscillations (red line) and rig downward progression (blue line) at first 1 seconds and (d) time history of conductor oscillation in 1 second for solid state relay frequency of 8 Hz.

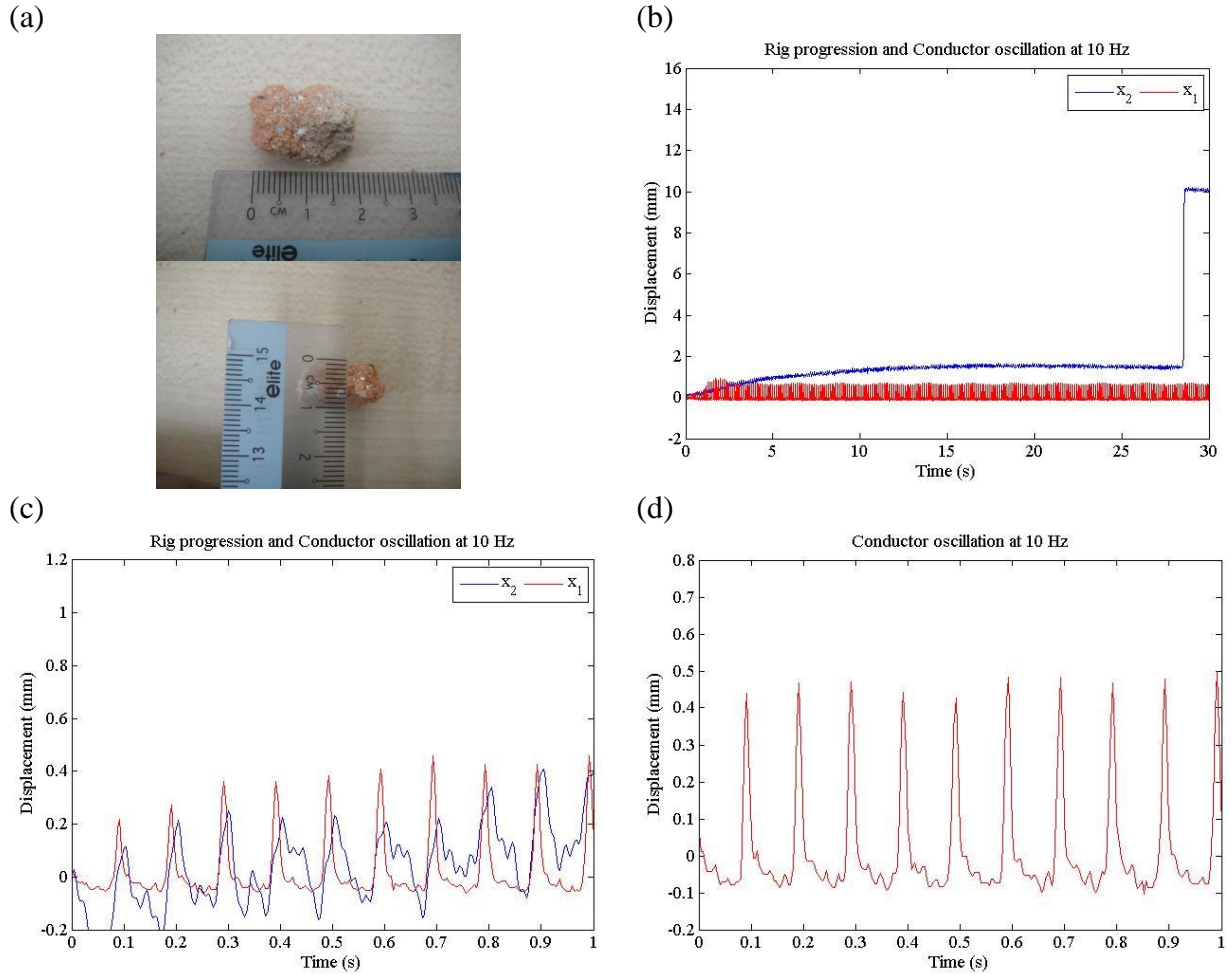


Figure 3.29: Showing the (a) brick sample of 1 cm thickness, (b) combined time history of conductor oscillations (red line) and rig downward progression (blue line), (c) zoomed in time history of conductor oscillations (red line) and rig downward progression (blue line) at first 1 seconds and (d) time history of conductor oscillation in 1 second for solid state relay frequency of 10 Hz.

The brick samples used have the same thickness of 1 cm to ensure consistency in experiment environment and resistive force. The brick sample is kept to be small so that complete fracture of sample could be achieved in the shortest duration. In Figure 3.21 (b)

to Figure 3.29 (b), red line represents the conductor oscillations, x_1 in conjunction with the downward progression of the rig, x_2 into brick sample represented by the blue line.

The frequency response of the oscillations of the conductor bar reflects the signal frequency input of solid state relay. Amplitude of oscillation has decreased significantly compared to the one degree-of-freedom system experiment, due to the resistive force of the brick sample. Besides that, it is observed that the oscillation has a more irregular impact contact. This is caused by direct contact of the vibro-impact system to the brick sample, vibrating locally as micro-progression is being made in response to the impact received. With naked eye, almost no noticeable progression is made on the brick sample for several minutes, and a sudden drop occurs, cutting the sample into half. It is suggested through the recorded displacement-time history of the rig downward progression that very small downward progression is made along vibro-impact machine operation, and the drastic decrease in displacement signifies full crack propagation, causing the vibro-impact system to drop.

Figure 3.21 (c) to Figure 3.29 (c) is the zoomed in time histories that focus the initial progression and oscillations. It shows that rig progression is achieved by each impact made by the conductor bar. Figure 3.21 (d) to Figure 3.29 (d) show time histories of steady state oscillations of conductor bar in 1 second. As previous experiment results showed, frequency response of conductor oscillation and the solid state relay frequency are synchronised.

As mentioned earlier, the impact force is related to the amplitude of the conductor oscillation. The larger the amplitude, the stronger the impact force, thus promotes progression rate and completing the crack in a shorter duration. The average amplitude for 5 Hz and 10 Hz signal frequency is the highest among the range of 2 Hz to 10 Hz. This is supported by the one degree-of-freedom experiments that showed similar observations. Overall, this section proved the ability of the vibro-impact system operating in vertical orientation and able to produce impact force strong enough to penetrate brittle material, in this case brick pieces.

3.5 Two degree-of-freedom electro-vibroimpact system in Horizontal Orientation

The vibro-impact system is tested under soil condition in horizontal orientation. The bolt head that is used for vertical orientation experiment is replaced with a mole head. The moling head is made of aluminium, with a total length of 300 mm and increasing cross section diameter from 10 mm, to 30 mm and to 60 mm. The mole head is designed in such way that soil resistance increases as the machine progresses further. The mole head is attached to the vibro-impact system via a 20 mm screwthread to the stop that receives the impacts.

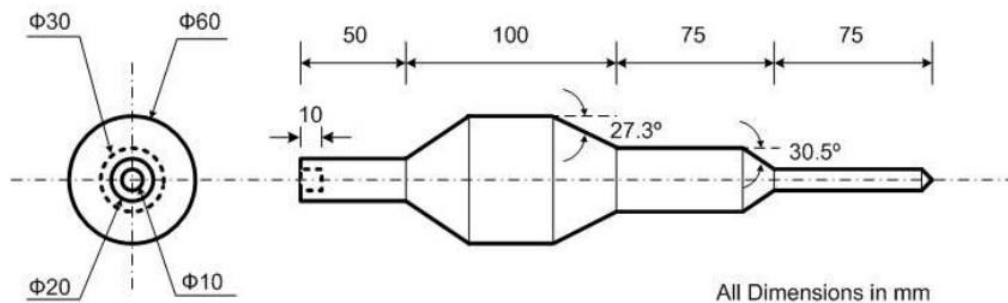


Figure 3.30: Schematic of mole head.

A rigid frame with a horizontal flat surface is used to support and elevate the vibro-impact system to the height of the tunnel entry. A long aluminium plate is placed under the system as a guiding rail to the tunnel entry. The plate is clamped onto the rigid frame, preventing it from moving under the effect of the system's vibration and forward progression. The experimental setup of a horizontal two-degrees-of-freedom is shown in a photograph of Figure 3.31 and its schematic diagram in Figure 3.32.

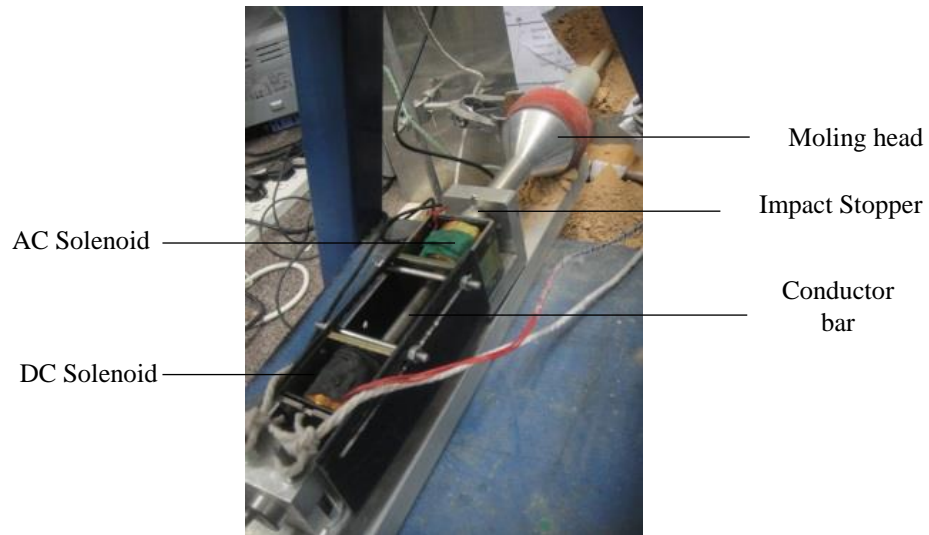


Figure 3.31: Diagram of the experimental rig in horizontal orientation.

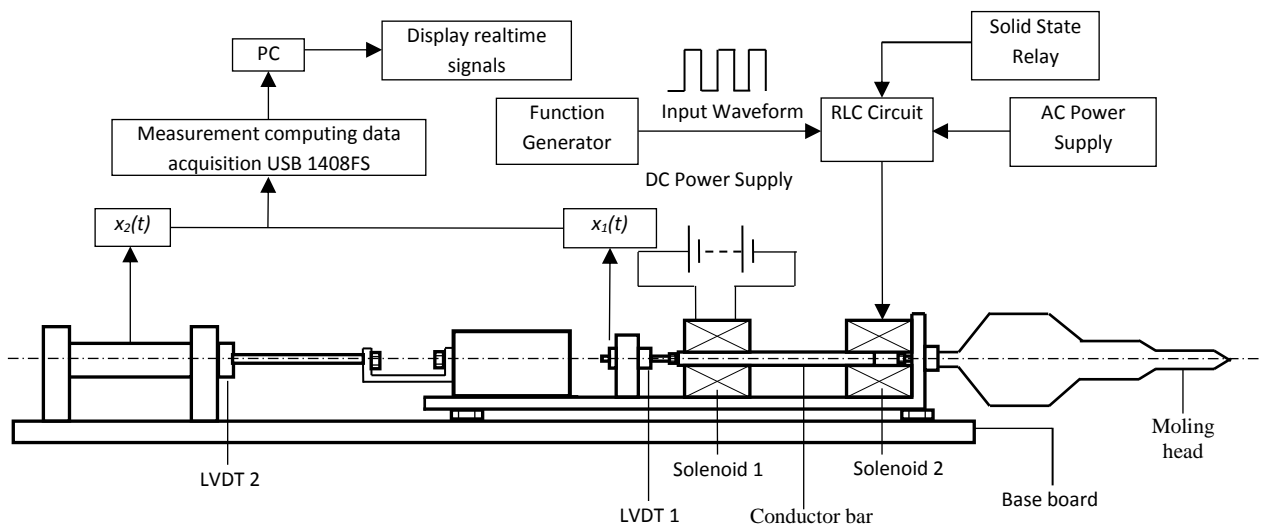


Figure 3.32: Schematic diagram of the experimental rig in horizontal orientation.

It is suggested by Krivstov and Wiercigroch [24] that static forces applied in the same direction of the periodic impacts promotes higher MRR. As such, it also improves the progression rate of rig into soil. In order to achieve the effect of a static force constantly applying force directing the rig into the moling direction, a pulley and weight system is being added.

Two strings are tied to the left and right sides of the vibro-impact machine. The other ends of both strings are tied to a weight hanger, which force can be added by inserting weight of desired mass into the hanger. The strings are pulled forward and the direction is changed upward by bending over two retort stand, pulled over a pulley that is fastened to the wall of the soil box using a G-clamp. A total of 3.11 kg of weight is added as static force.

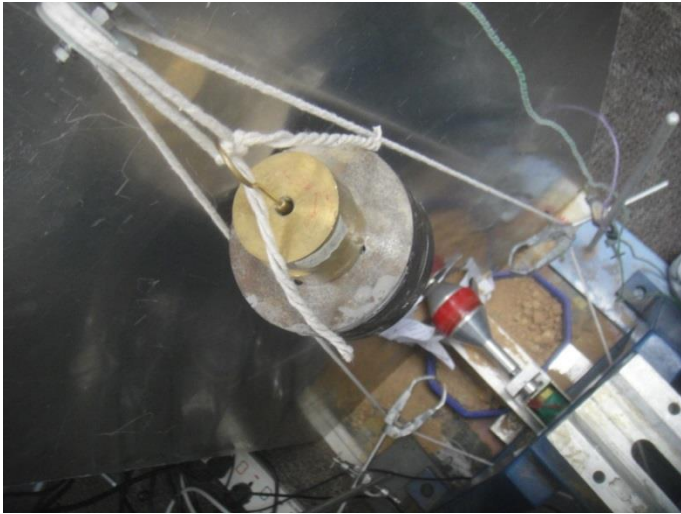


Figure 3.33: Diagram of the static load suspended by pullies.

The weight is slightly lifted up before the operation starts so that no static force is exerted. The AC solenoid is then turned on, followed by gradually increasing the DC power supply until periodic vibro-impact motion is achieved. The weight is then released to pull the strings downward, through changing direction using the pulley and retort stands, pulling the vibro-impact system forward with a steady force. The schematic diagram of the experimental setup is shown in Figure 3.34.

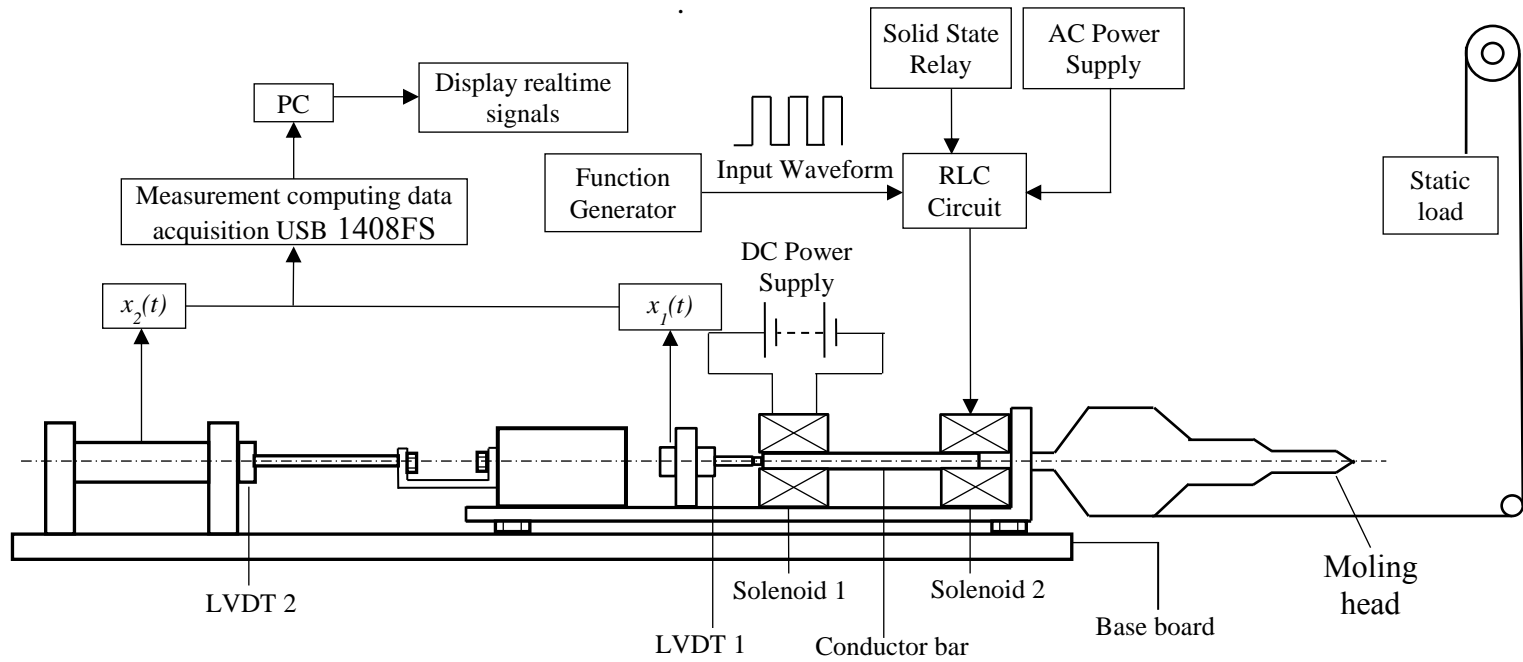


Figure 3.34: Schematic diagram of the vibro-impact machine with static load.

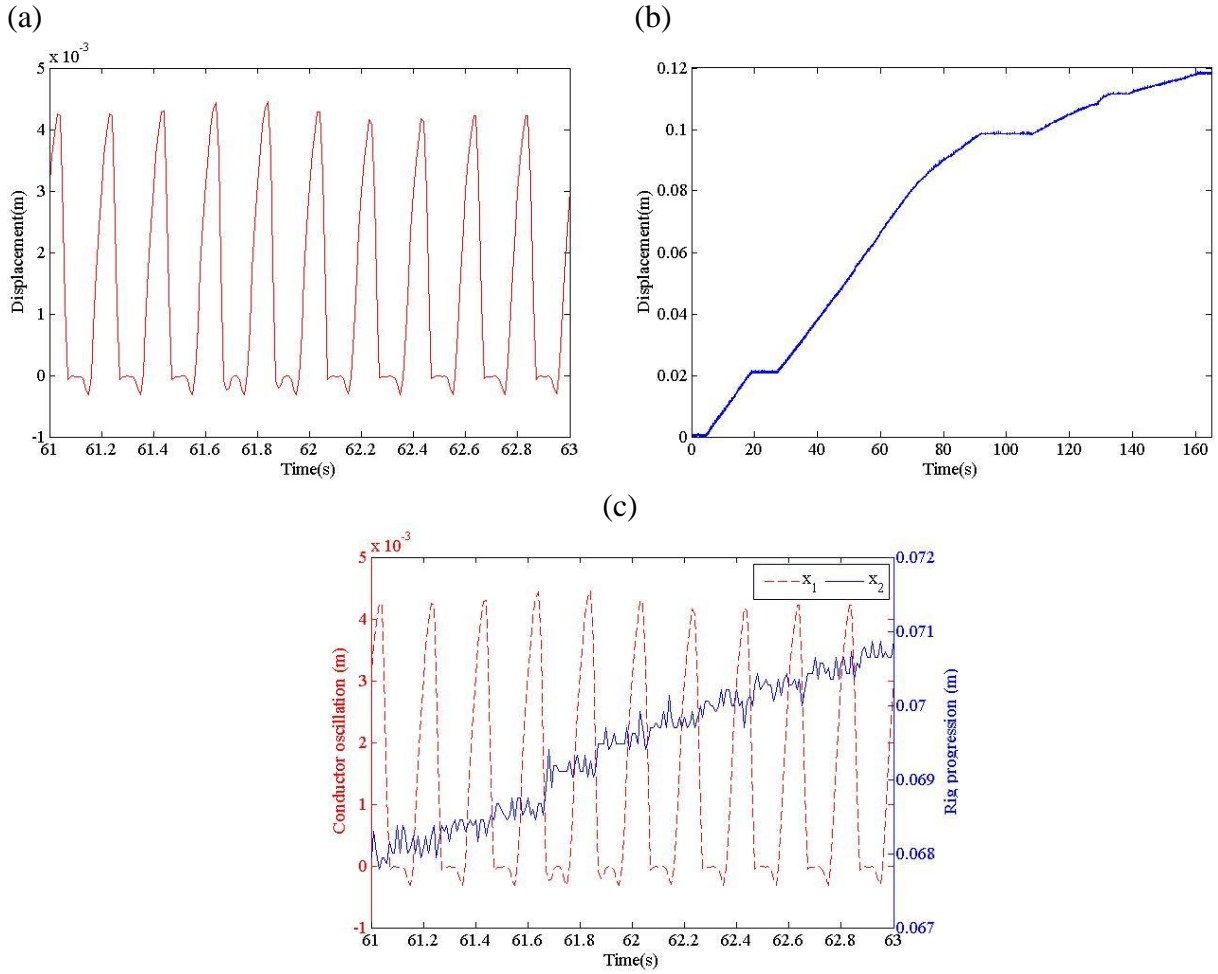


Figure 3.35: Time histories of (a) conductor bar oscillation, (b) progression rate of the vibro-impact rig and (c) superimpose time history of conductor oscillation (dotted red line) and rig progression (blue line) at operating frequency of 5 Hz.

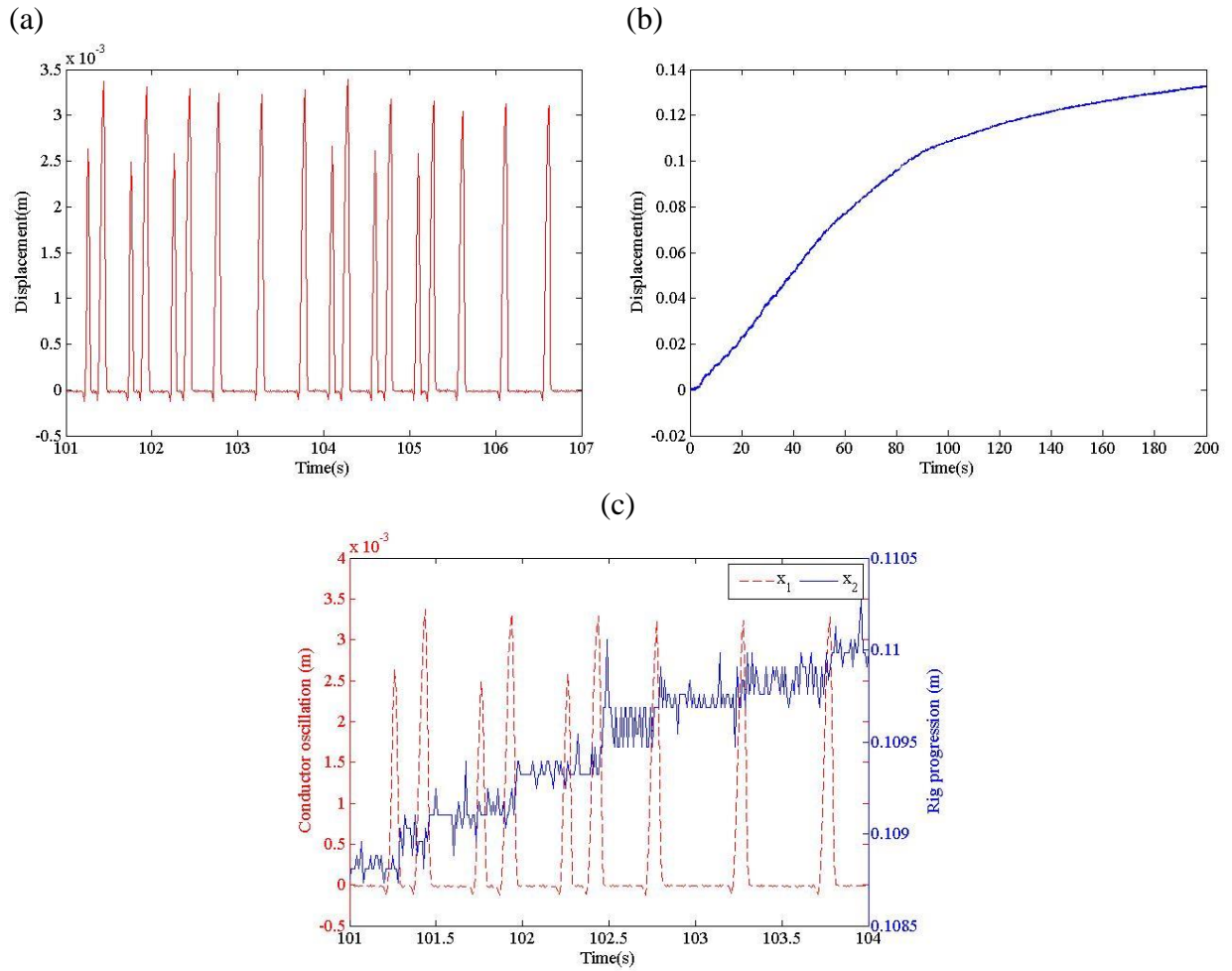


Figure 3.36: Time histories of (a) conductor bar oscillation, (b) progression rate of the vibro-impact rig and (c) superimpose time history of conductor oscillation (dotted red line) and rig progression (blue line) at operating frequency of 6 Hz.

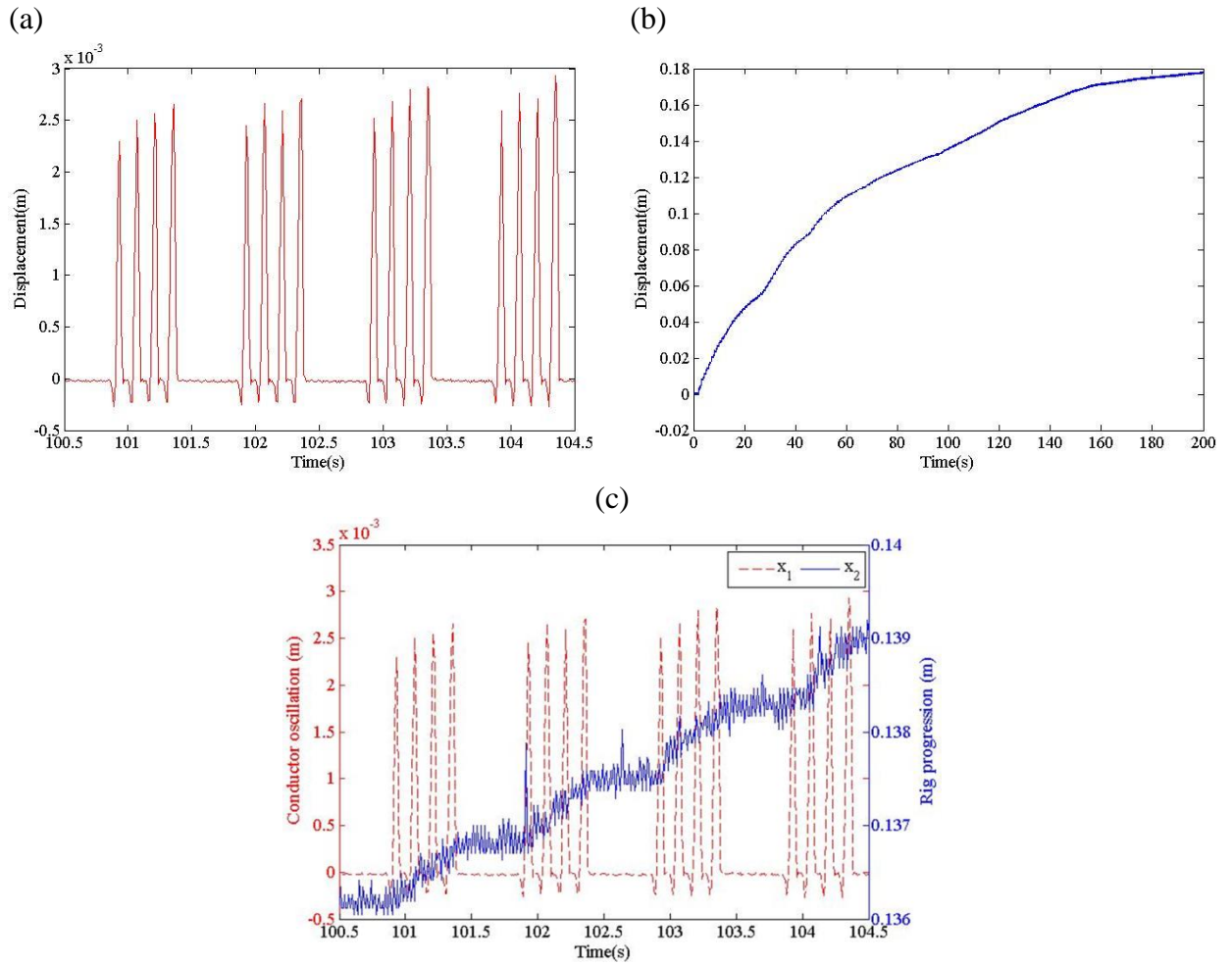


Figure 3.37: Time histories of (a) conductor bar oscillation, (b) progression rate of the vibro-impact rig and (c) superimpose time history of conductor oscillation (dotted red line) and rig progression (blue line) at operating frequency of 7 Hz.

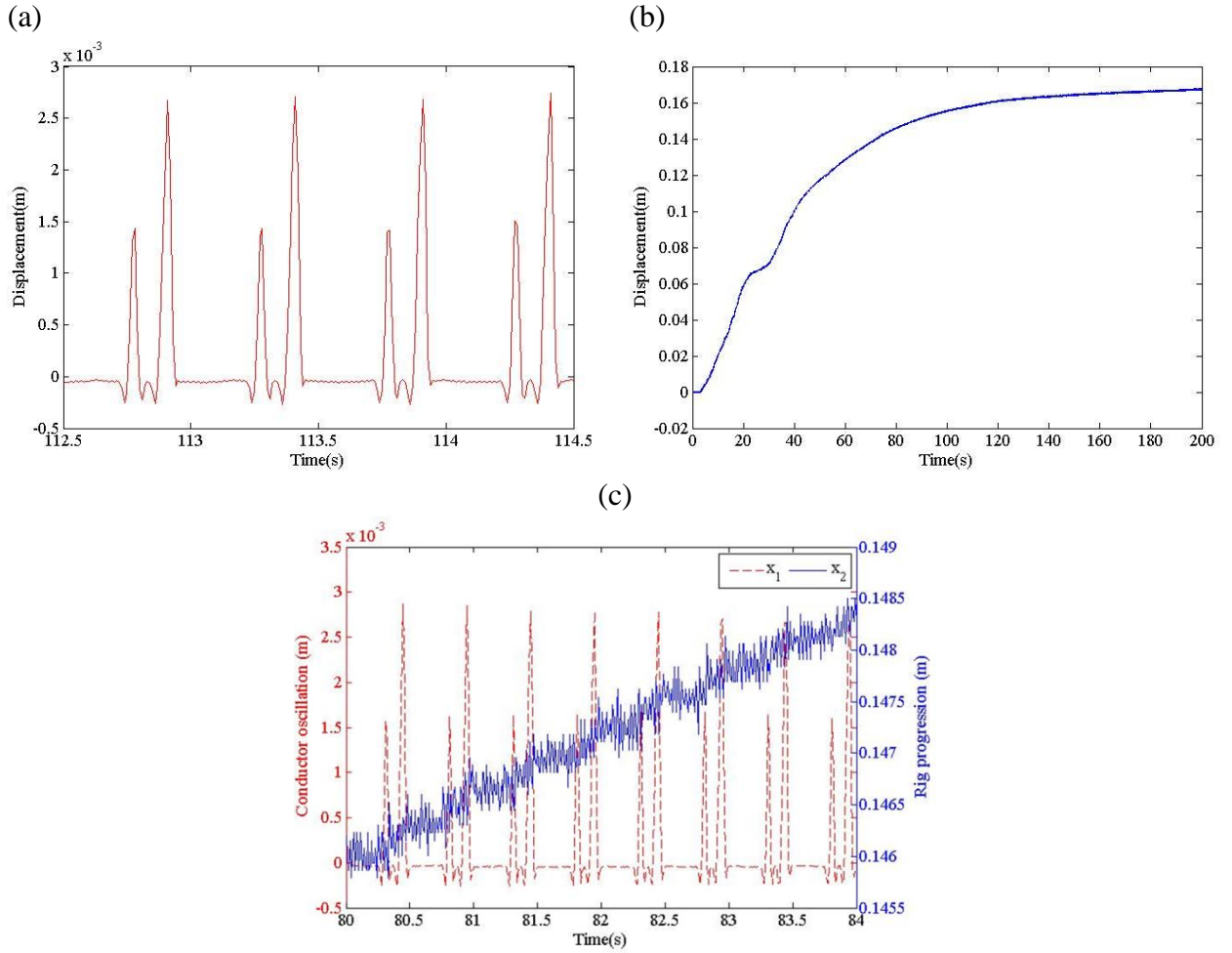


Figure 3.38: Time histories of (a) conductor bar oscillation, (b) progression rate of the vibro-impact rig and (c) superimpose time history of conductor oscillation (dotted red line) and rig progression (blue line) at operating frequency of 8 Hz.

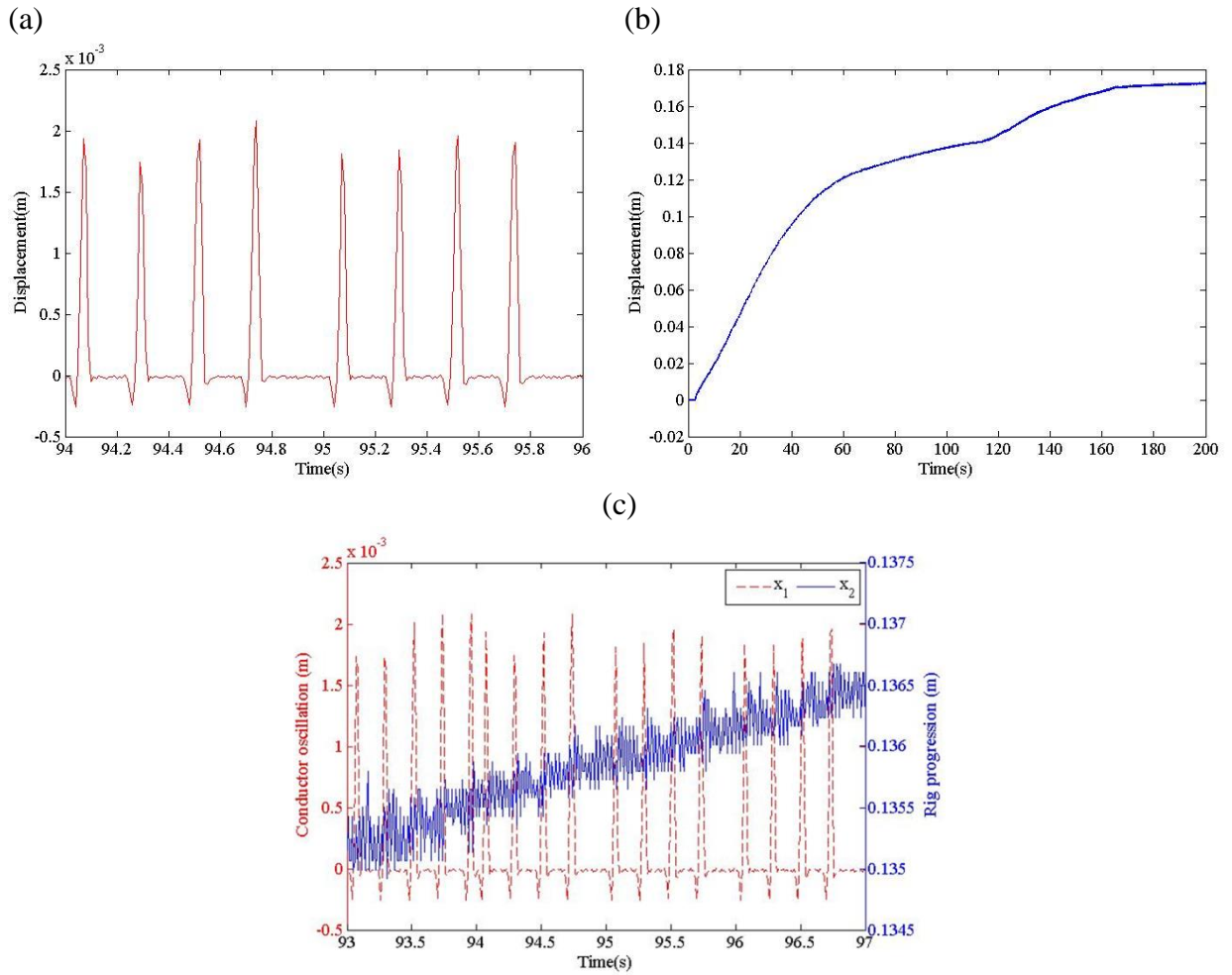


Figure 3.39: Time histories of (a) conductor bar oscillation, (b) progression rate of the vibro-impact rig and (c) superimpose time history of conductor oscillation (dotted red line) and rig progression (blue line) at operating frequency of 9 Hz.

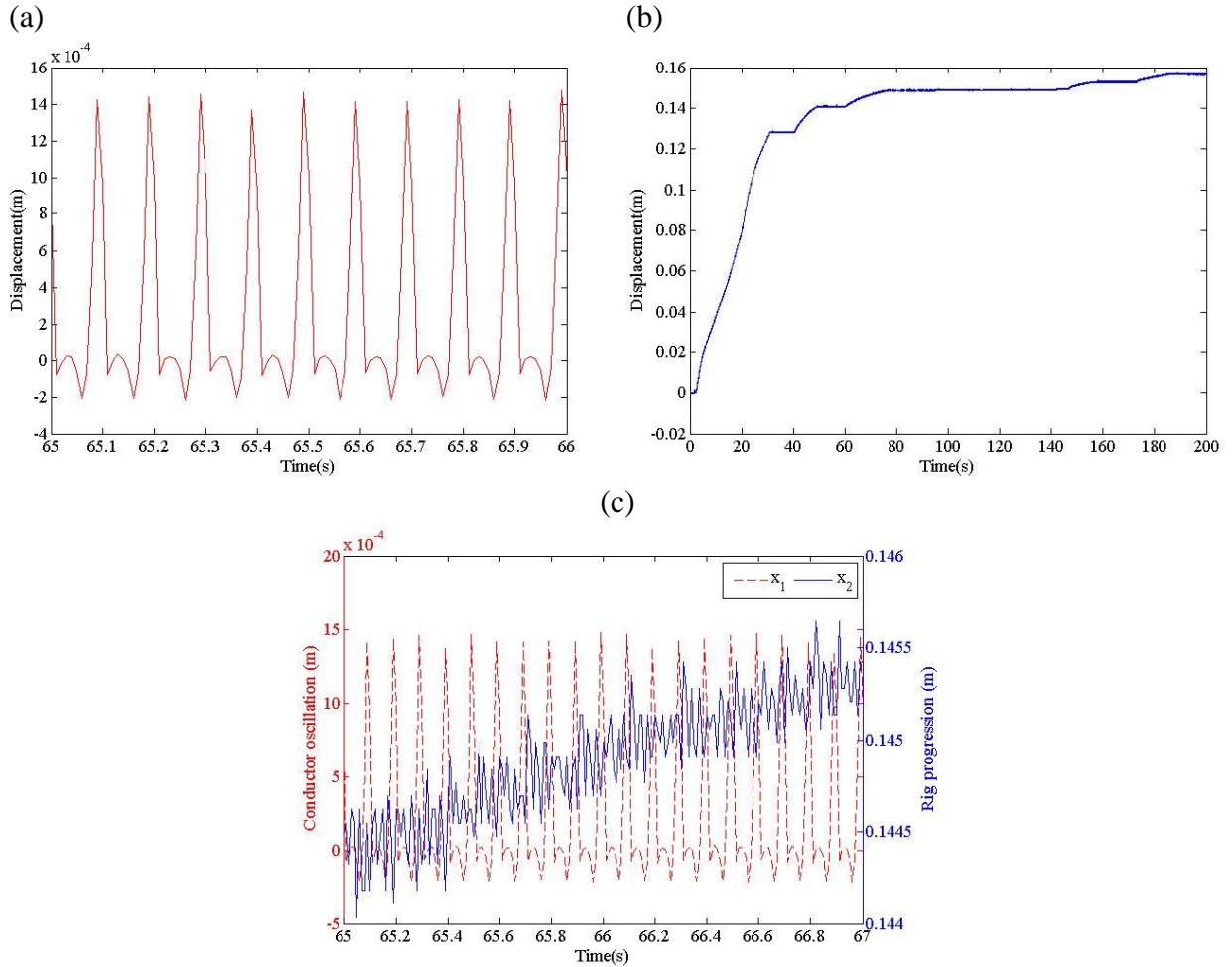


Figure 3.40: Time histories of (a) conductor bar oscillation, (b) progression rate of the vibro-impact rig and (c) superimpose time history of conductor oscillation (dotted red line) and rig progression (blue line) at operating frequency of 10 Hz.

Similar to the experiments performed for one a degree-of-freedom and two degree-of-freedom system in vertical orientation, the latter experiment in a horizontal orientation in soil conditions is repeated by varying its signal frequency of solid state relay from 5 Hz to 10 Hz. It is observed that frequency response in Figure 3.35 (a) to Figure 3.40 (a) did not agree with the input frequency value except for 5 Hz and 10 Hz that still remains

in period-1 motion. Figure (b) of the above graphs shows the progression of vibro-impact system into soil. The general trend shows that the rig progresses with relatively high progression rate, and it gradually decreases along time, finally come to a flat line, indicating no progression. The progression behavior is affected by the operating frequency. As operating frequency increases, initial progression rate is higher. In addition, the maximum displacement the system can achieved before progression stop is higher as signal frequency is higher.

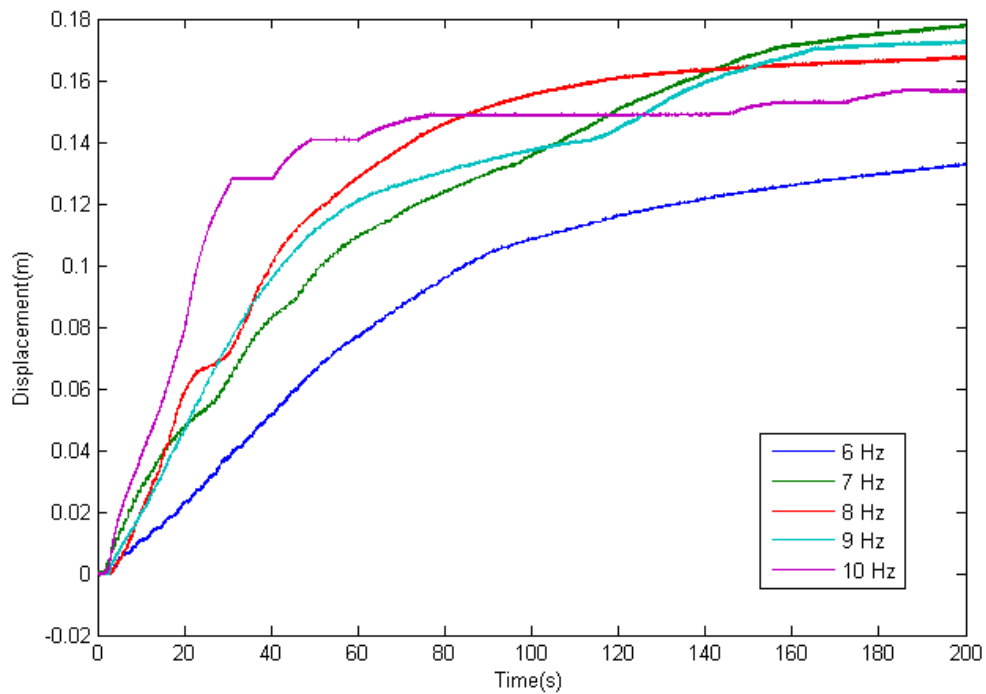


Figure 3.41: Rig progression comparison of various operating frequency.

Figure (c) of 3.35 to 3.40 show superimpose graphs of conductor oscillation and progression rate. Increment of progression displacement only occurs during impact or oscillations of the conductor bar. This proved that rig progression is highly dependent on the periodic forces.

3.6 Conclusions

Optimisation of electro-vibroimpact system has been achieved, culminating in horizontal deployment of experimental rig. It is now capable of penetrating into soil medium, assisted by a small static force. Development of this prototype was initiated by replacement of mechanical spring with permanent magnet. To address issues related to declining magnetic strength with time and repeated impacts, this magnet was, in turn, substituted by an electromagnet; a solenoid was powered by direct current. Positive results in breaking brick vertically downwards encouraged further testing in a horizontal orientation to penetrate into soil. This was successful when operated with assistance from a nominal static force.

A first solenoid in this new electro-vibroimpact system is connected to an AC power supply, and is switched on and off periodically using a solid state relay. A second solenoid was powered by a DC power supply. The interaction between these two sources of electromagnetic fluxes, and ferrous conductor results in vibro-impact oscillatory motion of conductor bar within the solenoids. In a vertical orientation, the impact generated by the collision of conductor bar and rigid stop is transmitted to a brick sample. By using a conductor of mass 0.155 kg, it is possible to penetrate through and fracture a brick sample of thickness 1.5 cm in a brittle manner. A direct current power supply of 24 V and alternating current of 90 V, has been found to be the most ideal ratio of voltages for optimal operation.

A position of stop needs to be at 0 mm and static mass is 3.11 kg. Stones have also been broken as well. The new design is simple and elegant, eliminating the use of bulky components while operating in arbitrary environments. The friction force between conductor bar and the solenoid wall is negligible in a vertical orientation, and is more pronounced in the horizontal direction.

The experimental rig is modelled mathematically and analysed numerically in Chapter 5. The mathematical model is described in the next chapter. The model equation will be based on the physical setup. Numerical results obtained by solving the mathematical model are compared with the acquired experimental results to investigate experimental correlation.

CHAPTER 4

MATHEMATICAL MODEL OF ELECTRO-VIBROIMPACT SYSTEM

4.1 Introduction

Chapter 3 outlined the experimental outcomes using the rig setup described in section 3.3, where the relative displacement of the conductor bar within a range of Solid State Relay Logic (SSRL) operating frequency is recorded. In order to support the experimental results, validation is done using the numerical results obtained through MATLAB simulation of the derived mathematical model, with parameters obtained from the experimental rig. A mathematical model is required in order to study the machine's qualitative dynamic responses and to aid the design and parameter tuning on the machine.

The model for the electro-vibro impact machine is presented in this chapter. The purpose of this model is to predict the dynamic response of conductor and electrical output of the solenoid. From the results presented in Chapter 3, it is shown that the operating frequency of SSRL greatly affects the frequency response and slightly changes the amplitude of conductor oscillation. Thus, the objective of this chapter is to obtain the numerical time histories at various solid state relay frequencies. The numerical results are then being compared with the experimental time histories.

The approximate analytical solution is derived using model of the conductor bar, which involves electromagnetic force from both solenoids. However, the approximate solution only covers the range of motion of free oscillation without impacts. The model is then extended to obtain an actual system with impacts, which leads to discontinuous vibro-impact system characteristics. The phase space is subdivided into two regions which describe oscillation without impacts and with impacts, respectively, where the analytical solution of each region is known. One approach to solve discontinuous system is by “gluing together” [41] local solutions obtained by solving the problem in the continuous regions. The model equation is shifted between regions at the impact point. Locating the impact point can be done precisely by implementing bisection root finding algorithms. As the conductor is oscillating under the influence of electromagnets, the solution of model equation without impact represents the dynamics response in the free region, and when the point of impact is detected, the model equation with impact becomes the active equation and its solution represents the dynamics response from the impact point onwards. The equation switches back to model equation without impact as the conductor displacement leaves the impact point, and the procedure is repeated. Due to the complexity of the mathematical model, a combination of analytical and numerical means is used to solve the discontinuous equations.

Overall, this chapter shows the derivation of the dual-source vibro-impact analytical model in the form of discontinuous system and solving it using a numerical method. The time histories produced by numerical simulation are presented in later sections of this chapter, followed by the comparison and joint graphs of numerical and experimental

results. The validations are done through investigating the similarities in the aspects of frequency response, oscillation waveform and amplitude of the results.

4.2 Mathematical Model

The current mathematical model involves Newtonian mechanics forces and electromagnetic forces generated by the alternating current (AC) and direct current (DC) solenoids. Such solenoid forces have been observed to be dependent on the relay switching frequency [21] by Ho and Woo, also known as the system's operating frequency and position of the oscillatory conductor. These aspects in the mathematical model have been obtained by measurements in part, in the form of semi-empirical results.

In order to obtain a simplified mathematical model, a few assumptions are made:

- Only single degree-of-freedom motion is allowed for the conductor bar, which is the vertical translational motion.
- The impact stopper is being modelled as a high stiffness spring that acts on the conductor bar during soft impact, providing restoring force to resist the conductor bar from progressing downwards.
- The electromagnetic force of Solenoid 1, powered by DC supply, is a function of conductor displacement from the solenoid.
- The electromagnetic force of Solenoid 2, powered by AC supply, is a function of both conductor displacement from the solenoid and time.
- The friction force between conductor bar surface and solenoid inner wall is assumed to be negligible.

- In the inductance test, a solenoid is assumed to be modelled by a pure resistor and its inductance powered by an AC power.

The mathematical equation used to simulate the oscillation consists of the second derivative of displacement, x , which is the acceleration of the conductor bar:

$$\ddot{x}_1 = \frac{1}{m_1} \left[-F_1 + F_2 - \begin{cases} kx_1 + c\dot{x}_1, & \text{if } x_1 > 0 \\ 0, & \text{else} \end{cases} \right] \quad (4.1)$$

and also the second derivative of current in the coil, i ,

$$\frac{d^2i}{dt^2} = \frac{1}{L} \left[\omega P_c V_s \cos(\omega t) - \left(R + 2 \frac{\partial L}{\partial x} \frac{dx}{dt} \right) \frac{di}{dt} - \left(\frac{1}{C} + \frac{\partial^2 L}{\partial x^2} \left(\frac{dx}{dt} \right)^2 + \frac{\partial L}{\partial x} \frac{d^2x}{dt^2} \right) i \right] \quad (4.2)$$

In order to analyse the situation in a more precise manner, the overall analysis is categorized to a free region and an impact region. The free region relates to the motion of conductor when it is free to slide between the solenoids without vertical constraint. The impact region relates to the conductor having contact with the stopper, where additional stiffness and damping is applied to the equations of motion to describe the reaction of impact surface.

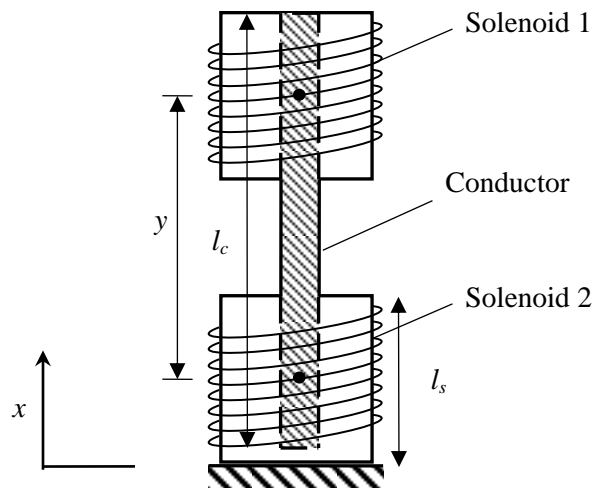


Figure 4.1: Schematic drawing of conductor and solenoids.

Figure 4.1 shows the schematic diagram of one degree-of-freedom conductor in the vibro-impact rig setup. Let F_1 and F_2 be the electromagnetic forces for Solenoid 1 and Solenoid 2, respectively. Meanwhile, m denotes the mass of conductor, where x denotes the displacement of the oscillating conductor, upward direction signifies positive displacement. The vertical distance between the centres of both Solenoid 1 and Solenoid 2 is denoted by y . The length of each solenoid is l_s while the length of conductor is l_c . The values of these parameters are measured to be $y = 0.108$ m, $l_c = 0.141$ m, $l_s = 0.05$ m and $m = 0.155$ kg. At the free region, the free body diagram of the conductor with mass, m is shown in Figure 4.2 (a). Solenoid 1, powered by DC power supply of 15V, is attracting the conductor upwards to the solenoid's centre with a force, F_1 . At the same time, Solenoid 2, connected to AC power supply of peak voltage 25 V, applies a periodic downward force, F_2 , together with the weight of the conductor, which itself pulls the conductor downward. The equation of motion in the free region is derived as below:

$$m\ddot{x} = F_1 - F_2 - mg, \text{ at } x > 0 \quad (4.3)$$

Impact occurs only when the conductor comes into contact with the stopper, where displacement, x , is 0 m. At impact region, the free body diagram of the conductor with mass, m is shown in Figure 4.2 (b). Solenoid 1 with electromagnetic force of F_1 pulls the conductor upwards while Solenoid 2 with electromagnetic force of F_2 attracts the conductor downwards in free region. The stopper acts as a restoring spring that bounces the conductor back to the free region. An addition of stiffness, k , and damping, c , of the

stopper is included in the equation of motion as the restoring force, as shown in Equation (4.4).

$$m\ddot{x} + c\dot{x} + kx = F_1 - F_2 - mg, \text{ at } x \leq 0 \quad (4.4)$$

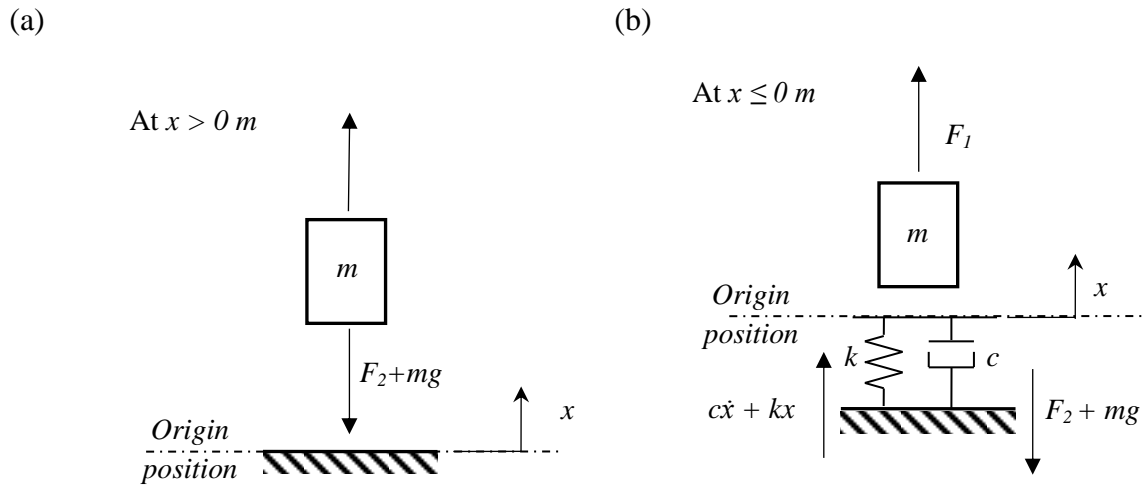


Figure 4.2: Free body diagram of conductor bar in (a) the free region, and (b) the impact region.

4.3 Empirical or semi-empirical formulae

The mechanical and electrical response of individual electromagnetic forces are analysed to investigate their dynamics effect and contributions to the vibro-impact system. This can be executed by solving the discontinuous equation of motion without including the other electromagnetic force component. For example, to obtain the dynamics response of the system under the effect of DC electromagnetic force, F_1 , the AC electromagnetic force, F_2 , is neglected, or assumed to be 0 N at all time. By performing test with just individual solenoid, in this case, Solenoid 1, the function of F_1 ,

which describes the relationship of electromagnetic force and the relative distance of conductor bar to the solenoid could be determined and being used as the component in Equation (4.3) and (4.4) to complete the numerical integration.

The magnetic force in Newtons (N) for Solenoid 1, F_1 , powered by a DC supply of 15 V, is a function of conductor displacement in the solenoid. The function could be determined by measuring the attraction force with a spring balance attached to the conductor bar, while sliding the conductor along Solenoid 1, recording the force reading at various displacements. The displacement in this case refers to the relative displacement of centre of conductor with respect to the centre of Solenoid 1, denoted by x_a .

$$\begin{aligned}
 x_a &= y + \frac{l_s}{2} - \frac{l_c}{2} - x \\
 &= 0.108 \text{ m} + \frac{0.05 \text{ m}}{2} - \frac{0.141 \text{ m}}{2} - x \\
 &= 0.0625 \text{ m} - x
 \end{aligned} \tag{4.5}$$

Equation (4.5) above shows the relation between conductor's relative displacement, x_a , from Solenoid 1 with the conductor displacement from stopper, x , derived from the schematic diagram shown in Figure 4.3. The origin of x_a is set at the centre of Solenoid 1, with upward direction assumed as positive displacement. Thus, as the centre of the conductor bar is at a point higher than the centre of Solenoid 1, displacement x_a is

positive. When the centre of conductor is at a position below the centre of Solenoid 1, x_a has negative sign.

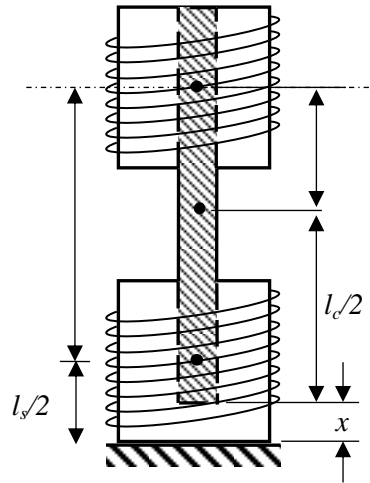


Figure 4.3: Schematic of conductor bar's relative position with respect to the center of Solenoid 1.

The values of the DC electromagnetic force, F_l , obtained from spring balance are curve-fitted to a function of relative displacement, x_a . The electromagnetic force acting on the conductor has a cubic relationship with respect to the relative displacement. At the exact centre of Solenoid 1 where $x_a = 0$ m, the force pulling the conductor equals to the conductor's weight in order to balance and hold it at that position.

The experimental setup to determine F_l is shown in Figure 4.4. A spring balance that measures pulling force is attached to the conductor, which the hook of the spring balance is holding onto a ring extension, thread into one end of the conductor bar. DC voltage supply, connected to Solenoid 1, is adjusted to a fixed value at 20 V. By running several tests, it shows that the electromagnetic force produced by 20 V of DC voltage

supply is able to balance with the electromagnetic force of 80 V AC power supply to Solenoid 2, which is the maximum allowable AC voltage of TIRA Power Amplifier Type BAA 120. Balancing of electromagnetic force refers to the ability of the electromagnetic forces of Solenoid 1 and Solenoid 2 to interact without one overwhelming the other, which in the balanced region, producing an oscillatory motion of the conductor bar.

The conductor bar was initially placed at the centre of Solenoid 1, where relative displacement, x_a is at its origin, 0 m. The conductor bar was gradually displaced further from Solenoid 1, increasing the value of x_a . Figure 4.4 shows the experiment setup, the solenoid is placed horizontally to exclude the effect of conductor bar's weight on the spring mass. Solenoid 1 is clamped on an aluminium plate to be fully constrained, so that it does not slide while changing the position of conductor.

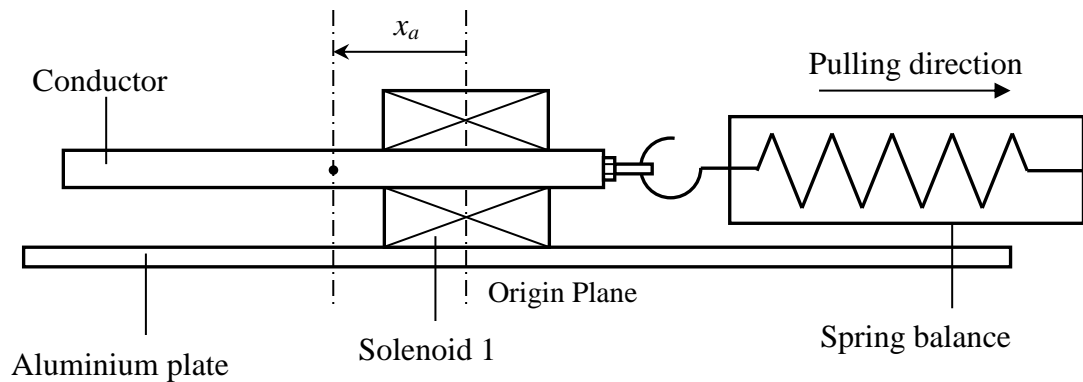


Figure 4.4: Schematic diagram of experimental setup to quantify electromagnetic force of DC solenoid.

The electromagnetic force changes gradually as reaction of change in distance of the magnetized object (conductor bar) and is measured by the spring balance. A measuring scale is taped onto the conductor bar, allowing the relative displacement of conductor bar from solenoid to be determined. The force reading shown on the spring balance is recorded at every change of relative displacement. The interval of relative displacement change is set to 0.005 m.

The values of electromagnetic force against relative displacement of the conductor bar, obtained by the outlined procedure, are tabulated in Table 4.1. The range of relative displacement measured is from 0 m to 0.029 m, the electromagnetic field of solenoid has no effect on the conductor bar (no attraction force) when it travels beyond this range. In high relative displacement range, more than 0.025 m, the interval used is reduced to 0.001 m to facilitate the high sensitivity of attraction force increment towards small displacement change.

Table 4.1: Conductor displacement from Solenoid 1 and electromagnetic force at 20 V.

Relative Displacement (m)	Reading on spring balance (N)
0	0
0.005	0
0.010	0.2
0.015	0.4
0.020	0.9
0.025	1.5
0.027	2.1
0.028	2.9
0.029	3.6

The opposite side of the solenoid ($-0.029 \text{ m} < x_a < 0 \text{ m}$) would have identical attraction force. Thus, the curve is symmetrical at y-axis ($x_a = 0 \text{ m}$). However, the electromagnetic force pulls the magnetized object towards the centre of the solenoid at all time, causing the attraction force at negative displacement acts in an opposite direction compared to attraction force at positive displacement. Consequently, the attraction force at negative displacement decreases in the same trend as the increment in the positive displacement region.

The data is then plotted as graph of solenoid attraction force against conductor relative displacement, x_a in Figure 4.5 to show the relation. The crosses on the graph represents the experimental data of Table 4.1, the solid line represents the curve fit line of the data. The electromagnetic force increases as the relative displacement increases. The increment of attraction is drastic when the conductor bar travels further from the origin of solenoid. As the conductor bar approaches the origin of solenoid, where the relative displacement is near to 0 m, there is almost no change in electromagnetic force. At zero relative displacement, the position of conductor bar at the centre of solenoid has no attraction force, approximately 0 N.

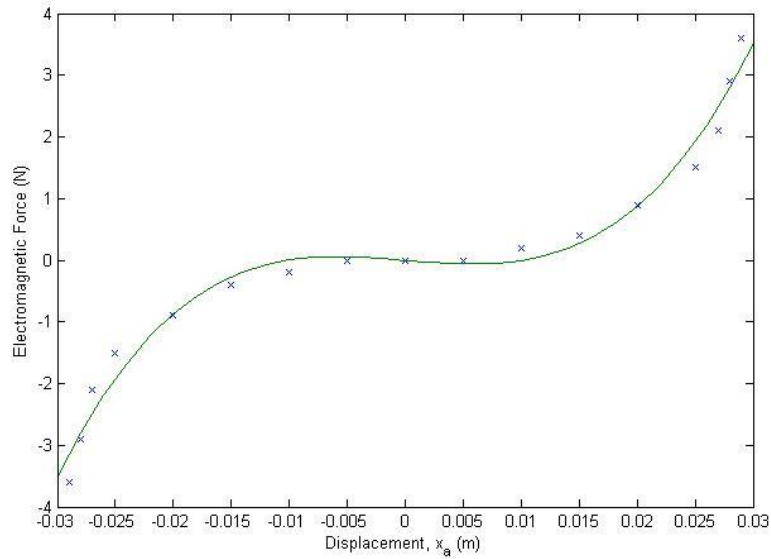


Figure 4.5: Graph of solenoid attractive force against conductor displacement at 20 V, crosses represents experimental data and solid line represents curve fitted line.

The curve fit line for the data is shown in Figure 4.5 is shown in Equation (4.6). A cubic equation (3rd order polynomial function) is used to describe the curve as electromagnetic force changes from negative values to positive values with a drastic change at larger displacement and stays constant in the vicinity of the point of inflection. It is the simplest function that describes the curve with minimum numbers of parameters involved.

$$F_{Solenoid\ 1} = 1.473 \times 10^5 x_a^3 + 1.625 \times 10^{-14} x_a^2 - 15.38 x_a \quad (4.6)$$

Figure 4.5 describes the relationship of electromagnetic force, F_I with the relative displacement, x_a of conductor bar to Solenoid 1. This is essential to observe the effect of Solenoid 1, connected to DC power supply upon the oscillating magnetised object as an individual system. The outcome of this test, shown in Equation (4.6) would represent the component of Solenoid 1 in the overall system's equation of motion. The right hand side

of equation (4.6) is multiplied by -1, representing a restoring force against the motion of the conductor bar. Equation (4.6) is also being shifted 1.55 N above, the value of the conductor bar's weight, as the experiment rig operates in vertical direction, which the weight of the conductor bar is balanced by the electromagnetic force at the centre of the solenoid. Equation (4.7) shows the function of electromagnetic force for Solenoid 1 as a component in the experimental rig.

$$F_1 = -1.473 \times 10^5 x_a^3 - 1.625 \times 10^{-14} x_a^2 + 15.38 x_a + 1.55 \quad (4.7)$$

It is also crucial to look at the contribution of Solenoid 1 in terms of the displacement, x of conductor bar according to the experimental rig's origin (at the surface of impact stopper). Figure 4.6 is a graph plotted with electromagnetic force, F_1 against the absolute displacement, x of conductor bar.

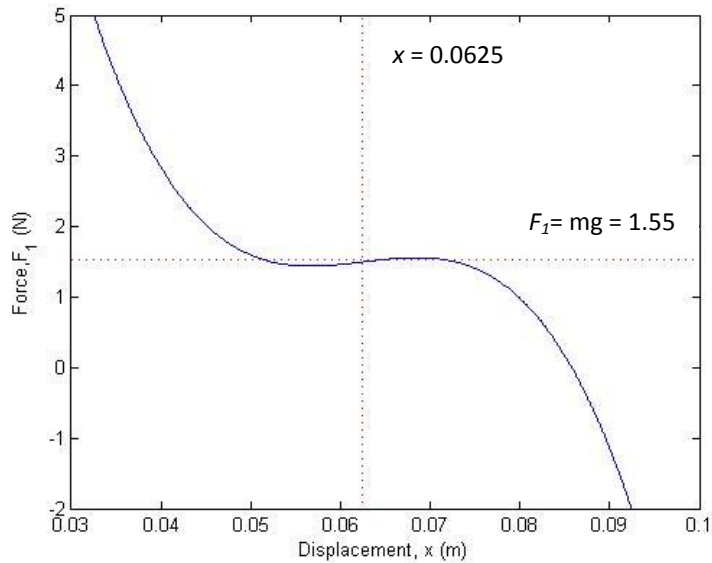


Figure 4.6: Plot of DC electromagnetic force against absolute conductor displacement.

From Figure 4.6, the general curve shape of the electromagnetic force against displacement is similar to Figure 4.5. As the displacement increases, the electromagnetic

force increases as well. At point (0.0625 m, 1.55 N) marked the intersection of both horizontal and vertical dotted lines, which is also the point of inflection. Displacement at $x = 0.0625$ m is the centre of Solenoid 1, and 1.55 N is equal to the weight of conductor bar itself. It shows that as the conductor bar reaches the centre of Solenoid 1, the upward attraction force cancels of the weight of conductor bar, causing zero resultant force acting on the bar, achieving a static equilibrium at that point. As the conductor travels above the solenoid ($x > 0.0625$ m), the upward attraction force is weaker than the weight of conductor bar, causing a downward resultant force acting upon the conductor bar. On the other hand, as the conductor bar travels below the solenoid, ($x < 0.0625$ m), the upward attraction force is larger than the weight of conductor bar, resulting in an upward force acting upon the conductor bar itself. Overall, Solenoid 1 acts as a restoring spring that tries to keep the conductor bar at the solenoid's origin. In the operation of the electro vibro-impact rig, this aspect of Solenoid 1 recovers the position of conductor bar after having contact with the impact point, preparing to stroke as the Solenoid 2 pulls in downward, creating the next impact.

By solving the equation of motion involving F_I and mg only, the time history is plotted in Figure 4.7. It is expected that at the initial position where the conductor is at rest at the stopper, $x = 0$ m, F_I would pull the conductor upward, and as it reaches the position of Solenoid 1, $x = 0.625$ m, it overshoots due to the inertia of conductor. It later recovers its position at the centre of Solenoid 1 ($x = 0.0625$ m), due to the electromagnetic force restoring the conductor position and holding it at the solenoid's origin. The change of

sign in Equation (4.7) implies that the solenoid acts as a restoring force. Figure 4.7 validates the role of Solenoid 1 as a restoring spring in the system.

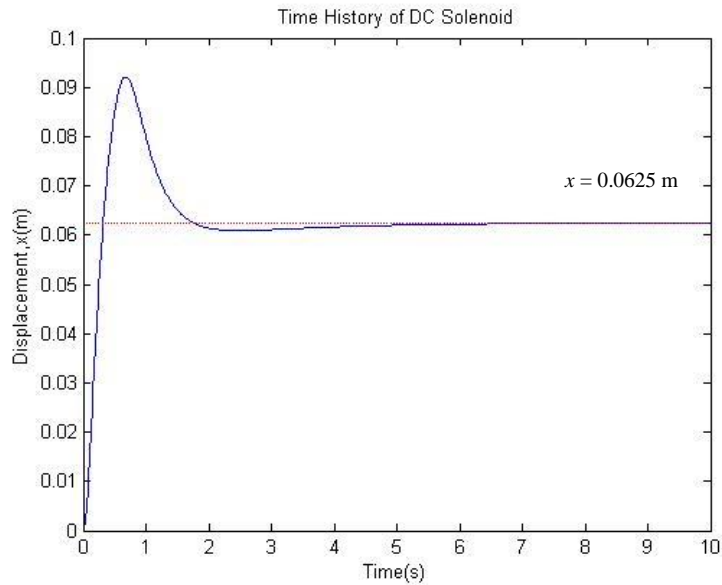


Figure 4.7: Time history of model with DC solenoid and weight.

Solenoid 2 is powered by an AC supply connected to a Solid State Relay (SSRL) that alternates the signal from ON to OFF in a certain operating frequency, Ω . Solenoid 2 is fixed below Solenoid 1, where the electromagnetic force attracts the conductor downward to collide with the stopper when switched ON, creating impact. While switched OFF, it releases the conductor upwards by the effect of Solenoid 1.

The generic expression for electromagnetic force in Newton (N) for Solenoid 2, F_2 , is shown in Equation (4.6), where x_b is the relative displacement of the conductor to the centre of Solenoid 2, and i as the current in Ampere (A) of AC power supply which is also a function of time, t . L is inductance in Henry (H) of the solenoid, and it is a function of the relative displacement, x_b in metre (m) of conductor inside the solenoid.

$$F_2 = \frac{1}{2} i^2 \frac{\partial L}{\partial x_b} \quad (4.8)$$

The relative displacement of conductor bar to the centre of Solenoid 2 is calculated using the formula below.

$$\begin{aligned} x_b &= \frac{l_c}{2} + x - \frac{l_s}{2} \\ &= \frac{0.141}{2} + x - \frac{0.05}{2} \\ &= 0.0455 + x \end{aligned} \quad (4.9)$$

Figure 4.8 and Equation (4.9) show the derivation of conductor relative displacement from Solenoid 2. The relative displacement, x_b is the distance from the centre of conductor to the centre of Solenoid 2. Relative displacement x_b will always be positive due to the existence of the stopper as a displacement constraint, where the centre of conductor will never travel below the centre of Solenoid 2.

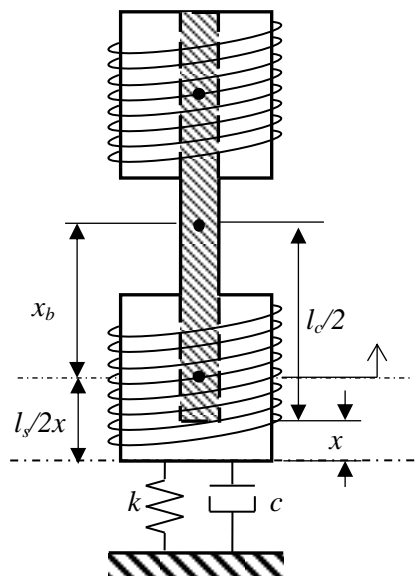


Figure 4.8: Schematic of conductor's relative position with respect to Solenoid 2.

4.4 Obtaining an Inductance Equation of Circuit

Inductance of the system circuit is needed to solve Equation (4.8), which is a function of conductor relative displacement with respect to the centre of Solenoid 2. In order to measure the inductance of the circuit, a test circuit, as shown in Figure 4.9 is constructed. A resistor, R_a is added in series to the solenoid. The solenoid is assumed to be modelled by a pure resistor, R_s , in series with its inductance, L , and powered by AC power. The supplied AC voltage, V_{ss} oscillates in a square waveform with a given frequency, f , in Hz. The potential difference over the resistor, R_a , is measured using a multimeter, denoted as V_0 .

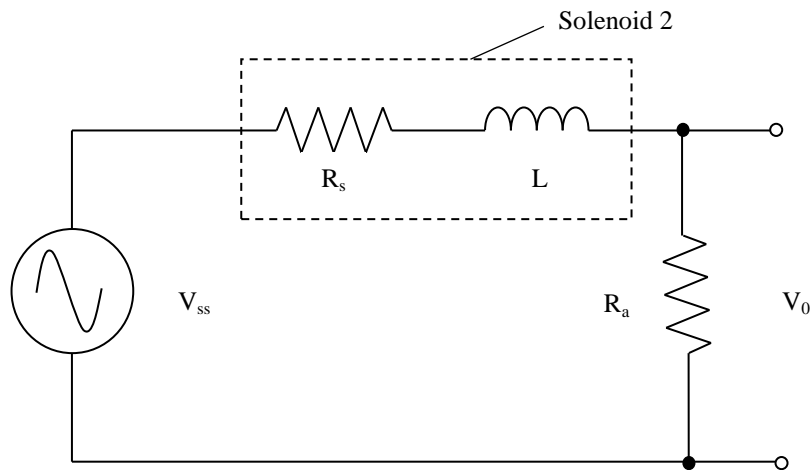


Figure 4.9: Schematic diagram of Solenoid 2 with resistor in series circuit.

Through measurement, the inductance of Solenoid 2 connected to AC power is obtained. The general relationship between ratio of potential difference and voltage supply with the electrical components is shown in the equation below:

$$\frac{V_0}{V_{ss}} = \frac{R_a}{\sqrt{(R_a + R_s)^2 + Q^2}} \quad (4.10)$$

Where Q is the impedance of the inductance, L , given by:

$$Q = 2\pi f_L L \quad (4.11)$$

By substituting the impedance into the equation, the inductance of the solenoid can be expressed as below:

$$L = \frac{1}{2\pi f_L} \sqrt{\left(\frac{R_a V_{ss}}{V_0}\right)^2 - (R_a + R_s)^2} \quad (4.12)$$

From the solenoid connected in series to the resistor, the parameters values are $R_a = 46.8 \Omega$, $R_s = 50 \Omega$, $f_L = 66 \text{ Hz}$ and $V_{ss} = 70 \text{ V}$. The value of V_{ss} , R_a and R_s are determined by connecting a multimeter to the respective components in the circuit. The displacement of the conductor bar from solenoid, x_b is measured by a labelled scale on the bar. The output voltage of the constructed circuit, V_0 , which is also the potential difference across resistor R_a is measured using a multimeter. Inductance at the respective displacement is calculated by substituting each component into Equation (4.12) which expresses the inductance in terms of resistance, frequency and voltage. The values of measured and calculated components are summarized in Table 4.2.

Table 4.2: Inductance at various position of conductor bar in Solenoid 2.

Position, x_b (m)	V_o (V)	L (H)
0.003	5.3	1.45830095
0.005	5.3	1.45830095
0.010	5.4	1.43060983
0.015	5.5	1.40391276
0.017	5.6	1.37815644
0.020	5.7	1.35329137
0.022	5.8	1.32927141
0.025	5.9	1.30605357
0.026	6.0	1.28359774
0.027	6.1	1.26186641
0.028	6.4	1.20067966
0.029	6.9	1.11031587
0.030	7.4	1.03191737
0.031	7.9	0.96321002
0.032	8.2	0.9258989
0.033	8.5	0.89114228
0.034	8.9	0.84832641
0.035	9.4	0.79974854
0.036	9.8	0.76431379
0.037	10.3	0.72372028
0.038	10.7	0.69384413
0.039	11.2	0.65933898
0.040	11.6	0.63375051
0.041	12.0	0.60975805
0.042	12.3	0.5927165
0.043	12.6	0.5764261
0.044	12.9	0.56083376
0.045	13.2	0.5458912

The inductance of solenoid is symmetrical with respect to its center, where conductor displacement, $x_b = 0$ m. The collected inductance is being curve fitted in Gaussian's form, shown by Equation (4.13) with the value of constant L_0 , A and B listed below.

$$L = L_0 + \frac{A}{B\sqrt{\pi/2}} e^{-2\left(\frac{x_b}{B}\right)^2} \quad (4.13)$$

$$L_0 = 0.48 \text{ H} \quad A = 0.048 \text{ H} \quad B = 0.039$$

Figure 4.10 shows the graph of inductance value collected through the test circuit plotted in crosses and solid line plotting the curve fitted Gaussian's form.

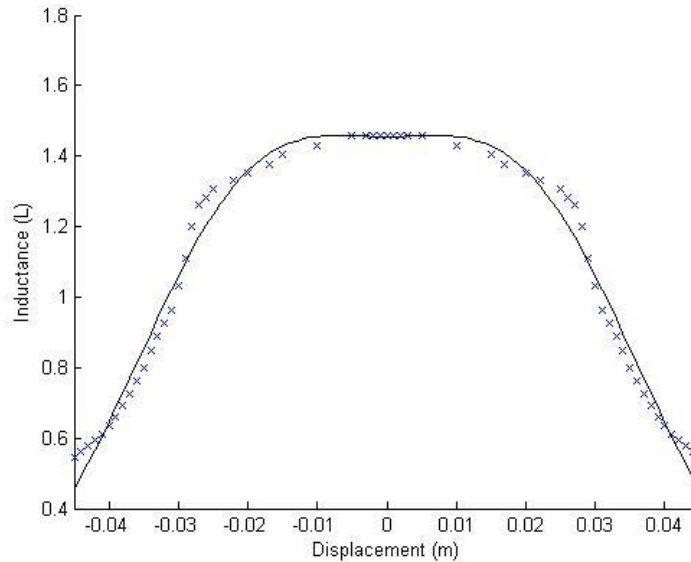


Figure 4.10: Inductance value of experiment data and Gaussian's form.

Differentiation of inductance in Equation (4.13) with respect to conductor displacement, x_b is done. The first derivative of L is necessary to be applied in Equation (4.8). Furthermore, the second derivative of L is also needed to solve the differential equation of current in a solenoid, expressed in Equation (4.2).

The first and second derivative of inductance in Gaussian's form could be obtained, shown in Equations (4.14) and (4.15), respectively. The plots of first and second derivative of inductance against conductor displacement are shown in Figures 4.11 and 4.12, respectively.

$$\frac{\partial L}{\partial x_b} = \frac{-4Ax_b}{B^3 \sqrt{\pi/2}} e^{-2\left(\frac{x_b}{B}\right)^2} \quad (4.14)$$

$$\frac{\partial^2 L}{\partial x_b^2} = \frac{-4A \left(1 - \left(\frac{2x_b}{B}\right)^2\right)}{B^3 \sqrt{\pi/2}} e^{-2\left(\frac{x_b}{B}\right)^2} \quad (4.15)$$

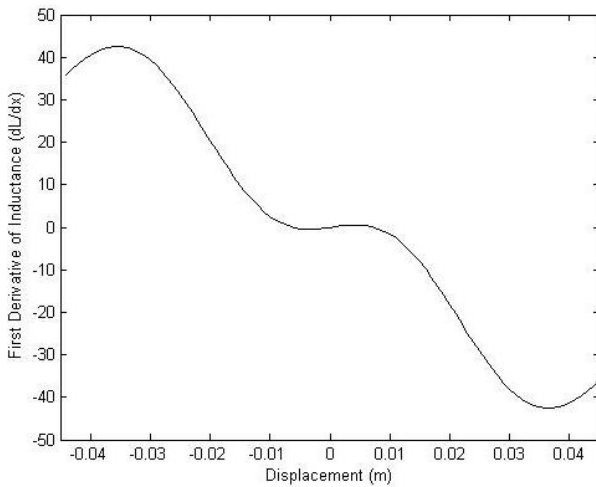


Figure 4.11: Gaussian's form first derivative of inductance against conductor displacement.

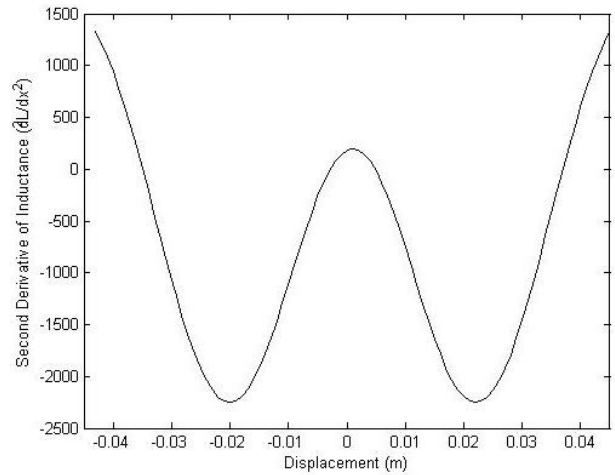


Figure 4.12: Gaussian's form second derivative of inductance against conductor displacement.

4.5 Equation of current variation

After obtaining the equation of conductor relative displacement, x_b , and inductance, L , current passing through the coil of Solenoid 2, i , is needed to solve Equation (4.8). The current, i passing through the coils of the solenoid, can be expressed as a differential equation.

$$L \frac{d^2 i}{dt^2} + \left[R + 2 \frac{\partial L}{\partial x_b} \frac{dx_b}{dt} \right] \frac{di}{dt} + \left[\frac{1}{C} + \frac{\partial^2 L}{\partial x_b^2} \left(\frac{dx_b}{dt} \right)^2 + \frac{\partial L}{\partial x_b} \frac{d^2 x_b}{dt^2} \right] i = \omega P V_s \cos(\omega t) \quad (4.16)$$

In the formula above, R denotes the resistance of the coils, C is the capacitance in the circuit, ω is the angular velocity of power supply, $\omega = 2\pi f$, where f is the system frequency of main supply in Hz, P is the switching control governed by the operating frequency, Ω , for AC current in Hz and V_s is the voltage supply. The parameter values are $R = 30 \Omega$, $C = 0.0003 \text{ F}$, $f = 50 \text{ Hz}$ and $V_s = 25 \text{ V}$.

The right side of Equation (4.16) is the derivative of voltage supply with respect to time under the switching effect of Solid State Relay Logic (SSRL) which is connected to Solenoid 2. The AC power is supplied by TIRA Power Amplifier Type BAA 120 which adopts the waveform of common household main electric supply. The magnitude of the AC power is adjusted using the amplifier, fixed at $V_s = 25 \text{ V}$ in this experiment. Figure 4.13 shows a general waveform of the AC power from the main electric supply, showed in the form of $A \sin(2\pi f t)$, where A is the amplitude of the AC power and f is the frequency of AC power in Hz. As mentioned, the magnitude of the supplied AC power

to Solenoid 2 is adjusted to 25 V, we acquire that main supply is a form of sinusoidal wave that oscillates in the frequency of 50 Hz.

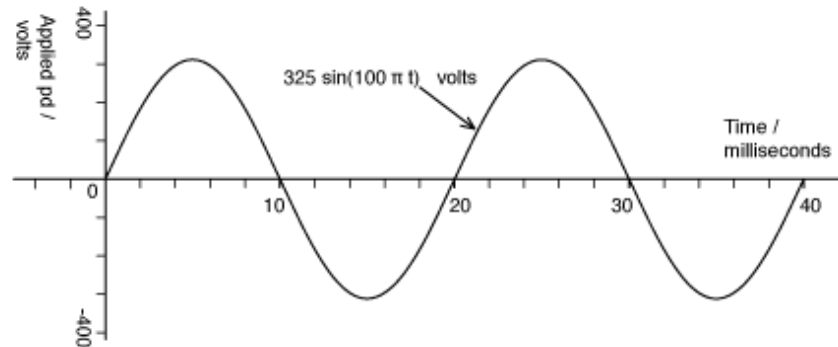
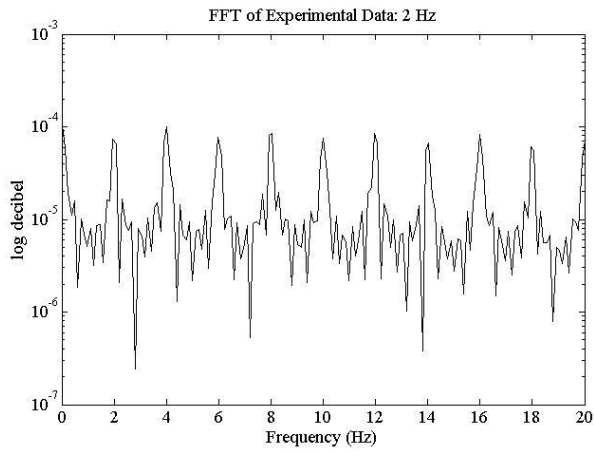


Figure 4.13: Waveform of main electric supply.

The system frequency of main supply, f can also be obtained through experimental results by performing Fast Fourier Transform (FFT) on the experimental data. By converting experimental data of one degree-of-freedom oscillation in Figure 3.8 to 3.16 from time domain into frequency domain, the frequency that has the largest influence on the system can be determined. The frequencies that govern the oscillations are shown with peaks of high magnitude in the FFT graphs. Figure 4.14 to 4.22 shows the graphs of experimental data with operating frequency of 2 Hz to 10 Hz in frequency domain. Figure 4.14 (a) to 4.22 (a) shows the frequency domain in range of 0 Hz to 20 Hz to monitor low frequencies involved, while Figure 4.14 (b) to 4.22 (b) shows the frequency domain in range of 40 Hz to 60 Hz to monitor high frequencies, especially the main supply with system frequency of 50 Hz.

(a)



(b)

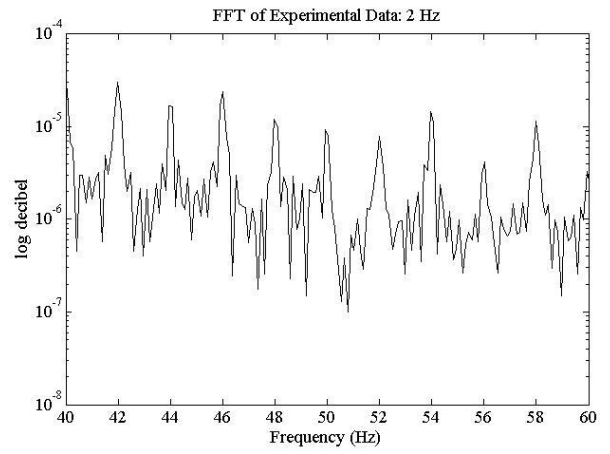
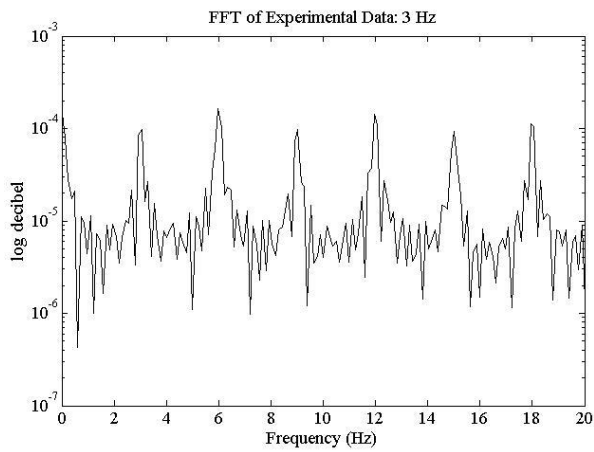


Figure 4.14: FFT of experimental data at operating frequency 2 Hz at range (a) 0-20 Hz and (b) 40-60 Hz.

(a)



(b)

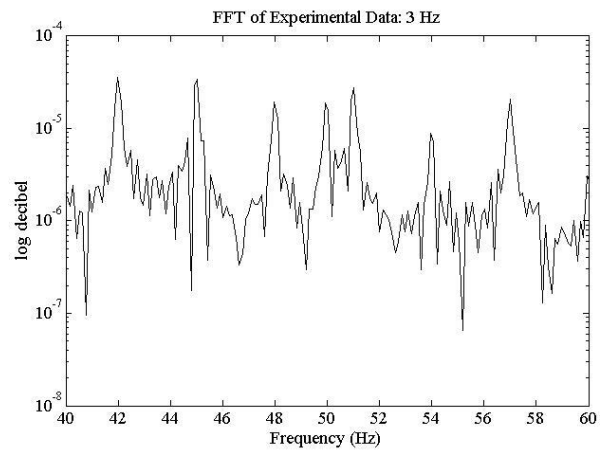
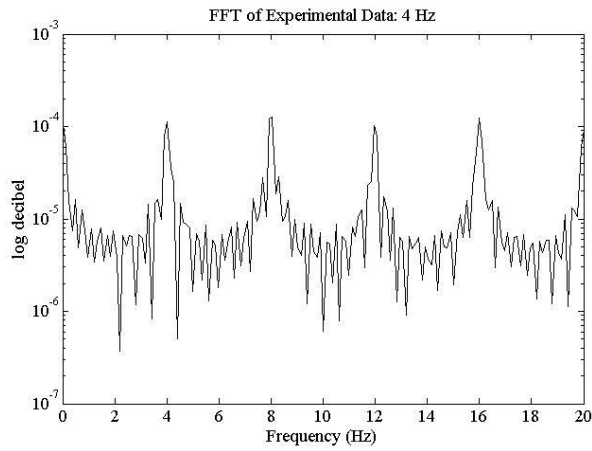


Figure 4.15: Fourier Transform of experimental data at operating frequency 3 Hz at range (a) 0-20 Hz and (b) 40-60 Hz.

(a)



(b)

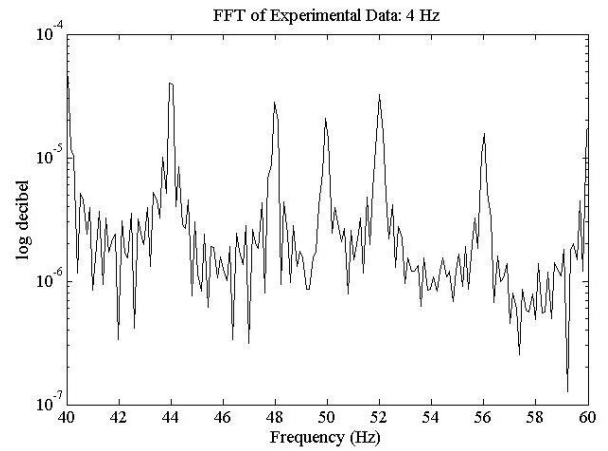
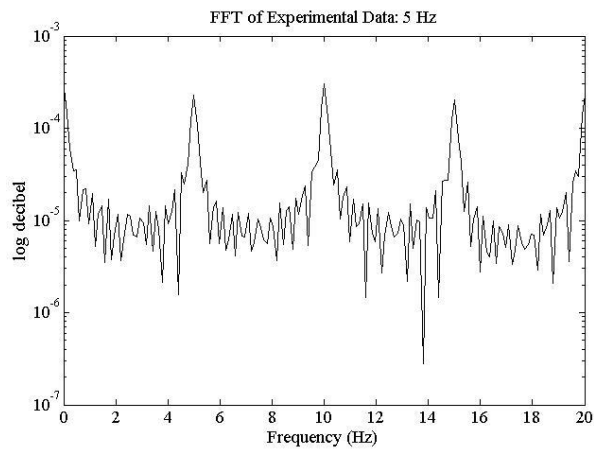


Figure 4.16: Fourier Transform of experimental data at operating frequency 4 Hz at range (a) 0-20 Hz and (b) 40-60 Hz.

(a)



(b)

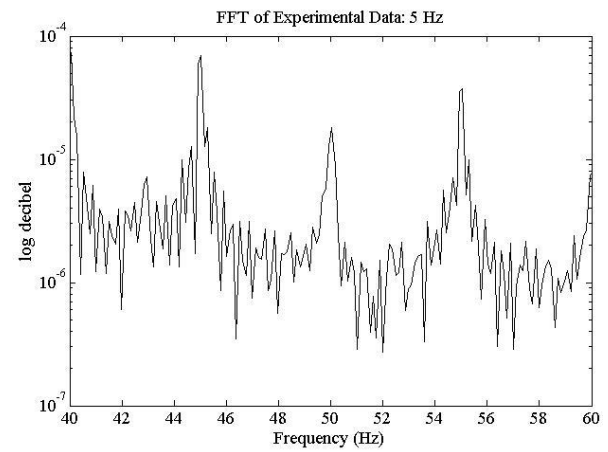


Figure 4.17: Fourier Transform of experimental data at operating frequency 5 Hz at range (a) 0-20 Hz and (b) 40-60 Hz.

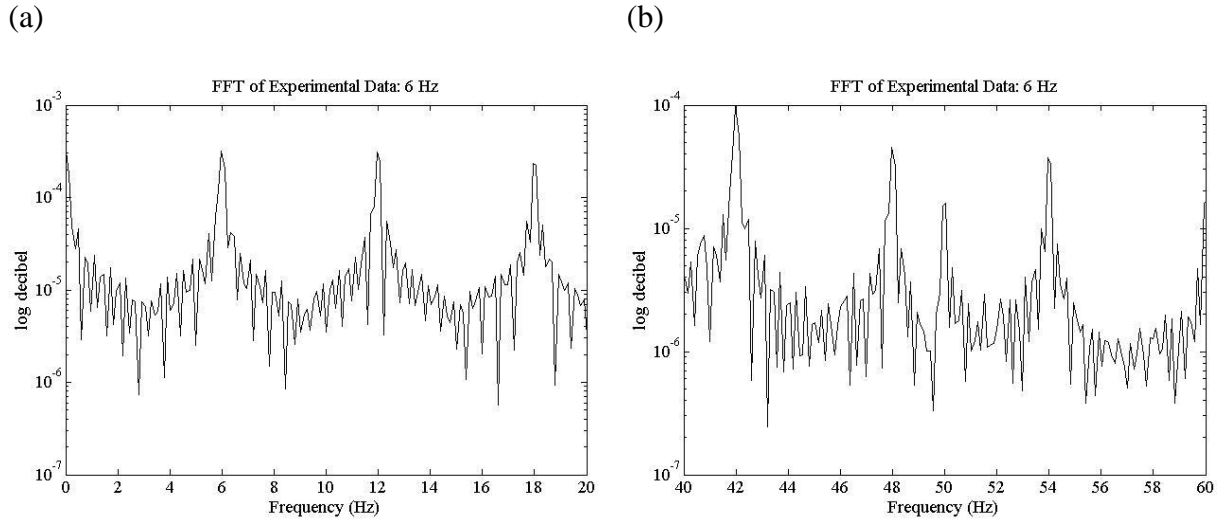


Figure 4.18: Fourier Transform of experimental data at operating frequency 6 Hz at range (a) 0-20 Hz and (b) 40-60 Hz.

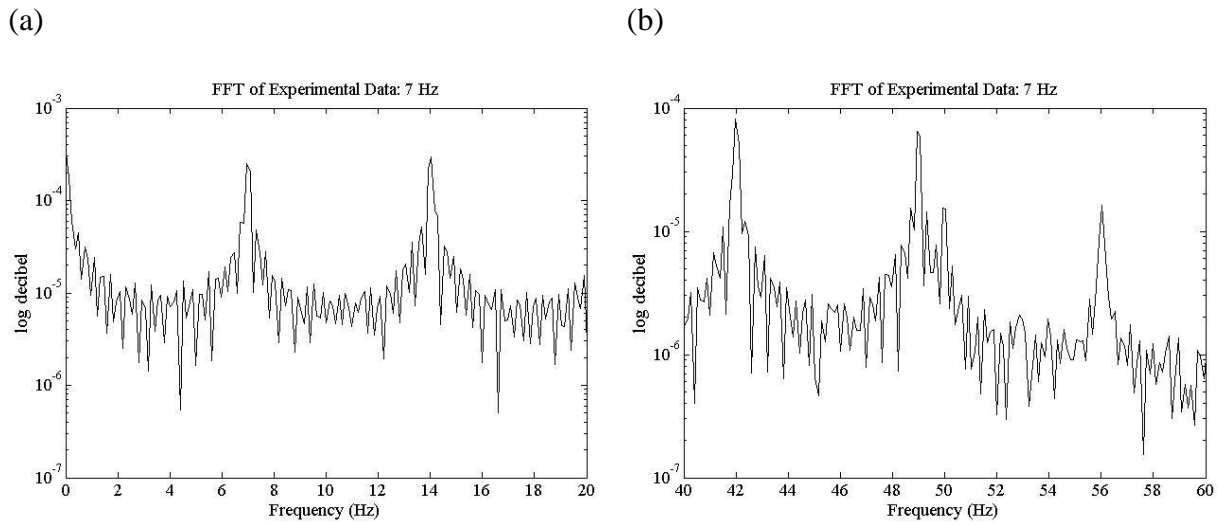
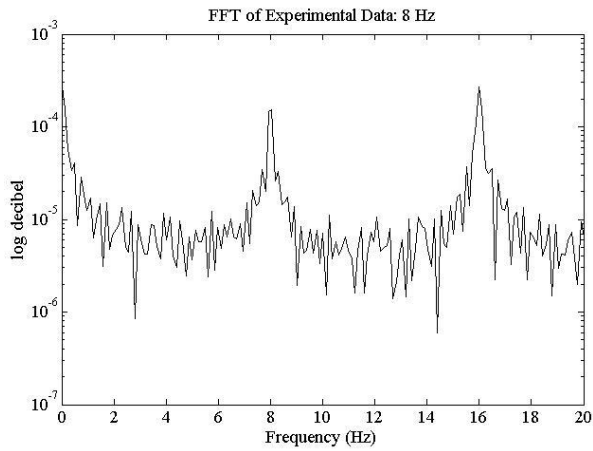


Figure 4.19: Fourier Transform of experimental data at operating frequency 7 Hz at range (a) 0-20 Hz and (b) 40-60 Hz.

(a)



(b)

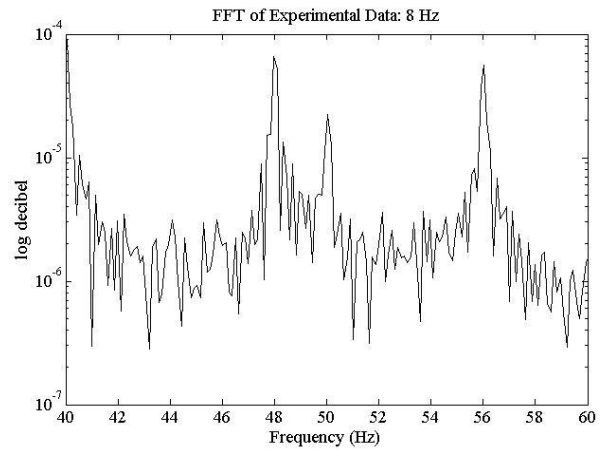
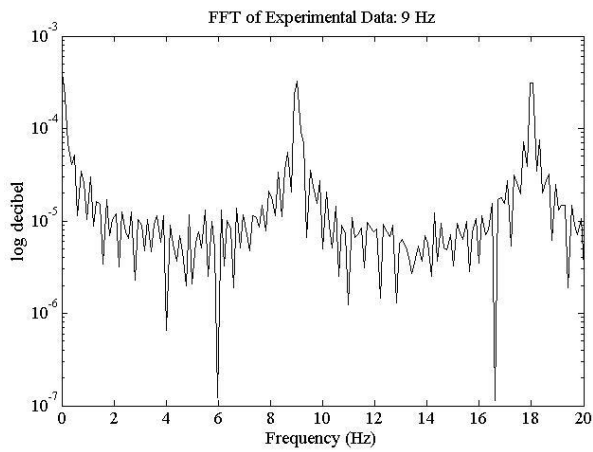


Figure 4.20: Fourier Transform of experimental data at operating frequency 8 Hz at range (a) 0-20 Hz and (b) 40-60 Hz.

(a)



(b)

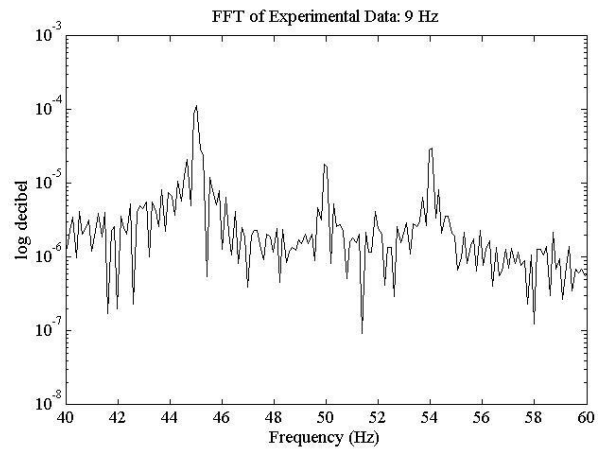


Figure 4.21: Fourier Transform of experimental data at operating frequency 9 Hz at range (a) 0-20 Hz and (b) 40-60 Hz.

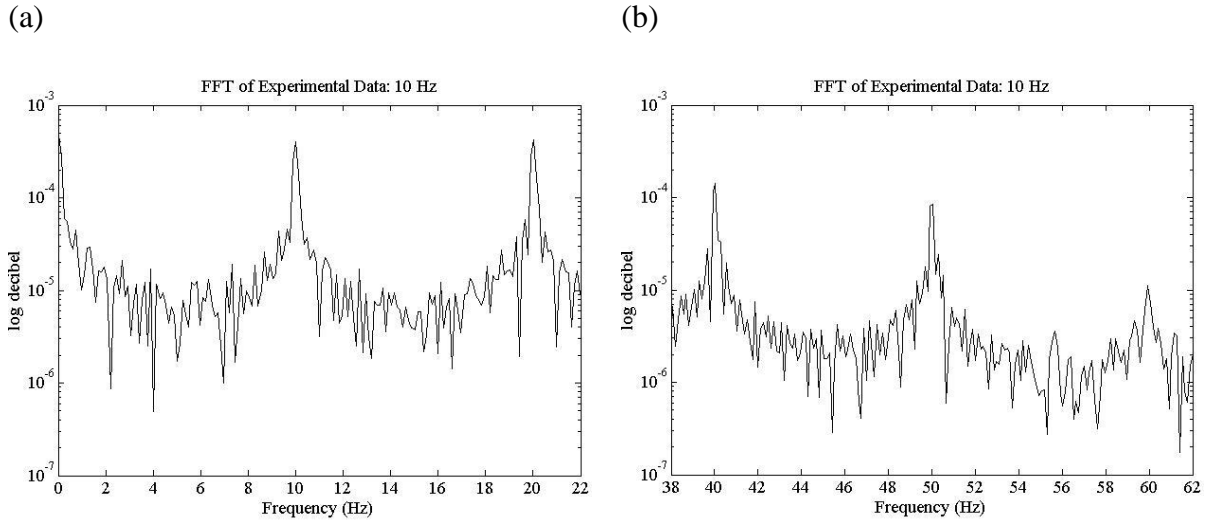


Figure 4.22: Fourier Transform of experimental data at operating frequency 10 Hz at range (a) 0-22 Hz and (b) 38-62 Hz.

The general trend in the FFT graphs shows that the first peak occurs at the frequency value of the solid state relay operating frequency used in the system. Besides that, there are peaks at every multiple of the operating frequencies. For example, the operating frequency used in Figure 4.14 (a) is a FFT diagram of experimental data with solid state relay frequency of 2 Hz, the first peak that occurs is at 2 Hz, and the other peaks occur at its multiples, which are 4 Hz, 6 Hz, 8 Hz and so on. The peaks occur at the multiples of operating frequency are caused by the non-linearity in the system. In figure 4.14 (b) to 4.22 (b), there is also a peak recorded at 50 Hz of every experimental data, which signifies the frequency of the main supply.

The solid state relay logic switch (SSRL) that alternates the signal from ON to OFF by an operating frequency is expressed by Equation (4.17). As the SSRL is in ON region, the multiplier of voltage supply, P_c is 1. On the other hand, the multiplier of voltage supply, P_c is 0 when the SSRL is switched to off.

$$P_c = \begin{cases} 1, & \text{if } t \left(\text{mod} \frac{2\pi}{\Omega} \right) < \frac{2\pi}{\Omega} \\ 0, & \text{else} \end{cases} \quad (4.17)$$

The switching signal of SSRL with the operating frequency, Ω of 5 Hz is plotted in Figure 4.23. It shows that the multiplier, P_c switching from 1 to 0, emulating an ON and OFF switching signal. The switching occurs 5 times in 1 second, showing that the frequency response agrees with the operating frequency applied to the system.

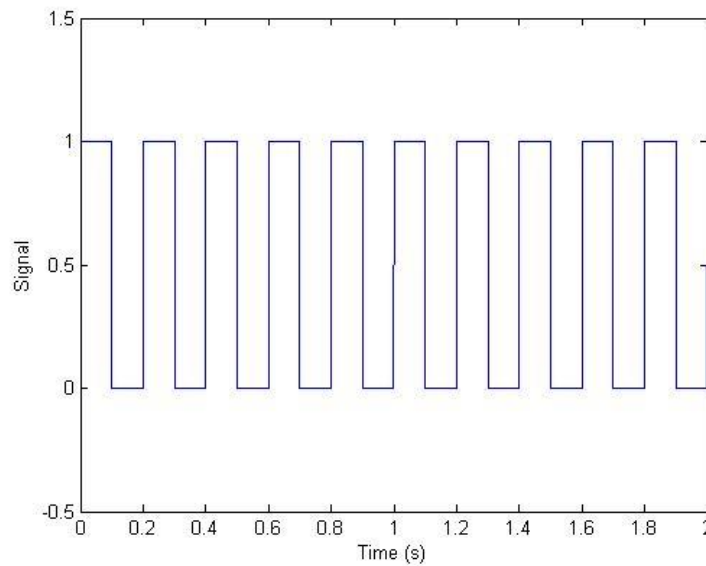


Figure 4.23: Switching solid state relay signal against time.

In Figure 4.24, the combined waveform of the main supply (sinusoidal wave oscillating in 50 Hz with amplitude of 25 V) and SSRL (switching between ON and OFF with

operating frequency of 5 Hz) is showed. The AC power supplied oscillates from 0 V to 25 V, showing the power provided to Solenoid 2.

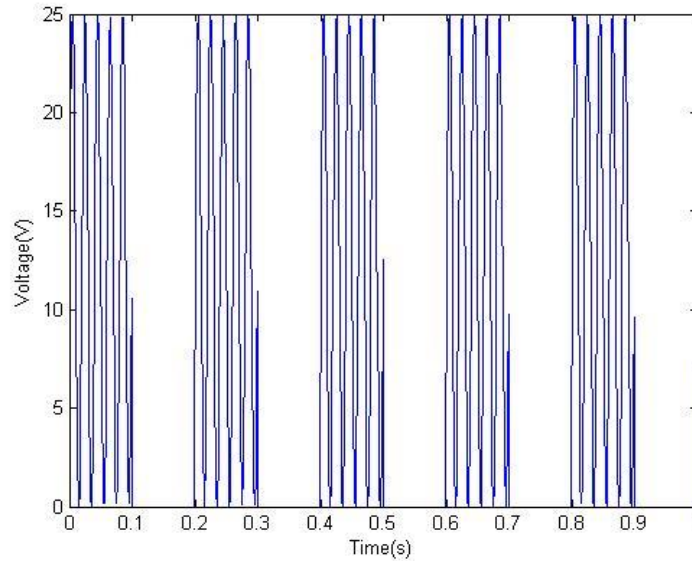


Figure 4.24: Combined effect of main supply and SSRL switching at operating frequency of 5 Hz.

In Figure 4.25, the time history of activating only the AC solenoid is simulated. It shows that the conductor travels from the origin position ($x_0 = 0$ m) to the direction of Solenoid 2's centre position ($x = -0.0455$ m), and oscillates about the position. The oscillations initiate with large amplitude in the transient region, gradually reduces to constant amplitude in steady state region. At steady state, the amplitude of oscillation is very small, with maximum displacement of -0.0446 m and minimum displacement of -0.0464 m, oscillating at the centre of Solenoid 2.

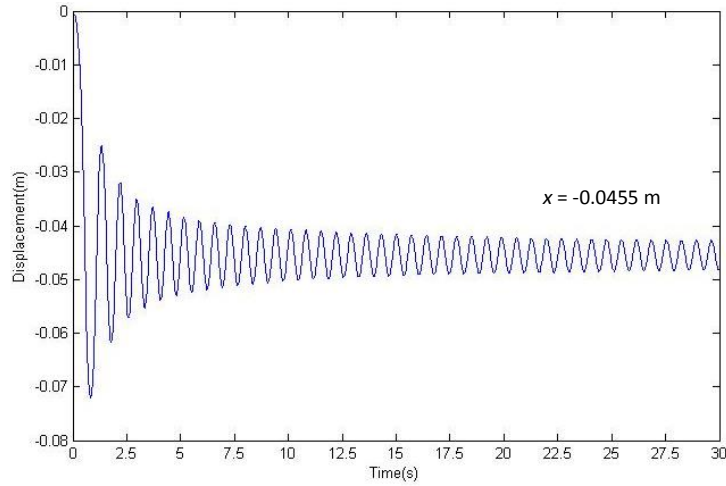


Figure 4.25: Time history of conductor bar oscillation with only AC solenoid.

Applying the mathematical model of AC Solenoid into the equation of motion of conductor bar, the time history of conductor displacement under the effect of Solenoid 2 with a stop is shown in Figure 4.26. From experimental observation, by switching on the AC supply, conductor vibrates locally without making any significant displacement. The numerical solution correlates with the mentioned observation as the steady states oscillations indicate negligible oscillation along zero displacement.

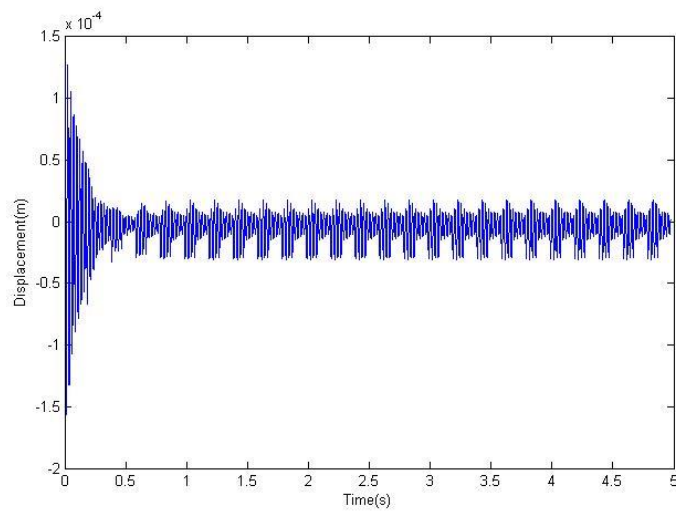


Figure 4.26: Graph of AC electromagnetic force against time, t .

4.6 Mathematical Model of One Degree-of-freedom Electro-vibroimpact System

After validating the electromagnetic forces component individually, the mathematical model is solved numerically to obtain the dynamics and electrical response of the vibro-impact machine. In order to solve the mechanical and electrical differential equations simultaneously, a Runge-Kutta algorithm, expressed as an equivalent set of state space first order equation is used. The discontinuous system expressed in Equations (4.3) and (4.4) is defined as two first order differential equations, by replacing the terms into $x = x_1$ and $v = \dot{x}_1$. Equation (4.16) that expresses the current is defined as $i = I$ and $z = \frac{di}{dt}$. Numerical simulation using Dynamics software [38] is performed, where the outputs are displacement, x current, i and the first derivatives, x' and i' along the fixed time span. Equation (4.16) shows the mathematical model to solve for one degree-of-freedom oscillation.

$$\left\{ \begin{array}{l} \ddot{x}_1 = \frac{1}{m_1} \left[-F_1 + F_2 - mg - \begin{cases} kx_1 + c\dot{x}_1, & \text{if } x_1 > 0 \\ 0, & \text{else} \end{cases} \right] \\ \frac{d^2i}{dt^2} = \frac{1}{L} \left[\omega P_c V_s \cos(\omega t) - \left(R + 2 \frac{\partial L}{\partial x_b} \frac{dx_b}{dt} \right) \frac{di}{dt} - \left(\frac{1}{C} + \frac{\partial^2 L}{\partial x_b^2} \left(\frac{dx_b}{dt} \right)^2 + \frac{\partial L}{\partial x_b} \frac{d^2x_b}{dt^2} \right) i \right] \end{array} \right. \quad (4.18)$$

The set of differential equations for free region, when $x > 0$ m are:

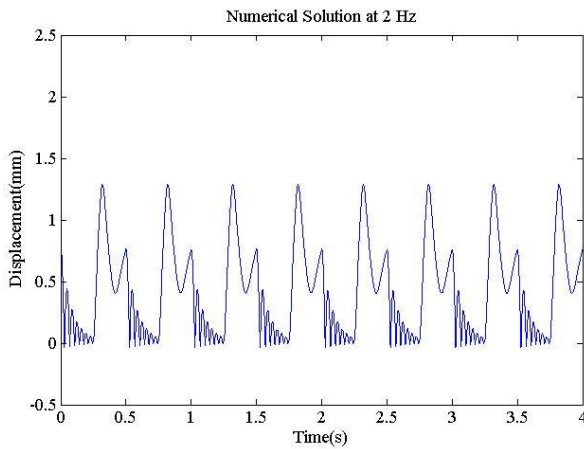
$$\left\{ \begin{array}{l} x' = v \\ v' = \frac{1}{m} [F_1 - F_2 - mg] \\ i' = z \\ z' = \frac{1}{L} \left[\omega P_c V_s \cos(\omega t) - \left(R + 2 \frac{\partial L}{\partial x_b} v \right) z - \left(\frac{1}{C} + \frac{\partial^2 L}{\partial x_b^2} (v)^2 + \frac{\partial L}{\partial x_b} v' \right) i \right] \end{array} \right. \quad (4.19)$$

The impact region is expressed by including the stiffness, k and damping coefficient, c components into the mechanical system, which occurs at $x_l \leq 0$ m.

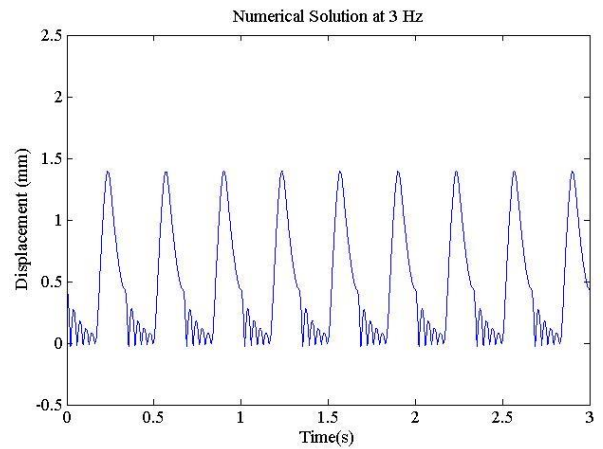
$$\left\{ \begin{array}{l} x' = v \\ v' = \frac{1}{m} [F_1 - F_2 - mg - cv - kx] \\ i' = z \\ z' = \frac{1}{L} \left[\omega P_c V_s \cos(\omega t) - \left(R + 2 \frac{\partial L}{\partial x_b} v \right) z - \left(\frac{1}{C} + \frac{\partial^2 L}{\partial x_b^2} (v)^2 + \frac{\partial L}{\partial x_b} v' \right) i \right] \end{array} \right. \quad (4.20)$$

Figure 4.27 shows the simulation result of solving the above differential equations simultaneously, which is the system motion equation with operating frequency of 5 Hz using MATLAB. The output displacement, x is generated over time by using simulation time step, t_s of 0.001 s. The blue line signifies displacement in the free region, while red represents displacement in impact region. The circles are the points where equation switches from free region to impact region. The switching is made precisely by implementing root finding bisection method when displacement crosses 0 m (the impact surface) with absolute tolerance, Δ of 1×10^{-6} m.

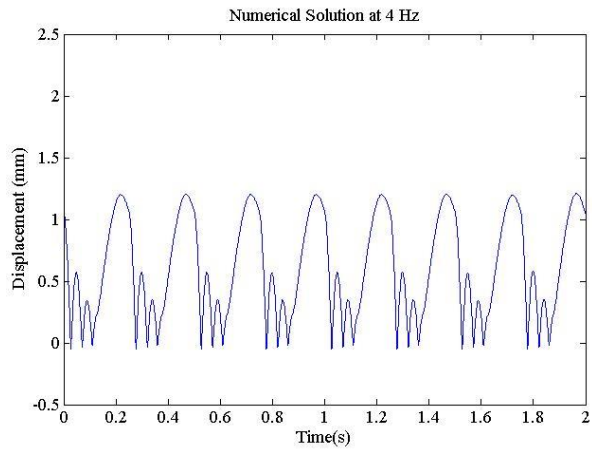
(a)



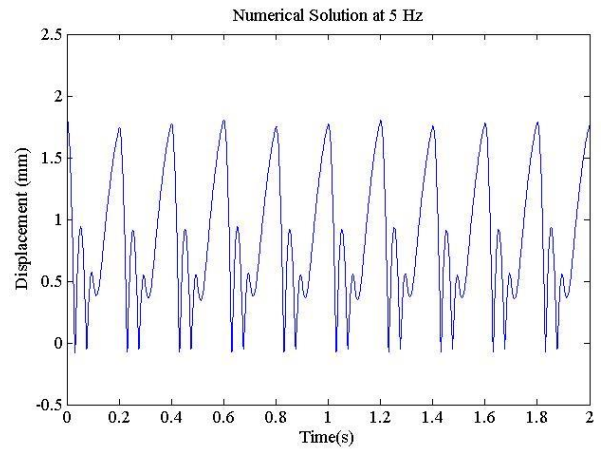
(b)



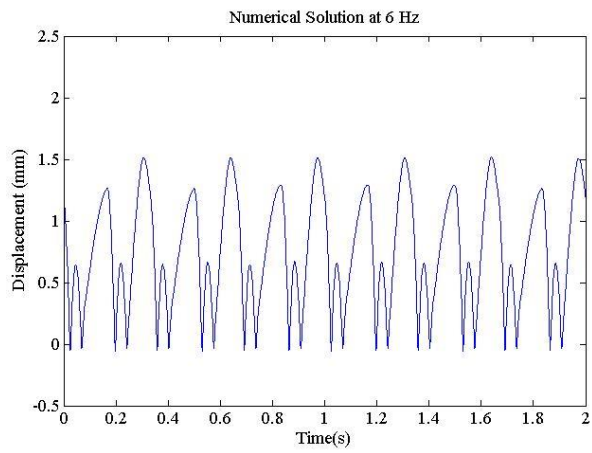
(c)



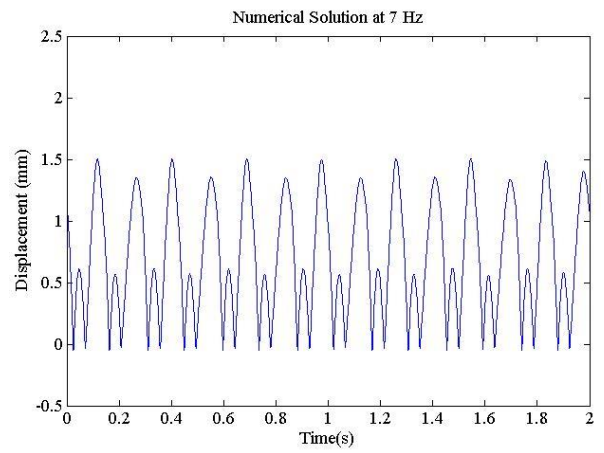
(d)



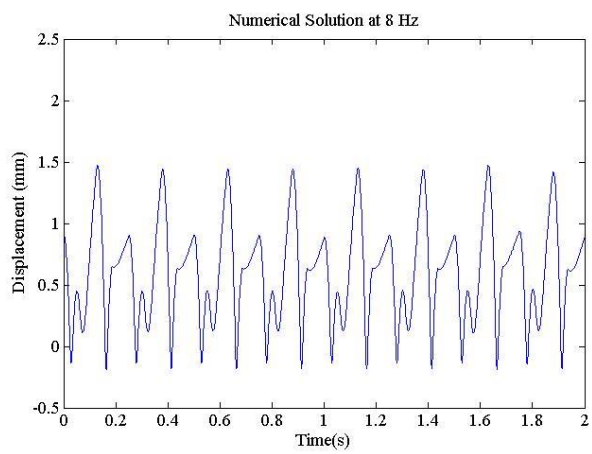
(e)



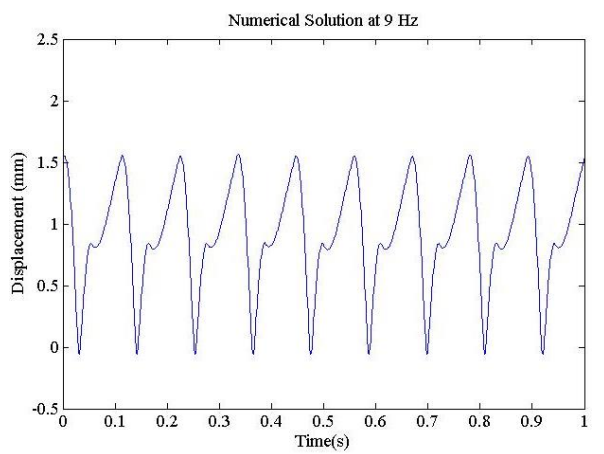
(f)



(g)



(h)



(i)

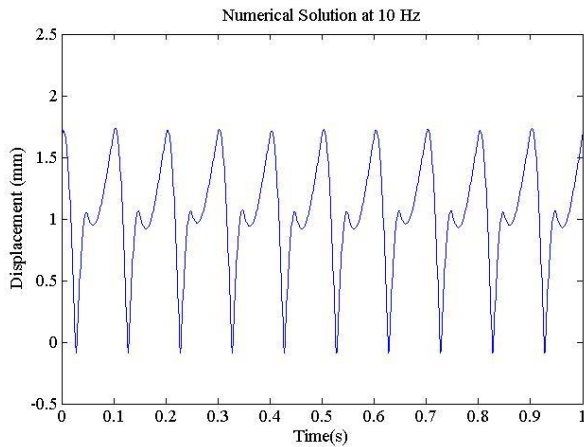


Figure 4.27: Numerical time history at operating frequency (a) 2 Hz, (b) 3 Hz, (c) 4 Hz, (d) 5 Hz, (e) 6 Hz, (f) 7 Hz, (g) 8 Hz, (h) 9 Hz and (i) 10 Hz obtained from Matlab simulation.

From Figure 4.27, the numerical solution of one degree-of-freedom electro-vibroimpact system shows variation of frequency responses. Amplitude of oscillations has high correlation between experimental and numerical results. Period-1 oscillation is observed for Figure 4.27 (a) to (d) and (h) to (i), which are time histories of solid state relay frequency of 2 Hz, 3 Hz, 4 Hz, 5 Hz, 9 Hz and 10 Hz. Numerical results of solid state relay frequencies of 6 Hz, 7 Hz and 8 Hz showed Period-2 oscillations.

4.7 Mathematical Model of Two Degree-of-freedom Electro-vibroimpact System

An addition equation of motion of rig progression, x_2 is included to solve the 2 degrees-of-freedom system. The mass of the system, m_2 is 2.643 kg. The relative displacement of oscillating bar is replaced as $(x_1 - x_2)$, since x_1 represents the absolute displacement of oscillating bar in the rig.

$$\left\{ \begin{array}{l} \ddot{x}_1 = \frac{1}{m_1} \left[-F_1 + F_2 - \begin{cases} k(x_1 - x_2) + c(\dot{x}_1 - \dot{x}_2), & \text{if } (x_1 - x_2) > 0 \\ 0, & \text{else} \end{cases} \right] \\ \ddot{x}_2 = \frac{1}{m_2} \left[F_1 - F_2 + \begin{cases} k(x_1 - x_2) + c(\dot{x}_1 - \dot{x}_2), & \text{if } (x_1 - x_2) > 0 \\ 0, & \text{else} \end{cases} \right. \\ \quad \left. + F_f - F_S(\dot{x}_2 - \dot{x}_1) \begin{cases} 1, & \text{if } (\dot{x}_2 - \dot{x}_1) > 0 \\ -1, & \text{else} \end{cases} \right] \\ \frac{d^2 i}{dt^2} = \frac{1}{L} \left[\omega P_c V_S \cos(\omega t) - \left(R + 2 \frac{\partial L}{\partial x_b} \frac{d(x_1 - x_2)}{dt} \right) \frac{d(\dot{x}_1 - \dot{x}_2)}{dt} \right. \\ \quad \left. - \left(\frac{1}{C} + \frac{\partial^2 L}{\partial x_b^2} \left(\frac{d(x_1 - x_2)}{dt} \right)^2 + \frac{\partial L}{\partial x_b} \frac{d^2(x_1 - x_2)}{dt^2} \right) i \right] \end{array} \right. \quad (4.21)$$

The force components experienced by Mass 1 act as reaction forces on Mass 2, thus the components are included in the equation of motion of rig progression in opposite sign. Soil friction is modelled as a damper, where a damping constant is associated with the rig's velocity. The nonlinearity of soil friction, F_s , models the behaviour of resistive force acting in the opposite direction of motion. A constant value, 31.1 N is added to the equation of motion to represent the static force, F_f . The two degree-of-freedom experiment is executed in horizontal orientation. At such, the gravitational force of oscillating bar is neglected.

The solution is obtained using similar method as the one degree-of-freedom numerical results using Dynamics software [38]. The state space is expanded to accommodate $w = x_2$ and $y = \dot{x}_2$.

The set of differential equations for free region, when $x > 0$ m are:

$$\left\{ \begin{array}{l} x' = v \\ v' = \frac{1}{m} [F_1 - F_2 - c(v - y) - k(x - w)] \\ w' = y \\ y' = \frac{1}{m_2} [F_1 - F_2 + k(x - w) + c(v - y) + F_f - F_s(y - v) \begin{cases} 1, & \text{if } (y - v) > 0 \\ -1, & \text{else} \end{cases}] \\ i' = z \\ z' = \frac{1}{L} \left[\omega P_c V_s \cos(\omega t) - \left(R + 2 \frac{\partial L}{\partial x_b} (v - y) \right) z - \left(\frac{1}{C} + \frac{\partial^2 L}{\partial x_b^2} (v - y)^2 + \frac{\partial L}{\partial x_b} (v' - y') \right) i \right] \end{array} \right. \quad (4.22)$$

Stiffness and damping of the stop are included in the impact region:

$$\left\{ \begin{array}{l} x' = v \\ v' = \frac{1}{m} [F_1 - F_2 - c(v - y) - k(x - w)] \\ w' = y \\ y' = \frac{1}{m_2} [F_1 - F_2 + k(x - w) + c(v - y) + F_f - F_s(y - v) \begin{cases} 1, & \text{if } (y - v) > 0 \\ -1, & \text{else} \end{cases}] \\ i' = z \\ z' = \frac{1}{L} \left[\omega P_c V_s \cos(\omega t) - \left(R + 2 \frac{\partial L}{\partial x_b} (v - y) \right) z - \left(\frac{1}{C} + \frac{\partial^2 L}{\partial x_b^2} (v - y)^2 + \frac{\partial L}{\partial x_b} (v' - y') \right) i \right] \end{array} \right. \quad (4.23)$$

The obtained numerical results, time histories of oscillation bar, x_1 and rig progression x_2 are presented in Figure 4.28 to Figure 4.32. The solid blue line represents experimental results while dotted green line represents numerical results.

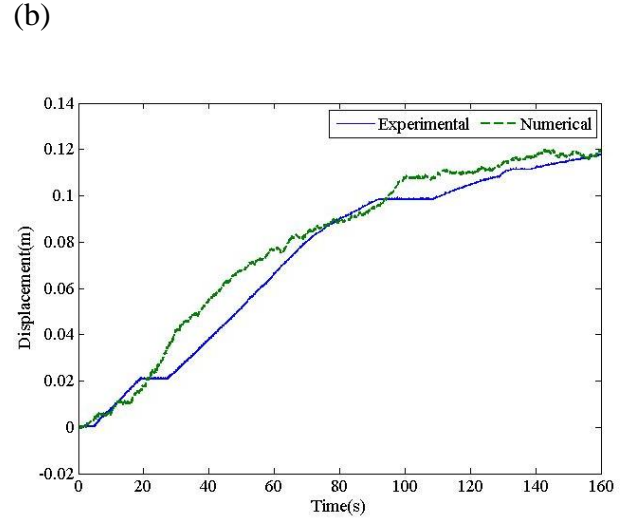
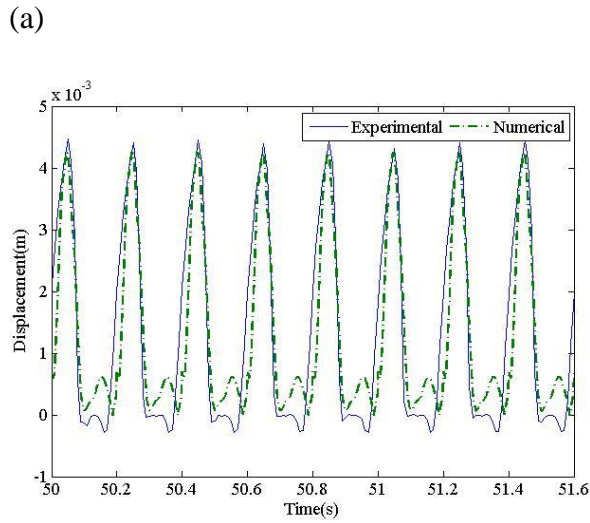


Figure 4.28: Comparison of experimental (blue line) and numerical (dotted green line) results of (a) Conductor oscillation and (b) Rig progression of 5 Hz operating frequency.

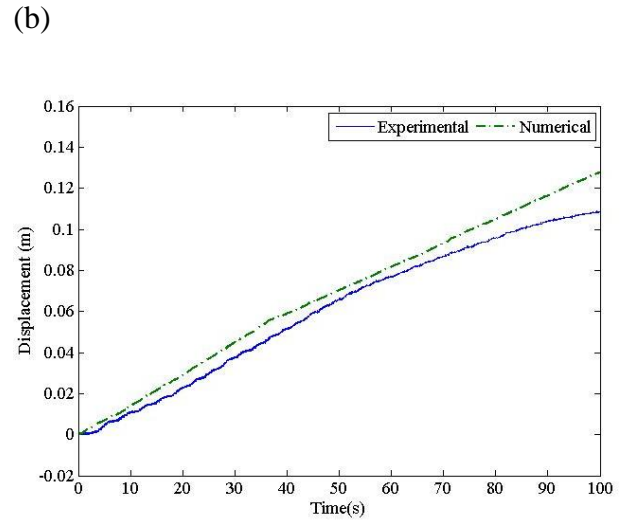
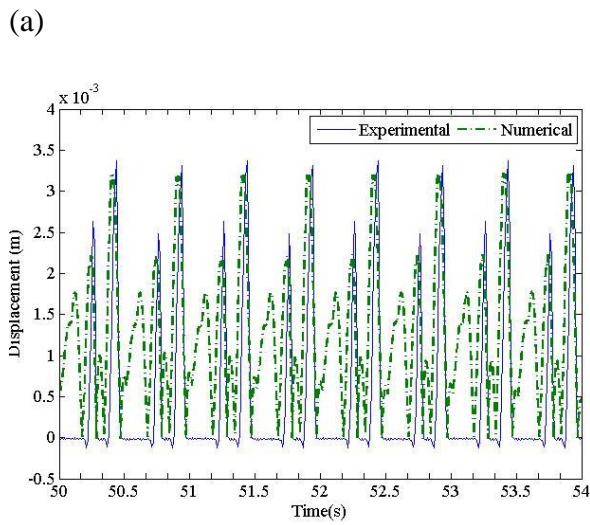
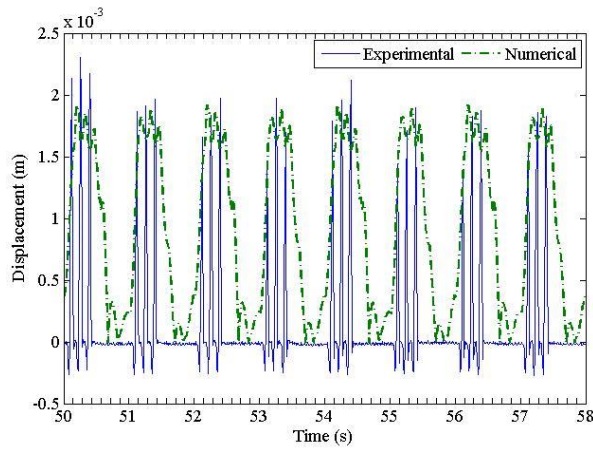


Figure 4.29: Comparison of experimental (blue line) and numerical (dotted green line) results of (a) Conductor oscillation and (b) Rig progression of 6 Hz operating frequency.

(a)



(b)

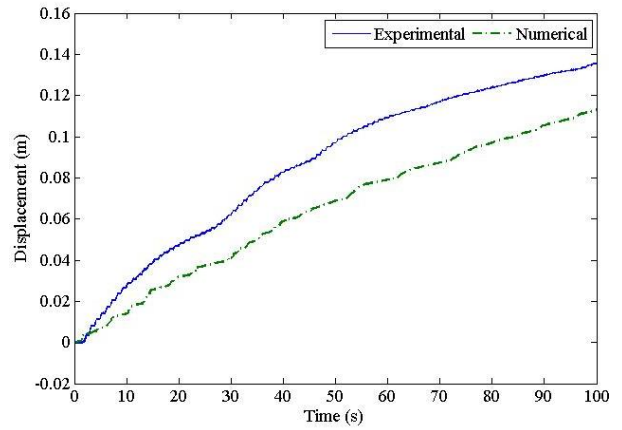
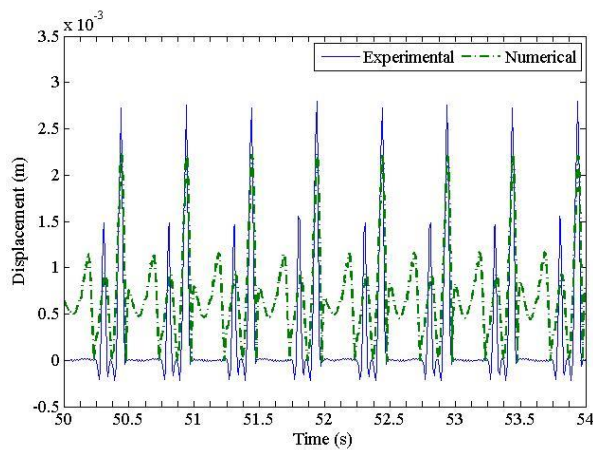


Figure 4.30: Comparison of experimental (blue line) and numerical (dotted green line) results of (a) Conductor oscillation and (b) Rig progression of 7 Hz operating frequency.

(a)



(b)

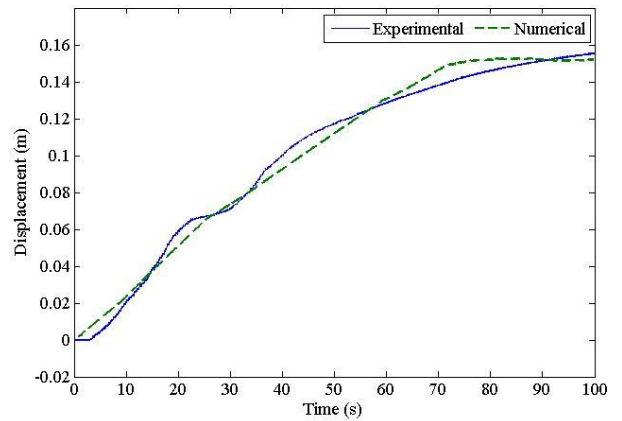


Figure 4.31: Comparison of experimental (blue line) and numerical (dotted green line) results of (a) Conductor oscillation and (b) Rig progression of 8 Hz operating frequency.

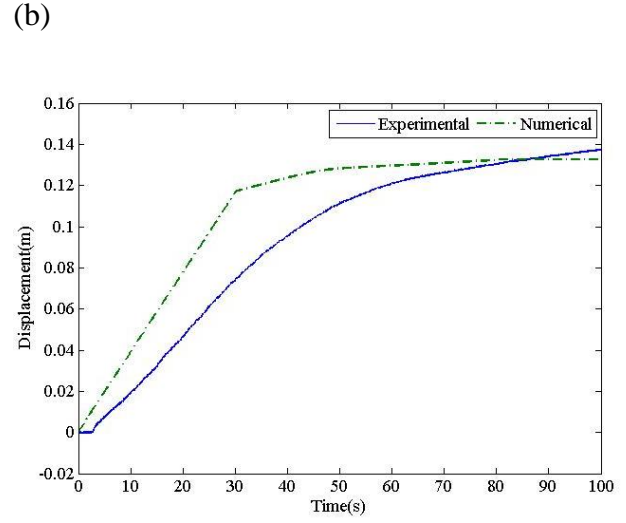
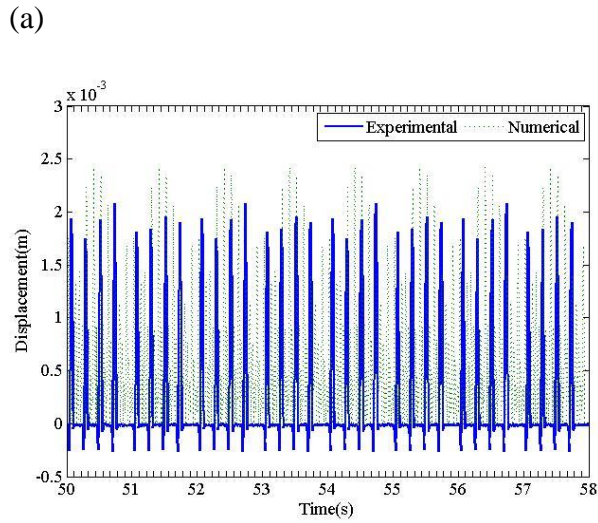


Figure 4.32: Comparison of experimental (blue line) and numerical (dotted green line) results of (a) Conductor oscillation and (b) Rig progression of 9 Hz operating frequency.

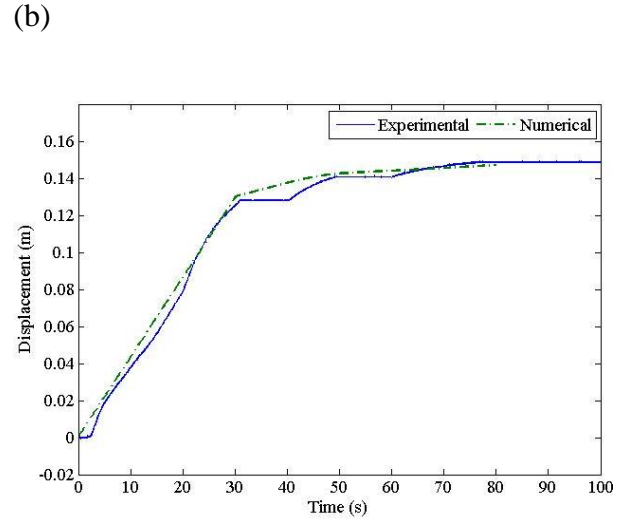
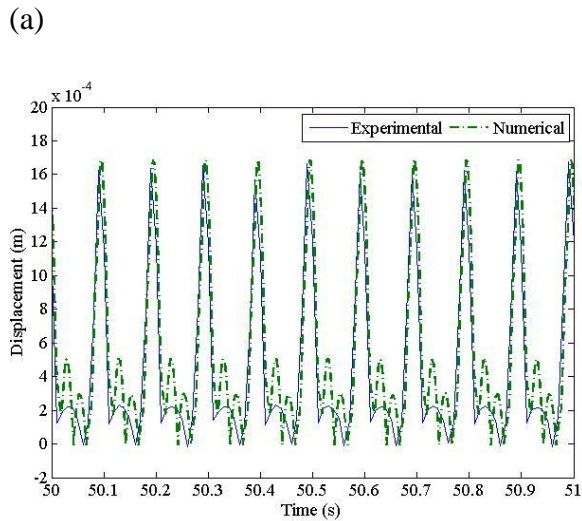


Figure 4.33: Comparison of experimental (blue line) and numerical (dotted green line) results of (a) Conductor oscillation and (b) Rig progression of 10 Hz operating frequency.

4.8 Experimental Correlation

The numerical results obtained in Figure 4.27 are to be compared with the experimental results which operate using the same operating frequency for model validation. The experimental results shown are in steady state, where the numerical results presented are also steady state oscillations.

Comparing the numerical result with the experimental data, there are a few observations made. For one degree-of-freedom system, the frequency response matches the solid state relay frequency for 2 Hz, 3 Hz, 4 Hz, 5 Hz, 9 Hz and 10 Hz experiments. Duration of a period of oscillation for 6 Hz, 7 Hz and 8 Hz are double of the input signal period duration, resulting in Period-2 oscillations. The experimental counterparts show Period-1 oscillations. Besides that, the amplitude of oscillations matches between both experimental and numerical results with minor differences. Amplitude of conductor oscillation is a crucial criterion as it is directly proportional to impact force upon the impact surface. Impact force varies by changing the operating frequency.

Both experimental and numerical waveforms show a high oscillation peak followed by a low oscillation peak. The differences are in the width/duration of reaching the peak. Numerically, the conductor leaves the impact region almost immediately after impact, and rises to the next oscillation vertex. However, the experimental data suggests that the conductor has a stick-slip motion at impact region, where it stays for a longer duration before rising to the next oscillation peak. It is possibly due to the assumption of stopper

as a spring of high stiffness, where some energy in the motion might be absorbed which created the stick-slip motion.

Comparisons of numerical and experimental two degree-of-freedom system solutions in Figure 4.28 to Figure 4.33 show several similarities and limitations. Frequency responses of conductor bar have good correlation which both experimental and numerical results achieve an agreement. Waveforms of oscillations contradict between both solutions except for the optimum solid state relay frequency at 5 Hz and 10 Hz experiments. A critical limitation of the mathematical model is that it is unable to properly model the soil friction force acting on the vibro-impact machine. Numerical rig progression time histories do not compliment the experimental results in terms of progression rate and maximum displacement achieved. Although the general trend of progressions are the same, where gradient of progression gradually decreases, reaching a flat line where progression stops.

4.9 Conclusions

The dynamic response of the vibro-impact system is highly affected by the electromagnetic forces induced by the DC solenoid and AC solenoid. The motion equation derived from the dynamics equation of the oscillating bar is modelled as a discontinuous system, where the impact point distinguishes the equation in the free region and impact regions.

The DC solenoid electromagnetic force is expressed in a cubic polynomial form which varies with the conductor displacement. The force equation is validated through experiment on the solenoid itself by obtaining force reading at varies conductor bar position.

Similarly, the AC solenoid consists of conductor displacement-dependent nonlinear force expressed in the form of second order ordinary differential equations, which the second derivative of current through the solenoid is a function of position, velocity of the conductor bar and inductance of solenoid. Inductance of solenoid, which is also displacement-dependent is measured experimentally by constructing a test circuit, and a Gaussian function is curve-fitted.

Dynamics software is sufficient to solve the mathematical model simultaneously with the electrical equation which describes the AC solenoid electromagnetic force using numerical simulation. The Runge-Kutta approach is applied, where each second order differential equation is replaced by two first order differential equations, forming a state-space of four equations.

Validation and comparison of experimental and numerical results of the system under same operating parameters is done. There is correlation in terms of oscillatory frequency response, amplitude and waveform.

CHAPTER 5

PROTOTYPE ELECTRO-VIBROIMPACT SYSTEM

5.1 Introduction

This chapter describes a culmination of experience in experimental work, especially to enclose electro-vibroimpact mechanism in an aluminium cylinder, so as to keep soil outside this cylinder and not come into contact with electromechanical components. Construction of prototype experimental rig had been undertaken by Winson Khoo, Gak-Chun Lee, Zhen-Yue Lim and Zheng-Yang Tai in a group project as part of undergraduate assessment [50]. A cylindrical housing had been machined, to house a base plate on which solenoids, vibro-impact oscillating bar, and stop are lined up. Circuitry external to cylindrical housing consist of RLC circuit contained in a transparent acrylic box. The function generator is replaced by a timer circuit. There is also an option of a direct current supply using batteries, which is useful for civil engineering deployment. To maintain consistency of current magnitude, a laboratory direct current power supply has been used. Experimental equipment is thus compact, and operation is straightforward.

5.2 Prototype Experimental Rig Description

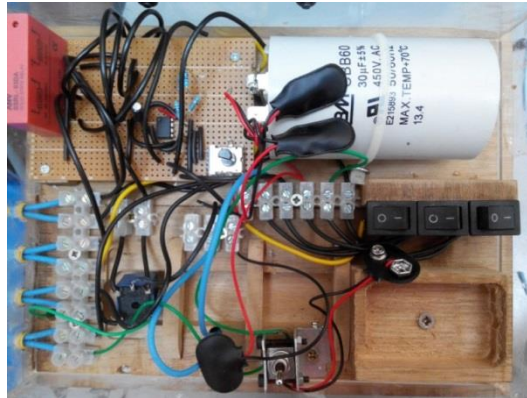
The pair of solenoids from the previous rig forms an integral part of prototype experimental rig. A mild steel cylindrical bar is actuated within the solenoids,

necessitating a periodic switching on and off which is now affected by a Texas Instruments LM555 timer. A direct current power supply to this timer is sufficient.

Supply of alternating current to solenoid had previously been facilitated by a variac so that flexibility of voltage magnitude was possible. A step-down transformer converts a potential difference from the mains, which is 240 V, to 120 V. By direct connection to a variable resistor potentiometer, voltage is adjusted further to 80 V. This has been found to be an optimum value to generate effective vibro-impact forward progression motion.

Periodic switching on and off of solid state relay by timer is equivalent to a square wave signal. An important feature of prototype electro-vibroimpact mechanism is that both the solid state relay of the AC circuit and also an electromechanical relay of the DC circuit are switched by the same square wave. For the DC circuit, the electromechanical relay will be activated when the signal voltage from the solid state relay is non-zero, disconnecting the DC circuit. It means that the DC circuit is always turned off when the AC circuit is on, and vice versa. This causes the oscillating bar only moving towards one side or towards one solenoid which the circuit is switched on at one time. Progression rates into soil have been observed to be increased after implementing this new arrangement.

(a)



(b)

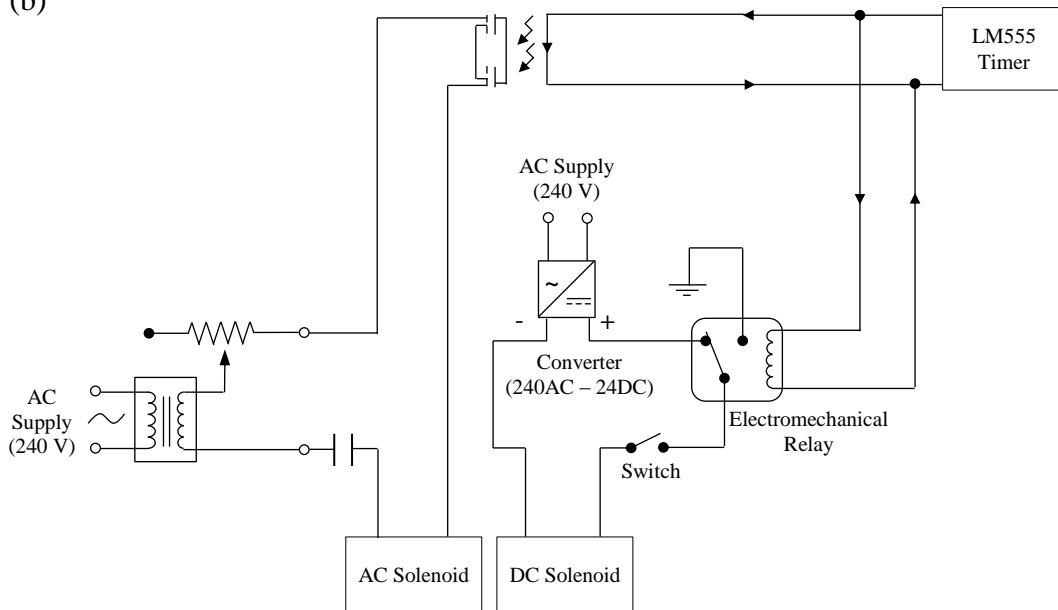


Figure 5.1: (a) Photograph of circuitry for alternating and direct current, and (b) corresponding schematic.

This modification of the circuit improves the consistency of vibro-impact oscillations of the impact bar within the solenoid, possibly by halting electromagnetic resistance by the DC solenoid to its motion towards AC solenoid and stop. There may be interactions between AC and DC solenoids which may be still useful for vibro-impact forward progression, though. It is convenient to determine the optimal distance between

solenoids since both electromagnets would not be turned on at the same time. The magnitude of voltage supply required is also less.

By replacing the function generator to control the operating frequency of the SSRL, the timer rates the time period of an ON/OFF cycle. The timer is configured to work in an Astable mode. Charging and discharging time, the values of resistor R_1 , R_2 and capacitor C_1 determine the frequency of the timer as shown in the calculations below.



Figure 5.2: The circuit board LM555 the timer and potentiometer that manipulates the operating frequency of AC power supply.

Table 5.1: Calculations of operating frequency of timer.

Charge Time, t_c (s)	$0.693(R_1 + R_2)C_1$
Discharge Time, t_D (s)	$0.693(R_2)C_1$
Total Cycle Time, T_{CD} (s)	$t_c + t_D = 0.693(R_1 + 2R_2)C_1$
Operating Frequency (Hz)	$\frac{1}{T} = \frac{1.44}{(R_1 + 2R_2)C_1}$

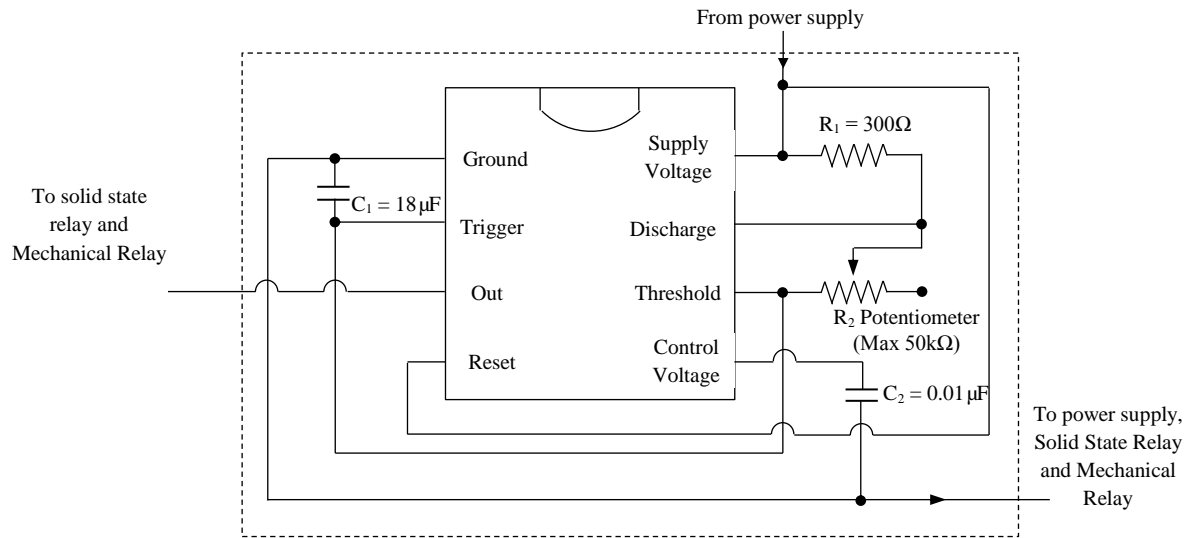


Figure 5.3: Schematic diagram of the LM555 Timer.

Through experimental trials, by setting R_1 to 300Ω , the operating signal provides approximately 50% of the duty cycle without being affected by the value of R_2 . By setting a capacitance value, C_1 as a constant of $18 \mu\text{F}$, the operating frequency to be manipulated may be varied when a potentiometer functions as a variable resistance, R_2 .

A hollow aluminium cylinder houses the major components of the electro-vibroimpact machine. To facilitate progression into soil for at least one metre, the length of the moling head is 145 mm; and that of the cylinder is 255 mm. The outer and inner diameters of the cylinder were machined in accordance to the size of the largest component that it houses, which is the solenoid. The solenoid has a rectangular cross section of dimensions 47.5 mm by 41.5 mm. It follows that a minimum inner diameter of 63 mm is required. A nominal thickness of 2 mm, results in an outer diameter 67 mm.

(a)



(b)



Figure 5.4: Photograph of (a) moling head connected to the body cover and (b) that of the bolted plate cover of the moling head connector.

A housing covers the front part of the cylinder. The moling head is connected to the cylinder with M3 bolts fastened to two tapped holes with matching threads. The diameter of the circular housing to the moling head is equal to the inner diameter (63 mm) of the aluminium cylinder. A hollow cylinder of 35 mm outer diameter and 25 mm inner diameter towards one end is mechanically attached to the head using two M3 bolts symmetrically arranged over the cross-section. The base plate on which solenoids reside is secured to the aluminium cylinder by virtue of two 4 mm tapped holes with internal threads. A cylindrical platform of 5 mm thickness functions as a stop to vibratory motion. The platform resides inside the aluminium cylinder, connecting the solenoid to the moling head.

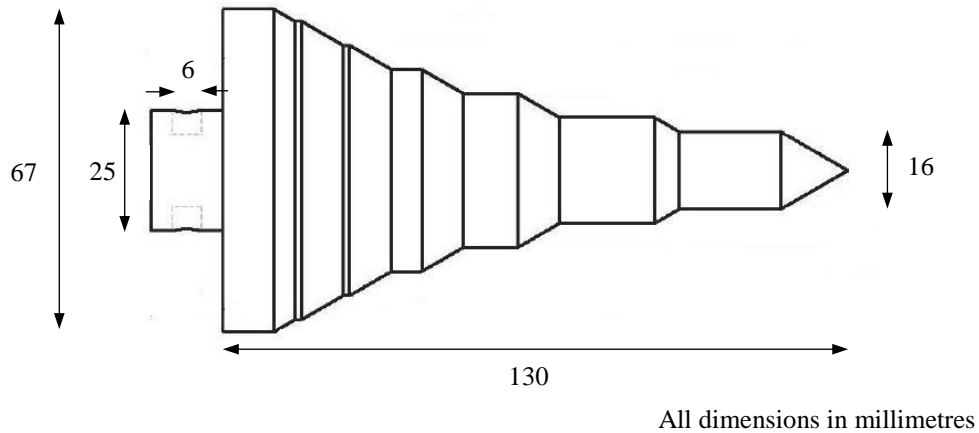


Figure 5.5 Engineering drawing of moling head and aluminium cylinder.

An overall schematic of prototype experimental rig is illustrated in Figure 5.8. To initiate penetration into soil, for example in a laboratory or civil engineering application, an effective method is to start machine operation to enter a vertical force of soil, so that progression is in a horizontal direction. Since prototype electro-vibroimpact system has a mass of less than 3 kg (main body and moling head), it is possible to use a guide rail or launch frame to support the prototype in a horizontal orientation before the operation starts, and also at the initial stages of soil progression. A launch frame is designed and manufactured to support the weight of the electro-vibroimpact system as well as maintain linear, horizontal motion. It is made of aluminium, which is non-ferrous and affects electromagnetic fluxes from the solenoids minimally. Height is also adjustable, accommodating various entry elevations. The plates supporting the experimental rig can be fastened to 20 positions equally distributed along vertical bars 0.5 m in height. The plates are designed as a pair of upside down plates making up a ‘V’-shape, as shown in Figure 6.6 (b). Unnecessary motion to the left or right would be minimized as the weight

keeps the prototype at the centre of the launch frame, allowing only horizontal movement in the direction of forward progression. Rollers from elements of two abacuses are added onto the platforms to minimize surface friction between rig and the launch frame, decreasing resistive forces during rig progression into soil.

With soil progression, soil compaction is inevitable. As soil density increases, soil above prototype is less than that below. As a consequence, experimental rig tends to move gradually upwards with time and unable to maintain a perfect horizontal progression. Additional rollers are installed on the launch frame facing downwards, to maintain elevation. As such, the launch frame streamlines the operation of prototype by providing position support, minimising surface friction and constraints the rig to move in a perfect horizontal direction.

(a)



(b)



Figure 5.6: The launch frame in (a) upper side view and (b) upper front view.

In Section 3.5, experimental work had identified a need for a static force to complement dynamic impact forces such that horizontal soil progression is possible. A previous manifestation of the static force was suspended weights. Gravitational forces are redirected horizontally by passing strings over pulley systems. The static force was varied by the number of weights. Some monitoring of the balancing of the weights and position of string on pulley so that they remain in position during operation was found necessary. Significant periodic vibration and impacts especially have a potential to destabilise suspended static weights. To address this issue, a linear actuator provides a reliable and constant immobilised force to assist forward progression.

The linear actuator is immobilised on a separate rigid frame using G-clamps. In this way, a static force may be fully transferred to electro-vibroimpact system without loss of energy. After full extension, it is also capable of complete and automatic retraction by straight forward electromechanical means. Being a single machine with only one moving component, wear and fatigue from vibro-impact forces is minimal. The end of the extension rod is mechanically fastened to the electro-vibroimpact system using bolts and nuts, ensuring secure connection and full transmission of static force.

(a)



(b)

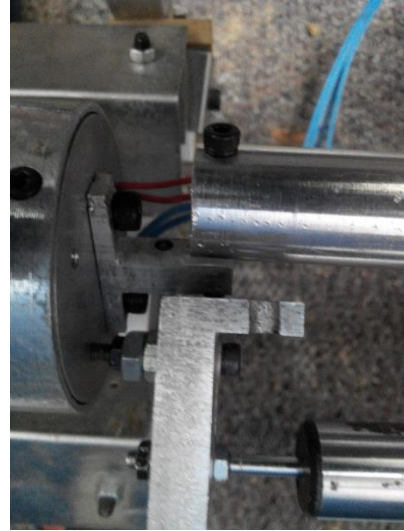


Figure 5.7: (a) Cytron MO-HTA1800-200 linear actuator and (b) the bolted connection from the actuator to the vibro-impact rig body.

Technical specifications of linear actuator confirm that only a nominal power input is required. Cytron technologies product code MO-HTA1800-200 features an extension rod capable of extending up to 200 mm, can exert a unidirectional axial force of 750 N. The electronic circuit that controls this linear actuator consists of a battery, switch, and a double pole double throw (DPDT) switch. The 9V battery acts as a power supply, and the main switch turns the circuit on/off to start or stop the movement of the linear actuator. The DPDT switch also functions to reverse the polarity of the electrical signal in the linear actuator. If the potential difference of the signal received by the linear actuator is positive, the linear actuator will extend, assisting soil progression of electro-vibroimpact rig into soil with a static force. By switching the DPDT to another pole, the potential difference is negative, resulting in the linear actuator retracting, withdraw experimental rig from soil.

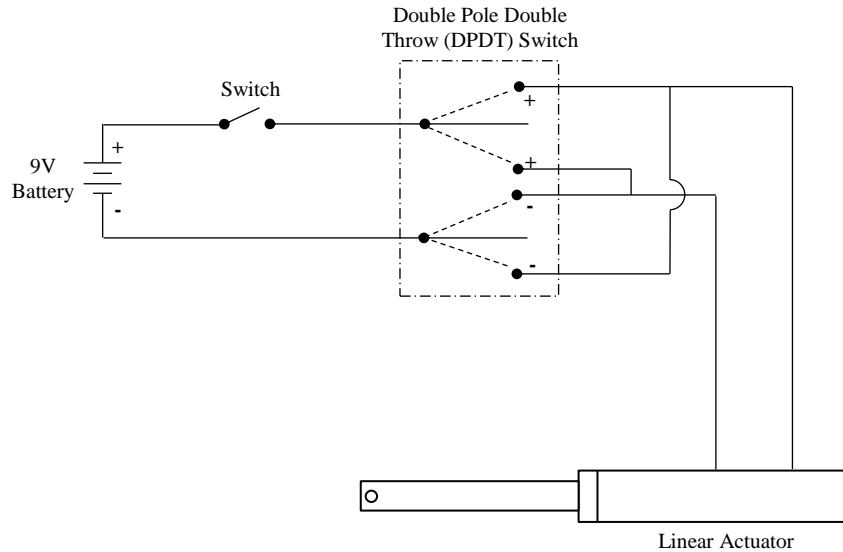


Figure 5.8: Schematic of circuitry operating a linear actuator.

A particular voltage advantage of using this linear actuator is especially at the extreme end of travel into a box of soil, progression rate declines. It is possible to increase a magnitude of static force readily so that an average rate of forward drift may be maintained.

The clayey soil is stored in an aluminium box of dimension 1 m (length) by 0.6 m (width) by 1 m (height). The soil fills up the box up to a height of 0.4 m height, making up to approximately 0.24 m^3 of soil. A circular opening of diameter 15 mm is drilled with its centre at the height of 20 mm from the bottom. This circular opening allows the moling head to enter into the soil. The soil is being subjected to a surcharge of 19 kg, using a slab of concrete. This covers a distance from point of entry into soil of 0.55 m. A piece of paper is taped to point of entry when no experiments are conducted to keep clay within the soil box.

(a)



(b)



Figure 5.9: (a) The soil box that contains soil with a circular opening for entry of motion and (b) the concrete slab which acts as surcharge on the soil for the first 0.55 m after entry.

5.3 Schematic Diagram

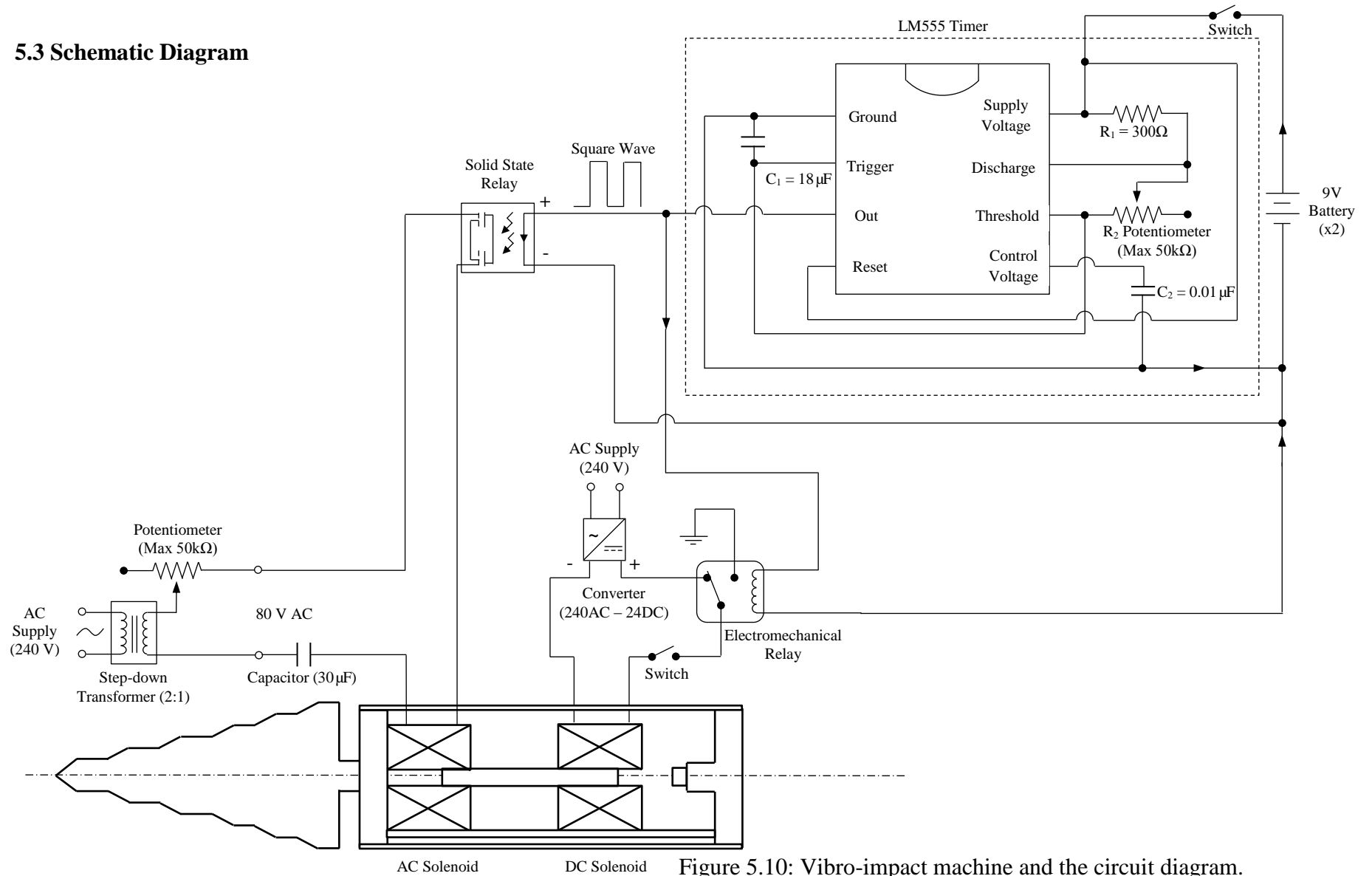


Figure 5.10: Vibro-impact machine and the circuit diagram.

5.4 Results and Discussion

The launch frame is placed right in front of the point of entry into soil, so that moling head is in contact with the soil. The aluminium cylinder is placed on the launch frame, so that its direction and angle is consistent with that of linear actuator. These initial conditions are consistent for all experimental work. A Solartron linear variable displacement transducer (LVDT) of model number 922945 is attached to the rear of the prototype rig using bolts and nuts to acquire data pertaining to forward progression rate.

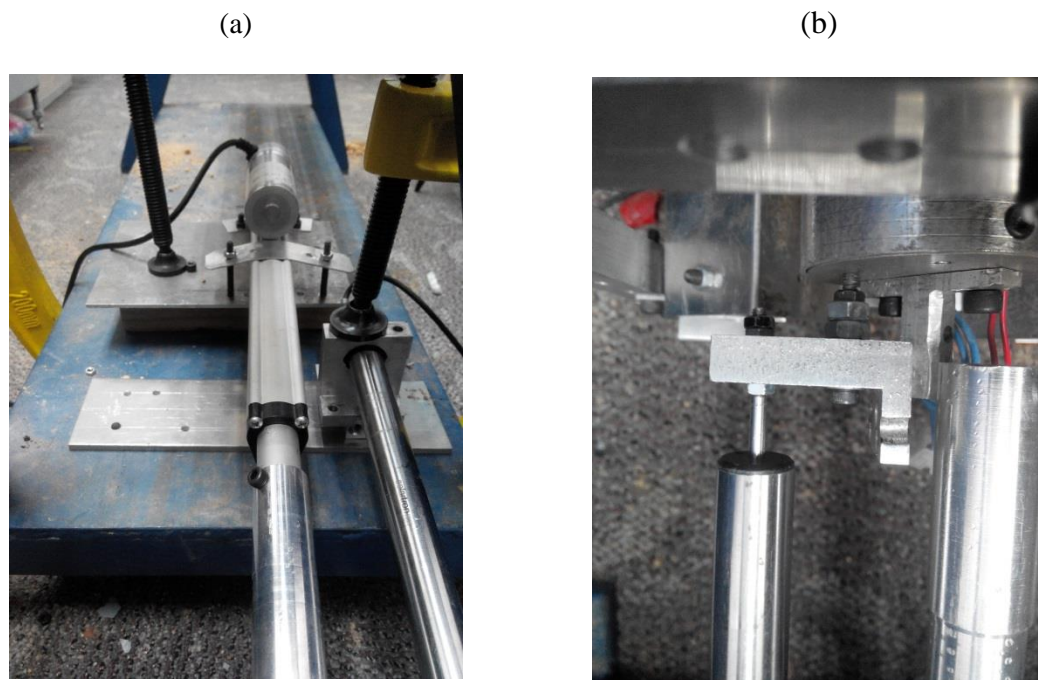


Figure 5.11: (a) LVDT and linear actuator installed at the rigid frame and (b) their connection to the rear end of prototype rig.

There are three voltage quantities which influence range of progression, and work has been undertaken to identify an optimal ratio between voltage of alternating current and that supplied to linear actuator. This optimal ratio is indicative of a working proportional

relationship between dynamic forcing and static component, inspired by a result reported by Krivtsov et al [25]. A range of AC power supply voltage was varied from 40 V to 110 V with 10 V intervals. AC supply that is lower than 40 V has been found to be insufficient to produce consistent periodic vibro-impact oscillations. Voltages larger than 120 V being supplied to the solenoid may generate currents which may damage the solenoid.

A sampling rate of 100 Hz has been used to acquire data from linear variable displacement transducer, which has been found to be sufficient to plot a detailed progression graph. Response data appear to be progressing forward while oscillating locally at high frequencies. This is possibly caused by the sufficient sensitivity of linear variable displacement transducer detecting small amplitudes vibrations. At the same time, another possibility is the instability of voltage response from the LVDT, such that the output voltage fluctuates within a small range of error. The data is smoothed by using a moving average filter, applying a local regression using weighted linear least squares (*loess*) method at a span of 10%.

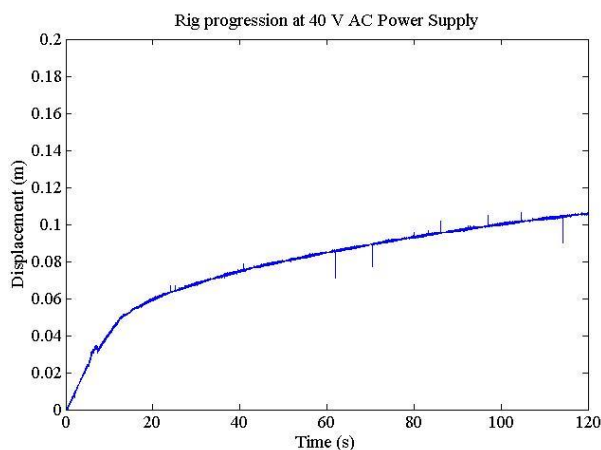


Figure 5.12: Time history of rig progression before smoothing.

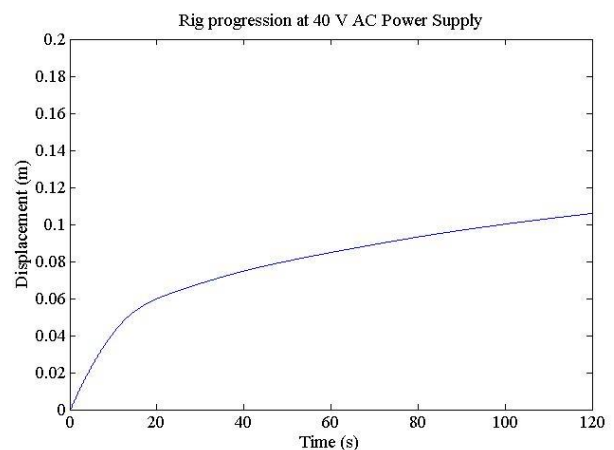
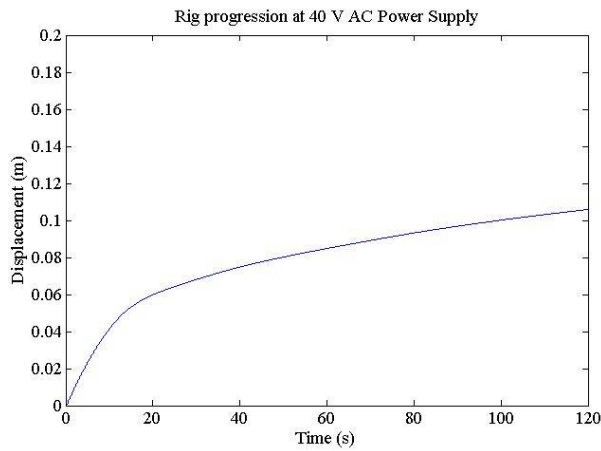


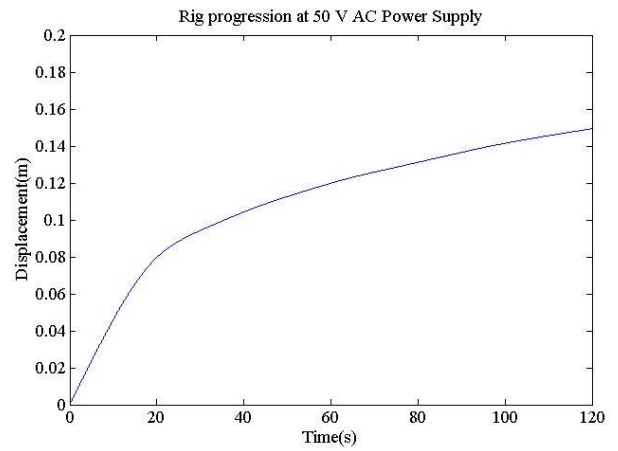
Figure 5.13: Time history of rig progression after smoothing.

The first 120 seconds data is recorded to investigate the relationship between initial progression rate and supply of alternating current. Since maximum extension length of transducer is 0.2 m, this is a reason for the upper limit value of vertical axis in Figure 5.12 and 5.13. Figures 5.14 and 5.15 document a set of data pertaining to AC supply ranging from 40 V to 110 V, for a timer frequency of 6 Hz and 8 V supplied to linear actuator. 24 V from converted alternating current supports direct current to a second solenoid.

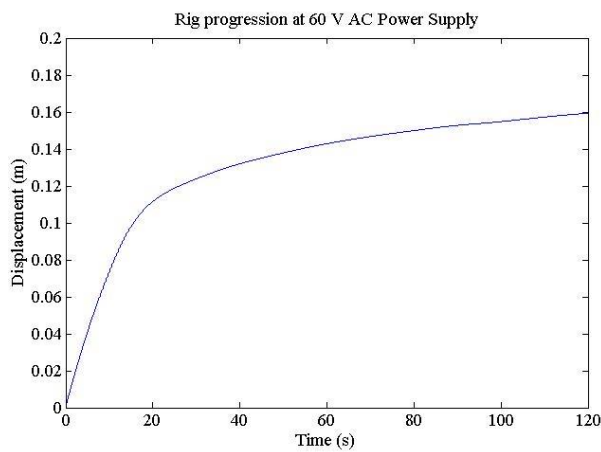
(a)



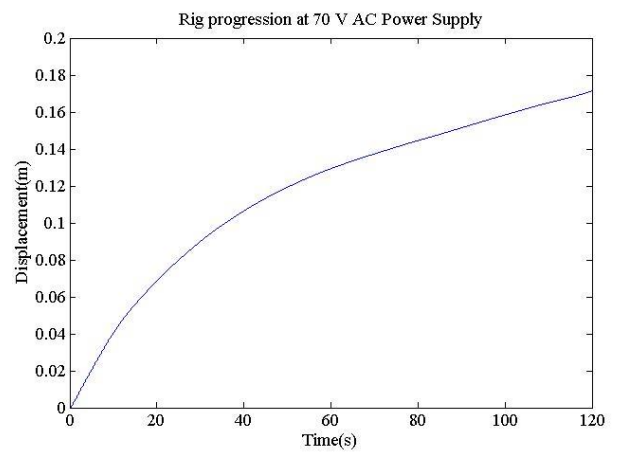
(b)



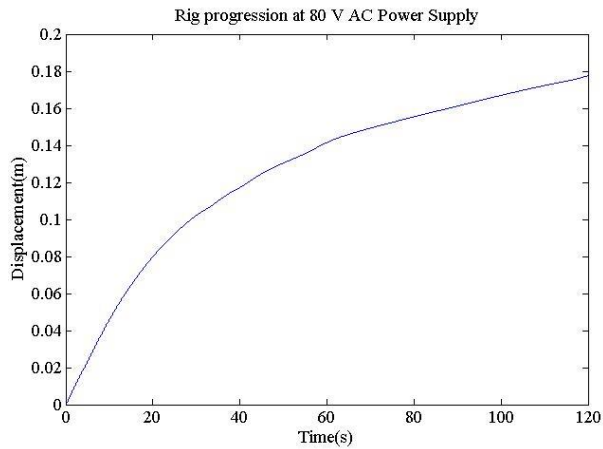
(c)



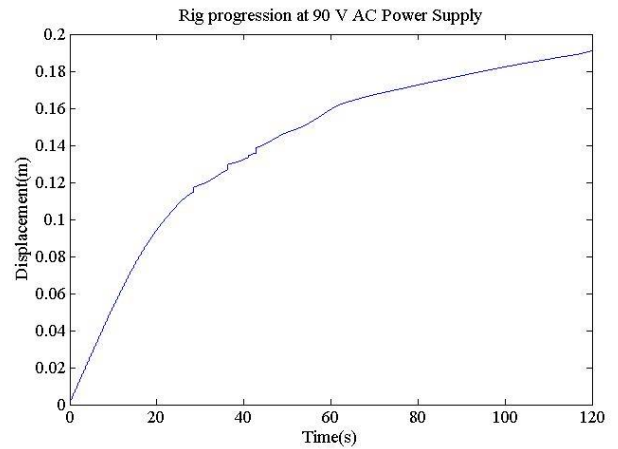
(d)



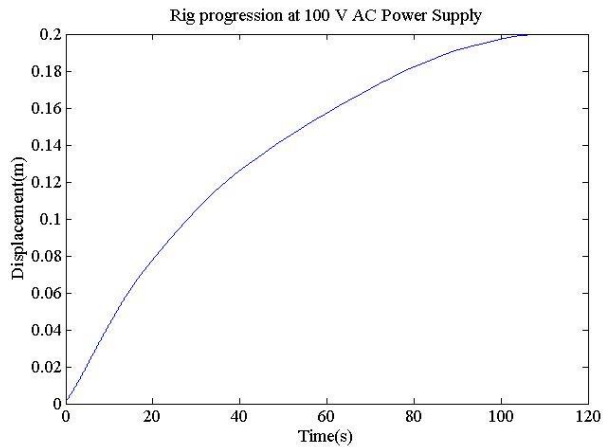
(e)



(f)



(g)



(h)

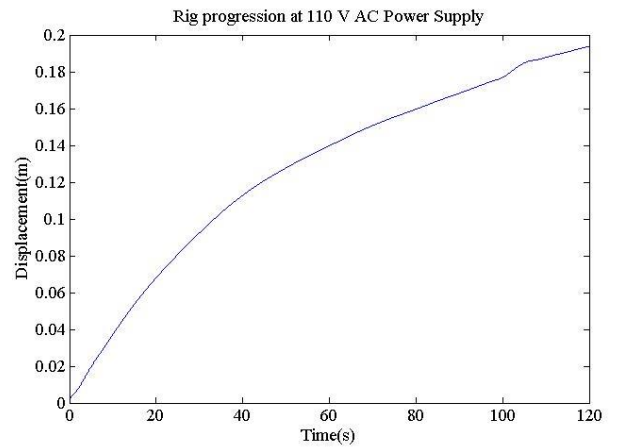


Figure 5.14: Time histories of rig progression into soil at (a) 40 V AC, (b) 50 V AC, (c) 60 V AC, (d) 70 V, (e) 80 V AC, (f) 90 V AC, (g) 100 V AC and (h) 110 V AC power supply, 6 Hz signal frequency and 8 V DC supplied to linear actuator.

From the above data, it shows that rig progression rate is initially high and gradually decreases over time. As the machine progresses into soil further, the soil compresses and thus increasing the resistance against rig movement. At lower range of AC voltage supply,

for 40 V, 50 V and 60 V, average progression rate increases as AC voltage supply increases. However, progression rate decreases drastically beyond 20 s of operation.

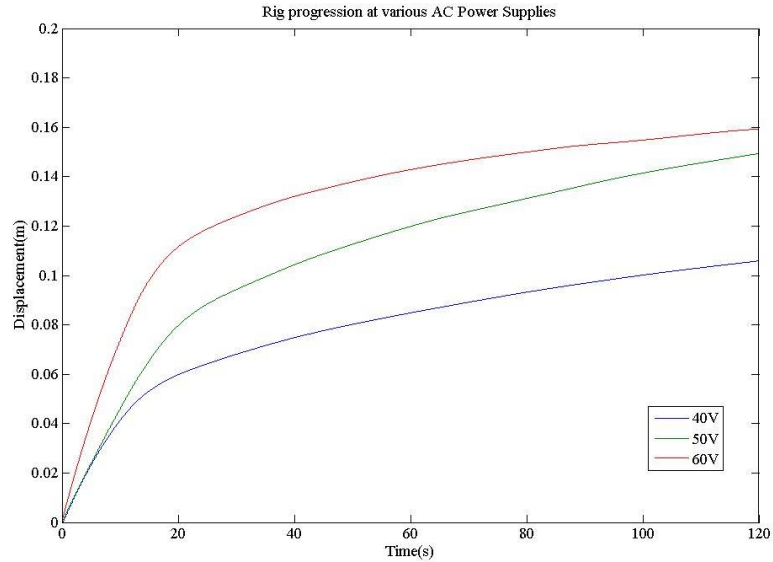


Figure 5.15: Comparison of rig progression at 40 V, 50 V and 60 V of AC power supply.

It also suggests that higher AC power supply motivates greater maximum displacement.

As it is observed that at the mark of 120 s, the displacements of increasing AC voltage are 0.116 m, 0.150 m and 0.160 m.

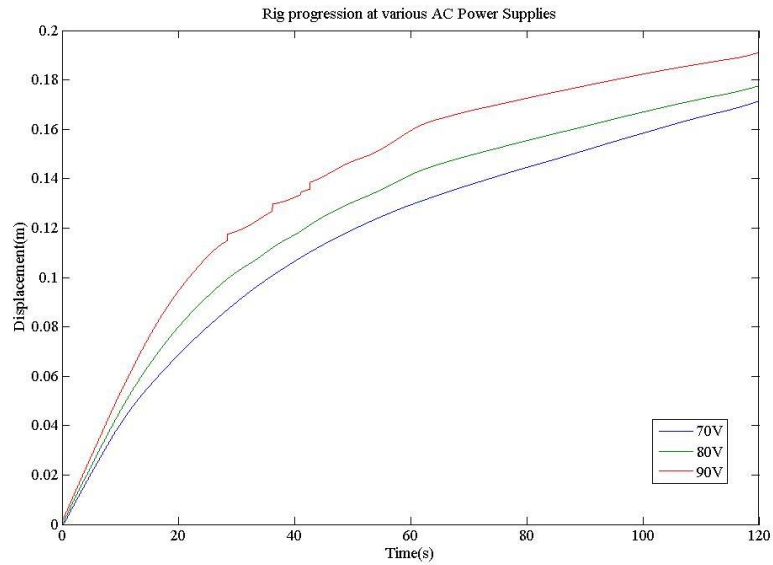
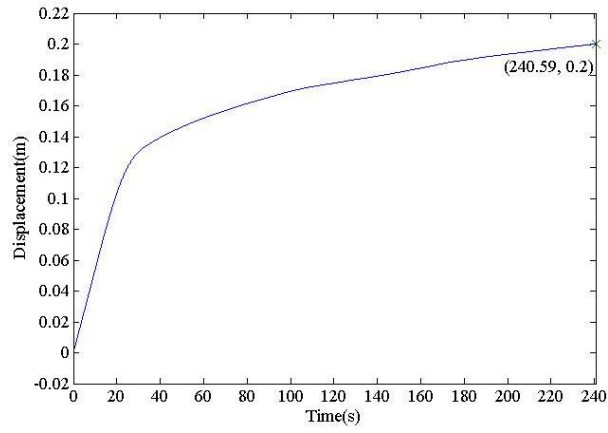


Figure 5.16: Comparison of rig progression at 70 V, 80 V and 90 V of AC power supply.

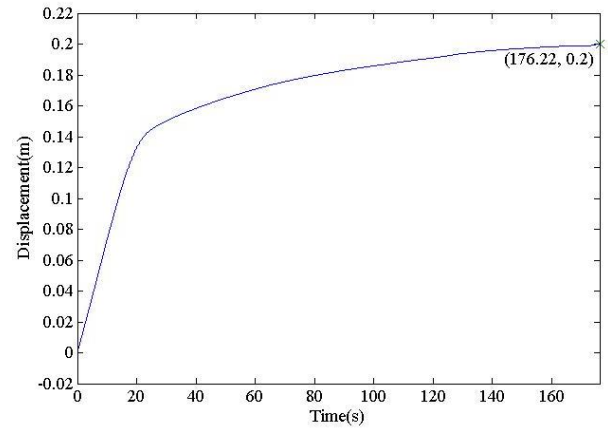
Figure 5.16 shows the time histories of higher voltages of AC supply at 70 V, 80 V and 90 V. Progression rate did not deteriorate drastically, compared to the voltages in Figure 5.15. Both progression rate and maximum displacement increase as AC supply increases.

Variation of direct current supply to linear actuator, while keeping other system parameter values constant sheds some light on the effect of static force.

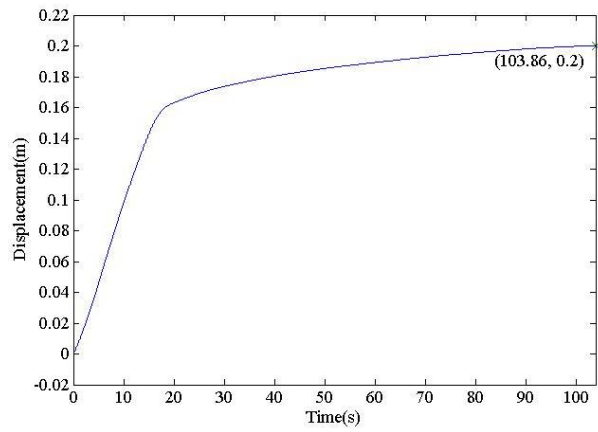
(a)



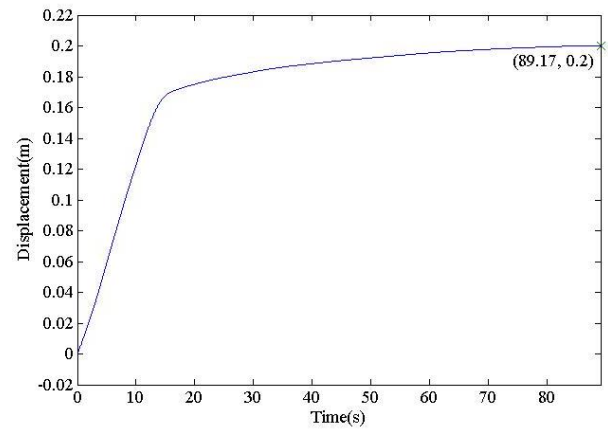
(b)



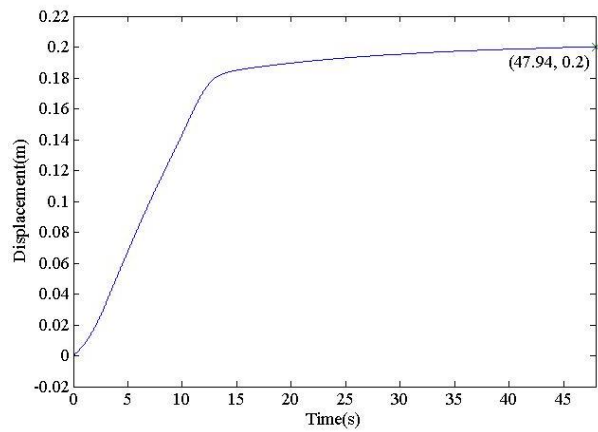
(c)



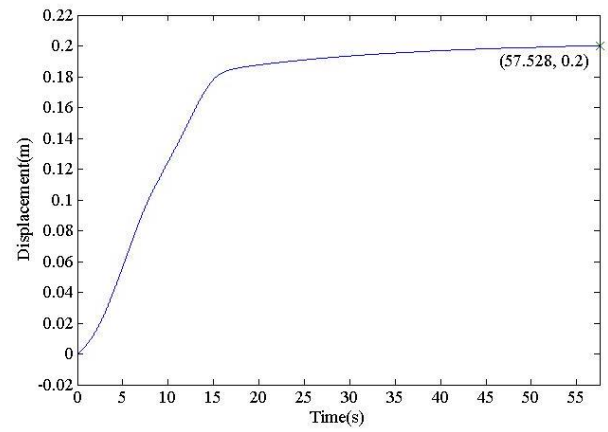
(d)



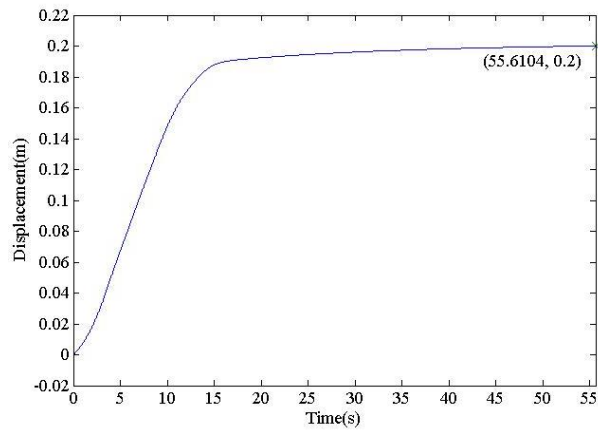
(e)



(f)



(g)



(h)

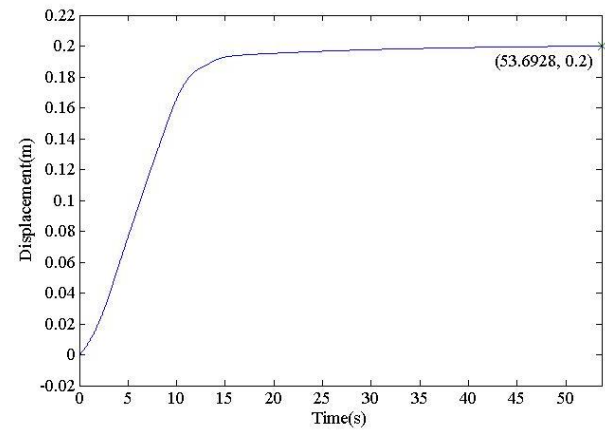


Figure 5.17: Time histories of rig progression into soil at (a) 6 V, (b) 8 V, (c) 10 V, (d) 12 V, (e) 14 V, (f) 16 V, (g) 18 V and (h) 20 V DC supplied to linear actuator, 50 V AC power supply and 6 Hz signal frequency.

The results in Figure 5.14 and 5.17 seem to indicate that the higher the voltage supplied to the linear actuator, the faster the progression rate. This relationship is summarised in Figure 5.18.

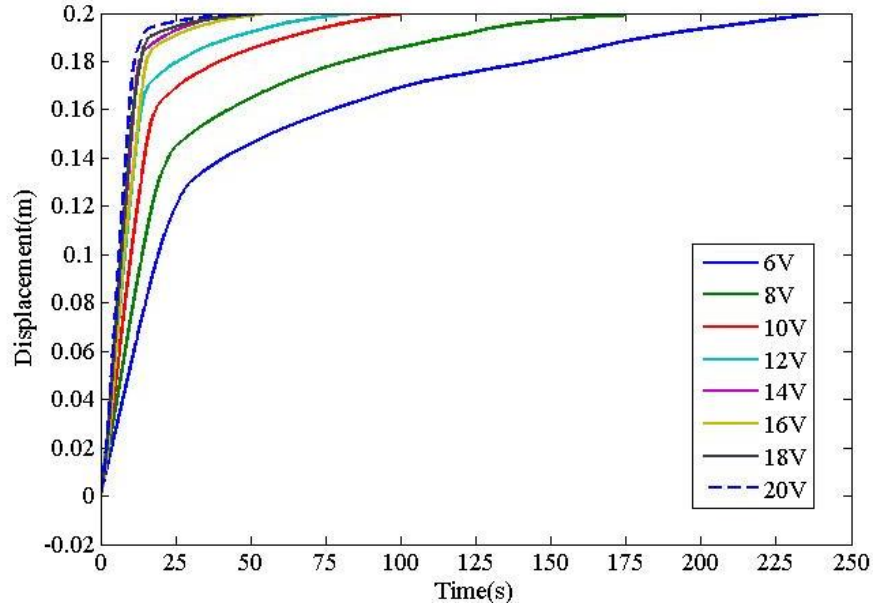


Figure 5.18: Combined time histories of rig progression into soil at various voltages supplied to linear actuator and at 50 V alternating supply to solenoid.

Especially at voltages ranging from 6 V to 14 V, progression rate experiences significant deterioration. At 6 V, for example, a considerable decrease in gradient occurs when soil penetration is of an order of 0.13 m. This trend is found in static force of 6 V to 14 V, where progression rate is lower for 16 V. Progression rate increases slightly as static force increases at 16 V and higher. As the static force increases, it is possible to sustain high progression rate until larger distances of soil progression before the progression reaches a flat line. In particular, at 8 V, the progression rate decreases sharply at 0.15 m. The coordinates of the final value of the graph is showed in a bracket, indicating the duration of the rig reaches exactly 0.2 m progression.

Table 5.2: Progression rate at different ratios of dynamic to static force at 50 V
alternating supply to solenoid.

DC Power Supply to Linear Actuator (V)	AC Power Supply to Solenoid (V)	Ratio of AC to DC supply (V/V)	Time taken to reach 0.2 m displacement (s)	Progression rate ($\times 10^{-3}$ m/s)
6	50	8.333	240.59	0.8313
8	50	6.250	176.22	1.1349
10	50	5.000	103.86	1.9257
12	50	4.167	89.170	2.2429
14	50	3.571	47.940	4.1719
16	50	3.125	57.528	3.4766
18	50	2.778	55.610	3.5964
20	50	2.500	53.693	3.7249

Additional series of experiments to vary direct current supply to linear actuator have been conducted for higher values of the alternating current supply, especially suitable for periodic impacts from 70 V to 90 V. The results are shown in Appendix D, the combined time histories are shown in Figure 5.19 and 5.20. Table 5.3 and 5.4 in the following page gives a flavour of these observations.

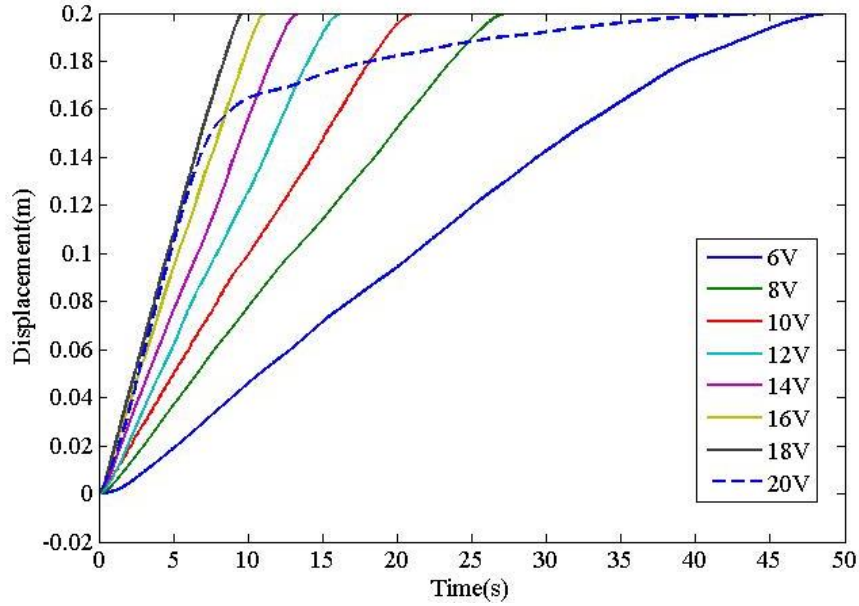


Figure 5.19: Combined time histories of rig progression into soil at various voltages supplied to linear actuator and at 50 V alternating supply to solenoid.

Table 5.3: Progression rate at different ratios of dynamic to static force at 70 V alternating supply to solenoid.

DC Power Supply to Linear Actuator (V)	AC Power Supply to Solenoid (V)	Ratio of AC to DC supply (V/V)	Time taken to reach 0.2 m displacement (s)	Progression rate ($\times 10^{-3}$ m/s)
6	70	11.667	49.31	4.0559
8	70	8.750	27.51	7.2701
10	70	7.000	21.21	9.4295
12	70	5.833	16.32	12.2549
14	70	5.000	13.53	14.7820
16	70	4.375	11.28	17.7305
18	70	3.889	9.76	20.4918
20	70	3.500	44.41	4.5035

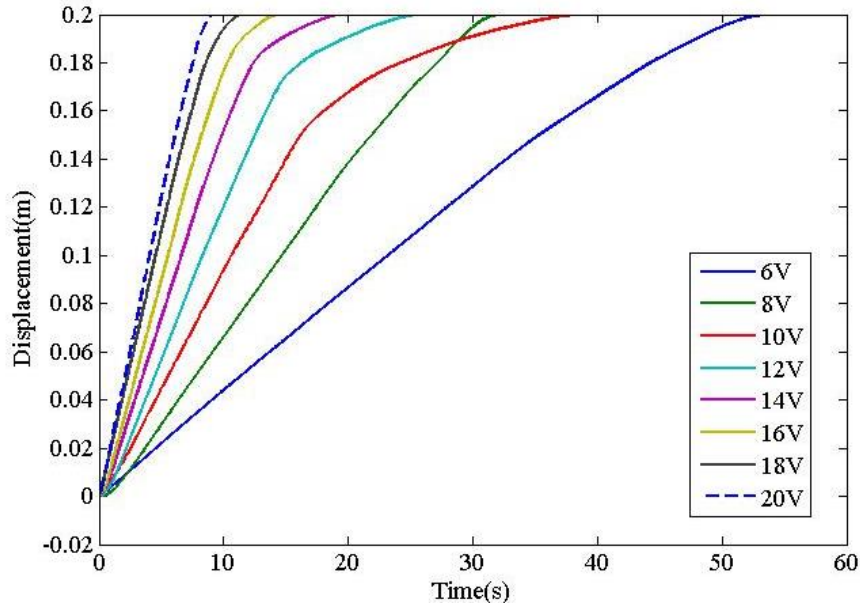


Figure 5.20: Combined time histories of rig progression into soil at various voltages supplied to linear actuator and at 50 V alternating supply to solenoid.

Table 5.4 Progression rate at different ratios of dynamic to static force at 90 V alternating supply to solenoid.

DC Power Supply to Linear Actuator (V)	AC Power Supply to Solenoid (V)	Ratio of AC to DC supply (V/V)	Time taken to reach 0.2 m displacement (s)	Progression rate ($\times 10^{-3}$ m/s)
6	90	15.000	54.06	3.6996
8	90	11.250	32.42	6.1690
10	90	9.000	40.62	4.9237
12	90	7.500	25.9	7.7220
14	90	6.429	19.65	10.1781
16	90	5.625	15.10	13.2450
18	90	5.000	11.46	17.4520
20	90	4.500	9.16	21.8341

The experimental results seem to suggest that the progression rate is increased when the ratio of AC to DC supply is lower. From Table 5.3, a notable deterioration of progression rate is found between 18 V to 20 V DC supply, dropping from 20.4918 mm/s to 4.5035 mm/s. At voltages lower than 18 V, the progression rate gradually increases with DC supply. This suggests that a ratio of 3.889, 70 V AC supply to 18 V DC supply could be an optimum.

To implement a more complete parametric study, the operating frequency of the solid state relay is varied. The tested frequencies include 4 Hz, 5 Hz, 6 Hz, 7 Hz and 8 Hz. The oscillations are not consistent at operating frequencies higher than 8 Hz, due to a difficulty in producing effective periodic impacts. This could be caused by turning the AC solenoid on and off in a short time period, where the oscillating bar is pulled back to the AC solenoid before it is recovered to a position at the DC solenoid for a complete stroke. In addition, signal frequencies lower than 4 Hz could not generate a complete stroke of the oscillating bar to create periodic impact. The signal frequency can be changed by adjusting the potentiometer connected to the solid state relay.

The AC and DC supply to the solenoids are set at 90 V and 24 V in a first instance, while 10 V supplied to linear actuator. The ratio of the chosen AC and DC supplies to solenoids ensures operation without overheating in short periods of time, AC voltages higher than 90 V usually causes overheating to occur even sooner.

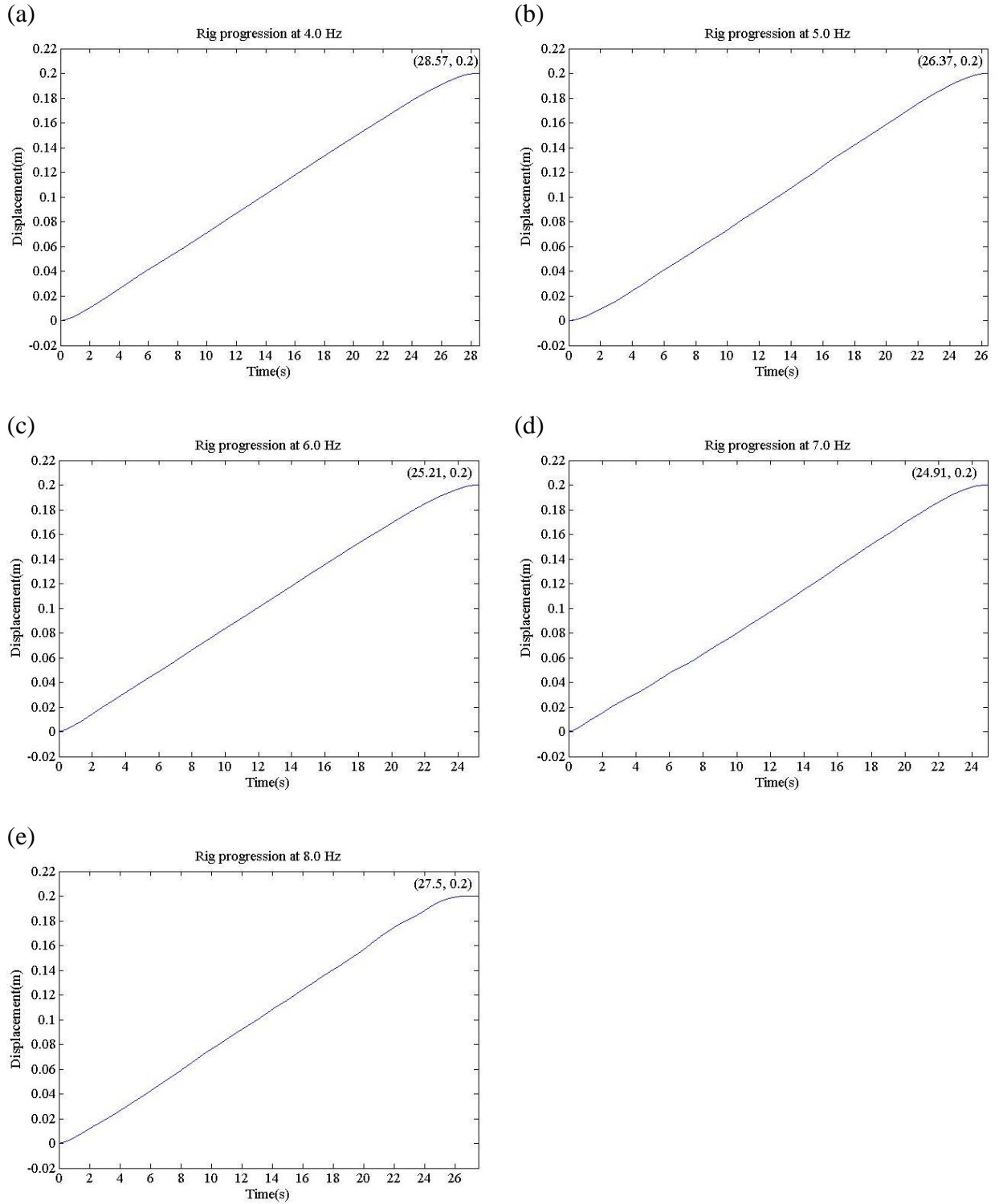


Figure 5.21: Time histories of rig progression into soil at (a) 4 Hz, (b) 5 Hz, (c) 6 Hz, (d) 7 Hz and (e) 8 Hz signal frequency, 90 V AC power to solenoid and 10 V DC supply to linear actuator.

Figure 5.21 lists results for frequencies ranging from 4 Hz to 8 Hz in steps of 1 Hz. A trend of increasing progression rate up to 7 Hz (from 0.0070 m/s to 0.00803 m/s), and decreases at 8 Hz (0.00727 m/s). In Appendix E, the experimental time histories of rig progression of same range at 0.2 Hz intervals are shown. This documents the effect of gradual increment in relay frequency.

From Table 5.5, progression rates peak between at 5.2 Hz to 6.2 Hz. For operating frequency higher than the suggested range, progression rate gradually decrease with increase of signal frequency, especially beyond 8.0 Hz. In excess of 8 Hz, instability of oscillations from periodic vibro-impact may have had a negative effect. An optimum operating frequency for this electro-vibroimpact system is approximately 6 Hz.

Table 5.5: Progression rate of vibro-impact machine at varying signal frequencies.

Operating frequency (Hz)	Time taken to achieve 0.2 m displacement (s)	Progression rate ($\times 10^{-3}$ m/s)
4.0	28.57	7.0003
4.2	28.44	7.0323
4.4	26.84	7.4517
4.6	27.26	7.3367
4.8	26.59	7.5216
5.0	26.37	7.5844
5.2	24.97	8.0096
5.4	24.90	8.0321
5.6	25.59	7.8155
5.8	25.75	7.7669
6.0	25.21	7.9334
6.2	25.39	7.8771
6.4	26.62	7.5131
6.6	26.38	7.5815
6.8	25.62	7.8064
7.0	24.91	8.0289
7.2	25.26	7.9178
7.4	26.11	7.6599
7.6	27.74	7.2098
7.8	27.64	7.2359
8.0	27.50	7.2727
8.2	28.85	6.9324
8.4	31.35	6.3796
8.6	37.86	5.2826
8.8	31.94	6.2617

The ability of the electro-vibro impact machine to progress into soil end to end of the soil box is tested. The soil box has a length of 1 m, which also shows that the maximum displacement. Since the maximum stroke of the linear variable displacement transducer is 0.2 m and the maximum extension length linear actuator could extend is 0.3 m, a following procedure is adopted for this test.

Progression for the first 0.15 m is observed for a stationary linear variable displacement transducer and linear actuator. On reaching 0.15 m, the position of the rig is maintained. The clamps of the LVDT and linear actuator are released, and the two instruments are brought forward so that the paused position is the new 'starting' point. They are then clamped to that position as operation resumes. The process of moving the LVDT and linear actuator forward is repeated for successive distances of 0.15 m, until the rig reaches its maximum displacement at the other end of the soil.

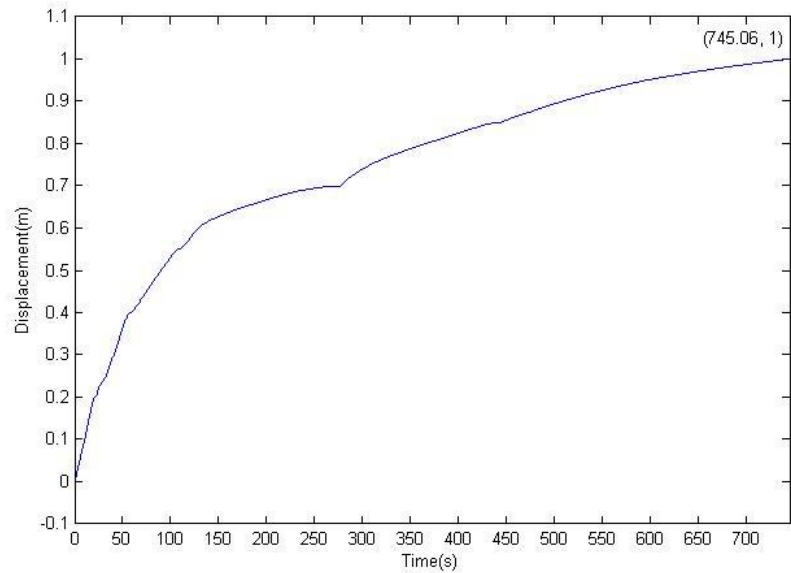


Figure 5.22: Time history of rig progression of vibro-impact machine into the soil box with continuous measurement at 6 Hz signal frequency, 90 V AC supply to the periodic impact and 10 V DC supply to the static force.

The total displacement achieved is 0.9 m for a total cumulative time of 745.9 s. It achieves an overall average progression rate of 0.001207 m/s (or 1.207 mm/s). It is observed that there is a considerable retardation of progression rate after 0.5 m of displacement. This is probably due to the soil too deep in the box, not able to exit the box as the rig displaces the soil volume, resulting in compaction of soil and increasing of soil resistance. The initial average gradient made is 0.004308 m/s (4.308 mm/s), and declines to an average gradient of 0.000649 m/s (0.649 mm/s). From a positive point of view, the electro vibro-impact system is able to progress into a useful depth of soil.

5.5 Conclusions

A prototype of the electro-vibroimpact system, able to progress into soil without exposing the core electrical components to soil medium was tested. A cylindrical case houses the solenoids and oscillating bar. Optimisation of the vibro-impact motion is achieved by addition of LM555 timer that switches DC supply off while AC supply is on, and vice versa. The timer also replaced a function generator in supplying square waves to a solid state relay. Static force is exerted using a linear actuator, improving the implementation of magnitude and direction. The electrical circuitry is housed within an acrylic box.

Forward progression of rig was measured by variation of signal frequency, AC supply and DC voltage supply to the linear actuator. Progression rate is affected by solid state relay frequency. Optimum rig progression is found in the range of 5.2 Hz to 6.2 Hz, resulting in highest progression rate due to maximised impact. Magnitude of AC supply increases progression rate of rig. A ratio of 3.889, for which the static force is approximately 25% of AC supply to the solenoid is optimal. The highest progression rate observed is 21.8341 mm/s, with 6 Hz solid state relay frequency, 90 V AC supply and 20 V to linear actuator.

CHAPTER 6

CONCLUSIONS

This thesis describes the modification and development of an optimised electro-vibroimpact system which is capable of penetrating horizontally into soil medium and brick material, and can also break stones. Design and manufacture of experimental rig, derivation of mathematical models and optimal operation of prototype rig have been integral parts of this work.

6.1 Optimised electro-vibroimpact system

Further to a mechanical spring and ferrous conductor actuated by a double solenoid arrangement has formed a core of robust and effective experimental rig. This electro-mechanical system is, at the same time, compact in geometry and has other advantages such as:

- It is possible to initiate or turn off of the system from a remote position.
- An experimentalist is able to vary system parameters from a remote position.
- A compact geometry, such that tunnels created in soil are of a size of fibre-optic cable or pipe.
- Vibro-impact oscillations are maintained by adjusting electromagnetic forces from solenoids.
- Effective forward progression rate, pertinent to engineering application.

Experimental development has undergone three stages. A one degree-of-freedom system focusing on vibro-impact oscillations of conductor bar is tested by fastening experimental rig to a rigid frame. A parametric study was then conducted, helping to gain insight to nonlinear dynamic responses of vibro-impact motion. Period-1 motion has been mostly observed, of which amplitude of waveform can be increased by amplifying AC supply voltage. An optimum operating frequency for most consistent oscillations and significant impact is 10 Hz. The required voltage supplies of direct current and alternating current are 24 V and 90 V respectively. Especially due to a high voltages of the latter, overheating is frequent, which affects inductance characteristics and the stability of electromagnetic flux and vibro-impact oscillations.

In a second stage, a two degree-of-freedom system is tested in a vertical orientation for penetration into soil. Its weight contributes to a static force from gravity, soil progression is achieved. Experimental downward progression of the rig into brittle material is also observed. With a sharpened bolt acting on the material surface, rig progression rate is low at 0.01 mm/s while cracks propagate within the material. At a critical crack length, brittle fracture occurs and sharpened bolt penetrates through the thickness of the material. The brick samples used are of 10 mm thickness. Time needs to be taken to initiate and propagate a crack until the material develops a sufficient stress concentration.

A third stage optimises a two degree-of-freedom system in a horizontal orientation. The electro-vibroimpact rig overcomes under soil resistive forces without assistance of gravity. The test rig is placed horizontally on a rigid frame located in front of the soil box.

Progression into soil with surcharge of 19 kg is most effective when there is periodic impact. Soil compaction decreases progression rate considerably deeper into the soil. At the other end of this soil box, an increased static force maintains forward drift. The length of tunnel contributes to a side resistance, which increases with time. Operating frequency of switching on and off a solenoid is instrumental to a higher progression rate. By adding suspended weights acting via a pulley on the system, static force is exerted in the same direction of the impact force, and this arrangement was later replaced by a linear actuator.

A prototype rig included the following features:

- An aluminium cylinder contains the solenoids and oscillating bar, allowing the rig to continue progressing and preventing the main components from being damaged by soil.
- Electronic components such as DC power supply and function generator have been substituted to a converter and timer circuit to improve setup time and mobility, as well as facilitate operation.
- The inclusion of a timer that switches one solenoid off while the other is on, and vice versa, improves the consistency of oscillation. This also increases the impact force as the AC solenoid does not need to overcome the restoring force applied by the DC solenoid in the opposite direction.
- Static force is applied using a linear actuator that extends at a constant speed. The static force could be varied by adjusting through the voltage supplied to the linear actuator.

- A launch frame ensures the vibroimpact machine is horizontally aligned to the axis of progressive motion. The rollers minimise surface friction between the prototype and launch frame.

6.2 Mathematical Model

A mathematical model of electro-vibroimpact system has been derived. A discontinuous function is used to model the nonlinearity due to impact, separating the dynamic response into two cases of impact and non-impact. The electromagnetic force of solenoids characterised empirically by experiment measurement. The governing frequency of the vibro-impact oscillations is based on the switching frequency of solid state relay. A mains supply frequency of 50 Hz is also described in the model, resulting peak in a peak frequency of 50 Hz observed in frequency domains of all experimental data. The discontinuity of a solid state relay switching signal is modelled as a piecewise function.

The one degree-of-freedom system model consists of an equation of motion for the oscillating bar, coupled with the electrical current equation of AC supply solenoid. The equations are solved by direct numerical integration using a Runge-Kutta method. Despite minor differences in waveform, there is correlation in frequency and qualitative system response for Period-1 vibro-impact oscillations. The two degree-of-freedom system in horizontal orientation is modelled with an additional equation of motion for the progression of rig into soil. A difference between experimental and numerical results is in waveform of conductor bar oscillations. However, frequency response matches. The rate of progression of experimental rig into soil showing an increasing displacement with

gradual decline of progression rate could be numerically predicted, despite quantitative differences. This perhaps can be addressed with a more advanced friction model of soil resistance.

6.3 Recommendations for future work

The maximum displacement of the rig into soil is limited by the stroke of the linear actuator that provides a static force. A technological implementation to address this could be a series connection of linear actuators, to increase a maximum stroke value.

Prolonged usage of solenoid results in overheating. Inductance characteristics of solenoid are altered which change electromagnetic force instrumental to actuation of vibro-impact system. Selection of an alternative solenoid geometry with a larger cross-sectional area of wire would permit a higher current flow and minimise generation of heat.

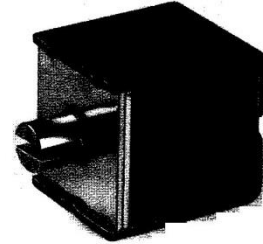
Improvement of mathematical model to numerically predict rig progression into soil is necessary. Soil resistive force increases with increasing progression due to soil compaction. The soil model suggested by Pavlovskaja [40] would be a good substitute. Insight perhaps, could be gained from a particle mechanics or finite element point of view.

APPENDIX A

DATASHEET OF RS 346-356 SOLENOID

Solenoids

**Series 43
high force/stroke ratio
solenoid**



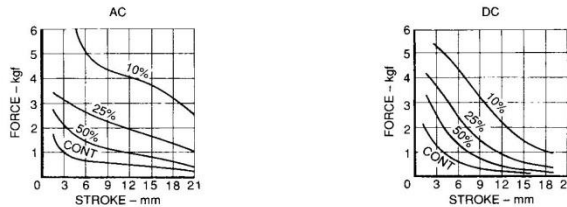
GENERAL DESCRIPTION

- AC & DC types
- Pull and thrust versions
- Shading ring for quiet AC operation
- Suitable for heavy duty applications

PERFORMANCE

	ITEM	SPECIFICATION
Electrical	Maximum on Time	See table below
	Closed power (continuous rating)	AC: 20VA DC: 12W.
	Maximum permissible voltage	240V
	Insulation	All coils tested to frame at 1500V RMS 50Hz.
Mechanical	Weight	Total: 425g. approx. Plunger: 49g
	Ambient temperature	The information given on this page is based on a room temperature of 20°C allowing for a nominal 75°C temperature rise in the coil.
	Force/stroke curves	These force curves show average performance only. In addition to normal manufacturing tolerances, deviations can be expected at some voltages due to the coil winding tolerances.

FORCE/STROKE CURVE



MAXIMUM ON TIME

	10%		25%		50%	
	1 cycle	Cont. cycling	1 cycle	Cont. cycling	1 cycle	Cont. cycling
AC	65 sec	5 sec	7.75 min	1.25 min	14.5 min	2 min
DC	55 sec	35 sec	3.5 min	2 min	7 min	4.25 min

APPENDIX B

MATLAB SCRIPT OF PLOTTING DATA FROM EXPERIMENTAL RESULTS

Table B.1 Matlab script that plot time history of 1 D.O.F experimental result for oscillating bar.

```
load h10;
x = h10(:,1);
y1 = 1.33*h10(:,3);

plot(x,y1,'k');
xlabel('Time (s)')
ylabel('Displacement (mm)')
title('Oscillation of 10 Hz')
```

Table B.2: Matlab script that plot time history of 1 D.O.F experimental result compared to numerical simulation from Dynamics.

```
load h10;
x1 = h10(:,1)-15.005;
y1 = (1.33*h10(:,3)-12.45)/1000;

load Dten.ttd;
x2 = Dten(:,1);
y2 = Dten(:,2);

plot(x1,y1,'r',x2,y2,'b:');
xlabel('Time (s)')
ylabel('Displacement (m)')
title('Oscillation of 10 Hz')
hleg1 = legend('Experimental','Numerical');
```

Table B.3: Matlab script that plot time history of 2 D.O.F experimental result for oscillating bar and rig progression.

```

st = 0.01; %sampling time
ar = 0.00075; %LVDT 1 conversion coefficient
br = 0.03; %LVDT 2 conversion coefficient

load f10.txt
x1a = ((f10(:,1))*ar)+0.00508;
x1b = -(f10(:,2))*br+0.0687;
t1 = [1:numel(x1a)]*st;

[AX,H1,H2]=plotyy(t1(6500:6700),x1a(6500:6700),t1(6500:6700),x1b(6500:6700),'plot')
set(get(AX(1),'Ylabel'),'String','Conductor oscillation (m)')
set(get(AX(2),'Ylabel'),'String','Rig progression (m)')
set(H1,'LineStyle','--')
set(H2,'LineStyle','-')
xlabel('Time(s)');

```

Table B.4: Matlab script of fast fourier transform analysis on experimental data to obtain the frequency domain plot.

```

clc;
clear;
load N4.txt;
xn = N4(:,1);
yn = N4(:,2);

dt = 0.001;
t = [xn(1):dt:xn(end)];

for u = 1:length(t)
    i = find(xn==t(u));
    if numel(i)>0
        p(u) = yn(i);
    else
        n1 = find(xn<t(u));
        na = n1(end);
        n2 = find(xn>t(u));
        nb = n2(1);
        p(u) = (yn(nb)-yn(na))/(xn(nb)-xn(na))*(t(u)-xn(na))+yn(na);
    end
end
end

```

```
T = dt; %Sampling time
fs = 1/T; %Sampling frequency
x = p; %displacement data
L = length(x); %length of data
n = 2^(nextpow2(L)); %next power of 2
y = fft(x,n)/L;
Y = 2*abs(y(1:n/2+1));
f = fs/2*linspace(0,1,n/2+1);
semilogy(f',Y,'k');
xlim([0 55]);
xlabel('Frequency (Hz)');
ylabel('log decibel');
title('FFT of Experimental Data: 4 Hz');
```

APPENDIX C

MATLAB AND DYNAMICS SCRIPT OF NUMERICAL SOLUTION OF THE VIBRO- IMPACT SYSTEM

Table C.1: Matlab script describing the mathematical model of a vibro-impact system in 1 D.O.F experiment.

```
clc;
clear;

% Parameter Definition
global m w c1 k1 cF1 e t0 x0 k tf h g R C f xF1 xF2;

t0 = 0;
tf = 3;
x0 = [0;0;0.1]; %Initial conditions
h = 0.001; %Time step
k = 5;

m = 0.155; %Conductor mass
w = 2*pi*50; %Main supply frequency
c1 = 10; %Stopper damping
k1 = 100000; %Stopper stiffness
g = 9.81; %Gravity
e = 0; %Clearance
R = 25; %Resistance
C = 0.00028; %Capacitor
f = 10; %SSLR frequency

% Graph specifications
hold on
xlabel('Time(s)');
ylabel('Displacement(m)');
zlabel('Velocity(m/s)');
grid on
disp('    Time(s) Displacement(m) Velocity(m/s)')
P = [t0,x0(1),x0(2)];

while t0<tf-h

fname = 'analysisA';
```

```

options = odeset('RelTol',1e-9,'AbsTol',[1e-9 1e-4 1e-4 1e-4]);
[T,X] = ode15s(fname,[t0 tf],[x0(1) x0(2) x0(3) x0(4)],options);
X1 = X(:,1); X2 = X(:,2); X3 = X(:,3); X4 = X(:,4);
[F1] = DC(X1);
[F2] = AC(X1,X3);

%Root Finding=====
indX = find(X1<e);
if numel(indX)<=1
    plot3(T,X1,X2,'b');
    np = numel(X1);
    P(end+1:end+np-1,:) = [T(2:end),X1(2:end),X2(2:end)];
else
    if indX(1)==1;
        na = indX(2)-1;
        nb = indX(2);
    else
        na = indX(1)-1;
        nb = indX(1);
    end
    a = T(na);
    b = T(nb);
    t0 = a;
    x0 = [X1(na);X2(na);X3(na);X4(na)];
    delta = 1E-6;
    plot3(T(1:na),X1(1:na),X2(1:na),'b');
    P(end+1:end+na-1,:) = [T(2:na),X1(2:na),X2(2:na)];
    if abs(X1(nb))<delta
        root = b;
    else
        root = rB(fname,delta,a,b,delta);
    end
    [T,X] = ode15s(fname,[t0 root],[x0(1) x0(2) x0(3) x0(4)],options);
    X1 = X(:,1); X2 = X(:,2); X3 = X(:,3); X4 = X(:,4);
    [F1] = DC(X1);
    [F2] = AC(X1,X3);
    plot3(T,X1,X2,'k');
    np = numel(X1);
    P(end+1:end+np-1,:) = [T(2:end),X1(2:end),X2(2:end)];
    scatter3(T(end),X1(end),X2(end),'k');
    str = sprintf('Root: [%7.6g, %7.6g, %7.6g]',T(end),X1(end),X2(end));
    disp(str)
end
t0 = T(end);
x0 = [X1(end);X2(end);X3(end);X4(end)];
%=====

fname = 'analysisC';

```

```

[T,X] = ode15s(fname,[t0 tf],[x0(1) x0(2) x0(3) x0(4)],options);
X1 = X(:,1); X2 = X(:,2); X3 = X(:,3); X4 = X(:,4);
[F1] = DC(X1);
[F2] = AC(X1,X3);

%Root Finding=====
indX = find(X1>e);
if numel(indX)<=1
    plot3(T,X1,X2,'r');
    np = numel(X1);
    P(end+1:end+np-1,:) = [T(2:end),X1(2:end),X2(2:end)];
else
    if indX(1)==1;
        na = indX(2)-1;
        nb = indX(2);
    else
        na = indX(1)-1;
        nb = indX(1);
    end
    a = T(na);
    b = T(nb);
    t0 = a;
    x0 = [X1(na);X2(na);X3(na);X4(na)];
    delta = 1E-6;
    plot3(T(1:na),X1(1:na),X2(1:na),'r');
    P(end+1:end+na-1,:) = [T(2:na),X1(2:na),X2(2:na)];
    if abs(X1(nb))<delta
        root = b;
    else
        root = rB(fname,delta,a,b,delta);
    end
    [T,X] = ode15s(fname,[t0 root],[x0(1) x0(2) x0(3) x0(4)],options);
    X1 = X(:,1); X2 = X(:,2); X3 = X(:,3); X4 = X(:,4);
    [F1] = DC(X1);
    [F2] = AC(X1,X3);
    plot3(T,X1,X2,'k');
    np = numel(X1);
    P(end+1:end+np-1,:) = [T(2:end),X1(2:end),X2(2:end)];
    scatter3(T(end),X1(end),X2(end),'k');
    str = sprintf('Root: [%7.6g, %7.6g, %7.6g]',T(end),X1(end),X2(end));
    disp(str)
end
t0 = T(end);
x0 = [X1(end);X2(end);X3(end);X4(end)];
%Root Finding=====
end

```

Table C.2: Sub-program representing the free region of 1 D.O.F oscillation mathematical model.

```

%Free region of the conductor bar

function [dx] = analysisA(t,x)

global m w g F2 cF1 R V C;

[SSLR] = Sw(t);
[L,dL,ddL] = Inductance(x(1));
F1 = DC(x(1));
F2 = AC(x(1),x(3));

dx = zeros(4,1);
dx(1) = x(2);
dx(2) = 1/m*(F1-(m*g)-F2);
dx(3) = x(4);
dx(4) = 1/L*(w*SSLR*V*cos(w*t)-(R+2*dL.*x(2))*x(4)-(1/C+ddL.*x(2).^2+dL*dx(2))*x(3));

```

Table C.3: Sub-program representing the impact region of 1 D.O.F oscillation mathematical model.

```

%Impact region of the conductor bar

function [dx] = analysisC(t,x)

global m w g F2 cF1 R V C c1 k1;

[SSLR] = Sw(t);
[L,dL,ddL] = Inductance(x(1));
F1 = DC(x(1));
F2 = AC(x(1),x(3));

dx = zeros(4,1);
dx(1) = x(2);
dx(2) = 1/m*(F1- (m*g)-F2-c1*x(2)-k1*x(1));
dx(3) = x(4);
dx(4) = 1/L*(w*SSLR*V*cos(w*t)-(R+2*dL.*x(2))*x(4)-(1/C+ddL.*x(2).^2+dL*dx(2))*x(3));

```

Table C.4: Matlab script describing the mathematical model of a vibro-impact system in 2 D.O.F horizontal orientation experiment.

```

clc;
clear;

% Parameter Definition
global m w c1 k1 cF1 e t0 x0 k tf h g R C f xF1 xF2;

t0 = 0;
tf = 3;
x0 = [0;0;0.1;0]; %Initial conditions
h = 0.001; %Time step
%k = 5;

m1 = 0.155; %Conductor mass
m2 = 2.643; %Rig mass
w = 2*pi*50; %Main supply frequency
c1 = 10; %Stopper damping
k1 = 100000; %Stopper stiffness
g = 9.81; %Gravity
e = 0; %Clearance
R = 25; %Resistance
C = 0.00028; %Capacitor
f = 10; %SSLR frequency
Fs = 135; %Soil friction
Ff = 31.1; %Static Force

hold on
xlabel('Time(s)');
ylabel('Displacement(m)');
zlabel('Displacement(m)');
grid on
disp('    Time(s) Displacement(m) Rig Progression(m/s)')
P = [t0,x0(1),x0(2),x0(3)];

while t0<tf-h

fname = 'analysisA';
options = odeset('RelTol',1e-9,'AbsTol',[1e-9 1e-4 1e-4 1e-4 1e-4 1e-4]);
[T,X] = ode15s(fname,[t0 tf],[x0(1) x0(2) x0(3) x0(4) x0(5) x0(6)],options);
X1 = X(:,1); X2 = X(:,2); X3 = X(:,3); X4 = X(:,4); X5 = X(:,5); X6 = X(:,6);
[F1] = DC(X1);
[F2] = AC(X1,X5);

%Root Finding=====
indX = find(X1<e);

```

```

if numel(indX)<=1
    plot3(T,X1,X3,'b');
    np = numel(X1);
    P(end+1:end+np-1,:) = [T(2:end),X1(2:end),X3(2:end)];
else
    if indX(1)==1;
        na = indX(2)-1;
        nb = indX(2);
    else
        na = indX(1)-1;
        nb = indX(1);
    end
    end
    a = T(na);
    b = T(nb);
    t0 = a;
    x0 = [X1(na);X2(na);X3(na);X4(na); X5(na);X6(na)];
    delta = 1E-6;
    plot3(T(1:na),X1(1:na),X3(1:na),'b');
    P(end+1:end+na-1,:) = [T(2:na),X1(2:na),X3(2:na)];
    if abs(X1(nb))<delta
        root = b;
    else
        root = rB(fname,delta,a,b,delta);
    end
    [T,X] = ode15s(fname,[t0 root],[x0(1) x0(2) x0(3) x0(4) x0(5) x0(6)],options);
    X1 = X(:,1); X2 = X(:,2);X3 = X(:,3); X4 = X(:,4); X5 = X(:,5); X6 = X(:,6);
    [F1] = DC(X1);
    [F2] = AC(X1,X5);
    plot3(T,X1,X3,'k');
    np = numel(X1);
    P(end+1:end+np-1,:) = [T(2:end),X1(2:end),X3(2:end)];
    scatter3(T(end),X1(end),X3(end),'k');
    str = sprintf('Root: [%7.6g, %7.6g, %7.6g]',T(end),X1(end),X3(end));
    disp(str)
end
t0 = T(end);
x0 = [X1(end);X2(end);X3(end);X4(end);X5(end);X6(end)];
%=====

fname = 'analysisC';
[T,X] = ode15s(fname,[t0 tf],[x0(1) x0(2) x0(3) x0(4) x0(5) x0(6)],options);
X1 = X(:,1); X2 = X(:,2);X3 = X(:,3); X4 = X(:,4); X5 = X(:,5); X6 = X(:,6);
[F1] = DC(X1);
[F2] = AC(X1,X5);

%Root Finding=====
indX = find(X1>e);
if numel(indX)<=1

```

```

plot3(T,X1,X3,'r');
np = numel(X1);
P(end+1:end+np-1,:) = [T(2:end),X1(2:end),X3(2:end)];
else
if indX(1)==1;
na = indX(2)-1;
nb = indX(2);
else
na = indX(1)-1;
nb = indX(1);
end
a = T(na);
b = T(nb);
t0 = a;
x0 = [X1(na);X2(na);X3(na);X4(na);X5(na);X6(na)];
delta = 1E-6;
plot3(T(1:na),X1(1:na),X2(1:na),'r');
P(end+1:end+na-1,:) = [T(2:na),X1(2:na),X3(2:na)];
if abs(X1(nb))<delta
root = b;
else
root = rB(fname,delta,a,b,delta);
end
[T,X] = ode15s(fname,[t0 root],[x0(1) x0(2) x0(3) x0(4) x0(5) x0(6)],options);
X1 = X(:,1); X2 = X(:,2); X3 = X(:,3); X4 = X(:,4); X5 = X(:,5); X6 = X(:,6);
[F1] = DC(X1);
[F2] = AC(X1,X5);
plot3(T,X1,X3,'k');
np = numel(X1);
P(end+1:end+np-1,:) = [T(2:end),X1(2:end),X3(2:end)];
scatter3(T(end),X1(end),X3(end),'k');
str = sprintf('Root: [%7.6g, %7.6g, %7.6g]',T(end),X1(end),X3(end));
disp(str)
end
t0 = T(end);
x0 = [X1(end);X2(end);X3(end);X4(end);X5(end);X6(end)];
%Root Finding=====
end

```

Table C.5: Sub-program representing the free region of 2 D.O.F oscillation mathematical model.

```

%Free region of the conductor bar

function [dx] = analysisA(t,x)

global m w g F2 cF1 R V C Fs;

[SSLR] = Sw(t);
[L,dL,ddL] = Inductance(x(1));
F1 = DC(x(1));
F2 = AC(x(1),x(5));

dx = zeros(6,1);
dx(1) = x(2);
dx(2) = 1/m1*(F1-F2);
dx(3) = x(4);
dx(4) = 1/m2*(-F1+F2-Fs*x(4)+Ff);
dx(5) = x(6);
dx(6) = 1/L*(w*SSLR*V*cos(w*t)-(R+2*dL.*x(2))*x(6)-(1/C+ddL.*x(2).^2+dL*dx(2))*x(5));

```

Table C.6: Sub-program representing the Impact region of 2 D.O.F oscillation mathematical model.

```

%Impact region of the conductor bar

function [dx] = analysisC(t,x)

global m w g F2 cF1 R V C c1 k1 Fs;

[SSLR] = Sw(t);
[L,dL,ddL] = Inductance(x(1));
F1 = DC(x(1));
F2 = AC(x(1),x(5));

dx = zeros(6,1);
dx(1) = x(2);
dx(2) = 1/m1*(F1-F2) -c1*x(2)-k1*x(1);
dx(3) = x(4);
dx(4) = 1/m2*(-F1+F2+c1*x(2)+k1*x(1)-Fs*x(4)+Ff);
dx(5) = x(6);
dx(6) = 1/L*(w*SSLR*V*cos(w*t)-(R+2*dL.*x(2))*x(6)-(1/C+ddL.*x(2).^2+dL*dx(2))*x(5));

```

Table C.7: Sub-program that determines the function and input parameters of 4th order Runge-Kutta method.

```

function [tvals,yvals] = FixedRK(fname,tf,h)
% [tvals,yvals] = FixedRK(fname,t0,y0,h,k,n)
% Produces approximate solution to the initial value problem
%
%    $y'(t) = f(t,y(t))$     $y(t_0) = y_0$ 
%
% using a strategy that is based upon a k-th order
% Runge-Kutta method. Step size is fixed.
%
% fname = string that names the function f.
% t0 = initial time.
% y0 = initial condition vector.
% h = step size.
% k = order of method. (1<=k<=5).
% n = number of steps to be taken,
%
% tvals is a column vector with tvals(j) = t0 + (j-1)h, j=1:n+1
% yvals is a matrix with yvals(j,:) = approximate solution at tvals(j), j=1:n+1

% This function comes from 'Introduction to Scientific Computing' by
% Charles F. Van Loan, Prentice-Hall, Upper Saddle River, NJ, p. 341.

global m F w c1 k1 k2 e t0 x0 k;

tc = t0;
yc = x0;
tvals = tc;
yvals = yc';
fc = feval(fname,tc,yc);
n = (tf-t0)/h;
for j=1:n
    [tc,yc,fc] = RKstep(fname,tc,yc,fc,h,k);
    yvals = [yvals; yc'];
    tvals = [tvals; tc];
end

```

Table C.8: Sub-program of 4th order Runge-Kutta operating algorithms.

```

function [tnew,ynew,fnew] = RKstep(fname,tc,yc,fc,h,k)
% [tnew,ynew,fnew] = RKStep(fname,tc,yc,fc,h,k)
% Single step of the kth order Runge-Kutta method.
%
% fname is a string that names a function of the form f(t,y)
% where t is a scalar and y is a column d-vector.
%
% yc is an approximate solution to  $y'(t) = f(t,y(t))$  at t=tc.

```

```

%
% fc = f(tc,yc).
%
% h is the time step.
%
% k is the order of the Runge-Kutta method used, 1<=k<=5.
%
% tnew=tc+h, ynew is an approximate solution at t=tnew, and
% fnew = f(tnew,ynew).

% This function comes from 'Introduction to Scientific Computing' by
% Charles F. Van Loan, Prentice-Hall, Upper Saddle River, NJ, p. 340.

if k==1
    k1 = h*fc;
    ynew = yc + k1;
elseif k==2
    k1 = h*fc;
    k2 = h*feval(fname,tc+h,yc+k1);
    ynew = yc + (k1 + k2)/2;
elseif k==3
    k1 = h*fc;
    k2 = h*feval(fname,tc+(h/2),yc+(k1/2));
    k3 = h*feval(fname,tc+h,yc-k1+2*k2);
    ynew = yc + (k1 + 4*k2 + k3)/6;
elseif k==4
    k1 = h*fc;
    k2 = h*feval(fname,tc+(h/2),yc+(k1/2));
    k3 = h*feval(fname,tc+(h/2),yc+(k2/2));
    k4 = h*feval(fname,tc+h,yc+k3);
    ynew = yc + (k1 + 2*k2 + 2*k3 + k4)/6;
elseif k==5
    k1 = h*fc;
    k2 = h*feval(fname,tc+(h/4),yc+(k1/4));
    k3 = h*feval(fname,tc+(3*h/8),yc+(3/32)*k1+(9/32)*k2);
    k4 = h*feval(fname,tc+(12/13)*h,yc+(1932/2197)*k1-(7200/2197)*k2+(7296/2197)*k3);
    k5 = h*feval(fname,tc+h,yc+(439/216)*k1 - 8*k2 + (3680/513)*k3 -(845/4104)*k4);
    k6 = h*feval(fname,tc+(1/2)*h,yc-(8/27)*k1 + 2*k2 -(3544/2565)*k3 + (1859/4104)*k4 -
(11/40)*k5);
    ynew = yc + (16/135)*k1 + (6656/12825)*k3 + (28561/56430)*k4 - (9/50)*k5 + (2/55)*k6;
end
tnew = tc+h;
fnew = feval(fname,tnew,ynew);

```

Table C.9: Sub-program of DC solenoid electromagnetic force as a function of bar position.

```

function [F1] = DC(x)
global m g;
xa = -(0.0625-x);
F1 = -1.473E5*xa.^3+1.652E-14*xa.^2-15.38*xa+m*g;

```

Table C.10: Sub-program script of AC solenoid electromagnetic force as a function of bar position and current within the solenoid.

```

function [F2] = AC(X1,X3)
[L,dL,ddL] = Inductance(X1);
F2 = 0.5.*dL.*(X3.^2);

```

Table C.11: Sub-program to calculate the inductance, first derivative and second derivatives of inductance values.

```

function [L,dL,ddL] = Inductance(x)
xb = x+0.0455;

L0 = 0.48;
A = 0.048;
B = 0.039;

L = L0+A/(B*sqrt(pi/2))*exp(-2*(xb/B).^2);
dL = -4*A*xb/(B^3*sqrt(pi/2)).*exp(-2*(xb/B).^2);
ddL = -4*A*(1-(2*xb/B).^2)/(B^3*sqrt(pi/2)).*exp(-2*(xb/B).^2);

```

Table C.12: Sub-program of SSRL in the function of time.

```

function [SSLR] = Sw(T)
global f
if T == 0
    ts = 1;
else
    ts = ceil((T)*2*f);
end
SSLR = mod(ts,2);
end

```

Table C.13: Sub-program of root finding algorithm to determine the point of time where region switches from free to impact.

```

function root = rB (fname,h,a,b,delta)

global m F w c1 k1 e t0 x0 k tf g;

[t1,x1] = FixedRK(fname,b,h);
x11 = x1(:,1);
fa = x11(1,1)-e;
%fb = x1(end,1)-e;
if fa<0 %When lower bound is negative
    indR = find(x11>e);
else
    indR = find(x11<e);
end
fb = x11(indR(1));

if fa*fb > 0
root = disp('Initial interval is not bracketing.')
    return
end
if nargin==3
    delta = 0;
end

while b-a>delta
    mid=(a+b)/2;
    [t,x] = FixedRK(fname,mid,h);
    fmid= x(end,1);
    if fa*fmid<=0
        b=mid;
        fb=fmid;
    else
        a=mid;
        fa=fmid;
    end
end
root=(a+b)/2;

```

Table C.14: Dynamics script that describes the mathematical model of 2 D.O.F vibro-impact machine.

```

OWN /* process defined below; 1 for map and 0 for Dif.Eqn.: */
0
"2DOF Vibro-Impact Mole Simulation with SSR Forcing
u:Relative Displ of metal bar
v:Rel Vel of metal bar
w:Displ of the mole
x:Vel of the mole
y:Current
z:First D of Current
"
"m1:=0.155
m2:=2.643
Lo:=0.48
A:= 0.048
B:= 0.039
L:= Lo + (A/(B*sqrt(pi/2)))*exp(-2*((s)/B)^2)
Ld:= -4*A*(s)/(B^3*sqrt(pi/2))* exp(-2*((s)/B)^2)
Ldd:=-4*A/(B^3*sqrt(pi/2))* exp(-2*((s)/B)^2)*(1-4*(s)^2/B^2)
P0:= if (v>0) then (1) else (if v<0 then (-1) else 0)
P1:= if ((s-C4)>0) then (C6*(s-C4)+C2*(u-x)) else (0)
P2:= if (x>0) then (1) else (if x<0 then (-1) else 0)
P3:= if (mod(t,2*pi/phi)<(pi/phi)) then (1) else (0) !!!Phi is the control Freq in Hz
Fm:=0.5*Ld*(y)^2
Fspr:= -1.4735*(s)^3 + 1.652e-14*(s)^2 - 15.38*(s)
s':=x-v
t':=1
u':=v
vd:=( Fm-P1-Fspr)/m1
v':=vd
w':=x
x':=( Fm+P1+Fspr-P2*C7+C5)/m2
y':=z
z':=(P3*1.4142*C10*C9*cos(C10*t)-(C8+2*Ld*v)*z-(1/C3+Ldd*(v)^2+Ld*vd)*y)/L"
"s:=0 t:= 0 u:=-0.022 v:=0 w:=0 x:=0 y:=0 z:=0
C1:=0 !spring stiffness
C2:=500 !damping
C3:=0.0003 !capacitance
phi:=2*pi*8 !control frequency
C4:=0 !clearance
C5:=31.1 !static force
C6:=1e6 !impact stiffness
C7:=1000 !soil friction
C8:=300 !resistance
C9:=50 !voltage supply
C10:=2*pi*50 !mains frequency
X_upper :=5 X_lower :=4 Y_upper :=0.1 Y_lower :=-0.1
XCO:=1 YCO:=0
SPC:=500

```

IPP:=1

APPENDIX D

TIME HISTORY OF VARYING DC POWER

SUPPLY TO LINEAR ACTUATOR

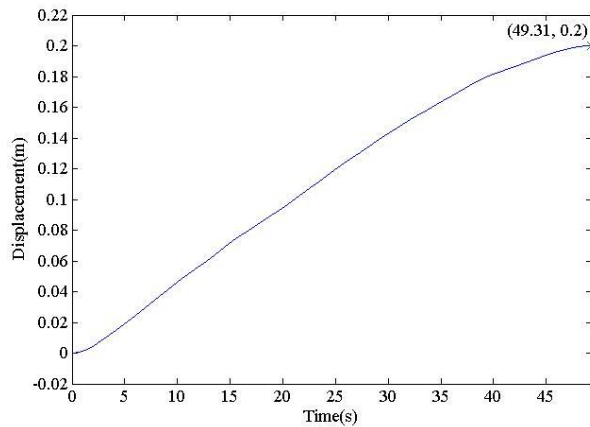


Figure D.1: Time history at 6 V DC power supply to linear actuator, 6 Hz of signal frequency and 70 V AC power to solenoid.

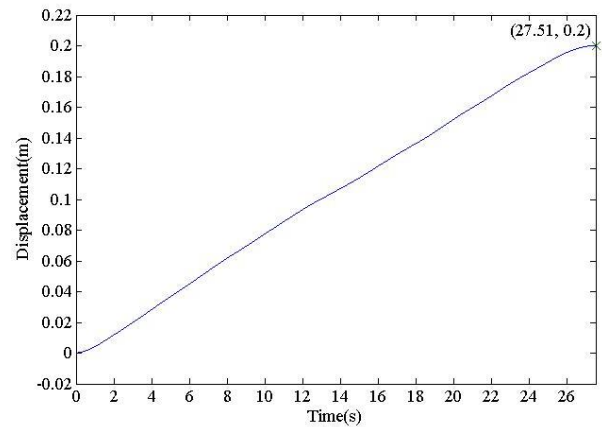


Figure D.2: Time history at 8 V DC power supply to linear actuator, 6 Hz of signal frequency and 70 V AC power to solenoid.

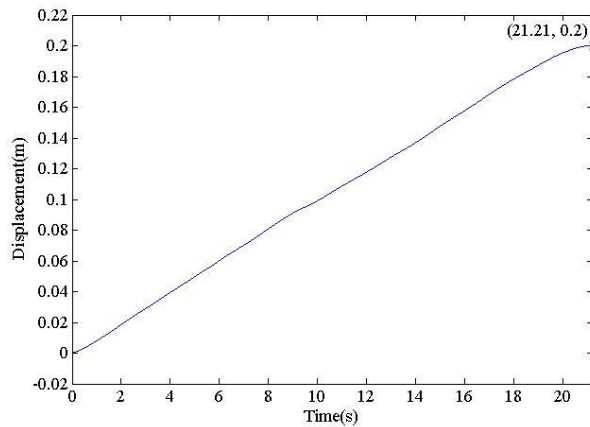


Figure D.3: Time history at 10 V DC power supply to linear actuator, 6 Hz of signal frequency and 70 V AC power to solenoid.

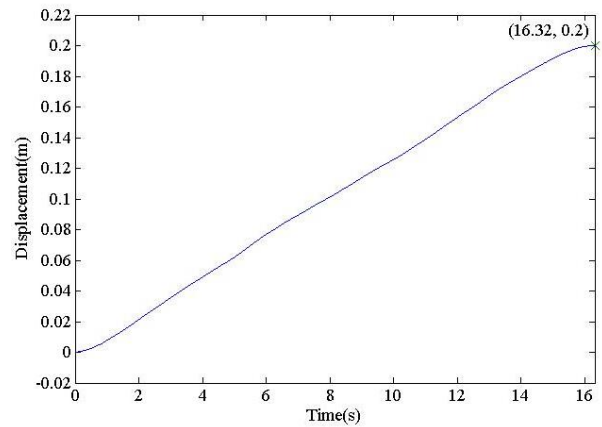


Figure D.4: Time history at 12 V DC power supply to linear actuator, 6 Hz of signal frequency and 70 V AC power to solenoid.

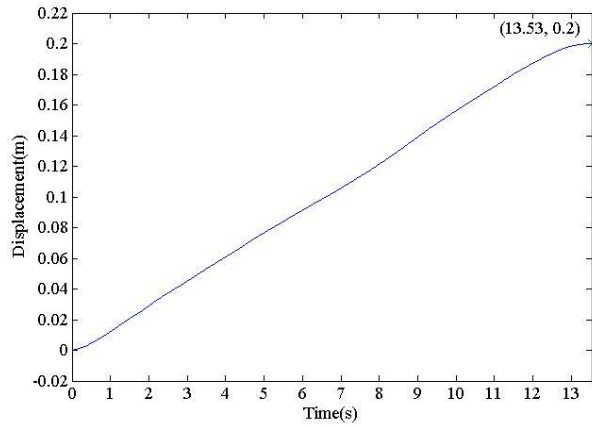


Figure D.5: Time history at 14 V DC power supply to linear actuator, 6 Hz of signal frequency and 70 V AC power to solenoid.

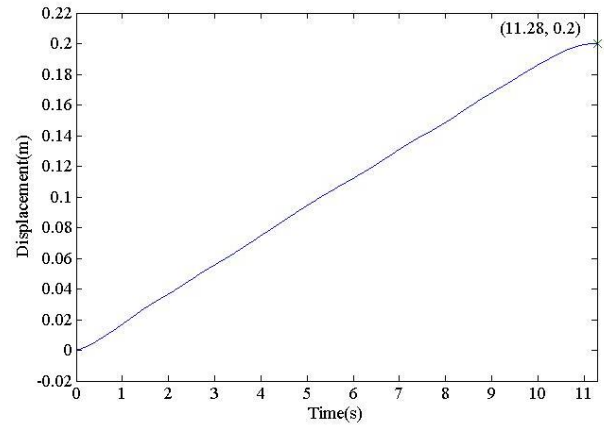


Figure D.6: Time history at 16 V DC power supply to linear actuator, 6 Hz of signal frequency and 70 V AC power to solenoid.

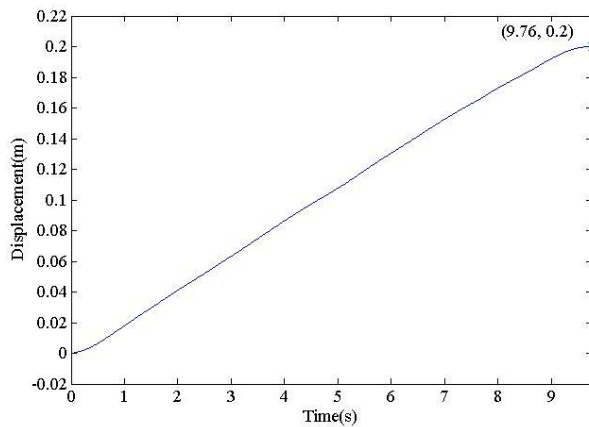


Figure D.7: Time history at 18 V DC power supply to linear actuator, 6 Hz of signal frequency and 70 V AC power to solenoid.

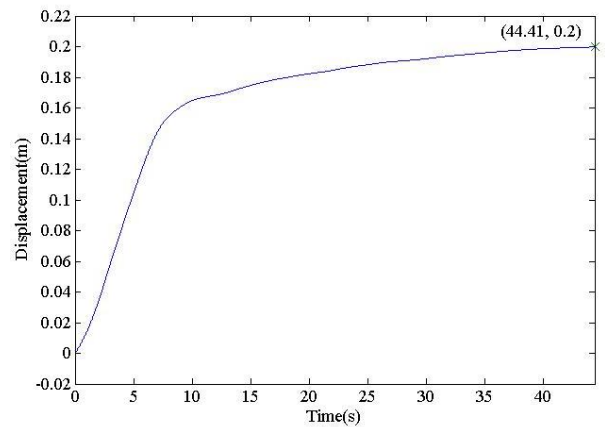


Figure D.8: Time history at 20 V DC power supply to linear actuator, 6 Hz of signal frequency and 70 V AC power to solenoid.

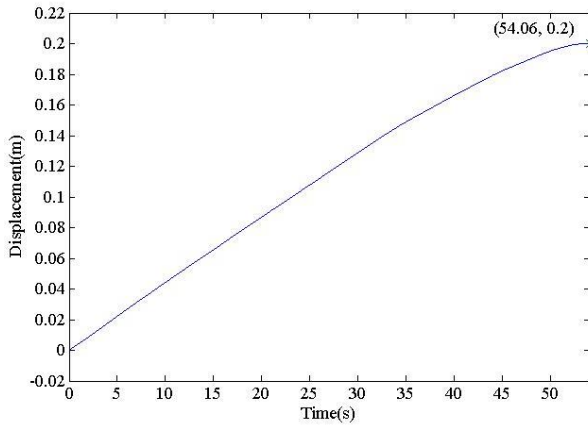


Figure D.9: Time history at 6 V DC power supply to linear actuator, 6 Hz of signal frequency and 90 V AC power to solenoid.

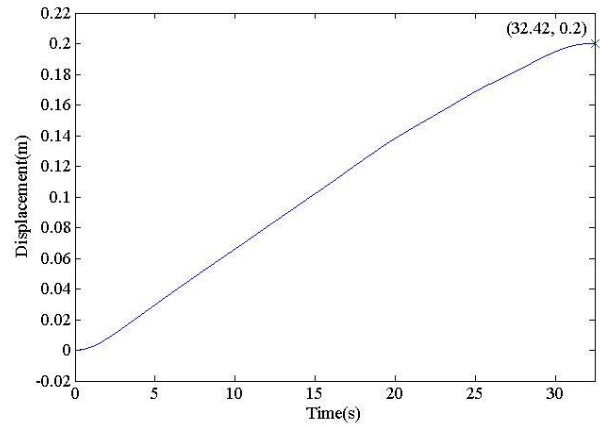


Figure D.10: Time history at 8 V DC power supply to linear actuator, 6 Hz of signal frequency and 90 V AC power to solenoid.

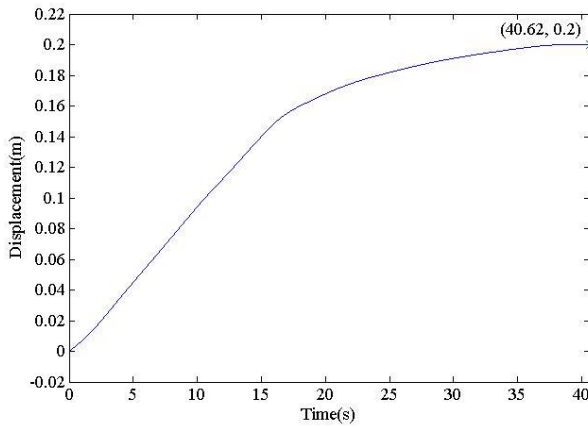


Figure D.11: Time history at 10 V DC power supply to linear actuator, 6 Hz of signal frequency and 90 V AC power to solenoid.

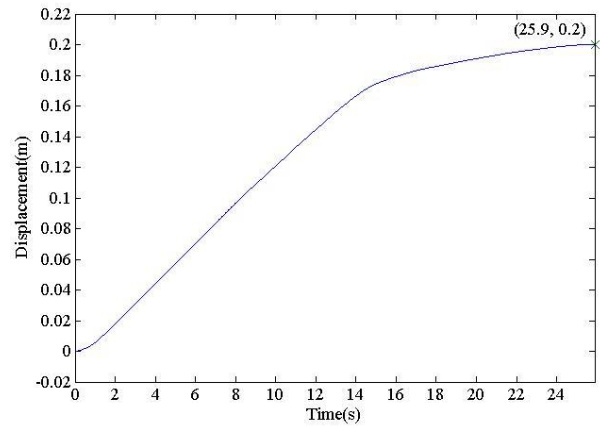


Figure D.12: Time history at 12 V DC power supply to linear actuator, 6 Hz of signal frequency and 90 V AC power to solenoid.

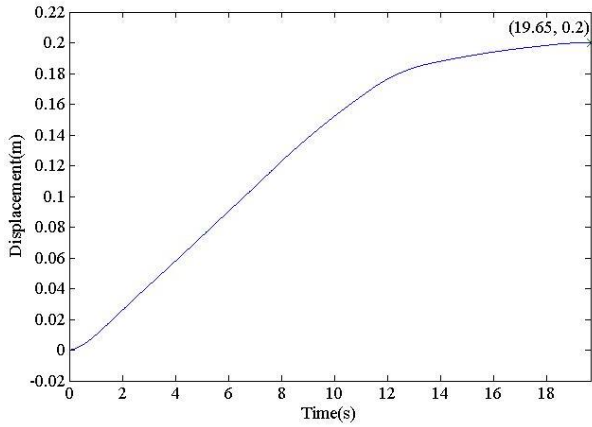


Figure D.13: Time history at 14 V DC power supply to linear actuator, 6 Hz of signal frequency and 90 V AC power to solenoid.

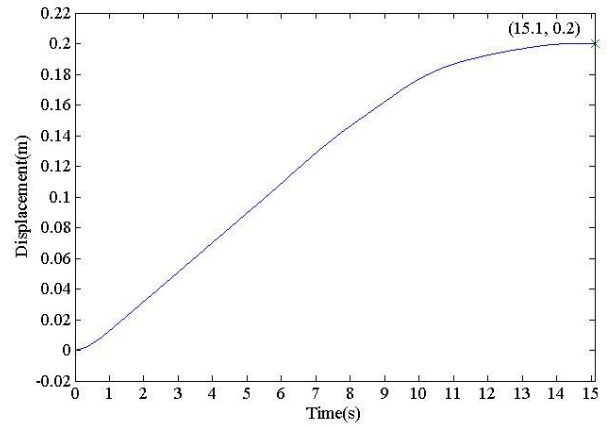


Figure D.14: Time history at 16 V DC power supply to linear actuator, 6 Hz of signal frequency and 90 V AC power to solenoid.

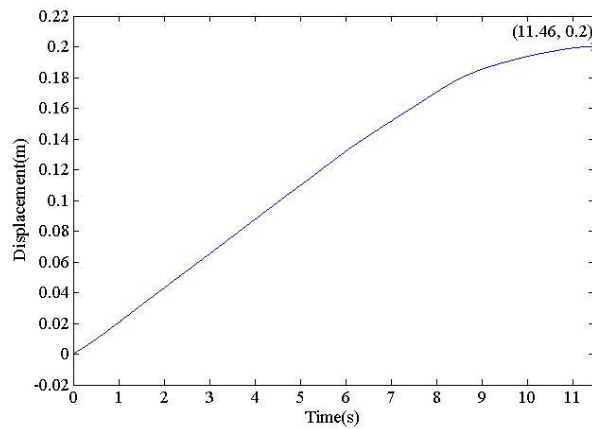


Figure D.15: Time history at 18 V DC power supply to linear actuator, 6 Hz of signal frequency and 90 V AC power to solenoid.

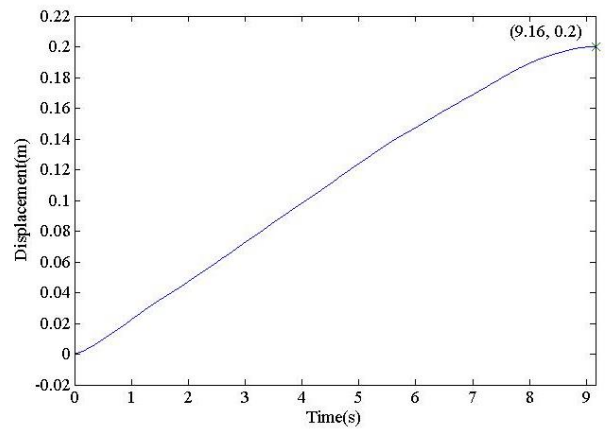


Figure D.16: Time history at 20 V DC power supply to linear actuator, 6 Hz of signal frequency and 90 V AC power to solenoid.

APPENDIX E

TIME HISTORY OF VARYING SSRL SIGNAL

FREQUENCY

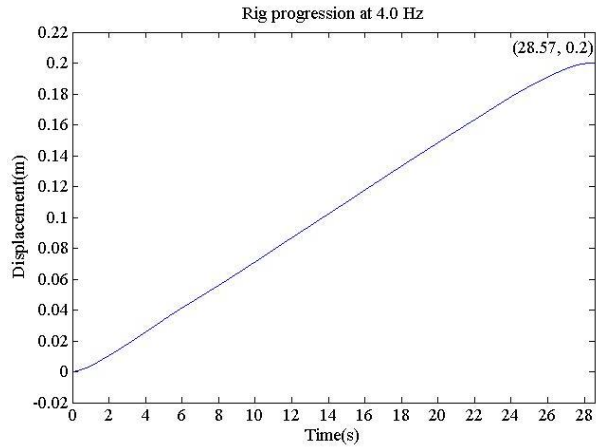


Figure E.1: Rig displacement for control signal frequency of 4.0 Hz.

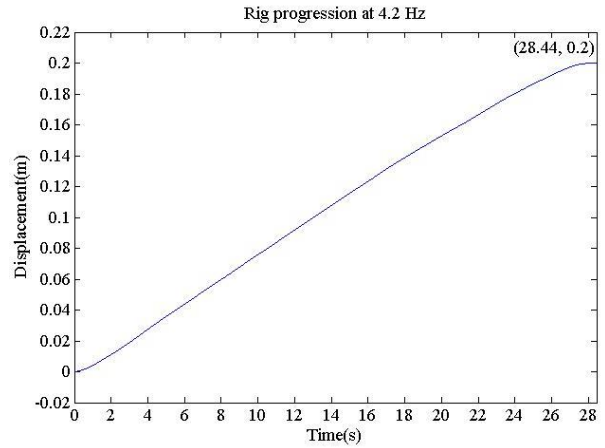


Figure E.2: Rig displacement for control signal frequency of 4.2 Hz.

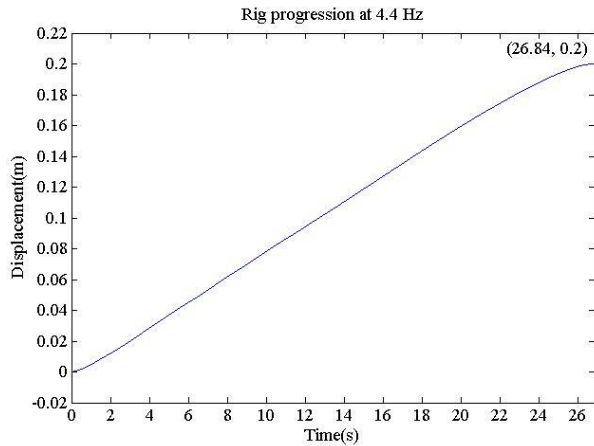


Figure E.3: Rig displacement for control signal frequency of 4.4 Hz.

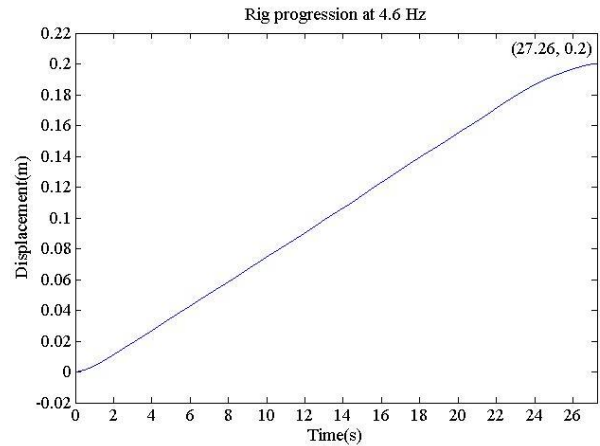


Figure E.4: Rig displacement for control signal frequency of 4.6 Hz.

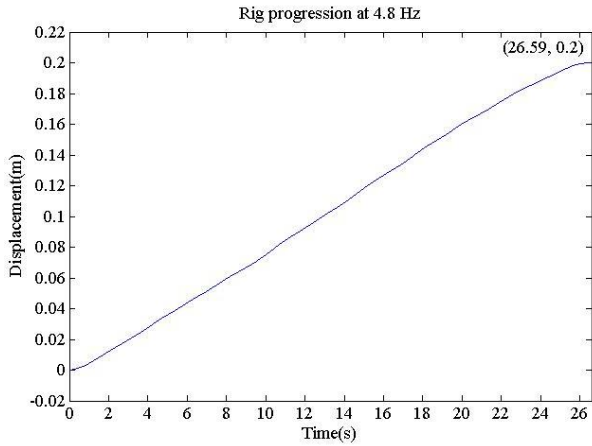


Figure E.5: Rig displacement for control signal frequency of 4.8 Hz.

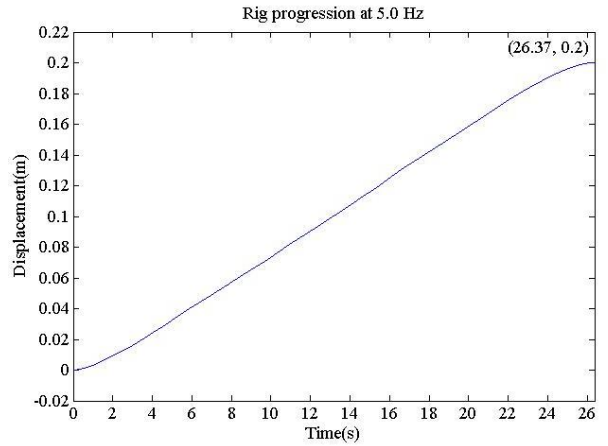


Figure E.6: Rig displacement for control signal frequency of 5.0 Hz.

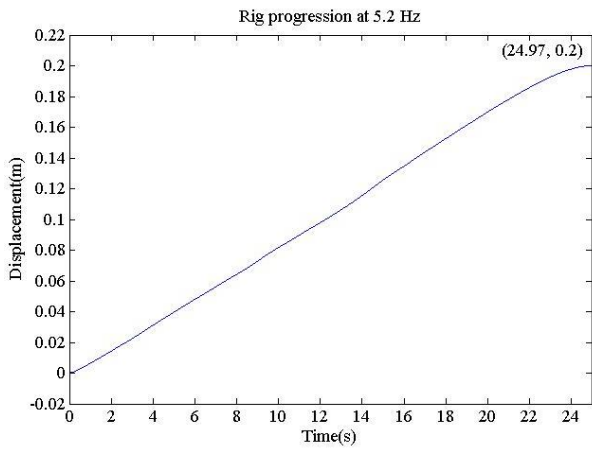


Figure E.7: Rig displacement for control signal frequency of 5.2 Hz.

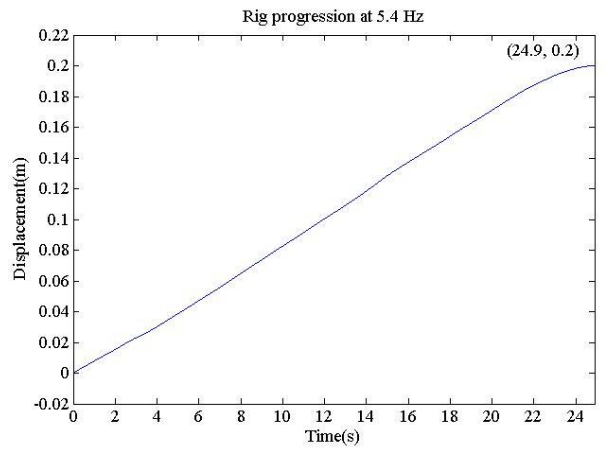


Figure E.8: Rig displacement for control signal frequency of 5.4 Hz.

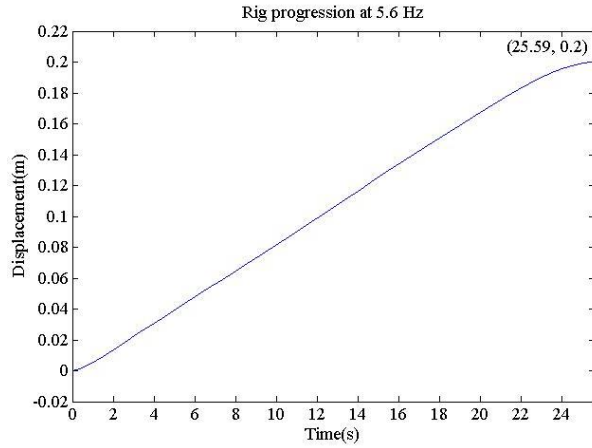


Figure E.9: Rig displacement for control signal frequency of 5.6 Hz.

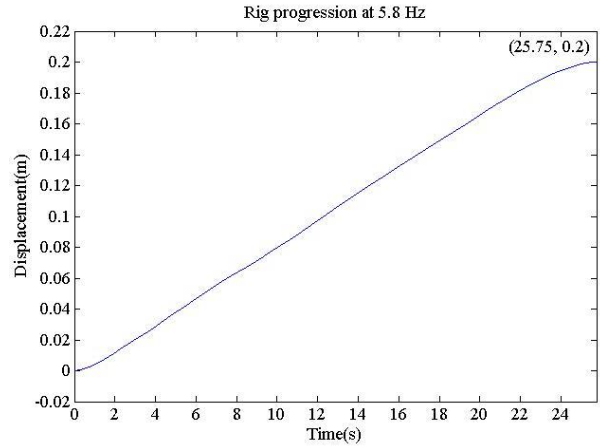


Figure E.10: Rig displacement for control signal frequency of 5.8 Hz.

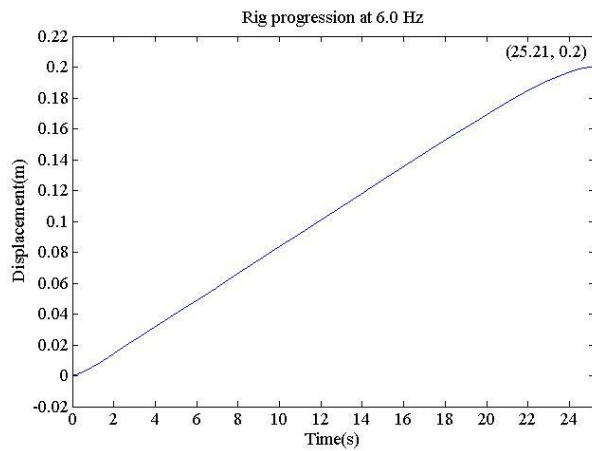


Figure E.11: Rig displacement for control signal frequency of 6.0 Hz.

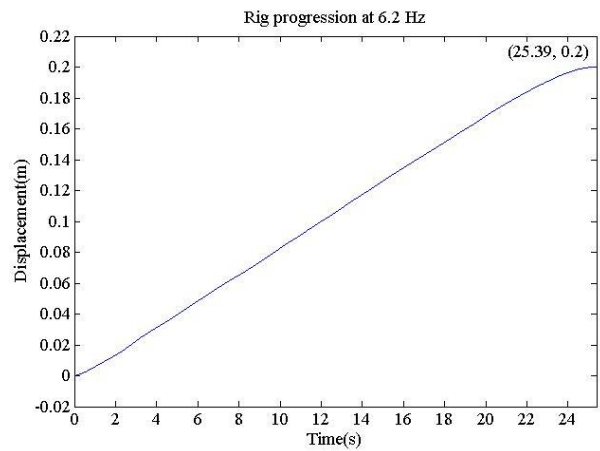


Figure E.12: Rig displacement for control signal frequency of 6.2 Hz.

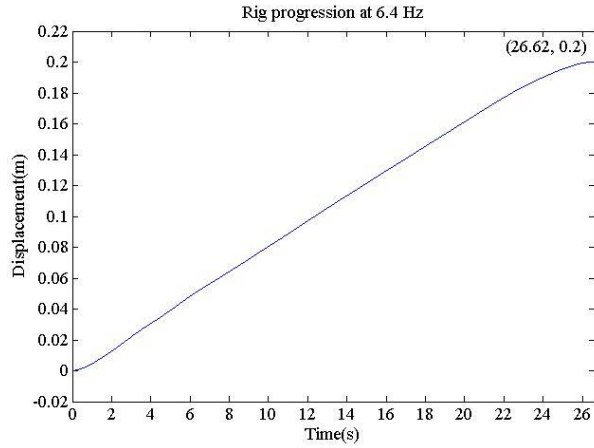


Figure E.13: Rig displacement for control signal
frequency of 6.4 Hz.

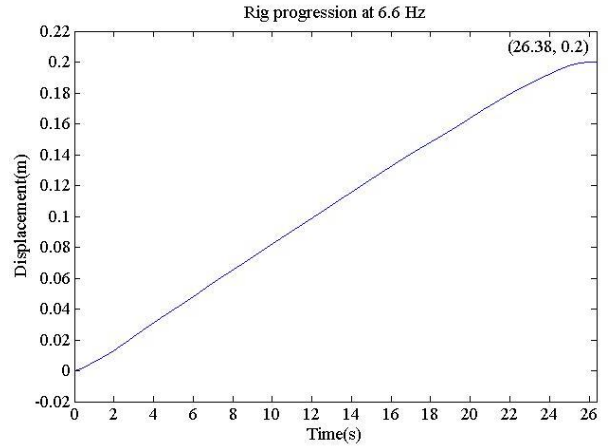


Figure E.14: Rig displacement for control signal
frequency of 6.6 Hz.

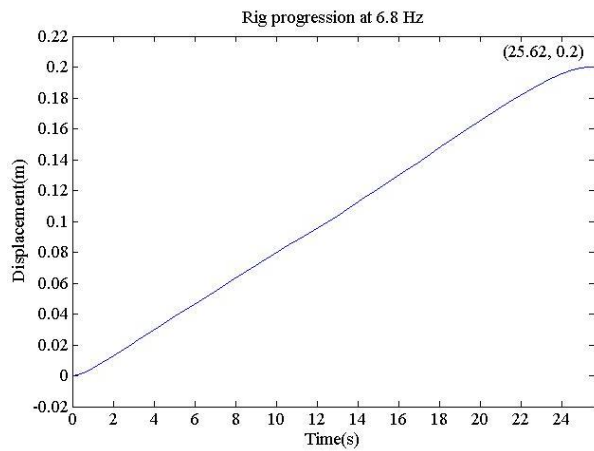


Figure E.15: Rig displacement for control signal
frequency of 6.8 Hz.

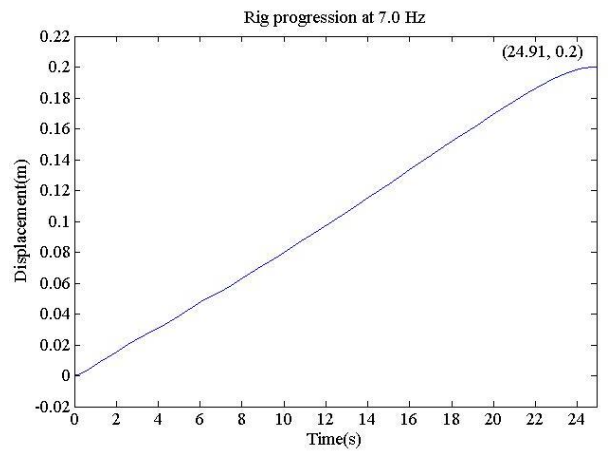


Figure E.16: Rig displacement for control signal
frequency of 7.0 Hz.

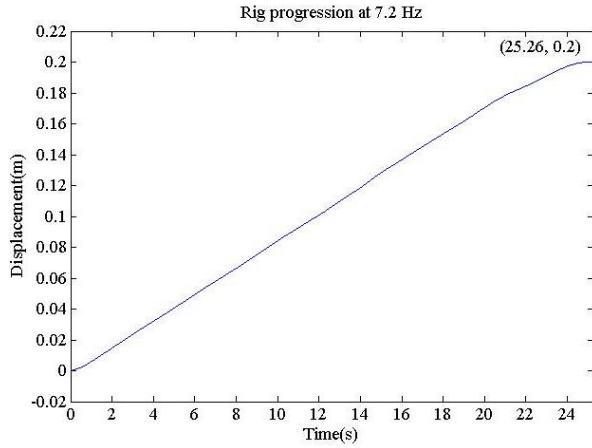


Figure E.17: Rig displacement for control signal
frequency of 7.2 Hz.

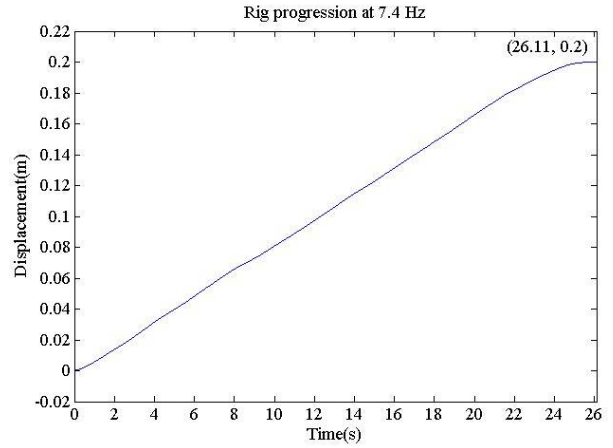


Figure E.18: Rig displacement for control signal
frequency of 7.4 Hz.

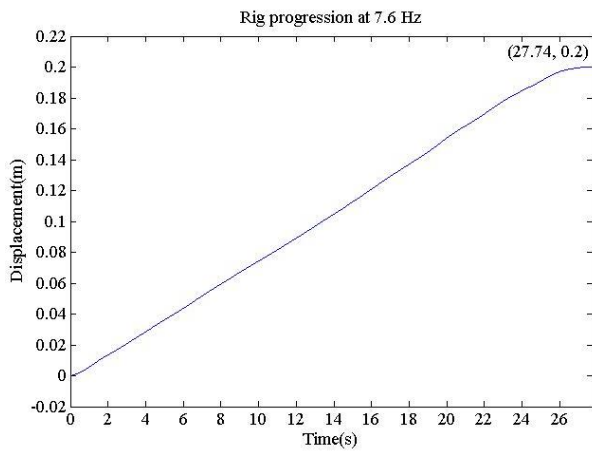


Figure E.19: Rig displacement for control signal
frequency of 7.6 Hz.

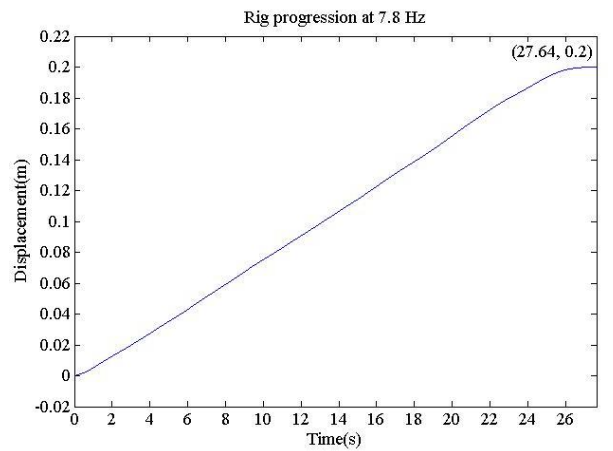


Figure E.20: Rig displacement for control signal
frequency of 7.8 Hz.

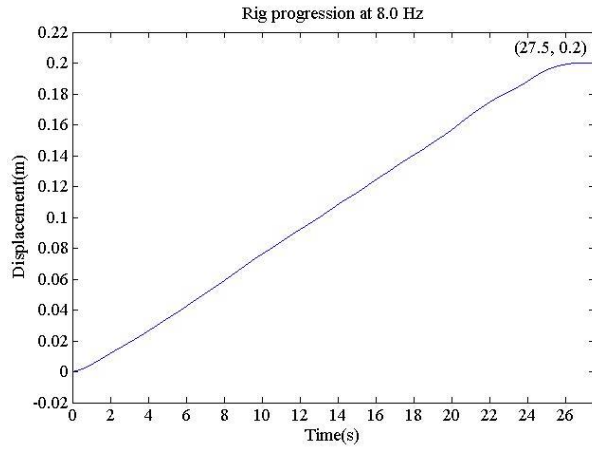


Figure E.21: Rig displacement for control signal frequency of 8.0 Hz.

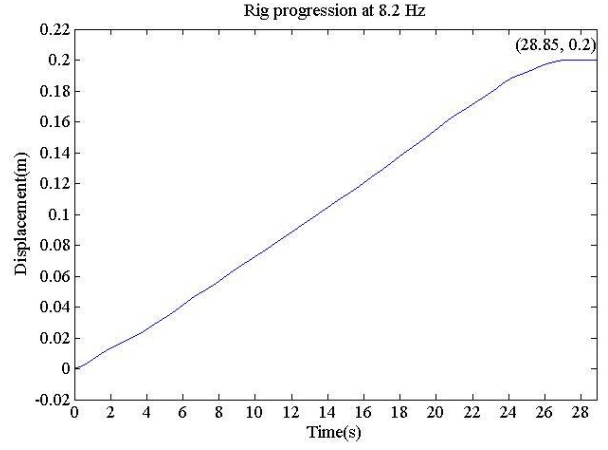


Figure E.22: Rig displacement for control signal frequency of 8.2 Hz.

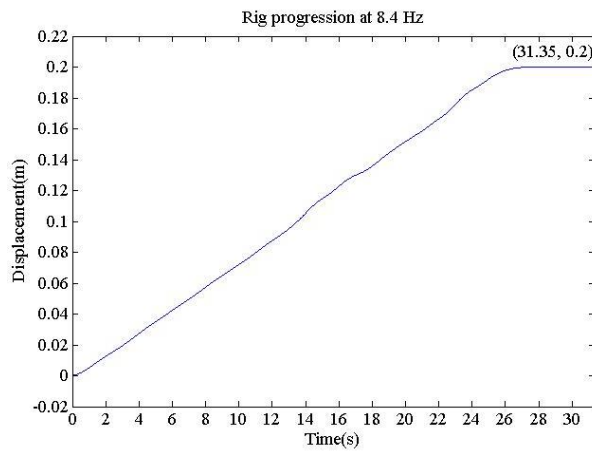


Figure E.23: Rig displacement for control signal frequency of 8.4 Hz.

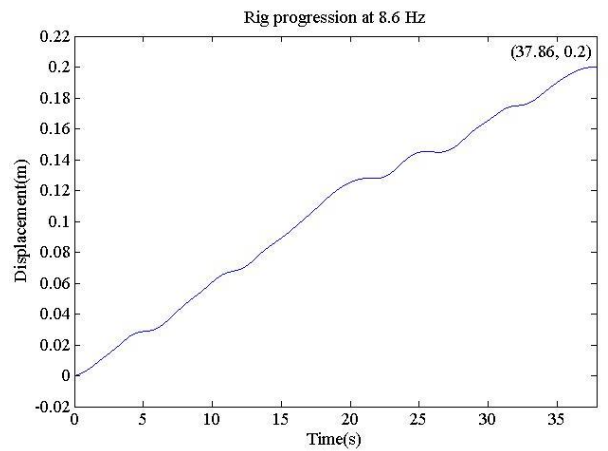


Figure E.24: Rig displacement for control signal frequency of 8.6 Hz.

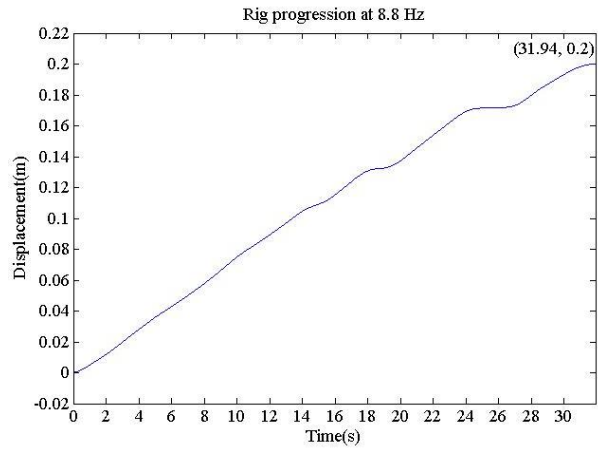


Figure E.25: Rig displacement for control signal
frequency of 8.8 Hz.

APPENDIX F

ENGINEERING DRAWING OF PROTOTYPE

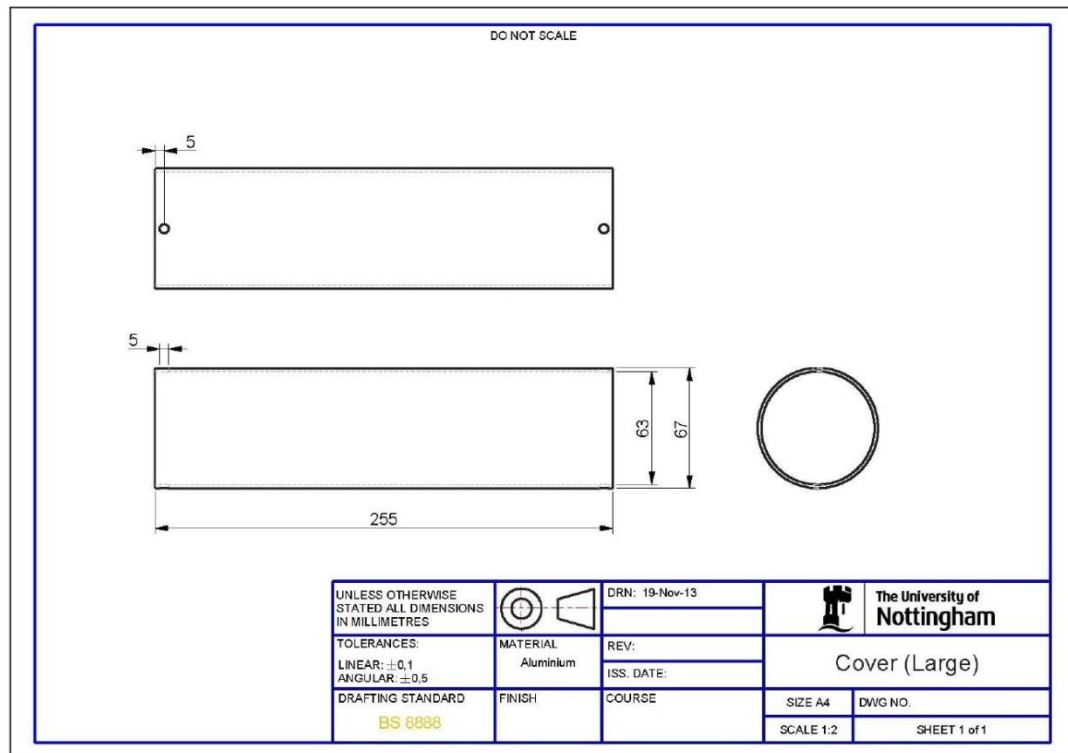


Table F.1: Housing cover detailed drawing.

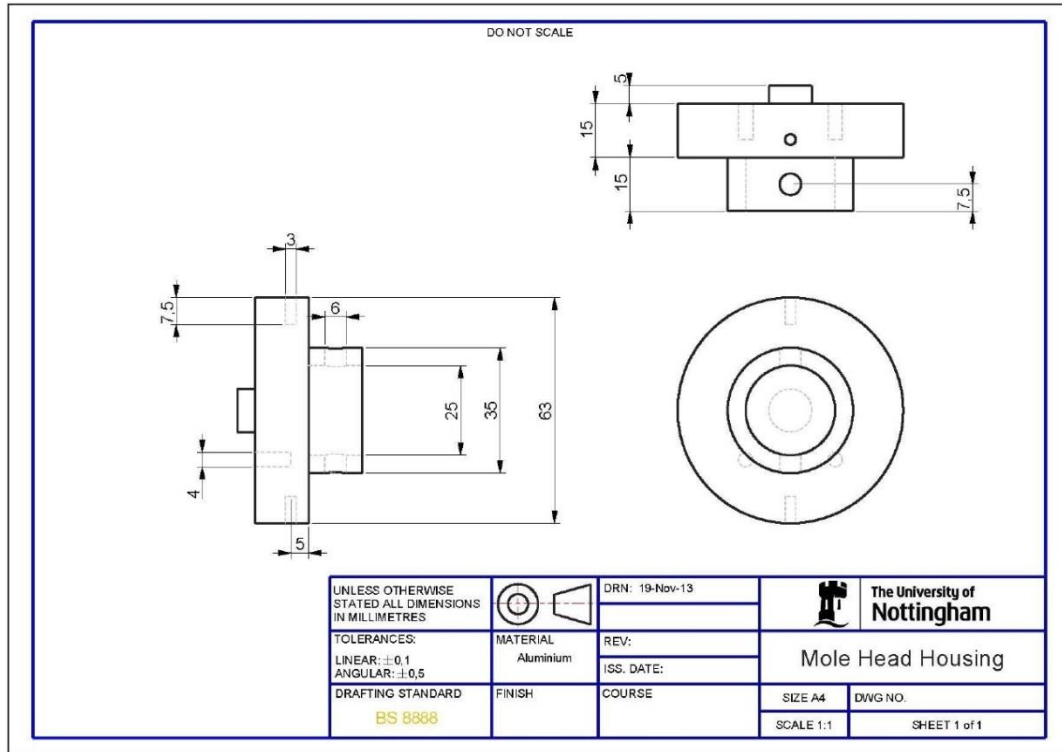


Table F.2: Mole head housing detailed drawing.

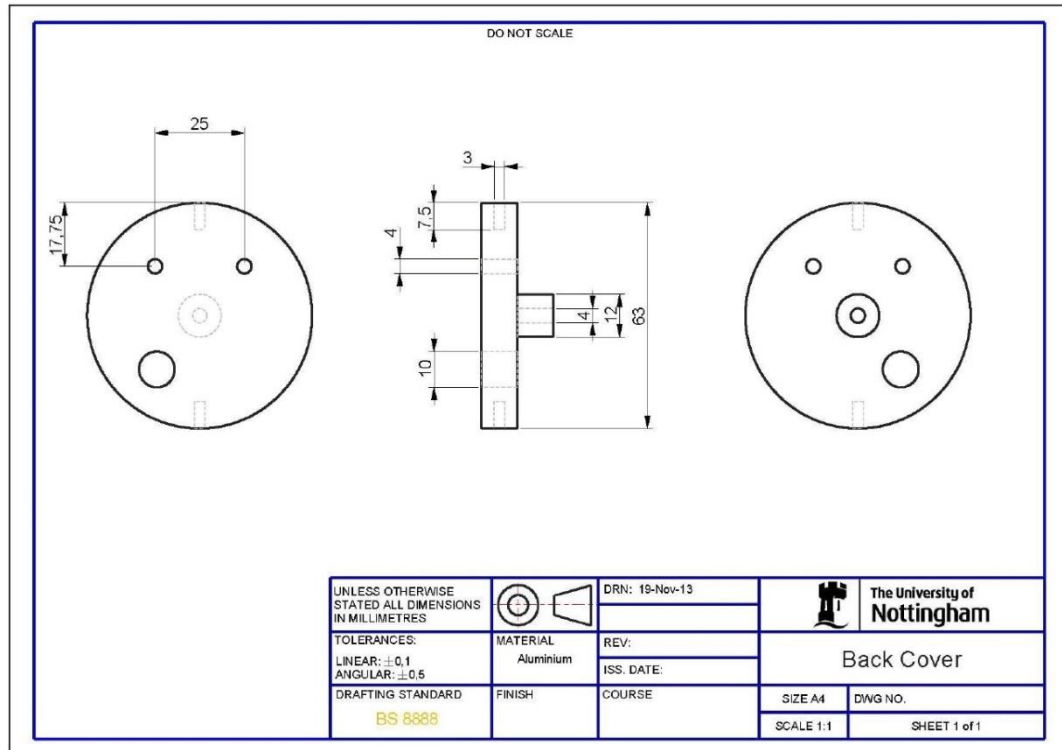


Table F.3: Back head housing detailed drawing.

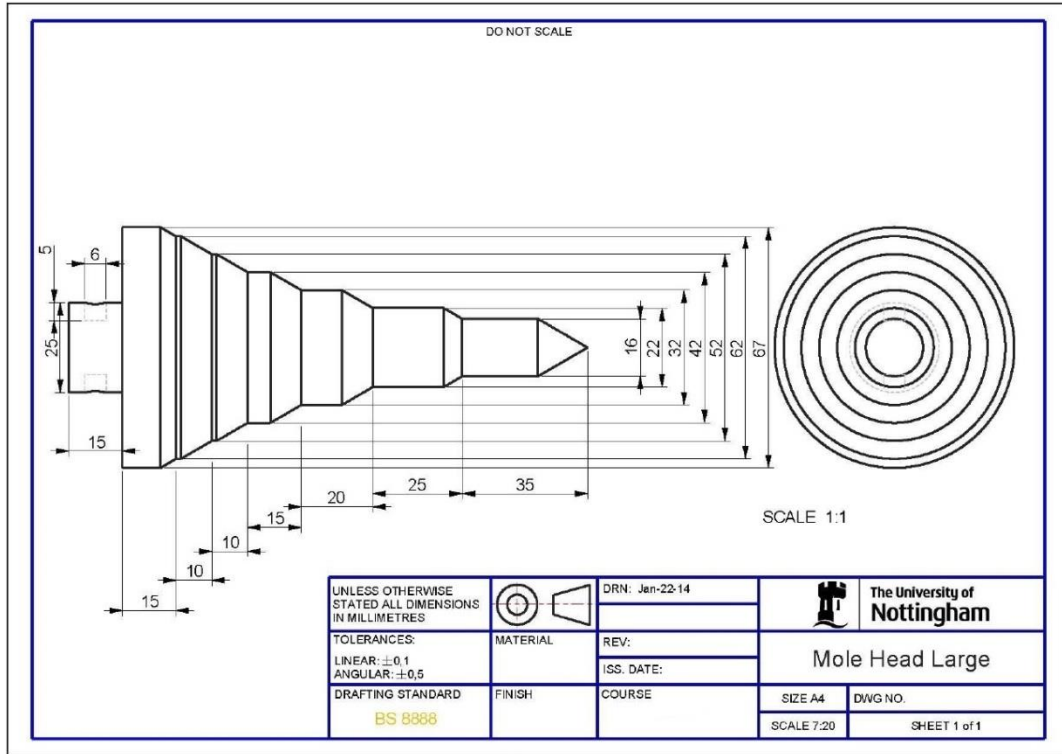


Table F.4: Mole head detailed drawing.

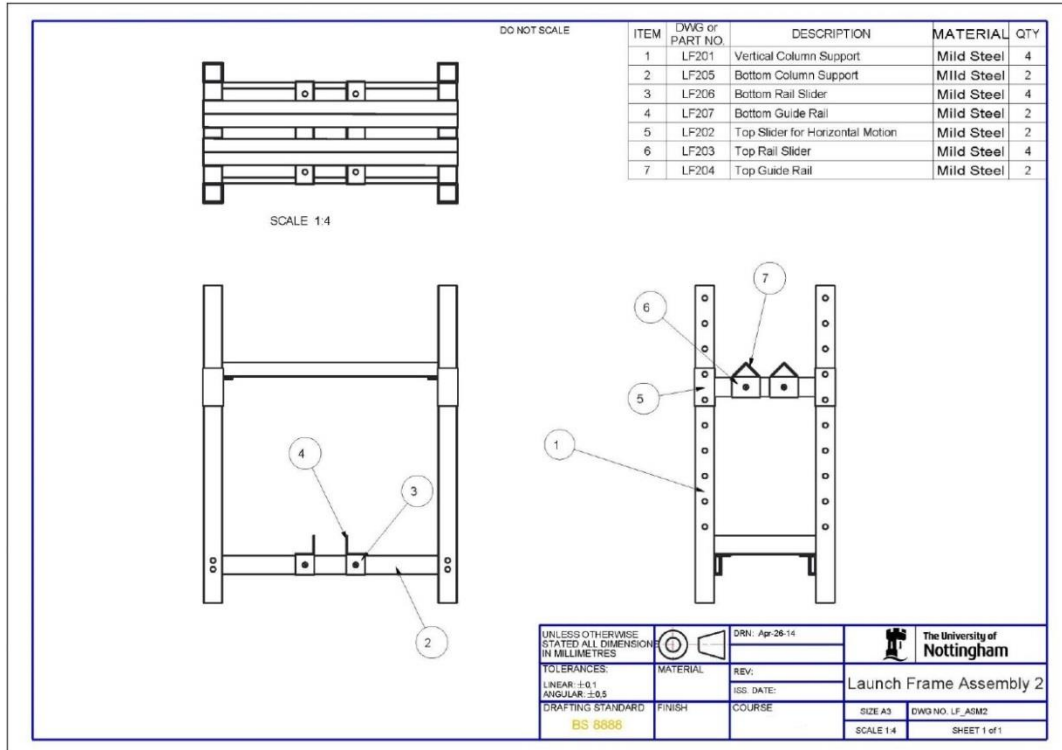


Table F.5: Schematic diagram of launch frame.

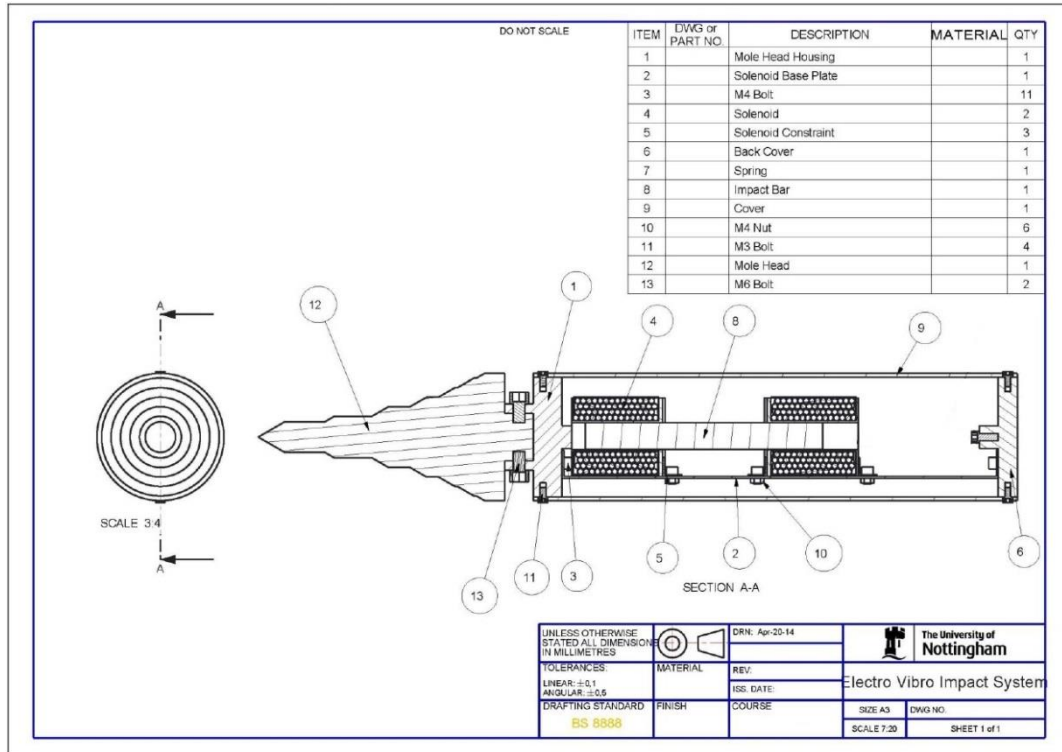


Table F.6: Schematic diagram of electro-vibroimpact prototype.

Reference

- [1] K. Ahn and S. Yokota, "Intelligent switching control of pneumatic actuator using on/off solenoid valves," *Mechatronics*, vol. 15, pp. 683-702, 2005.
- [2] V. I. Babitsky, *Theory of vibro-impact systems and applications*. Berlin: Springer-Verlag, 1998.
- [3] C. N. Bapat, "The General Motion of an Inclined Impact Damper with Friction," *Journal of Sound and Vibration*, vol. 184, pp. 417-427, 1995.
- [4] C. N. Bapat, "Periodic Motions of an Impact Oscillator," *Journal of Sound and Vibration*, vol. 209, pp. 43-60, 1998.
- [5] D. D. Barkan, *Dynamics of Bases and Foundations*. New York, 1962.
- [6] A. D. Batako, V. I. Babitsky, and N. A. Halliwell, "A self-excited system of percussive-rotary drilling," *Journal of Sound and Vibration*, vol. 259, pp. 97-118, 2003.
- [7] A. D. Batako, V. I. Babitsky, and N. A. Halliwell, "Modelling of vibro-impact penetration of self-exciting percussive-rotary drill bit," *Journal of Sound and Vibration*, vol. 271, pp. 209-225, 2004.
- [8] A. Benamar, "Dynamic pile response using two pile-driving techniques," *Soil Dynamics and Earthquake Engineering*, vol. 20, pp. 243-247, 2000.
- [9] J. J. Blakley, "A linear oscillating ferroresonant machine," *IEEE Transactions on Magnetics*, vol. 19, pp. 1574-1579, 1983.

- [10] Q. Cao, M. Wiercigroch, E. Pavlovskaia, C. Grebogi, and J. M. T. Thompson, "Archetypal Oscillator for Smooth and Discontinuous Dynamics," *Physical Review E*, vol. 74, pp. 1-5, 2006.
- [11] Q. Cao, M. Wiercigroch, E. Pavlovskaia, J. M. T. Thompson, and C. Grebogi, "Piecewise Linear Approach to an Archetypal Oscillator for Smooth and Discontinuous Dynamics," *Philosophical Transactions of the Royal Society-Part A*, vol. 366, pp. 635-652, 2008.
- [12] D. Chu and F. C. Moon, "Dynamic Instabilities in Magnetically Levitated Models," *Journal of Applied Physics*, vol. 54, pp. 1619-1625, 1982.
- [13] W.-C. Ding, J. H. Xie, and Q. G. Sun, "Interaction of Hopf and period doubling bifurcations of a vibro-impact system," *Journal of Sound and Vibration*, vol. 275, pp. 27-45, 2004.
- [14] C. W. Don, *Vibratory and impact-vibration pile driving equipment.*, Vulcanhammer, Available: <http://www.vulcanhammer.info/vibro/Vibrator.pdf>, (1998).
- [15] M. N. El-Derini, "Mathematical model of a solenoid for energy and force calculations," *J.Phys, D: Appl. Phys.*, vol. 17, pp. 503-508, 1984.
- [16] D.-M. Fang, X.-N. Wang, Y. Zhou, and X.-L. Zhao, "Fabrication and performance of a micromachined 3D solenoid inductor," *Microelectronics Journal*, vol. 37, pp. 948-951, 2005.
- [17] U. Galvanetto and S. R. Bishop, "Computational Techniques for Nonlinear Dynamics in Multiple Friction Oscillators," *Computer Methods in Applied Mechanics and Engineering*, vol. 163, pp. 373-382, 1998.

- [18] O. Gomis-Bellmunt, S. Galceran-Arellano, A. S. Andreu, D. Montesinos-Miracle, and L. F. Campanile, "Linear electromagnet actuator modeling for optimization of mechatronic and adaptronic systems," *Mechatronics*, vol. 17, pp. 153-163, 2006.
- [19] T. Hasegawa, K. Nakashima, F. Omatsu, and K. Ikuta, "Multi-directional micro-switching valve chip with rotary mechanism," *Sensors and Actuators A*, vol. 143, pp. 390-398, 2008.
- [20] J.-H. Ho, "Nonlinear Dynamics and Control of an Electro-vibro Impact System," PhD Thesis, The University of Nottingham, 2010.
- [21] J.-H. Ho and K.-C. Woo, "Approximate analytical solution describing oscillations of a conductor in a magnetic field," *Nonlinear Dynamics*, vol. 64, pp. 315-330, 2011.
- [22] E. Kallenbacha, H. Kuben, V. Zoppig, K. Feindta, R. Hermann, and F. Beyer, "New polarized electromagnetic actuators as integrated mechatronic components," *Design and application, Mechatronics*, vol. 9, pp. 769-784, 1999.
- [23] A. M. Krivtsov and M. Wiercigroch, "Dry Friction Model of Percussive Drilling," *Mechanica*, vol. 34, pp. 425-435, 1999.
- [24] A. M. Krivtsov and M. Wiercigroch, "Penetration rate prediction for percussive drilling via dry friction model," *Chaos, Solitons & Fractals*, vol. 11, pp. 2479-2485, 2000.
- [25] A. M. Krivtsov, E. Pavlovskaja, and M. Wiercigroch, "Impact fracture of rock materials due to percussive drilling action," in *XXI ICTAM*, Warsaw, Poland, 2004.

- [26] G. Luo and H. Yao, "Dynamics of a small vibro-impact pile driver," *Non-linear Analysis: Real World Applications*, vol. 9, pp. 1361-1377, 2008.
- [27] A. I. Markov, "Ultrasonic drilling and boring of hard non-metallic materials with diamond tools," *Stanki i Instrument*, vol. 48, p. 33, 1977.
- [28] E. A. Mendrela and Z. J. Pudlowski, "Transients and dynamics in a linear reluctance self-oscillating motor," *IEEE Transactions on Energy Conversion*, vol. 7, pp. 183-191, 1992.
- [29] E. A. Mendrela, "Comparison of the performance of a linear reluctance oscillating motor operating under AC supply with one under DC supply," *IEEE Transactions on Energy Conversion*, vol. 14, pp. 328-332, 1999.
- [30] C. Miller and L. Bredernyer, "Innovative safety valve selection techniques and data," *Journal of Hazardous Materials*, vol. 142, pp. 685-688, 2007.
- [31] F. C. Moon and S. W. Shaw, "Chaotic Vibrations of a Beam with Non-linear Boundary Conditions," *Journal of Non-Linear Mechanics*, vol. 18, pp. 465-477, 1983.
- [32] V.-D. Nguyen and K.-C. Woo, "New electro-vibro impact system," *Proceedings of the Institution of Mechanical Engineers Part C: Journal of Mechanical Engineering Science*, vol. 222, pp. 629-642, 2008.
- [33] V.-D. Nguyen and K.-C. Woo, "Nonlinear dynamic responses of new electro-vibroimpact system," *Journal of Sound and Vibration*, vol. 310, pp. 769-775, 2008.

- [34] V.-D. Nguyen, K.-C. Woo, and E. Pavlovskaja, "Experimental study and mathematical modeling of a new vibro-impact milling device," *International Journal of Non-linear Mechanics*, vol. 43, pp. 542-550, 2008.
- [35] A. B. Nordmark, "Non-periodic Motion caused by Grazing Incidence in an Impact Oscillator," *Journal of Sound and Vibration*, vol. 145, pp. 279-297, 1991.
- [36] A. B. Nordmark, "Existence of Periodic Orbits in Grazing Bifurcations of Impacting Mechanical Oscillators," *Institute of Physics Publishing, Nonlinearity*, vol. 14, pp. 1517-1542, 2001.
- [37] A. B. Nordmark, H. Dancowicz, and A. Champneys, "Discontinuity-induced Bifurcation in Systems with Impacts and Friction," *International Journal of Non-linear Mechanics*, vol. 44, pp. 1011-1023, 2009.
- [38] H. E. Nusse and J. A. Yorke, *Dynamics: Numerical Explorations*, Second Edition ed.: Springer, 1998.
- [39] H.-S. Park, J.-S. Hwang, W.-Y. Choi, D.-S. Shim, K.-W. Na, and S.-O. Choi, "Development of micro-fluxgate sensors with electroplated magnetic cores for electronic compass," *Sensors and Actuators A*, vol. 114, pp. 224-229, 2004.
- [40] E. Pavlovskaja, M. Wiercigroch, and C. Grebogi, "Two-dimensional Map for Impact Oscillator with Drift," *Physical Review E*, vol. 70, pp. 1-10, 2004.
- [41] F. Peterka, "Bifurcations and Transition Phenomena in an Impact Oscillator," *Chaos, Solitons and Fractals Vol7*, vol. 10, pp. 1635-1647, 1996.
- [42] F. Peterka, T. Kotera, and S. Ciperá, "Explanation of Appearance and Characteristics of Intermittency Chaos of Impact Oscillator," *Chaos, Solitons & Fractals*, vol. 19, pp. 1251-1259, 2004.

- [43] T. Pranoto, K. Nagaya, Y. Ebara, and Q. Q. Long, "Vibration suppression device using permanent-electromagnet and MRF shear damper," *Journal of Materials Processing Technology*, vol. 181, pp. 235-240, 2007.
- [44] R. Rashedin and T. Meydan, "Solenoid actuator for loudspeaker application," *Sensors and Actuators A*, vol. 129, pp. 220-223, 2006.
- [45] F. Satoru, "Electromagnetic passive dampers," presented at the 8th International Symposium on Magnetic Bearing, Mito, Japan, 2002.
- [46] S. W. Shaw and P. J. Holmes, "A Periodically Forced Impact Oscillator with Large Dissipation," *Journal of Applied Mechanics*, vol. 50, 1983.
- [47] S. W. Shaw and P. J. Holmes, "Periodically Forced Linear Oscillator with Impact: Chaos and Long-Period Motions," *Physical Review Letter*, vol. 51, pp. 623-626, 1983.
- [48] S. W. Shaw and P. J. Holmes, "A Periodically Forced Piecewise Linear Oscillator," *Journal of Sound and Vibration*, vol. 90, pp. 129-155, 1983.
- [49] T. Sugiura, H. Ura, and K. Kurado, "Magnetic stiffness of a coupled high-Tc superconducting levitation system," *Physica C*, vol. 392, pp. 648-653, 2003.
- [50] Z.-Y. Tai, W. Khoo, G.-C. Lee, and Z.-Y. Lim, "Compact Electro-vibro Impact System," M.Eng Final Year Project, Mechanical, Manufacture and Material Engineering, The University of Nottingham Malaysia Campus, Malaysia, 2014.
- [51] K.-N. Tamas, G. Stepan, and F. C. Moon, "Subcritical Hopf Bifurcation in the Delay Equation Model for Machine Tool Vibrations," *Nonlinear Dynamics*, vol. 26, pp. 121-142, 2001.

- [52] J. M. T. Thompson and R. Ghaffari, "Chaotic Dynamics of an Impact Oscillator," *Physical Review E*, vol. 27, pp. 1741-1743, 1983.
- [53] E. e. Topcu, I. Yuksel, and Z. Karmis, "Development of electro-pneumatic fast switching valve and investigation of its characteristics," *Mechatronics*, vol. 16, pp. 365-378, 2006.
- [54] S. A. Tsaplin, "Vibroudarnye Mekhanizmy Dlya Dorozhno-Mostovogo Stroitelstva (Impact-Vibration mechanisms for Road Bridge Construction).", Avtotransizdat, Moscow., 1953.
- [55] D. J. Wagg, G. Karpodinis, and S. R. Bishop, "An Experimental Study of the Impulse Response of a Vibro-Impacting Cantilever Beam," Earthquake Engineering Research Centre, University of Bristol, Queens Building, University Walk, Bristol BS8 1TR, U.K., 1999.
- [56] M. Wiercigroch, R. D. Neilson, and M. A. Player, "Material removal rate prediction for ultrasonic drilling of hard materials using an impact oscillator approach," *Physics Letters A*, vol. 259, pp. 91-96, 1999.
- [57] M. Wiercigroch, "Modelling of dynamical system with motion dependent discontinuities," *Chaos, Solitons and Fractals*, vol. 11, pp. 2429-2442, 2000.
- [58] M. Wiercigroch, A. M. Krivtsov, and J. Wojewoda, "Dynamics of high frequency percussive drilling of hard materials," presented at the Nonlinear Dynamics and Chaos of Mechanical Systems with Discontinuities, World Scientific, Singapore, 2000.

- [59] M. Wiercigroch, J. Wojewoda, and A. M. Krivtsov, "Dynamics of ultrasonic percussive drilling of hard rocks," *Journal of Sound and Vibration*, vol. 280, pp. 739-757, 2005.
- [60] K.-C. Woo, A. A. Rodger, R. D. Neilson, and M. Wiercigroch, "Application of the Harmonic Balance Method to Ground Molding Machines Operating in Periodic Regimes," *Chaos, Solitons and Fractals*, vol. 11, pp. 2515-2525, 2000.
- [61] Y. Xu and B. Jonesa, "Simple means of predicting the dynamic response of electromagnetic actuators," *Mechatronics*, vol. 7, pp. 589-598, 1997.
- [62] P. Yu, N. Popplewell, and A. H. Shah, "Instability Trends of Inertially Coupled Galloping, Part II: Periodic Vibrations," *Journal of Sound and Vibration*, vol. 183, pp. 679-691, 1995.